



ORBIT - Online Repository of Birkbeck Institutional Theses

Enabling Open Access to Birkbeck's Research Degree output

Variations in slip-rate and earthquake occurrence across 3D structural complexities on active normal faults

<https://eprints.bbk.ac.uk/id/eprint/40488/>

Version: Full Version

Citation: Iezzi, Francesco (2020) Variations in slip-rate and earthquake occurrence across 3D structural complexities on active normal faults. [Thesis] (Unpublished)

© 2020 The Author(s)

All material available through ORBIT is protected by intellectual property law, including copyright law.

Any use made of the contents should comply with the relevant law.

[Deposit Guide](#)
Contact: [email](#)

BIRKBECK, UNIVERSITY OF LONDON

**Variations in slip-rate and earthquake
occurrence across 3D structural
complexities on active normal faults**

Author:

Francesco Iezzi

Supervisors:

Prof. Gerald Roberts

Dr. Joanna Faure Walker

Thesis submitted to the

Department of Earth and Planetary Sciences

for the degree of

Doctor of Philosophy

Declaration

Declaration of originality

I, Francesco Iezzi, confirm that the work presented in this thesis is my own. Where information has been derived from other sources, I confirm that this has been indicated in the thesis.

Copyright declaration

The copyright of this thesis rest with the author. Researchers are free to copy, redistribute, remix and transform this thesis on the condition that it is appropriately attributed.

Doctoral committee

Prof. Gerald Roberts
Department of Earth and Planetary Sciences
Birkbeck, University of London
Dr. Joanna Faure Walker
Institute of Risk and Disaster Reduction
University College of London

Founding

This study was funded by NERC Studentship NE/L002485/1, NERC Standard Grant NE/I024127/1, NERC Urgency Grants NE/P01660X/1 and NE/P018858/1, CIAF NERC Grant Project 9183/1017.

*All that you touch
And all that you see
All that you taste
All you feel
And all that you love
And all that you hate
All you distrust
All you save
And all that you give
And all that you deal
And all that you buy
Beg, borrow or steal
And all you create
And all you destroy
And all that you do
And all that you say
And all that you eat
And everyone you meet
And all that you slight
And everyone you fight
And all that is now
And all that is gone
And all that's to come
And everything under the sun is in tune
But the sun is eclipsed by the moon*

(The Dark Side of the Moon, Pink Floyd)

Acknowledgments

To my dearest friends, without them I wouldn't be at this point.

To my family, who unconditionally supported me in every decision I took.

To London NERC DTP and Birkbeck, who put money on me.

To my DTP friends, who made this journey a long holiday.

To my Birkbeck crew, a family I choose.

To Joanna, always there, an inspiration.

To Gerald, a mentor, a friend.

To London, I did not know I could love and hate at the same time.

To everyone I met during these years, even for 10 minutes you have changed my life.

Abstract

This PhD thesis provides a series of studies on the relationship between the non-planar geometry and the seismic behaviour of active normal faults. Herein, several examples show that throw and fault dip increase within along-strike fault bends in order to preserve the horizontal strain-rate within the bend and along the fault. This has been demonstrated for a variety of normal faults (a) located in different geodynamic domains and (b) for measurements of throw taken over different time periods. Furthermore, throw enhancement within fault bends has been observed on (1) immature faults, where fault bends are still propagating up to the surface and are not yet fully established, (2) well-established single fault segments, where fault bends affect one continuous fault segment, and (3) densely-spaced fault systems arranged across strike (with fault spacing < 5 km), where a change in strike across several fault segments creates an overall bend in the system. The results presented in this thesis suggest that the relationship between the non-planar geometry and the distribution of throw is scale-independent, and can act across systems of faults if they are closely spaced across strike. Moreover, ^{36}Cl -cosmogenic dating of tectonically-exposed fault planes on faults spaced > 5 km across-strike shows that these faults are clustered, with a non-systematic alternance of periods of rapid slip accumulation (i.e. earthquake clustering) and periods of quiescence (i.e. earthquake anti-clustering); this suggests that parallel faults interact in terms of sharing the regional strain-rate, with switching activity that affects the slip-rate on a single fault. The results have implications for numerous and diverse aspects of the earthquake geology, such as interpretation of palaeoseismology studies including at trench sites and cosmogenic dating of fault planes, empirical scaling relationships, PSHA, and off-fault deformation.

Table of Contents

Chapter 1	1
Introduction	1
1.1 Introduction of the scientific problems	1
1.1.1 Overview on probabilistic seismic hazard analysis	1
1.1.2 The relationship between local non-planar fault geometry and slip-rates ...	4
1.2 Aims and objectives of the Thesis	11
1.3 Thesis structure	13
1.4 Author statement.....	16
Chapter 2	18
Literature and Geological Background	18
2.1 The growth of normal faults	18
2.1.1 Evolution of the fault growth process through time	23
2.2 Evolution of 3D structural complexities in normal faults.....	26
2.2.1 Growth and propagation of along-strike fault bends	26
2.2.2 Role of 3D structural complexities in normal fault dynamics	28
2.3 Classic field-based measurements of fault slip-rates.....	29
2.3.1 Palaeoseismology.....	29
2.3.2 Fault scarp profiles.....	33
2.3.3 Cosmogenic dating of fault scarps	34
2.3.3.1 Theory of cosmogenic dating of fault scarps	36
2.3.3.2 Literature review of cosmogenic ³⁶ Cl dating of fault scarps	40
2.3.3.3 Modelling procedures to recover slip histories from ³⁶ Cl data on fault planes	44

2.3.4 Summary of classic field-based measurements of fault slip-rates	46
2.4 Definition of the seismic potential of active faults	47
2.4.1 Empirical fault scaling relationships.....	47
2.4.2 Seismic moment of an active fault.....	50
2.5 Geological background of field areas	51
2.5.1 Central Apennines, Italy	51
2.5.2 Western Volcanic Zone, Iceland.....	56
2.5.3 Attica, Central Greece.....	59
2.6 Summary	60
Chapter 3	61
Methods.....	61
3.1 Quantitative analysis of the geometry and kinematics of faulting.....	61
3.2 Measurements of fault throw over different time scales.....	64
3.3 Cosmogenic nuclide analysis to gain information on fault slip.....	67
3.3.1 Samples collection	68
3.3.2 Samples preparation.....	70
3.3.3 Modelling of ³⁶ Cl data	70
Chapter 4	72
Coseismic throw variation across along-strike bends on well-defined single normal fault segments: implications for displacement versus length scaling of earthquake ruptures.	72
4.1 Summary	72
4.2 Introduction.....	73

4.3 Geological background of the 2016 Central Italy seismic sequence and of the Mt. Vettore fault.....	77
4.4 Methods.....	79
4.4.1 The relationship between strain, fault geometry and coseismic throw.....	85
4.5 Results.....	87
4.5.1 Field observations.....	87
4.5.2 Comparison between long-term and coseismic activity of Mt. Vettore fault.....	99
4.5.3 Modelling the expected throw within fault bends.....	101
4.5.3.1 <i>Earthquakes on the Mt. Vettore fault</i>	101
4.5.3.2 <i>Coseismic offsets for other large normal faulting earthquakes</i>	104
4.5.3.3 <i>Comparison between field measurements and predictions of D_{max} from existing scaling relationships</i>	111
4.6 Discussion.....	117
4.7 Conclusions.....	123
Chapter 5.....	125
Occurrence of partial and total coseismic ruptures of segmented normal fault systems: Insights from the Central Apennines, Italy.....	125
5.1 Summary.....	125
5.2 Introduction.....	126
5.3 Geological background of the 6 th April 2009 M_w 6.3 L'Aquila earthquake ...	129
5.4 Methods.....	134
5.5 Results.....	141
5.5.1 Analysis of the geometry of the Aterno Valley Fault System.....	141
5.5.2 Analysis of the throw profiles of the Aterno Valley Fault System.....	142

5.5.3 Comparison between the longer-term activity of the Aterno Valley Fault System and the M_w 6.3 L'Aquila Earthquake.....	144
5.5.4 Comparison between the long-term and post-LGM throw-rates along the Aterno Valley Fault System.....	146
5.6 Discussion.....	148
5.7 Conclusions.....	153
Chapter 6.....	155
Throw-rates variation within linkage zones during the growth of a normal fault: case studies from the Western Volcanic Zone, Iceland.	155
6.1 Summary.....	155
6.2 Introduction.....	156
6.3 Geological background of Thingvellir rift and Hengill volcanic complex.....	160
6.4 Methods.....	161
6.5 Results.....	165
6.5.1 Thingvellir rift.....	165
6.5.1.1 <i>Almannagja fault</i>	165
6.5.1.2 <i>W-dipping faults</i>	173
6.5.2 Hengill volcanic complex.....	177
6.6 Discussion.....	182
6.7 Conclusions.....	185
Chapter 7.....	188
Across-strike variations of fault slip-rates constrained using <i>in situ</i> cosmogenic ^{36}Cl concentrations.....	188
7.1 Summary.....	188

7.2 Introduction.....	189
7.3 Geological background of Attica	193
7.4 Site characterizations	195
7.4.1 Milesi fault.....	195
7.4.2 Malakasa fault.....	198
7.4.3 Fili fault.....	200
7.5 Modelling the measured ³⁶ Cl concentrations.....	203
7.6 Results.....	204
7.7 Discussion.....	210
7.8 Conclusions.....	214
Chapter 8.....	216
Discussion	216
8.1 Summary of findings from previous chapters and questions that arise.	216
8.2 Implications for palaeoseismology	218
8.2.1 Trench site interpretations.....	218
8.2.2 Cosmogenic dating of exposed fault planes.....	222
8.3 Implications for scaling relationships	225
8.4 Implications for studies of strain accumulations for fault systems with varied fault spacing.....	226
8.5 Effect of non-planar fault geometry on the seismic hazard assessments.....	227
8.6 Effect of non-planar fault geometry on the coseismic off-fault deformation .	233
8.7 The effect of non-planar fault geometry on modelling the long-term geomorphology associated with normal faulting.....	240
8.8 Implications for reverse and strike-slip faulting	244
8.9 Summary.....	246

<i>Chapter 9</i>	247
Conclusions	247
<i>List of references</i>	252
<i>Appendix</i>	282

List of figures

<i>Figure 1.1: Map showing the fault source inputs used to calculate the seismic hazard of Italy.</i>	3
<i>Figure 1.2: Map of the Parasano fault showing a breaching fault propagating through a relay zone.</i>	5
<i>Figure 1.3: Along-strike profiles of the total throw and throw-rates of the Parasano fault.</i>	6
<i>Figure 1.4: Principal strain-rates calculated over 15 ± 3 ka within 1×2 km grid boxes orientated with axes NW-SE and NE-SW along the Parasano fault.</i>	7
<i>Figure 1.5: Variations of the throw-rate values within a breaching fault, relative to the throw rates on the outer faults, because of the variation of the angle of strike (a) and dip (b) on the breaching fault, with constant horizontal strain-rate.</i>	8
<i>Figure 1.6: Relationship between fault strike, throw and strain-rate across an along-strike fault bend on the Campo Felice fault and on the Colfiorito fault (Central Apennines, Italy).</i>	9
<i>Figure 1.7: The “geometry-dependent throw-rate theory”</i>	10
<i>Figure 2.1: Log-log plot of Displacement (d) versus the fault length (L) for various fault populations from different tectonic settings.</i>	19
<i>Figure 2.2: Conceptual model of interaction of sub-parallel faults.</i>	21
<i>Figure 2.3: Growth of an idealized extensional fault array.</i>	22
<i>Figure 2.4: Fault map together with throw and throw-rate profiles for active normal faults in the Central Apennines, Italy.</i>	23
<i>Figure 2.5: Conceptual models for the growth of a normal fault through time.</i>	24
<i>Figure 2.6: Schematic illustration of the idealized d/L growth trajectories for fault growth processes.</i>	25
<i>Figure 2.7: Diagram showing the 3D evolution of an along-strike fault bend through fault propagation, linkage and coalescence.</i>	27
<i>Figure 2.8: Example of a palaeoseismological study carried out on the Paganica-San Demetrio fault, Central Apennines, Italy.</i>	31
<i>Figure 2.9: Example of a fault scarp profiles across the L'Aquila fault, Central Apennines, Italy.</i>	34
<i>Figure 2.10: Model of fault scarp exhumation and the predicted ^{36}Cl concentration profile produced.</i>	36
<i>Figure 2.11: Contribution of the various cosmogenic and radiogenic sources to the production of in situ ^{36}Cl in the first 10 m below the ground surface.</i>	38
<i>Figure 2.12: Schematic representation of the geometry of a normal fault scarp and the possible pathways of cosmic rays that will affect the samples.</i>	40
<i>Figure 2.13: ^{36}Cl data from the Sparta fault and from the Kaparelli fault.</i>	42

Figure 2.14: ^{36}Cl measurements collected for different faults in Central Italy.....	44
Figure 2.15: Empirical fault scaling relationships from Wells and Coppersmith, (1994)	49
Figure 2.16: D_{max} /fault length empirical fault scaling relationships from Manighetti et al. (2007) (a) and from Wesnousky (2008).	50
Figure 2.17: Structural map of Italy.....	53
Figure 2.18: Map of the principal active normal faults in Central Italy.....	54
Figure 2.19: Location map of the study areas in Iceland.....	57
Figure 2.20: Interplay between resurfacing lava flows and active faults.	58
Figure 2.21: Location map of the study area in central Greece	60
Figure 3.1: Relationship between fault trace and topography and construction of strike lines.	62
Figure 3.2: Analysis of strike variability of bedrock fault planes and slip vectors for the South Alkyonides fault, Greece.....	63
Figure 3.3: Sketch of a fault scarp showing the criteria to measure Holocene fault throw.....	65
Figure 3.4: Sketch of the measurements collected with the Trupulse 360R® laser range finder.....	66
Figure 3.5: Sketch of a field site on a normal fault scarp.	68
Figure 3.6: Field photo of a sampling location on the Fili fault, central Greece.....	69
Figure 4.1: Location map of the 2016 central Italy seismic sequence.....	78
Figure 4.2: Field observations of the surface ruptures along the Mt. Vettore fault.....	82
Figure 4.3: Geological cross-sections across pre-rift strata on the Mt. Vettore fault. ...	84
Figure 4.4: Map of the Mt. Vettore fault.....	89
Figure 4.5: Field data following the 24 th August 2016 M_w 6.0 earthquake..	94
Figure 4.6: Field data following the 24th August and 30th October earthquakes.....	95
Figure 4.7: Analysis of strike variability of bedrock fault planes and slip vectors.	96
Figure 4.8: Comparison between the measured slip vector azimuths from both earthquakes and the slope dip directions.....	98
Figure 4.9: Long-term activity of the Mt. Vettore fault	100
Figure 4.10: Modelling the 24 th August M_w 6.0 and 30 th October M_w 6.5 earthquakes bend.....	103
Figure 4.11: Modelling the 1887 M_w 7.5 Sonora (a) and the 1981, M_w 6.4-6.7 Corinth (b) earthquakes.....	105
Figure 4.12: Modelling of historical earthquakes that ruptured across along-strike fault bends	107
Figure 4.13: Analysis of the sensitivity of varying strike and dip in modelling the five earthquakes presented in this thesis.	110

<i>Figure 4.14: Comparison between D_{max} and the expected M_w for D_{max} for given fault lengths from field data obtained from the scaling relationships in Wells and Coppersmith (1994).</i>	112
<i>Figure 4.15: Fault model used to analyze the effect of fault bends on scaling relationships.</i>	114
<i>Figure 4.16: Effect of fault bends on scaling relationships, seismic moment and stress drops, using Wells and Coppersmith (1994).</i>	116
<i>Figure 4.17: Effect of fault bends on scaling relationships, seismic moment and stress drops, using Wesnousky (2008)</i>	117
<i>Figure 5.1: Location map of the Aterno Valley Fault System, Italy.</i>	130
<i>Figure 5.2: Coseismic ruptures following the 2009 L'Aquila earthquake</i>	131
<i>Figure 5.3: Palaeoseismological hypothesis of the occurrence of multi-fault earthquakes across the Aterno Valley Fault System.</i>	133
<i>Figure 5.4: Geological cross-sections built across the Aterno Valley Fault System.</i>	137
<i>Figure 5.5: Measurements of throw since the demise of the Last Glacial Maximum (15 ± 3 ka).</i>	139
<i>Figure 5.6: New field measurements of throw and throw-rates since the demise of the Last Glacial Maximum (15 ± 3 ka) from fault scarps located along the Aterno Valley Fault System.</i>	140
<i>Figure 5.7: Analysis of the geometry of the Aterno Valley Fault System.</i>	142
<i>Figure 5.8: Throw profiles of the Aterno Valley Fault System.</i>	146
<i>Figure 5.9: Comparison between the measured long-term throw profile and the predicted long-term throw profile of the Aterno Valley Fault System.</i>	148
<i>Figure 5.10: Complete and partial ruptures of the Aterno Valley Fault System.</i>	151
<i>Figure 6.1: Location map of the study areas in Iceland.</i>	159
<i>Figure 6.2: Cartoons of the field measurements</i>	163
<i>Figure 6.3: Field photos of the Almannagja fault.</i>	166
<i>Figure 6.4: Structural map of the Almannagja fault.</i>	167
<i>Figure 6.5: Detailed structural maps of the Almannagja fault.</i>	168
<i>Figure 6.6: Along-strike throw profile of the Almannagja fault.</i>	170
<i>Figure 6.7: Study of the drainage in the footwall of the Almannagja fault.</i>	172
<i>Figure 6.8: Field photos of the W-Dipping faults in the Thingvellir rift.</i>	174
<i>Figure 6.9: Structural maps of the W-Dipping faults.</i>	176
<i>Figure 6.10: Along-strike throw profiles of the W-Dipping faults.</i>	177
<i>Figure 6.11: Field photos of the Hengill volcanic complex.</i>	178
<i>Figure 6.12: Structural map of the faults studied in the Hengill volcanic complex.</i>	179
<i>Figure 6.13: Along-strike throw profiles for faults in the Hengill volcanic complex.</i>	181

<i>Figure 6.14: Fault growth model showing that fault bends present faster throw rates, compared to the throw-rates on faults immediately outside the bend, since the onset of the fault linkage processes.</i>	184
<i>Figure 7.1: Regional strain-rates, topography and location of faults, and historical earthquakes across central Italy.</i>	191
<i>Figure 7.2: Maps of Attica, Greece</i>	194
<i>Figure 7.3: Site characterization of the Milesi fault.</i>	197
<i>Figure 7.4: Site characterization of the Malakasa fault.</i>	199
<i>Figure 7.5: Site characterization of the Fili fault.</i>	202
<i>Figure 7.6: Modelling the ³⁶Cl concentrations measured on the Milesi fault, Malakasa fault and Fili fault</i>	205
<i>Figure 7.7: Slip histories and intensities for the three faults within the last 15 ka</i>	207
<i>Figure 7.8: Comparison between the age since the fault scarps started to be preserved, as estimated through the cosmogenic exposure modelling, and their elevation at which they are exposed at the surface.</i>	209
<i>Figure 7.9: Summary of the principal findings.</i>	211
<i>Figure 8.1: Map of the northern tip of the Fucino fault.</i>	220
<i>Figure 8.2: Schematic fault with a prominent bend in its central part and two sampling sites on outer fault and bend.</i>	223
<i>Figure 8.3: Modelling the ³⁶Cl concentrations on the hypothetical fault shown in Figure 8.2.</i>	224
<i>Figure 8.4: Overview of the results of this thesis.</i>	228
<i>Figure 8.5: The effect of slip-rate enhancements on the seismicity rates of faults.</i>	231
<i>Figure 8.6: Observed InSAR line-of-sight displacement for the 26th October 2016 M_w 5.9 and the 30th October 2016 M_w 6.5 earthquakes, Central Italy.</i>	235
<i>Figure 8.7: Coseismic slip distributions for the Mt. Vettore fault and the related off-fault vertical displacement patterns.</i>	237
<i>Figure 8.8: Off-fault displacement profiles performed for the InSAR-derived deformation field and for the two models performed in this thesis.</i>	238
<i>Figure 8.9: Fault model of central Italy from Guerts et al. (2018).</i>	241
<i>Figure 8.10: Off-fault deformation patterns calculated for a non-planar fault and for a fault with straight geometry</i>	242
<i>Figure 8.11: Profiles across the subsided and uplifted areas shown in Figure 8.10 for the two different fault models.</i>	243
<i>Figure 8.12: Kinematic data of the 1999 Chi Chi earthquake</i>	245

List of tables

<i>Table 4.1: Parameters used to model the earthquakes...</i>	<i>108</i>
<i>Table 5.5b: Measurements of post-LGM throw along the Aterno Valley Fault System</i>	<i>139</i>
<i>Table 8.1: Input values used to perform modelling into the MB tool...</i>	<i>230</i>
<i>Table 8.2: Output values released by the MB tool.....</i>	<i>230</i>

Chapter 1

Introduction

This chapter introduces the scientific problems and questions that will be addressed within this thesis. It presents the aims and objectives of the research and the structure of the PhD thesis.

1.1 Introduction of the scientific problems

1.1.1 Overview on probabilistic seismic hazard analysis

Probabilistic seismic hazard analysis (PSHA) aims to estimate the hazard of seismic-induced ground motion at a site by considering all the possible significant earthquakes affecting the area, evaluating the associated shaking at each site, and calculating the probabilities of these occurrences (National Research Council, Panel on Seismic Hazard Analysis, 1988). Two key parameters to estimate the probability of occurrence of a seismic event in a region are the fault slip-rate and the aperiodicity of the recurrence interval of a fault ($CV, \sqrt{Variance/Tmean}$; Pace et al., 2016). These parameters have large uncertainties, because of lack of time constraints for the fault activity and for the definition of an accurate earthquake recurrence interval. This PhD thesis aims to improve the knowledge on fault slip-rates and earthquake occurrence, studying how they relate to 3D structural complexities along active normal faults.

The above becomes important for seismic hazard assessments because in the last decade the PSHA community have focused on including active mapped faults and measured fault

slip-rates in hazard models (Stein et al., 2012; Field et al., 2014; Papanikolaou et al., 2015; Deligiannakis et al., 2016; Pace et al., 2016; Blumetti et al., 2017; Visini et al., 2019). This improves the spatial resolution in calculations of earthquake shaking occurrence and provides fault activity rates that do not suffer from incompleteness of the historical record or temporal earthquake clustering, which causes some active faults to not rupture within historical and instrumental observation windows. For example, Valentini et al. (2017) propose a seismic hazard model for Italy using active mapped faults as seismic sources and fault slip-rates to quantify the activity rates of faults, derived from geological, seismological and palaeoseismological data (Figure 1.1; Valentini et al., 2017).

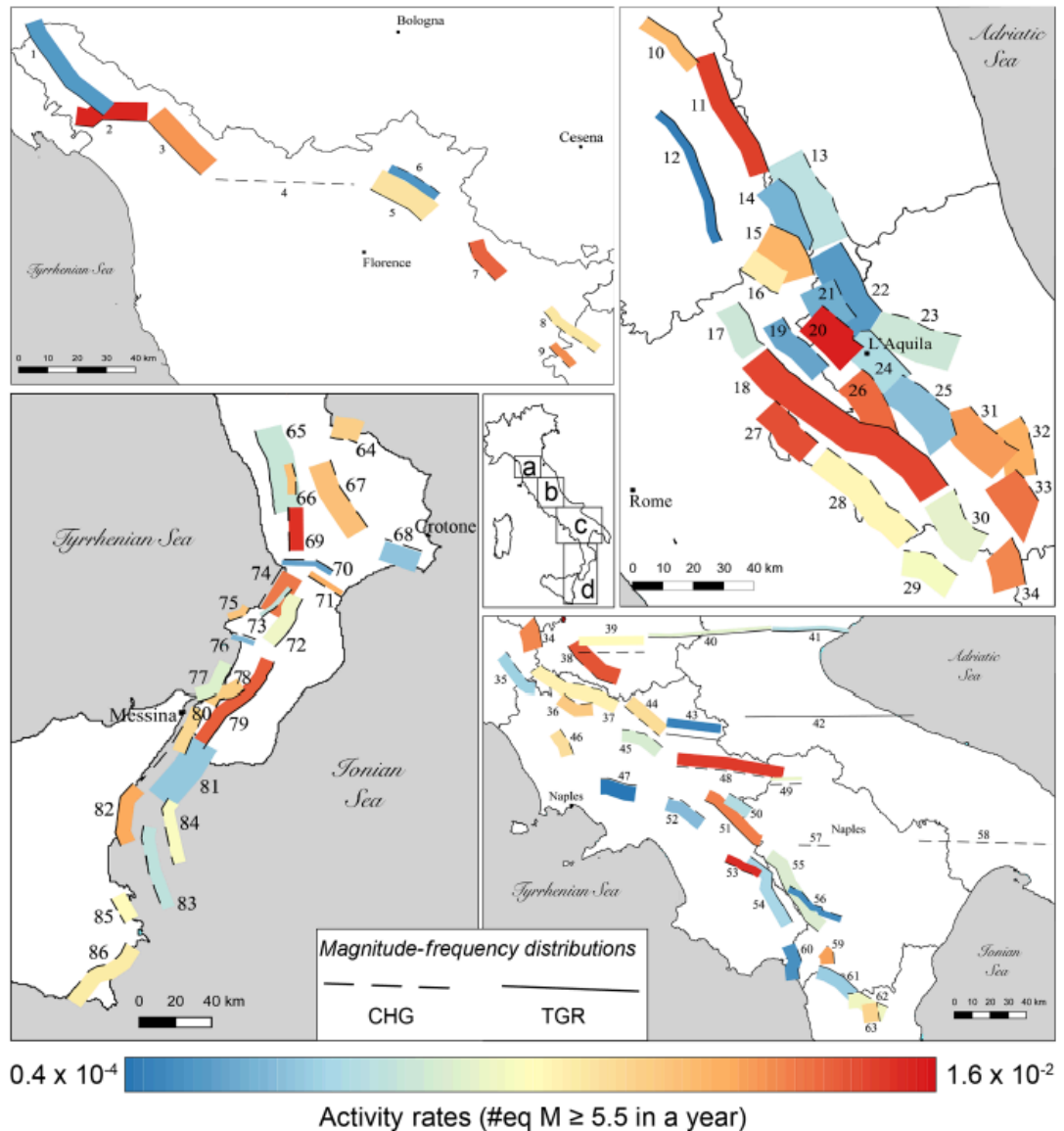


Figure 1.2: Map showing the fault source inputs used to calculate the seismic hazard of Italy in Valentini et al., 2017. The colour scale indicates the activity rate of each fault. From Valentini et al., 2017.

Models like that of Valentini et al. (2017) provide important insights into regional seismic hazard assessment, but yet they are based on two main assumptions. First, fault geometries are approximated as planar, and local 3D complexities in the fault geometry, such as along-strike fault bends, are not taken in account, and hence are assumed not to influence the hazard (Faure Walker et al., 2018; Iezzi et al., 2018). Second, each fault is assigned a uniform slip-rate, so slip-rate gradients along strike are assumed not

influence the hazard. These two assumptions are pointed out because recent works have suggested that 3D structural complexities along normal active faults can influence the slip-rate distribution along the fault (Faure Walker et al., 2009; 2015; Wilkinson et al., 2015; Mildon et al., 2016), for example increasing the slip-rate across along-strike fault bends. A systematic variation of slip-rates across 3D structural complexities will therefore be omitted from fault-based seismic hazard assessment, where slip-rates on simple planar faults are used to define the activity rates of faults (Faure Walker et al., 2018). This PhD thesis aims to explore the role of 3D structural complexities in the evolution and dynamics of active normal faults, in order to understand their relevance within fault-based seismic hazard assessments. In the next section the relationship between the local non-planar fault geometry and the fault slip-rate is introduced.

1.1.2 The relationship between local non-planar fault geometry and slip-rates

During the past decade, several papers have highlighted the existence of a relationship between the local non-planar fault geometry and the distribution of slip-rates along faults (Faure Walker et al., 2009; 2015; Wilkinson et al., 2015; Mildon et al., 2016). These works show that slip-rates in bends can be anomalous, compared to the expected value given the location along the fault, when measured across 3D structural complexities such as breaching faults and along-strike fault bends

Faure Walker et al. (2009) studied the Parasano Fault (Central Apennines, Italy). The fault exhibits a relay zone that is undergoing breaching, and a consistent slip vector azimuth along the entire fault (Figure 1.2). The authors show that minimum total throw measured over the whole history of slip on the fault and maximum throw-rate since 15 ± 3 ka are associated with the breach fault (Figure 1.3). The throw-rates were calculated from

the vertical offsets of a prominent rectilinear hill slope formed by erosion and deposition during the last glacial maximum (LGM), and preserved as climate change during the demise of the LGM decreased erosion and sedimentation rates. They noted that the 3D structural complexity of the breach fault in terms of its oblique strike compared to the overall strike of the Parasano fault, and the relatively steep dip ($67 \pm 5^\circ$ degrees in the breach fault; $61 \pm 5^\circ$ degrees for the outer faults).

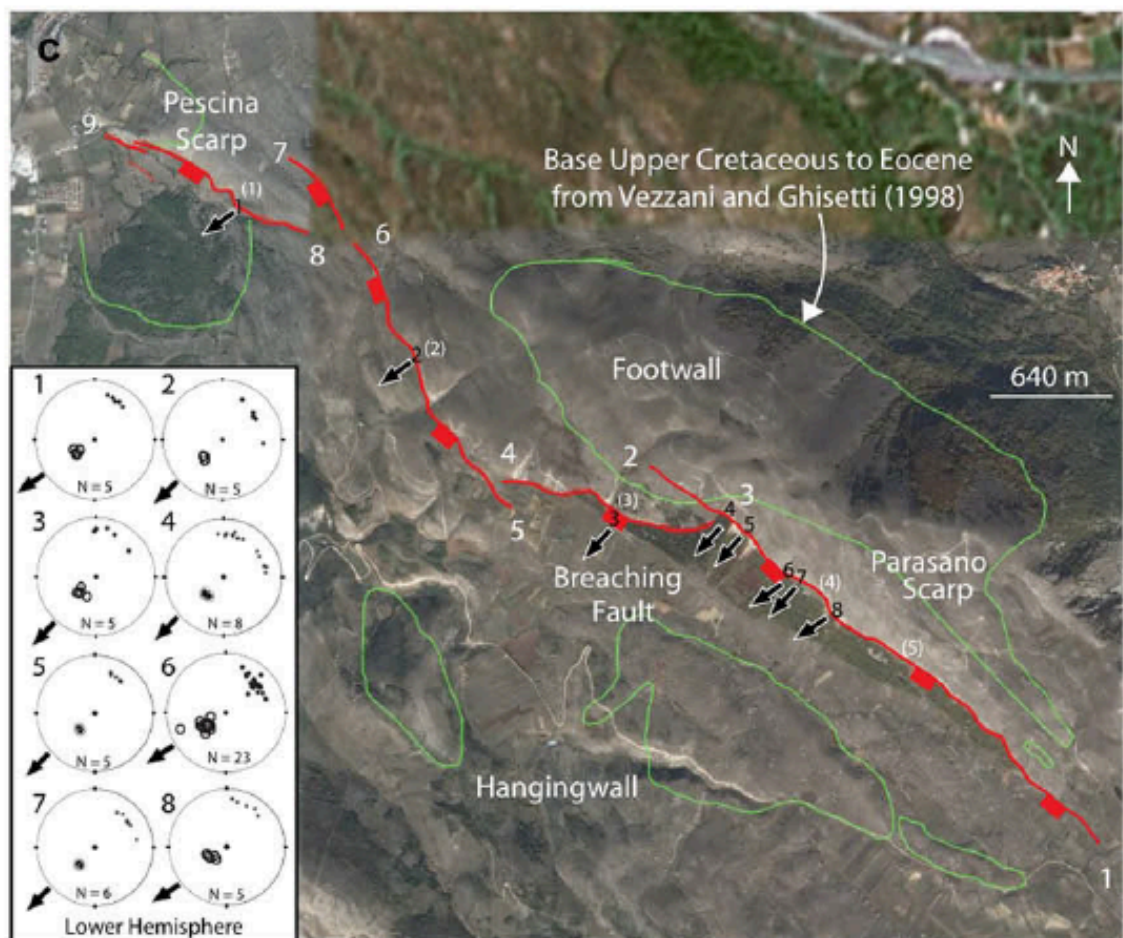


Figure 1.3: Map of the Parasano fault showing the location of the breaching fault propagating through a relay zone. Black arrows indicate that the slip vector azimuth is consistent along the entire fault trace. From Faure Walker et al., 2009.

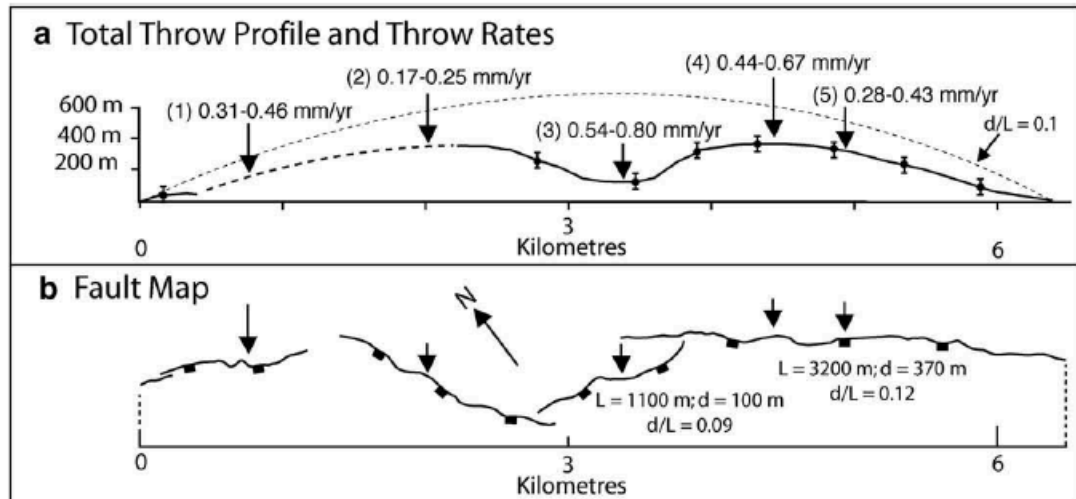


Figure 1.4: a) Along-strike profiles of the total throw and throw-rates of the Parasano fault. It shows that although the total throw is minimum in the location of the breaching fault, the throw-rates across the breaching fault are higher than the throw-rates on the faults outside the relay zone. b) Fault map of the Parasano fault. From Faure Walker et al., 2009.

To explain this discrepancy, the authors calculated the horizontal strain-rate along the Parasano fault within 1 x 2 km boxes using a modified version of the strain-rate equations from Kostrov (1974), that allows calculation of the strain-rate using field data as inputs. The calculations show that the strain-rate is highest associated with the breaching fault, decreases towards the overall fault tips (Figure 1.4; Faure Walker et al., 2009). Considering that strain-rates are commonly higher in the central part of a fault (e.g. Faure Walker et al., 2010), where the breaching fault is located, the authors suggest that these results are consistent with the outside faults and the breaching fault behaving as a single fault, with a classic distribution of maximum strain-rate in the centre of the fault and minimum strain-rates at the fault tips (Faure Walker et al., 2009). The low total throw is explained if the breach fault develops late in the faulting history, as it links two existing en-echelon faults.

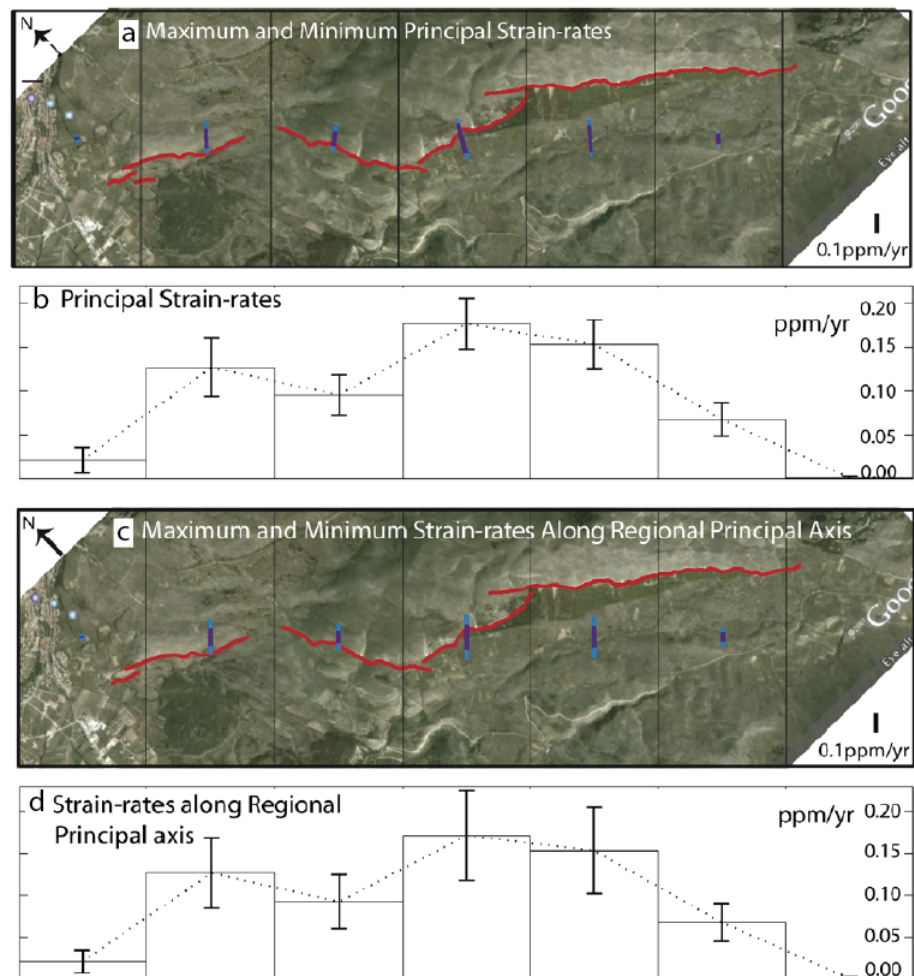


Figure 1.5: a) Principal strain-rates calculated over 15 ± 3 ka within 1×2 km grid boxes orientated with axes NW-SE and NE-SW; blue is maximum, purple is minimum. b) Graph of principal strain-rates showing the average principal strain-rates shown in a). c) and d) are maps and graphs of strain-rates along the regional principal axis of the entire fault (approximate SW-NE) within 1×2 km grid boxes orientated with axes NW-SE and NE-SW. From Faure Walker et al., 2009.

Following these findings, Faure Walker et al. (2009) developed theoretical calculations to evaluate the relationship between the local non-planar fault geometry, the horizontal strain-rate and the fault throw-rates (see the original paper for the equations describing this). These calculations show that fault strike and dip, fault throw, fault kinematics and horizontal strain-rates are interlinked variables. In order to conserve the principal horizontal strain-rate across the breaching fault, the throw-rate increases or decreases within the breaching fault, compared to the values on the outer faults, in response to the variation of the fault strike and dip across the breaching fault. This occurs with a consistent slip vector along the entire fault (Figure 1.5).

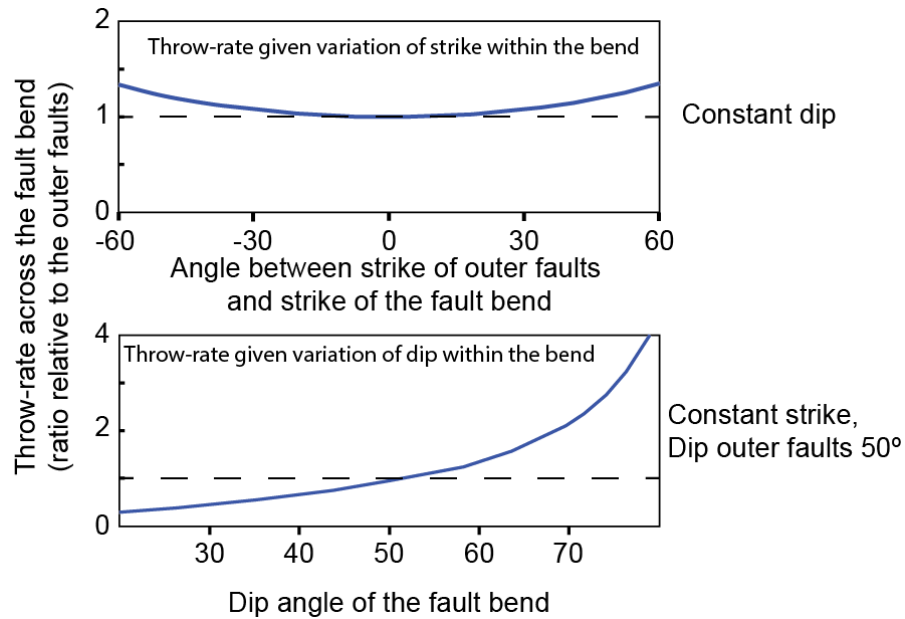


Figure 1.6: Variations of the throw-rate values within a breaching fault, relative to the throw-rates on the outer faults, because of the variation of the angle of strike (a) and dip (b) on the breaching fault, with constant horizontal strain-rate. Modified from Faure Walker et al., 2009.

Following these findings, Wilkinson et al. (2015) and Mildon et al. (2016) have studied natural examples of slip-rate variations across 3D structural complexities along active normal faults, and used the relationships to discuss their results.

Wilkinson et al. (2015) examined the Campo Felice fault (Central Apennines, Italy), which show a prominent along-strike fault bend in its strike, using structural geology and terrestrial laser scanning (Figure 1.6a). Detailed measurements of the fault strike, the post 15 ± 3 ka throw, and the strain-rate have been collected between the centre of the fault and the SE fault tip (Figure 1.6a). The field measurements show that across an along-strike fault bend the throw increases, but there is no increase in the strain-rate values calculated using the method of Faure Walker et al. (2009) (Figure 1.6a). Following these results, the authors suggest that the local throw-rate values are dependent on the geometry of the fault if strain-rate patterns are maintained.

Mildon et al. (2016) investigated the coseismic ruptures following the seismic sequence that occurred in Colfiorito, Central Italy, in 1997 (Figure 1.6b). The sequence culminated with three mainshocks with $M_w > 5.5$: the 26th September were recorded two earthquakes, M_w 5.7 and 6.0; the 14th October occurred the third mainshock, with M_w 5.6 (see references in Mildon et al., 2016). Structural mapping of the coseismic fresh stripe preserved on the bedrock fault planes by Mildon et al. (2016) suggests that fault strike, dip and coseismic throw are interlinked across a fault corrugation (small-scale fault bend): a change in strike orientation within the fault corrugation relates with increased fault dip and throw values within the corrugation (Figure 1.6b).

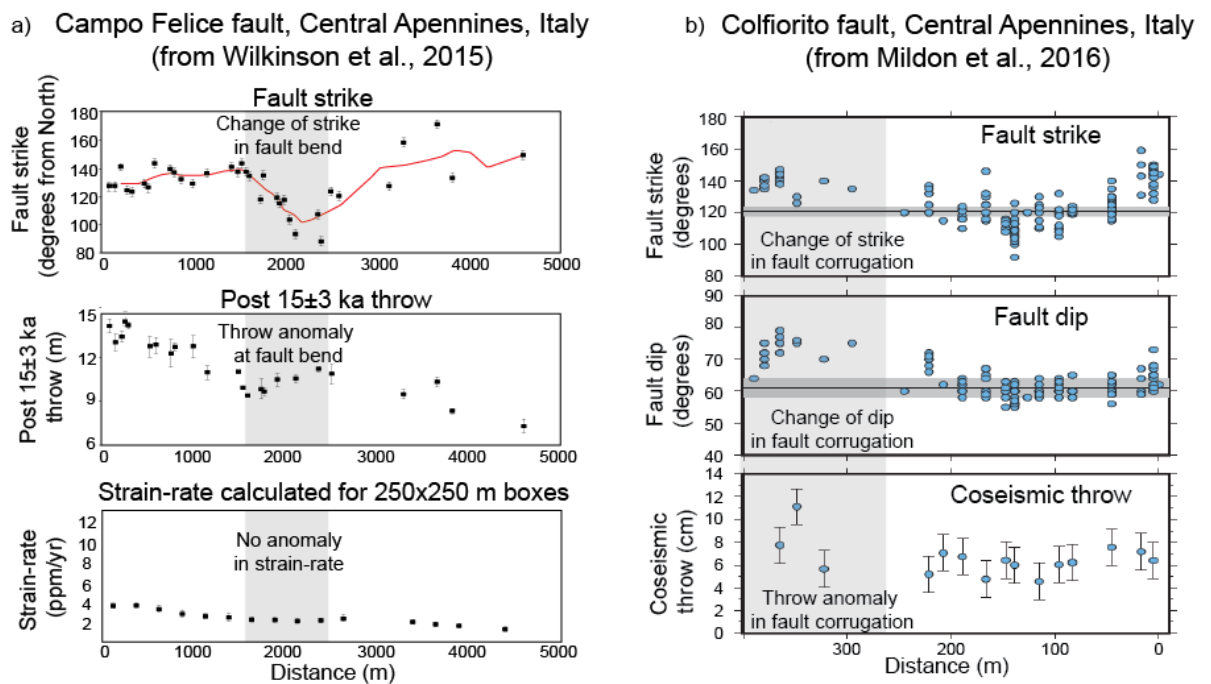


Figure 1.7: a) Relationship between fault strike, throw and strain-rate across an along-strike fault bend (grey area) on the Campo Felice fault (Central Apennines, Italy). 0 is the centre of the fault, distance increases towards the SE tip of the fault. Modified from Wilkinson et al., 2015. b) Relationship between fault strike, fault dip and the coseismic throw across a fault corrugation (grey area) on the Colfiorito fault (Central Apennines, Italy). Modified from Mildon et al., 2016.

All of these findings have been summarised in the “Geometry-dependent throw-rate theory”, which generalizes these results to the broad case of active normal faults (Figure 1.7; Faure Walker et al., 2015). This theory suggests that throw-rates might be higher or lower than the expected value given the location along the fault if these are sites of fault

linkage or sites with altering 3D orientation (e.g. along-strike fault bends). This is because if the strain-rate has to be preserved within along-strike fault bends, a higher throw-rate is required across a bend that has steeper dip and consistent dip-slip slip vector azimuth (Figure 1.7). This implies that values of slip-rates can be higher or lower than the expected, when measured across local complexities in the fault geometry.

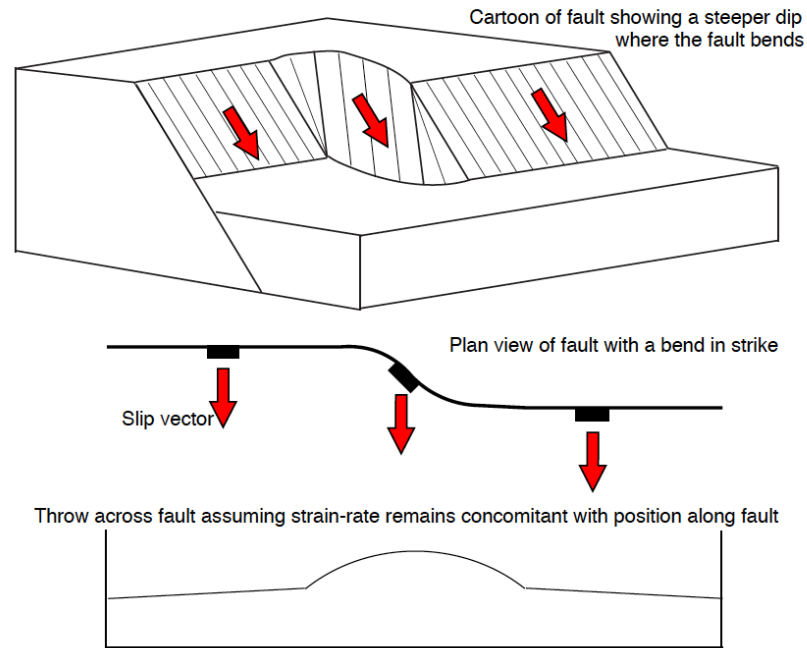


Figure 1.8: Cartoon showing the “geometry-dependent throw-rate theory”, which suggests a higher throw-rate across a fault segment that has more oblique strike and higher dip than the outer fault segments. From Faure Walker et al., 2015.

Overall, these results suggest that the local non-planar fault geometry produces slip-rate variations along active normal faults. However, there is a lack of natural examples of measurements around fault bends to assess whether such local slip-rate variations around fault bends are present during coseismic slip, when summed across regions containing a system of faults, and during the geometrical evolution of propagating/linking faults. It is also unclear whether such local slip-rate variations around fault bends differ in varied tectonic settings. Therefore, this PhD thesis aims to study different active normal faults, located in different geodynamic settings, in order to examine the consistency of the

relationship between 3D structural complexities and fault slip-rates measured over different time scales.

1.2 Aims and objectives of the Thesis

This thesis aims to explore the validity of the “Geometry-dependent throw-rate theory” for different typologies of normal faults, located in different geodynamic settings, studying slip-rate variations over different time scales. It also aims to evaluate the role that 3D structural complexities play in fault evolution and dynamics, in order to assess their importance for seismic hazard assessments. This is achieved by choosing field areas presenting (1) different geometries of active normal faults, (2) the possibility to measure slip-rates over different time scales and (3) located in different tectonic settings.

1) Studies have been conducted for coseismic ruptures on the Mt. Vettore fault, Central Apennines (Italy), which exhibits an along-strike fault bend on a well-defined fault segment. This fault ruptured twice during the 2016 Central Italy seismic sequence (Chiaraluce et al., 2017), and two mainshocks (24th August 2016 M_w 6.0, 30th October 2016 M_w 6.5) have produced two sets of coseismic ruptures within the fault bend and on the fault segments immediately outside the bend. Detailed field mapping of these coseismic ruptures, their relationship with longer term fault slip, and analysis of other coseismic ruptures from some of the largest historical normal-faulting earthquakes elsewhere in the world (USA, Mexico, Greece), allows to study the relationship between the local non-planar fault geometry and the distribution of coseismic throw associated with large normal faulting earthquakes, and how coseismic faulting produces longer term

fault offsets. This work is published in Iezzi et al. (2018) in the *Journal of Geophysical Research*.

2) Studies have been conducted on the Aterno Valley Fault System, Central Apennines (Italy), a segmented normal fault system that ruptured during the 2009 M_w 6.3 L'Aquila earthquake, and contains several active normal faults that appear to be cooperating in sharing the regional strain. An along-strike fault bend along the fault system causes a variation of strike across multiple fault segments. Measurements of the coseismic ruptures, the throw-rates cumulated over multiple seismic cycles (15 ± 3 ka), and of the geological throw have been analysed to explore the effect of the local non-planar fault geometry on slip-rates measured over different time scales for a segmented fault system. This work is published in Iezzi et al. (2019) in the *Journal of Structural Geology*.

3) Studies have been conducted on the Thingvellir rift and on the Hengill volcanic complex, Western Volcanic zone (Iceland). This field area is characterized by normal active faults propagating through recent Holocene lava flows, and faults appear at the surface with different stages of fault maturity. Structural maps and measurements of the fault offsets are collected to (1) explore the evolution of the slip-rates across 3D structural complexities at different stages of maturity, and (2) to test the validity of the “Geometry-dependent throw-rate theory” on a geodynamic domain of a mid-oceanic rift. This study is published in Iezzi et al. (2020) in *Journal of Structural Geology*.

4) Studies have been conducted in Attica, Central Greece, where measurements of the *in situ* cosmogenic ^{36}Cl exposure ages of fault planes have been performed on three active normal faults that are distributed across strike from one another. The *in situ* cosmogenic

³⁶Cl exposure ages can provide details of the timing of slip and earthquake activity. The faults in Attica are spaced across strike over a greater distance than the example from the Aterno Valley (Aterno Valley across strike spacing is $< \sim 5$ km; the Attica across strike spacing is ~ 5 -15 km). This study aims to investigate if the interaction between across-strike active normal faults differs due to fault spacing, causing variations of the slip-rate of faults.

This PhD thesis will use these findings from the above field areas to explore the influence of along-strike fault bends on fault evolution and fault dynamics, in order to evaluate the role of 3D structural complexities along active normal faults on the modern fault-based seismic hazard assessments.

1.3 Thesis structure

Chapter 1 introduces the scientific problems and objectives to be achieved in this thesis. It describes the current state-of-art of seismic hazard models and recent studies introducing the possible role played by 3D structural complexities in the distribution of slip-rates and into fault-based seismic hazard assessments.

Chapter 2 provides an overview of the earthquake science and describes the geological background underpinning the geographical study areas in this PhD thesis.

Chapter 3 describes the general methods used during this PhD thesis to achieve the objectives. It describes the techniques used to measure throw and throw rates in different time scales (coseismic throw, post-LGM throw (15 ± 3 ka), geological throw). It describes

the criteria used to pick a field site suitable for ^{36}Cl sampling and to perform the modelling of ^{36}Cl concentrations on fault planes.

Chapter 4 presents the results of the study conducted on the Mt. Vettore fault, Central Apennines, Italy. It shows that during the 2016 Central Italy seismic sequence, that ruptured the surface across an along-strike fault bend in the southern part of the fault in two separate earthquakes, the coseismic throw is consistently larger within the fault bend, when compared with coseismic throws immediately outside the fault bend. This chapter shows that larger coseismic throws within along-strike fault bends are a common feature for other historical large normal-faulting earthquakes. The chapter presents theoretical calculations showing that large coseismic throws within bends are needed in order to conserve the horizontal strain-rate, due to changes of fault strike and dip within the bend. This chapter explores the effect of fault bends on empirical fault scaling relationships, calculation of seismic moment and stress drop, explaining previously unexplained scatter in these scaling relationships (Iezzi et al., 2018).

Chapter 5 presents the results of the study conducted on the Aterno Valley Fault System, near L'Aquila, Central Apennines, Italy. It shows that an along-strike fault bend on a segmented normal fault system causes variation of slip-rates measured over different time scales. Moreover, it shows that structural geology can help to assess whether a segmented normal fault system has the potential to produce multi-fault earthquakes, during which earthquakes rupture multiple faults of the fault system. This chapter therefore discusses the role of structural geology and of fault bends in assessing the seismic potential of segmented normal fault systems (Iezzi et al., 2019).

Chapter 6 presents the results of the study conducted on the Western Volcanic Zone, Iceland. It shows that along-strike fault bends on normal faults propagating through recent lava flows causes slip-rate variations, independently from the state of maturity of the fault bend. This chapter discusses the implications of these findings in terms of fault growth models, and it shows that the “Geometry-dependent throw-rate theory” can be applied also in a geodynamic context of a mid-oceanic rift (Iezzi et al. 2020).

Chapter 7 presents the measurements of cosmogenic ^{36}Cl concentrations on fault planes of three faults across-strike distributed, located in Attica, Greece. It shows that the faults are clustered, with alternation through time of clusters and anticlusters of earthquakes. This chapter shows that the three faults are working together to accommodate the regional deformation, and that intervals of high activity rates on one fault corresponds to intervals of low activity rates on the other two faults.

Chapter 8 presents a general discussion of the findings obtained during this PhD thesis. It shows the implications of the effect of along-strike fault bends on (1) palaeoseismology studied through trenching, (2) gaining deformation rates from normal faults using cosmogenic isotopes, (3) scaling relationships, (4) fault spacing, (5) seismic hazard, (6) off-fault deformation, (7) the long-term geomorphology and geology of extensional basins, presenting implications for future works and (8) on behaviour and development of reverse and strike slip faults.

Chapter 9 presents the general conclusions of this PhD thesis.

1.4 Author statement

Chapter 4 - The author of this Thesis has personally collected the entirety of the field measurements shown in this Chapter.

Chapter 5 – The author of this Thesis has built geological cross-sections using published geological maps and fieldwork observations; Raw fault scarps profiles are provided to this thesis by Prof. Gerald Roberts, the author of this thesis performed their interpretations.

Chapter 6 – The author of this Thesis collected the entirety of the field measurements shown in this Chapter.

Chapter 7 – The author of this Thesis selected the studied faults, led field mapping to select the sampling sites and performed sampling of fault scarps; spent 2 weeks at SUERC to follow the samples preparation; modelled the ^{36}Cl concentrations adapting a published code.

The results presented in Chapter 4 are published in Iezzi et al. (2018) in *Journal of Geophysical Research: Solid Earth*.

The results presented in Chapter 5 are published in Iezzi et al. (2019) in *Journal of Structural Geology*.

The results presented in Chapter 6 are published in Iezzi et al. (2020) in *Journal of Structural Geology*.

The results presented in Chapter 7 are in preparation for submission in Iezzi et al. (2020) in *Geology*.

The author of this Thesis contributed as co-author in:

- Livio et al. (2016) –Provided field measurements of the surface ruptures and participated in the discussion of the results.

- Wilkinson et al. (2017) – Field measurements of surface ruptures; selection of locations for GNSS deployment and assistance in deployment.

- Mildon et al. (2017) – Definition of the trace of the Mt. Vettore fault. Provided field measurements of coseismic ruptures. Discussion of the results.

- Civico et al. (2018) and Villani et al. (2018) (EMERGEIO working group) – provided field measurements of coseismic ruptures.

Chapter 2

Literature and Geological Background

This chapter introduces the earthquake science at the base of this PhD thesis. It describes the process of growth of normal faults from a single isolated fault segment and how these faults interact within fault systems. It illustrates the growth and propagation of along-strike fault bends during fault linkage and outlines the current knowledge of the role of bends in fault dynamics and on the propagation of fault ruptures. This chapter introduces classic slip-rates measurements (palaeoseismology, fault scarp profiles and cosmogenic exposure dating of fault planes) and some of the parameters used to define the seismic potential of active faults (empirical fault scaling relationships, seismic moment, stress drop). It also introduces the geological background of the field areas.

2.1 The growth of normal faults

Natural datasets and analogue modelling show that isolated fault segments grow by tip propagation and accumulation of displacement. A global compilation of displacement (d) and fault length (L) data indicates a scaling relationship between these two dimensions, with a mean d/L ratio of 0.03 (Figure 2.1; Schlische et al., 1996). This means that as the fault accumulates displacement, it grows in length. This finding has strong implications for the processes of fault growth.

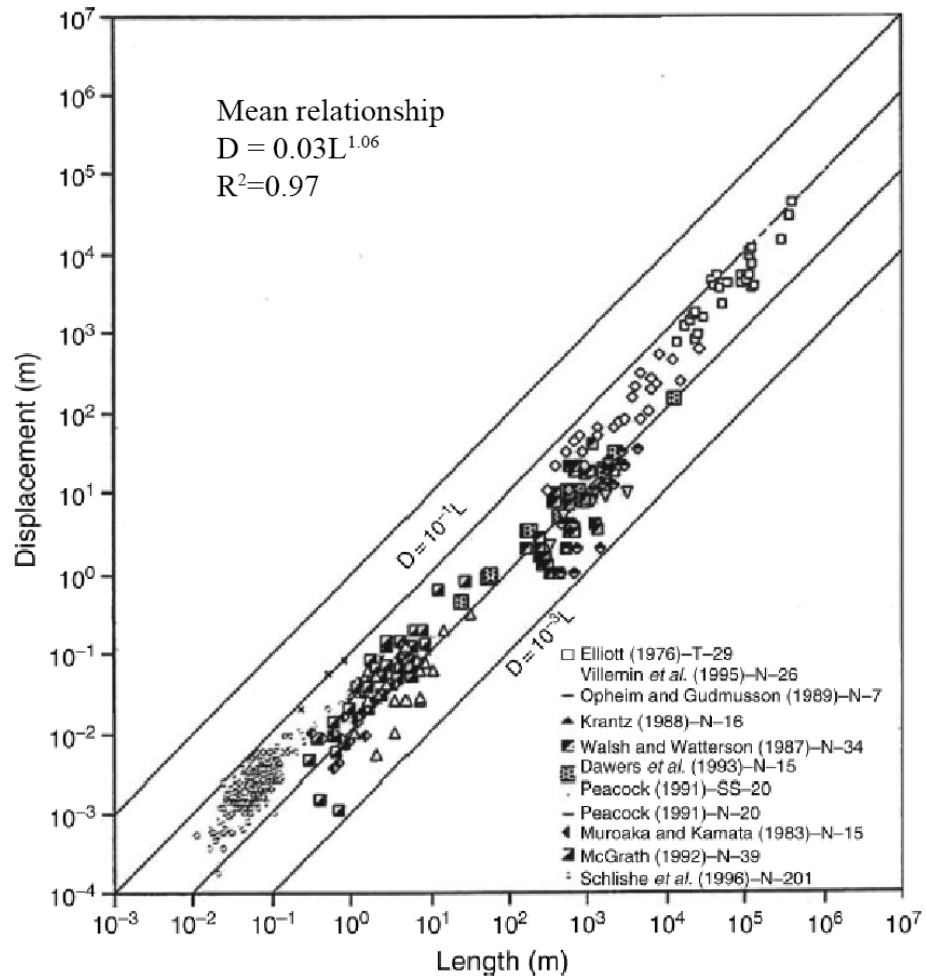


Figure 2.1: Log-log plot of Displacement (d) versus the fault length (L) for various fault populations from different tectonic settings. This shows that exist a roughly direct relationships between d and L , with a mean d/L ratio of 0.03. Modified from Scholz, 2018, after Schlishe *et al.*, 1996.

Normal faults do not usually grow as isolated fault segments, but rather they occur in fault populations that consist of a set of subparallel faults sharing the same slip vector (Scholz *et al.*, 2018). In this context, fault tip propagation leads to the overlap of individual faults, and can lead to linkage. This causes a mutual influence of the behaviour of the two adjacent faults.

A conceptual model proposed by Gupta and Scholz (2000) describes the evolution of two adjacent fault segments. If the lateral separation between the two faults is small enough, the fault tips will enter in the stress fields produced by slip on the adjacent fault. The fault

behaviour will start to be mutually influenced, and relay ramps will form in the overlapping zone between the two faults (Figure 2.2c-d). This mutual influence causes the two single faults to start acting as a single longer fault, in what is described as a “soft-linkage” of faults (Scholz, 2018). To respect the d/L ratio, the condition of fault linkage requires an adjustment in the distribution of slip on the newly formed fault, in order to recover the slip deficit (Figure 2.2c-d).

As the fault linkage persists, the relay ramp becomes breached, and smaller faults propagate through the relay zone and at both ends of the relay ramp (Figure 2.2e). The propagation of breaching faults persists until the two faults coalesce, in a situation of “hard-linkage” of faults (Scholz, 2018) (Figure 2.2f). The final configuration is a longer fault with the displacement profile having the same d/L scaling as the original single faults (Figure 2.2f).

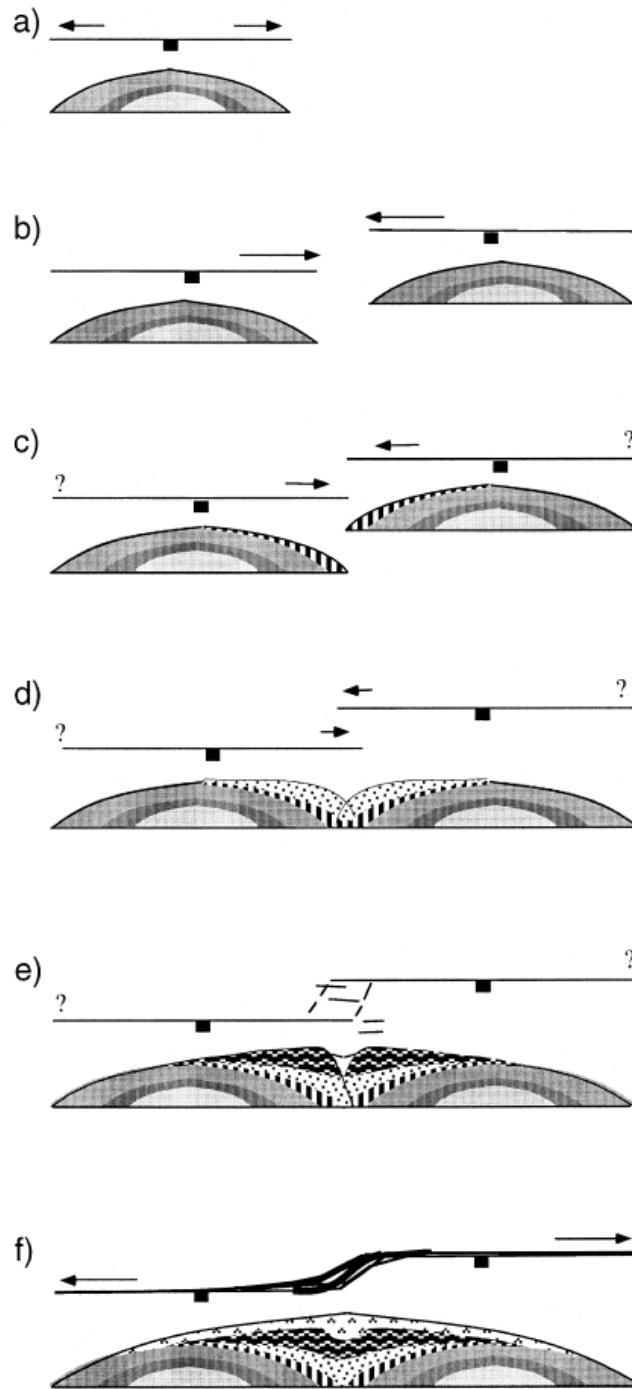


Figure 2.2: Conceptual model of interaction of sub-parallel faults. a-b) Adjacent single faults growing by tip propagation and displacement accumulation. c-d) Soft-linkage of faults: as the tip propagation persists, the two faults become close enough to mutually influence the behaviour, a relay ramp between the two faults form and they start to behave as a single longer fault. e) Relay ramp becomes breached, displacement profile continues to adjust to recover slope deficit. f) Hard-linkage of faults: faults coalesce, the final setting is a long fault trace with displacement profile of a single fault. From Gupta and Scholz, 2000

In complex normal fault arrays, interaction and linkage of originally isolated fault segments can occur over multiple adjacent faults. The link up of multiple smaller faults

produces fault lengths much greater than that expected for their single displacement profiles (Figure 2.3). To recover the slip deficit, Cowie and Roberts (2001) suggests a slip-rate gradient along the fault, with maximum slip-rates on the fault segments located in the central part of the array (Figure 2.3).

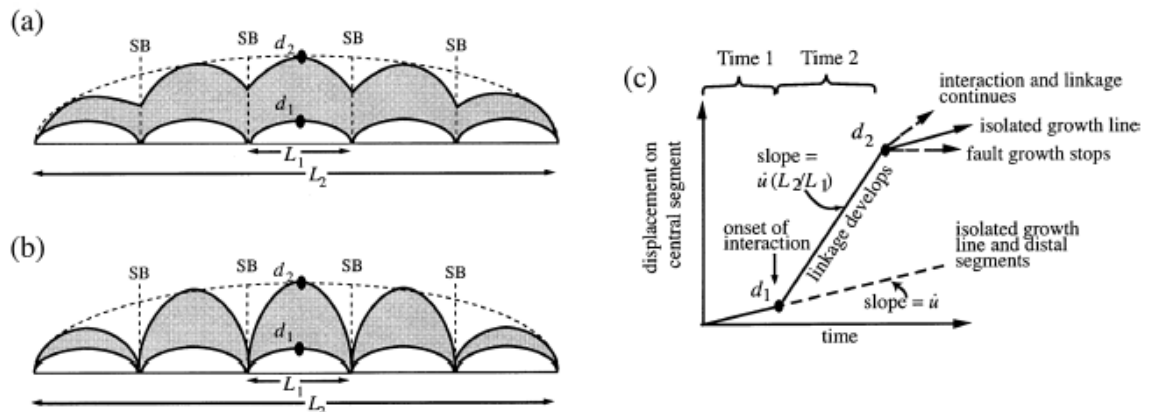


Figure 2.3: Growth of an idealized extensional fault array. In (a) the fault linkage occurs at the onset of profile re-adjustment, in (b) the linkage occurs late in the profile re-adjustment. (c) displacement as a function of time, showing that slip-rate sensibly increases as the fault interaction starts. From Cowie and Roberts, 2001.

Following this conceptual model, Cowie and Roberts (2001) suggest that in dense fault arrays, faults located in the centre of the fault array must have higher slip-rates than those located close to both ends of the array. This is confirmed by field measurements of throw-rates across normal faults within a dense fault system like the one in Central Apennines: throw-rates are maximum in the central part of the array, and decrease towards both ends of the fault system (Figure 2.4; Roberts and Michetti, 2004). These findings suggest that 17 active normal faults appear to be interacting and behaving as a larger “soft-linked” fault array which is 155 km in length and 55 km across strike, within which the fault slip-rates are working to adjust to the relative d/L ratio (Roberts and Michetti, 2004).

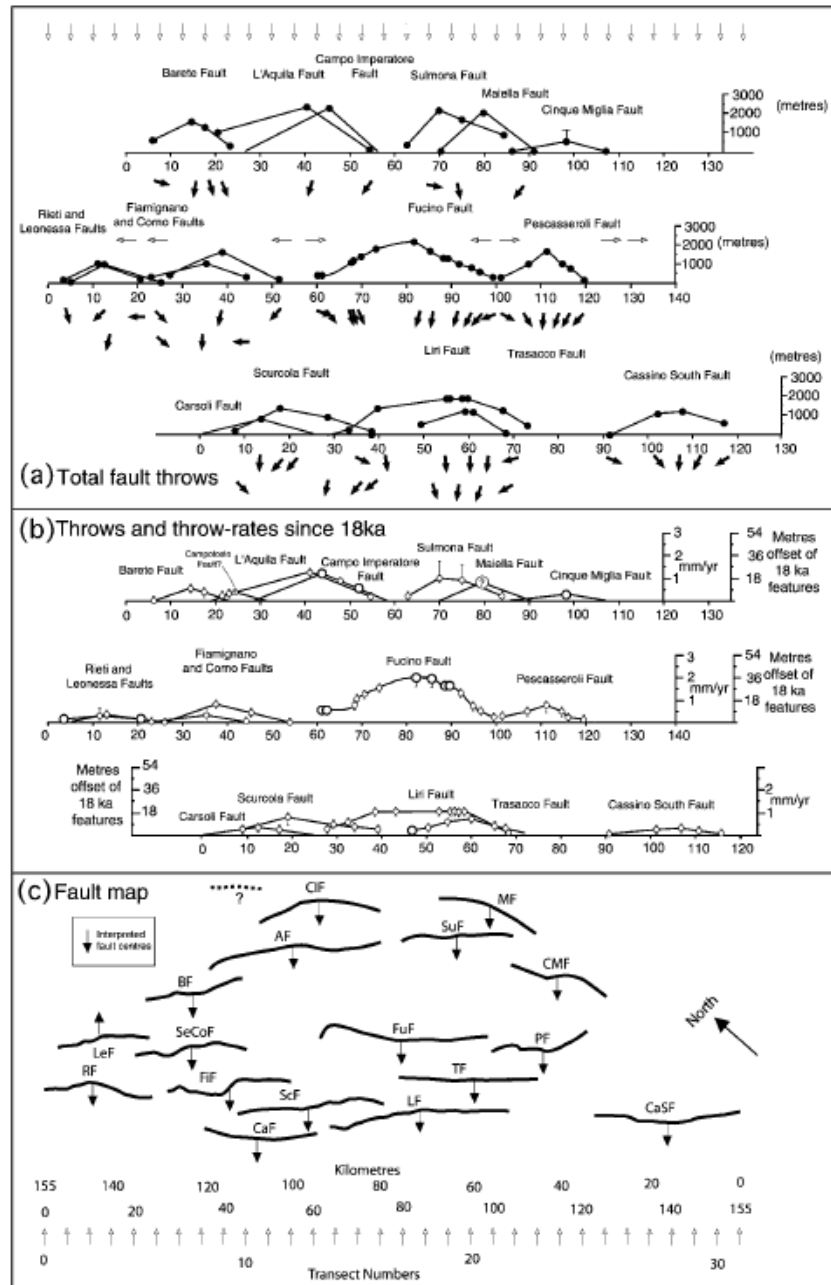


Figure 2.4: Fault map together with throw and throw-rate profiles for active normal faults in the Central Apennines, Italy. It shows that total throw (a) and throw-rates since 18ka (b) are maximum in the central part of the fault system and decrease towards the end of the fault system. This suggests that faults are part of a “soft-linked” fault array, and they are working in order to adapt the new d/L ratio. From Roberts and Michetti, 2004.

2.1.1 Evolution of the fault growth process through time

The previous section describes the process of normal fault growth as a combination of lateral propagation, linkage and displacement accumulation. Two further models have

been developed to refine how propagation, linkage and displacement accumulation occur through time: the “propagating fault model” and the “constant-length fault model” (Figure 2.5; Rotevatn et al., 2018). The propagating fault model suggests fault growth occurs via synchronous increase in fault length and displacement, whereas the constant length model suggests that faults establish early their fault lengths, and subsequently they grow by displacement accumulation (Figure 2.5; see Rotevatn et al. (2018), and references therein, for a review).

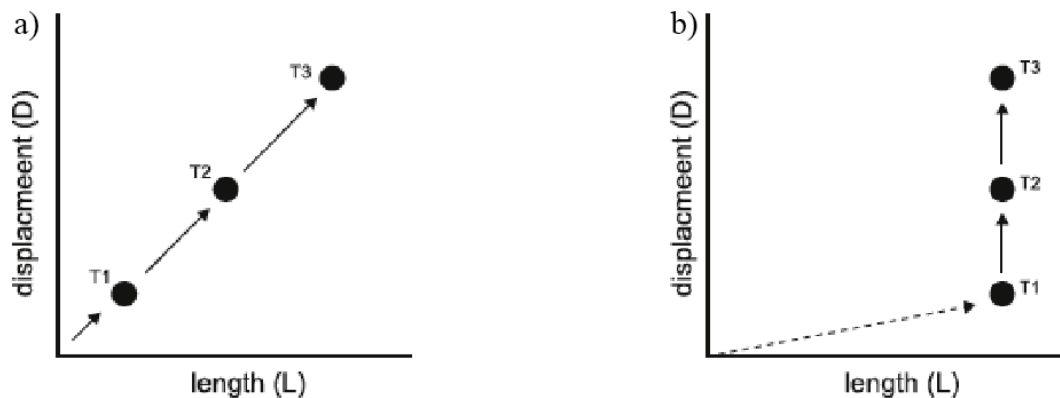


Figure 2.5: Conceptual models for the growth of a normal fault through time. a) Propagating fault model: the fault experiences synchronous growth in displacement and length through time. b) Constant-length fault model: the fault establishes first its length (T1), and subsequently grows in displacement accumulation. From Rotevatn et al., 2018.

Rotevatn et al. (2018) analysed a database of d/L data extracted at several points during the growth history of natural and experimentally reproduced faults. Their findings show that the early stages of fault growth are characterised by rapid fault lengthening and a variable amount of displacement accumulation (about 10-60% of the finite displacement), followed by stages dominated by displacement accumulation, without significant fault lengthening (Figure 2.6; Rotevatn et al., 2018). This suggests that fault growth proceeds with early establishment of fault length, and subsequent displacement accumulation in order to re-equilibrate the d/L ratio.

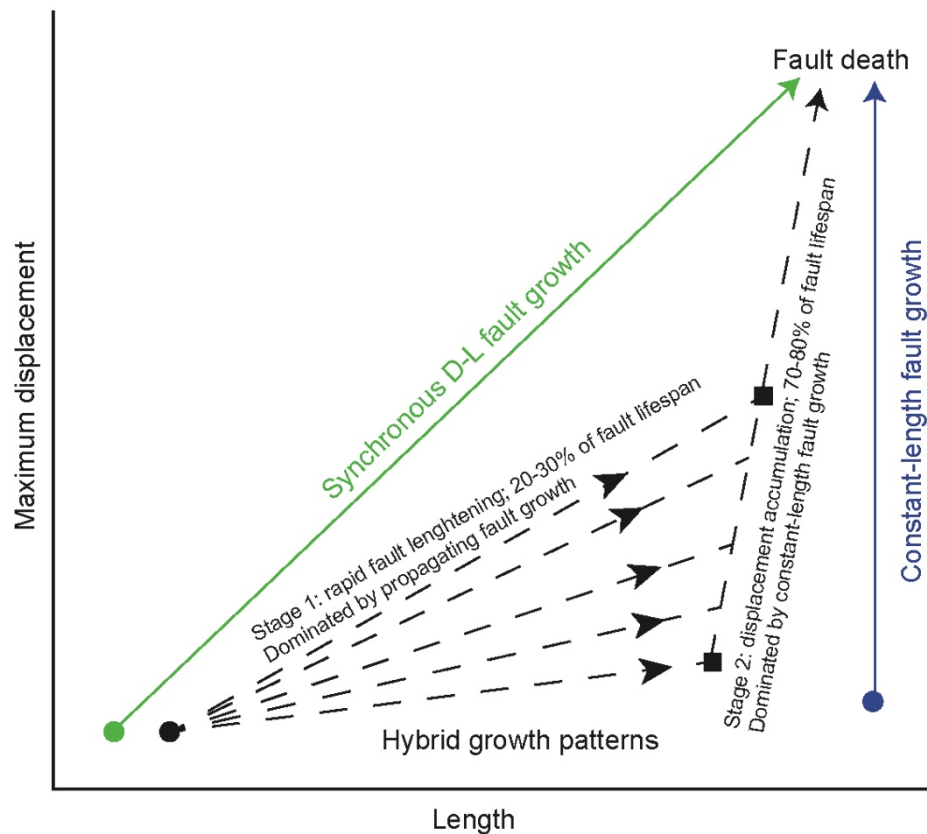


Figure 2.6: Schematic illustration of the idealized d/L growth trajectories for fault growth processes. Modified after Rotevatn et al., 2018.

Different factors can halt the growth in length of faults, and therefore control the length of fault segments. For instance, the thickness of the seismogenic layer is commonly thought to act as a control on the maximum length of the active faults (e.g. Jackson and White, 1989; Wells and Coppersmith, 1994). Moreover, the presence of pre-existing structural features can delimit the length of fault segments. For instance, the growth in length of a fault segment can be halted when this propagates up to a pre-existing fault with orthogonal strike.

During fault growth, along-strike fault bends develop as a consequence of the linkage of originally isolated fault segments (e.g. McLeod et al., 2000; Mansfield and Cartwright, 2001). The next section explores in detail the growth and propagation of the along-strike fault bends and their role in earthquake rupture propagation.

2.2 Evolution of 3D structural complexities in normal faults

This section introduces the evolution of along-strike fault bends during the fault linkage, with a particular focus on how the values of fault strike and dip evolve during the development of fault bends. This section also introduces the state-of-art, prior to this thesis, on the role of structural complexities, such as fault bends, in fault segmentation and on the seismic behaviour of active normal faults.

2.2.1 Growth and propagation of along-strike fault bends

The process of propagation of breach faults and growth of along-strike fault bends is described by analogue modelling (e.g. Manfield and Cartwright, 2001) and fault growth histories in nature described by stratigraphic evolution underpinned by 3D seismic reflection and age controls from wells (e.g. McLeod et al., 2000). Initially, separate faults grow by tip propagation, with en-echelon map geometries common (Figure 2.7b). During the fault linkage, new faults begin to grow in the relay zones between the en-echelon fault tips as incipient breach faults (fault c in Figure 2.7c; see McLeod et al. (2000) for real examples, their Figures 9 and 15, and Mansfield & Cartwright (2001) for examples in analogue experiments, their Figure 11). The dips of the new breach faults develop to accommodate the strain in the relay zone and the regional kinematics (see marker Y in Figure 2.7d; Roberts et al., 2007). Faults then link across the relay zones through tip propagation, followed by coalescence and linkage of breaching faults and the initial en-echelon faults (Figure 2.7d-f). The newly linked fault propagates up and down dip to increase the fault surface area through progressive deformation, until the coalescence is complete, and the along-strike bend fully established (Figure 2.7g).

A key point that emerges is that the dip value for the breach fault, which eventually becomes a fault bend, forms after the formation of the initial en-echelon faults and, in up-dip and down-dip locations, after the formation of a propagating fault within a bend (see Figure 2.7c-d). In other words, the change in strike across the fault bend controls the dip value of the fault bend. Hence, fault bends appear to be locations where both the strike and dip vary, implying therefore, that the throw must also vary (following Faure Walker et al., 2009).

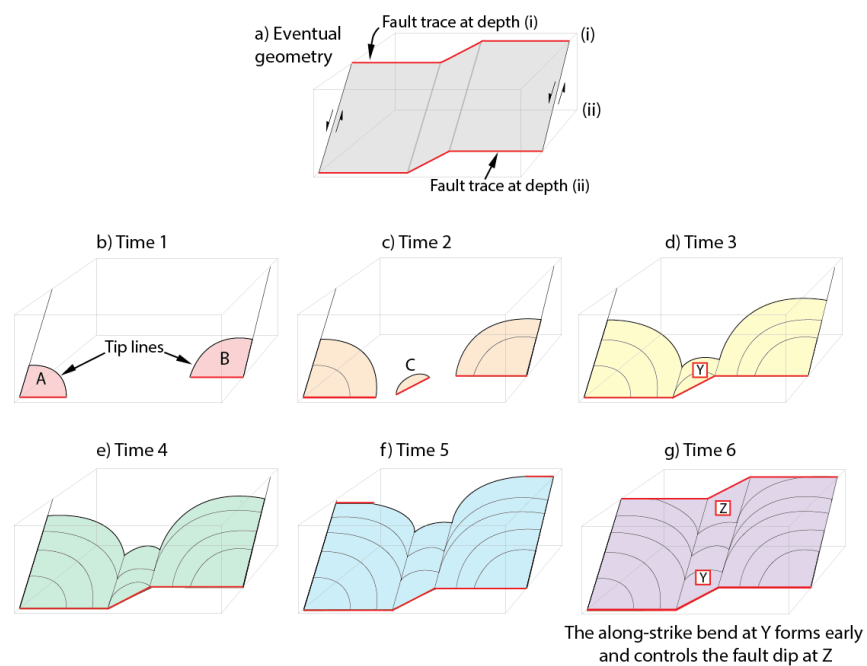


Figure 2.7: Diagram showing the 3D evolution of an along-strike fault bend through fault propagation, linkage and coalescence. a) 3D diagram of the eventual geometry of an along-strike fault bend that developed from two initial en-echelon normal faults at depth, which grew through along-strike and up-dip propagation, eventually coalescing into one linked fault surface through time. b) Time 1: The pink colour indicates the fault surface that has formed at this time, with the upper tip line indicated. The faults are still separate faults A and B. The traces of the faults on the lower surface of the box are indicated with a thick red line. c) Time 2: The orange colour indicates the fault surface has grown. The faults are still separate faults. A new breach fault C begins to grow to take up the strain between the two en-echelon faults, with a different value of dip when compared to the two faults, driven by the relationship between the principal strain and the fault strike. d) Time 3: The yellow colour indicates the fault surface has grown and now linked to form the fault surface at point Y. An along-strike fault bend has formed at depth and is propagating up-dip. e) Time 4: The green colour indicates further growth and upward propagation. The newly linked fault may also propagate down-dip, but this is not shown in this diagram. f) Time 5: Blue colour indicates further growth. The fault begins to intersect the top surface of the box, indicated by thick red lines. Like the bottom surface at time 1, the top surface at time 5 is deformed by two en-echelon faults. g) The purple colour indicates the final linked fault. The fault bend has fully propagated to the upper surface of the box. The fault surface at point Z forms at time 6. The dip at Z formed after the along-strike fault bend formed (time 3). This time sequence shows the developing along-strike fault bend is causal in forming the steep dip at Y and Z. From Iezzi et al., 2018; adapted from McLeod et al. (2000) and Manfield and Cartwright (2001).

2.2.2 Role of 3D structural complexities in normal fault dynamics

Empirical observations, supported by physical models examining rupture propagation and fault growth, show that 3D structural complexities, such as fault bends and steps in the fault trace, play a role in controlling the length of earthquake ruptures (Biasi and Wesnousky, 2017). In fact, bends and steps in the fault trace can act as impediments to rupture propagation. Hence, the size of earthquakes propagating on fault segments can be controlled by the presence of such 3D structural boundaries (Scholz, 2018). The reason why fault bends can act as barrier to rupture propagation is because they are site of changes in fault geometry, fault friction, elastic and gravitational energy, and inelastic rock deformation (Scholz, 2018). Recent works have focused attention on the role that 3D structural complexities exert on the propagation of fault ruptures, to understand whether coseismic ruptures propagate through these structures or they act as a barrier to their propagation.

Wesnousky (2008) and Biasi and Wesnousky (2016) compiled a database of coseismic surface ruptures of 75 continental earthquakes to evaluate the role steps in the fault traces (e.g. “soft-linked” faults) and fault bends (e.g. “hard-linked” faults) play in rupture propagations. These papers show that dip-slip fault ruptures have the capability to propagate across steps in the fault strike 5-7 km wide.

Biasi and Wesnousky (2017) use the above-mentioned database to study in detail the role of fault bends in the propagation of fault ruptures. Their findings suggest that dip-slip ruptures have the capability to propagate across bends with a change in angle of fault strike up to 50°.

Overall, these studies show that earthquake ruptures have the capability to propagate across along-strike fault bends, but they do not explore the evolution of the geometry, kinematics and rates of faulting within the bend once the coseismic rupture propagates through it. This PhD thesis therefore aims to fill this gap, studying how complexities such as fault bends affect the fault dynamics and the distribution of slip and slip-rates along the fault.

2.3 Classic field-based measurements of fault slip-rates

As described in Chapter 1, fault slip-rates are key to defining the activity rates of an active fault, and the “Geometry-dependent throw-rate theory” suggests slip-rate variations due to the effect of 3D structural complexities like along-strike fault bends. Therefore, field-based measurements of slip-rates are fundamental to understand the evolution of the geometry, kinematics and rates of faulting on active normal faults and for assessment of seismic hazard. Classic measurements of slip-rates are introduced in this section and discussed further in this thesis.

2.3.1 Palaeoseismology

Palaeoseismology is the study of past earthquakes, especially their location, timing and size (McCalpin, 2009). It consists of the identification of coseismic deformation of landforms and sediments produced during individual earthquakes (McCalpin, 2009). Palaeoseismology aims to reinforce the historical and instrumental records of seismicity

by describing and dating large past earthquakes that occurred either before the earliest records in the historical catalogue or in recent times (e.g. Michetti et al., 2005).

Palaeoseismological studies are commonly carried out through excavation of trenches, generally not exceeding 5 m depth, opened in agreement with the fault kinematics, e.g. perpendicular to the fault trace for extensional faults (Figure 2.8; Galli et al., 2008). Detailed logs of the trench walls are performed in order to identify evidence for individual palaeoearthquakes. The identification of palaeoearthquakes is mostly based on: (1) buried scarp-derived colluvial wedges and/or debris-filled fissures; (2) abrupt increases in the offset of stratigraphic units, or specific markers across the fault; (3) upward terminations of faults and cracks at the base or within a stratigraphic unit; (4) thickening of a stratigraphic unit across the fault, or deposition of a newly formed one (e.g., due to fault-induced damming of the drainage) (Galli et al., 2008).

In order to constrain the timings of palaeoearthquakes, organic material and charcoal found in key layers are commonly dated with radiometric techniques, i.e. radiocarbon (^{14}C), for example through accelerator mass spectrometry (AMS) (Galli et al., 2008). Generally, the time interval investigated by this type of palaeoseismology extends back to a few thousands of years (e.g. ~4-6 ka), although in some localities the investigations have been stretched up to 10-20 ka (e.g. McCalpin, 2009; Cinti et al., 2019). To derive the magnitude of the palaeoearthquakes, the offset associated with individual palaeoearthquakes is compared with empirical fault scaling relationships which relate the coseismic displacement to the magnitude of an earthquake (e.g. Wells and Coppersmith, 1994; see Section 2.4.1 for a review of the scaling relationships). Hence,

palaeoseismology characterizes the distribution and size of individual palaeoearthquakes in space and over time periods of thousands of years (McCalpin, 2009).

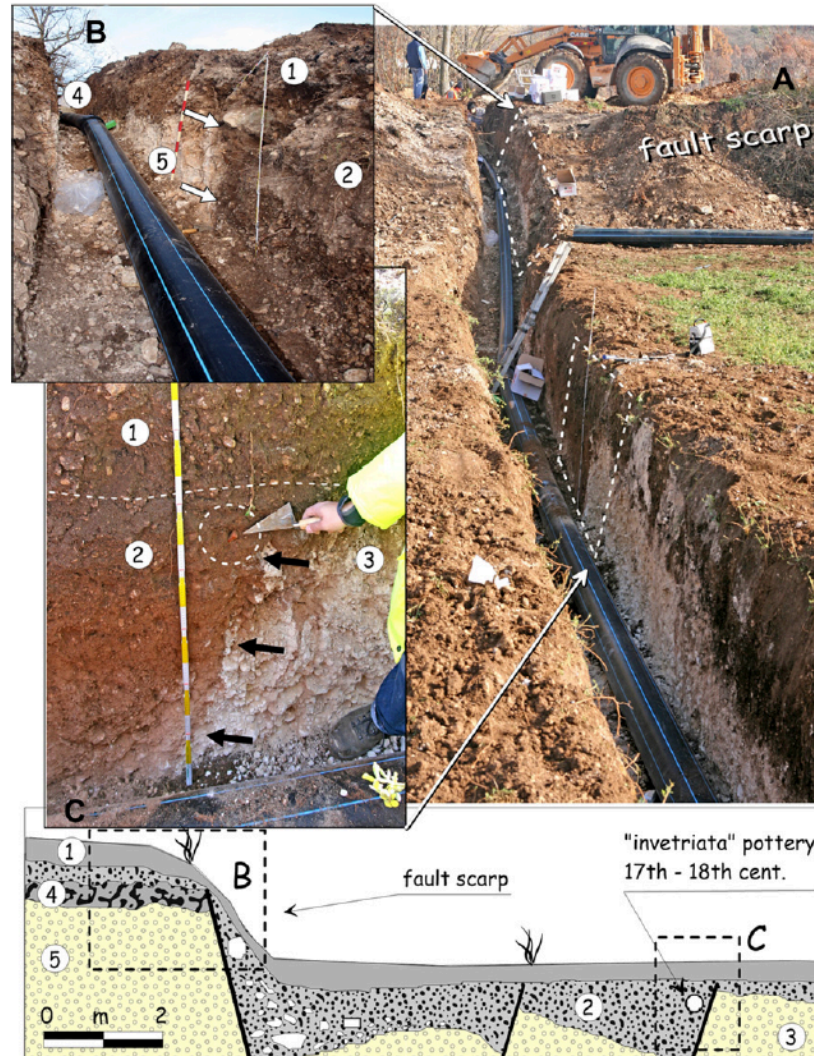


Figure 2.8: Example of a palaeoseismological study carried out on the Paganica-San Demetrio fault, Central Apennines, Italy. From Galli et al., 2010.

The main limits of palaeoseismological studies are: (1) they may produce an incomplete record of palaeoearthquakes, because only large earthquakes produce coseismic offsets at the Earth's surface, so small earthquakes may be missed; (2) surface features created by large earthquakes can become quickly modified, obscured and removed by common surficial processes (McCalpin et al., 2009). Moreover, faults might be composite

structures, especially when viewed at the scale of a trench excavation site (tens to hundreds of meters), with different fault splays distributed across strike (Michetti et al., 2005). In this context, earthquake ruptures may not occupy exactly the same trace every time. Hence, the variability in the localization of the surface ruptures of a fault through time makes palaeoseismic datasets generally insufficient to provide robust estimates of the variability in earthquake recurrence intervals or to precisely estimate fault slip rates (Michetti et al., 2005).

Another limit is that the time-span covered may be insufficient. For example, Papanikolaou et al. (2005) points out that slip-rates derived with palaeoseismological studies might not be representative of the long-term seismic behaviour of the fault, because of the limited time interval that palaeoseismology explores (few thousands of years). That is because slip-rates and average recurrence intervals have been proved to be variable through time, with earthquakes often clustered in time and clusters separated by relatively long periods of low activity (e.g. Cowie et al., 2017). If clusters and anticlusters are of the order of a few hundreds to thousands of years, then palaeoseismology may not be able to cover the entire cycle of slip-rate variations, and therefore the measured slip-rates may not represent the long-term activity rates of faults (Papanikolaou et al., 2005). Slip-rates that encompass earthquake clustering can be obtained by measuring the fault offset across preserved fault scarps, as showed in the next section.

2.3.2 Fault scarp profiles

The analysis of preserved tectonic landforms, such as fault scarps, allow measurements of slip-rates for time intervals longer than traditional trenching in palaeoseismology. Fault scarps form through repeated coseismic surface ruptures associated with large earthquakes (e.g. Stewart and Hancock, 1990). If the fault scarps displace features of known age, such as postglacial erosional surfaces, construction of topographic profiles perpendicular to the fault scarp provide quantitative data on the fault activity. The vertical offset measured across preserved fault scarps is assumed to be the total throw accumulated by the fault scarp since its onset, for sites where geomorphic processes have not disturbed the scarp formation and exhumation (Figure 2.9; Roberts and Michetti, 2004; Papanikolaou et al., 2005; Papanikolaou and Roberts, 2007; Galli et al., 2010; Cowie et al., 2017). If the age of the landforms is sensibly older than the fault recurrence interval, slip-rates derived from scarp profiles can be representative of a time interval which encompasses several seismic cycles, embedding cycles of earthquake clustering and anticlustering (Roberts and Michetti, 2004). Therefore, slip-rates from fault scarps can be representative of the long-term behaviour of the fault.

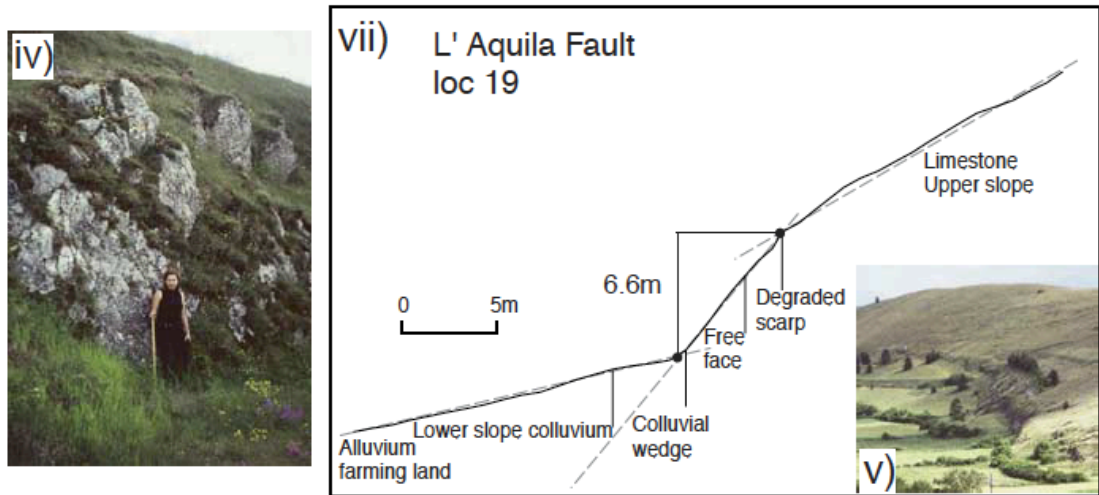


Figure 2.9: Example of a fault scarp profiles across the L' Aquila fault, Central Apennines, Italy. The upper and lower slopes formed during the LGM and stabilised during its demise at 15 ± 3 ka. 6.6 m slip in 15 ka implies a rate of vertical offset accumulation (throw-rate) of 0.44 mm/yr, averaged over 15 ka, and presumably over any earthquake clusters or anticlusters. From Papanikolaou et al., 2005.

As for palaeoseismology, also measurements of preserved fault scarps present some limitations. For instance, studies of fault scarps are favoured onto limestone fault scarps, given the good preservation of the fault scarps through time. Studies of fault scarps are more difficult to be performed on faults cutting through siliciclastic deposits, given the poor preservation of the scarps through time. Moreover, although fault scarp profiles provide slip-rates which encompass several seismic cycles, this approach is not able to reveal if the scarp formed with constant slip-rate, or it has experienced earthquake clusters and anti-clusters through time. This issue can be solved with measurements of the concentration of *in situ* cosmogenic ^{36}Cl isotopes along fault planes in preserved fault scarps, as described in the next section.

2.3.3 Cosmogenic dating of fault scarps

Cosmogenic dating is a methodology to define the surface exposure age of a section of rock, that is, when it emerged from beneath the ground to the Earth's surface. This section

gives a summary of how this works, with more detail given in the following sections. The exposure age can be measured from the abundance of cosmogenic isotopes that form in rock due to bombardment from high-energy cosmic particles, such as neutrons and muons, if the production rate is known. The production rate of the cosmogenic isotope depends on the isotope measured, and various site-specific effects, including the densities and elemental compositions of the rock type, and location and history of the site (e.g. latitude and elevation; palaeomagnetic field variation through time). In limestones, which contain abundant ^{40}Ca , the interaction between cosmic radiation (mainly neutrons and muons) and ^{40}Ca produces *in situ* cosmogenic ^{36}Cl . Cosmogenic dating of fault scarps is based on the progressive exhumation and exposure to cosmic radiation of the fault scarp during repeated earthquakes (Figure 2.10). As portions of the fault scarps are progressively exposed to the cosmic radiation, they start accumulating cosmogenic ^{36}Cl . Therefore, if the fault scarp is exhumed only by repeated earthquakes, and no geomorphic processes have contributed to exhumation, the concentration of cosmogenic ^{36}Cl increases up the dip of a fault plane exposed on a fault scarp by repeated surface-rupturing earthquakes (Figure 2.10; Palumbo et al., 2004).

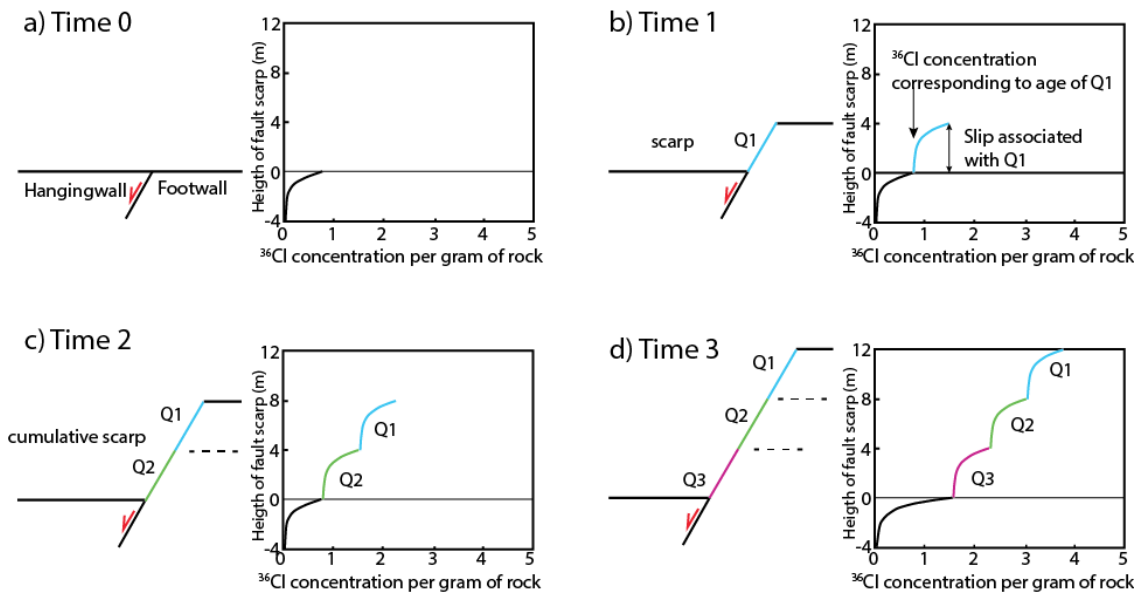


Figure 2.10: Model of fault scarp exhumation and the predicted ^{36}Cl concentration profile produced. At Time 0, the fault plane is not exhumed, yet some ^{36}Cl is accumulated beneath the ground surface depending on the density of the hangingwall material. Repeated earthquakes at different times cause a progressive exhumation of the fault plane, and this produces a progressive increase of ^{36}Cl concentration moving up the fault plane. Adapted from Palumbo et al., 2004.

Pioneering studies have shown that numerous samples can be taken up from a bedrock scarp and analysed which, when modelled, will give the exhumation history of the sampled section of the fault and therefore a long-term record of how the fault has slipped (e.g. Palumbo et al., 2004).

The next sections introduce more detail on the theory of cosmogenic dating of fault scarps and a background of published studies on exposure ages of fault planes.

2.3.3.1 Theory of cosmogenic dating of fault scarps

Cosmogenic nuclides are produced on Earth by the interaction of elements in the bedrock and high energy cosmic rays and particles (mainly neutrons and muons) that pass through the rock (Dunai, 2010). This cosmic-ray flux is a product of the explosion of supernovae, which are estimated to occur approximately every 50 years in our galaxy, and it is considered to be constant for the last 10 Ma (Dunai, 2010). The impact of the cosmic rays

with the surface generates specific cosmogenic nuclides. In limestones, ^{40}Ca , ^{39}K and ^{35}Cl , when exposed to cosmic rays, act as target elements producing *in situ* ^{36}Cl (Schlagenhauf et al., 2010).

There are four main processes that produce ^{36}Cl (from Schlagenhauf et al., 2010): 1) spallation of target elements Ca, K, Ti and Fe (mainly Ca in limestones), when high energy neutrons impact the target elements and break them into nuclides of smaller atomic mass; 2) slow negative muons may be captured by ^{40}Ca and ^{39}K resulting in the production of ^{36}Cl ; 3) low-energy neutrons, formed with the collision between the high-energy neutrons and atoms in the atmosphere and rocks, are absorbed by ^{35}Cl to form cosmogenic ^{36}Cl ; 4) in rocks with high concentrations of radioactive U and Th, their radiogenic decay produces slow neutrons that can be captured by ^{35}Cl to form ^{36}Cl . In limestones, the concentration of radioactive atoms is low, so the principal sources of ^{36}Cl are 1-3. The production rate from spallation of target ^{40}Ca has been estimated to be between 48.8 ± 3.5 and 66.8 ± 4.4 atoms of ^{36}Cl per gr of Ca per year (e.g. Schimmelpfennig et al., 2009). Measurements from a pure calcite sample gives a spallation production rate of 48.8 ± 3.5 atoms of ^{36}Cl per gr of Ca per year (Stone et al., 1996). Given that elementary production rates are better estimated when measured from isolated, pure chemical elements (Schimmelpfennig et al., 2009), the latter is the production rate adopted in this PhD thesis, although as described below, this value is iterated in the particular modelling software used in this thesis (see Beck et al., 2018). Because spallation is the most important source of ^{36}Cl in the first two meters of the surface (Figure 2.11), the spallation production rate of 48.8 ± 3.5 atoms of ^{36}Cl per gr of Ca per year can be representative of the ^{36}Cl production rate at the surface (Figure 2.11; Schlagenhauf et al., 2010).

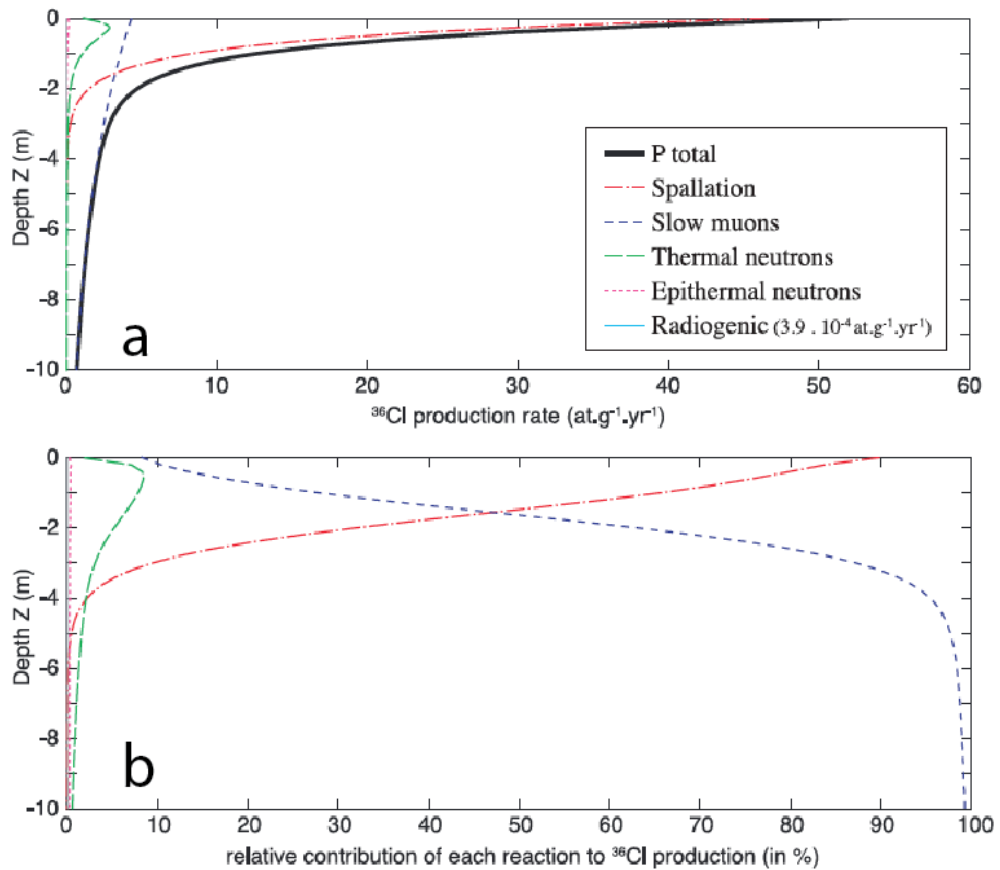


Figure 2.11: Contribution of the various cosmogenic and radiogenic sources to the production of *in situ* ^{36}Cl in the first 10 m below the ground surface. Calculations are performed for a horizontal surface of pure limestone. a) Production rates with depth for the different processes reactions. b) Relative contribution of each production process. Modified from Schlagenhauf et al., 2010.

The production rate of ^{36}Cl can be affected by several factors, related to secular variations of the cosmic rays. The flux of cosmic rays onto a particular rock surface varies according to the geomagnetic field, the latitude, the altitude and the topographic shielding (Schlagenhauf et al., 2010).

For short time intervals of study (e.g. 15 ± 3 ka), the geomagnetic field presents variations in both intensity and geometry (Merrill & McElhinny, 1983; Guyodo & Valet, 1999; Ohno and Hamano, 1993; Yang et al., 2000; Korte & Constable, 2005). Schlagenhauf et al. (2010) explored the effect of this variability on the cosmogenic production rates, concluding that it has a small effect on the production rate of ^{36}Cl . Hence, the

geomagnetic field can be assumed constant over the timescale of study of cosmogenic dating of fault scarps, and a particular model of its geometry and intensity is adopted as standard (see Beck et al. 2018).

The Earth magnetic field deflects cosmic radiation such that the cosmic-ray flux is minimum at the equator and increases with higher latitudes, becoming constant for latitudes greater than 60° (e.g. McElhinny and McFadden 1997). Therefore, the production rate must be corrected for the latitude of the sample site.

Cosmic rays lose energy during interaction with the atmosphere, so the total cosmic-ray flux that reaches the surface depends on the thickness of the atmosphere above the sample site. Hence, the production rate at the surface must be corrected for the altitude of the sample site.

The standard production rate assumes that the entire cosmic-ray flux reacts with the exposed rock, and there are no effects of topographic shielding around the sample site. This is a condition that rarely applies for fault scarps in nature, and therefore the production rate must be corrected for the shielding of the sample site due to the surrounding topography.

Cosmic rays can penetrate through the colluvium, and some significant production of ^{36}Cl occurs on buried fault planes within the top ~ 2 m of the surface (Figure 2.11a and 2.12a). Below this depth, the production rate significantly decreases (Figure 2.12). Overall, the total production rate of ^{36}Cl shows an exponential decay with depth. The density and elemental composition of the overlying colluvium in part affects the production rate of ^{36}Cl on buried fault planes: high-density colluvium will impede the cosmic flux and reduce the production rate, and some ^{36}Cl production within the colluvium may reduce the cosmic ray flux reaching the fault plane. Therefore, production rates must be corrected for the density and elemental composition of the colluvium.

palaeoseismic records, and therefore they can provide a better record of exhumation events. Samples have been collected every ~0.5 m along the fault plane, and the results confirmed that the concentration of ^{36}Cl increases up the scarp as the time of exposure increases. The authors claim to have recognised six different earthquakes and multiple temporal clusters of earthquakes. However, it has been noted that they have sampled in a quarry, and therefore the ages of the earthquakes are unlikely to be reliable because fault exposure might not be entirely related to tectonic movements. This prompted the importance of the good site characterization before sampling.

Mitchell et al. (2001) studied the exhumation history of the Nahef East normal fault, Israel. The authors highlighted the importance of choosing a site unaltered by erosional post-glacial processes. Their modelling identifies 4 – 6 slip events to build a 9 m fault scarp, with up to 2 m slip per event; it shows also that these could not be modelled with a constant-slip approach, indicating the occurrence of temporal clusters of earthquakes during the Holocene. However, the 2 m slip per event seems to be too large, considering the length of the fault (~3 km).

Benedetti et al. (2002) and Benedetti et al. (2003) have performed ^{36}Cl dating on two normal fault scarps in Greece, the Sparta fault and the Kaparelli fault respectively (Figure 2.13). The authors sampled a continuous ladder of samples up the fault plane, in order to identify single earthquakes as cusps formed by the exponential decay in the accumulation rate below the colluvial wedge (Figures 2.10 and 2.13 a and b). To achieve that, in their modelling neither the magnitude of slip nor the age of the earthquakes is fixed. The results from both faults suggest that these have moved episodically during the Holocene, with variable slip-rates through time.

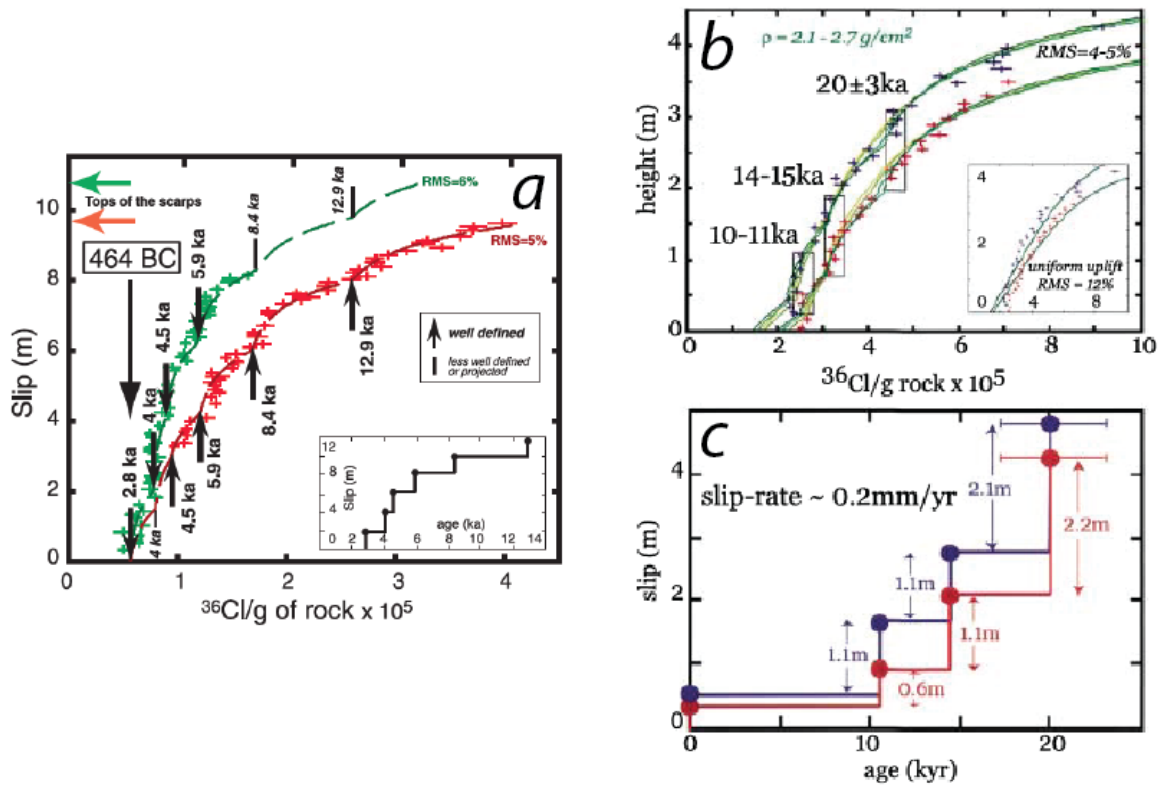


Figure 2.13: ^{36}Cl data from the Sparta fault (a; Benedetti et al., 2002) and from the Kaparelli fault (b and c; Benedetti et al., 2003). a) Data and models for two sites on the Sparta fault, the inset map shows the relative slip history (from Benedetti et al., 2002). b) Data and models of two sites on the Kaparelli fault (from Benedetti et al., 2003). c) Derived slip-rate histories for the sites on the Kaparelli fault (from Benedetti et al., 2003). The studies show the episodic activity of the normal faults during the Holocene. Modified from Benedetti et al., 2002; 2003.

In Central Italy, the Velino-Magnola fault has been intensively studied, with 5 separate sampling sites distributed along the fault trace (Palumbo et al., 2004; Schlagenhauf et al., 2010; Schlagenhauf et al., 2011). The studies suggested an episodic occurrence of earthquakes, with at least 9 large Holocene earthquakes. The study claims that all five sites record the same sequence of earthquake, so each earthquake ruptured the entire fault length. However, the concentrations of ^{36}Cl are very different at these sites, for example with the concentration at ground level ranging from ~ 1 atoms/g to ~ 4 atoms/g (see Schlagenhauf et al., 2009). In order to fit the 9 earthquakes to each site, the values of pre-exposure of rocks to cosmic radiation, that is the pre-exposure of the fault plane rocks during the long glacial period that preceded surface exposure, were varied

along the fault from 2.5 ka to 13 ka. This pre-exposure value is judged by these authors to be necessary to fully model the ^{36}Cl concentrations in the samples. However, the large variability of pre-exposure values applied, which have no independent verification, implies that the exhumation histories during the long glacial episode that predates the demise of the LGM was very different along the fault. It is unclear why these different pre-exposure histories would be produced. Thus, the lack of independent verification of pre-exposure ages calls into question whether the different sites along the fault all experienced synchronous earthquakes. Moreover, it is noted that several of the 5 sites are close to or within eroded gullies along the fault. These gullies may well invalidate the results from this study as the age of formation of the gullies and hence non-tectonic exhumation has not been considered. This is because the erosive activity of gullies might contribute to the exposure of fault planes, and therefore the exposure ages measured with cosmogenic dating can include tectonic and non-tectonic components.

Cowie et al. (2017) have sampled 5 different faults in Central Italy in order to study slip-rate fluctuations over multiple faults during the Holocene (Figure 2.14). Samples have been collected at sites where the authors could exclude any signs of erosion since the demise of the Last Glacial Maximum (15 ± 3 ka), and therefore the fault scarps have been built only by repeated earthquakes. Importantly, no pre-exposure of samples has been introduced in the modelling. The results show that each fault exhibits slip-rate fluctuations during the Holocene, and that adjacent faults within a dense fault system had different exhumation and hence slip histories. Some faults present rapid increase of cosmogenic ^{36}Cl moving up along large fault scarp (e.g. fast slip-rate faults), meanwhile other faults present slow increase of cosmogenic ^{36}Cl throughout the entire scarp (e.g. slow slip-rate faults), revealing slip-rate variability between faults.

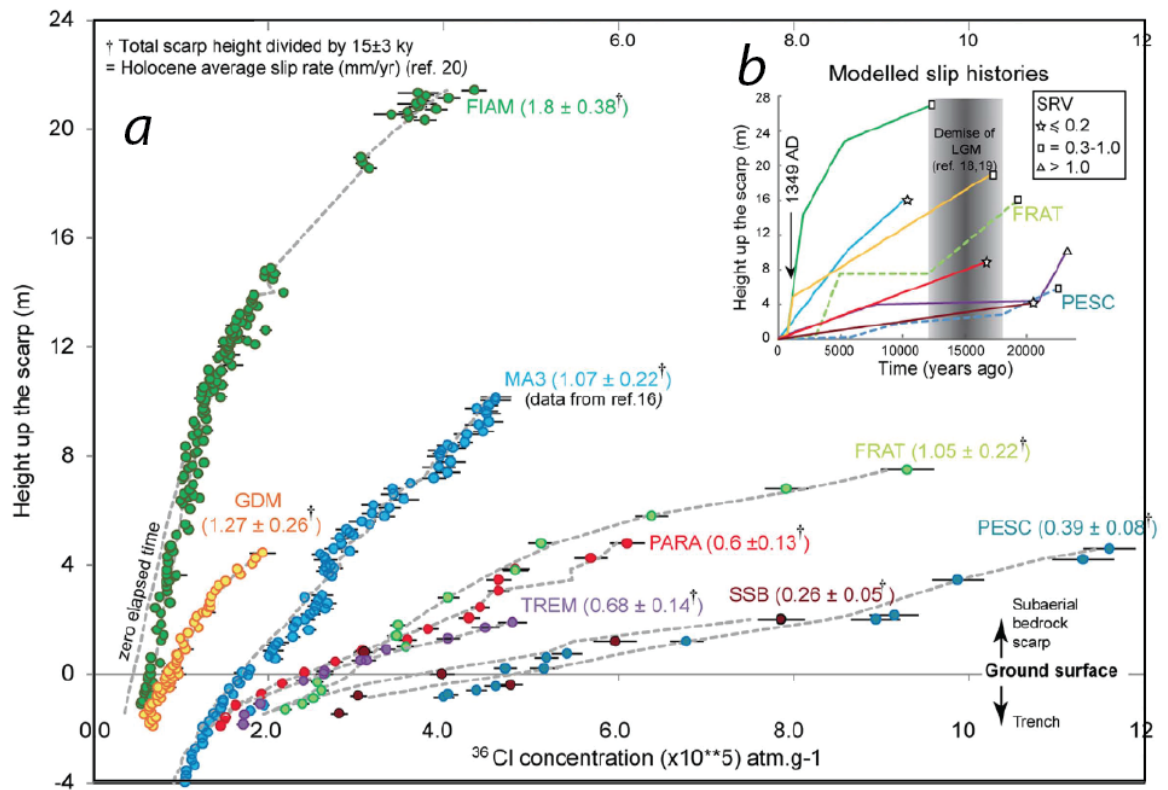


Figure 2.14: ^{36}Cl measurements collected for different faults in Central Italy. a) Measurements of the ^{36}Cl concentrations along the fault scarp heights. b) Fault slip histories derived from the ^{36}Cl concentrations in a). From Cowie et al., 2017.

2.3.3.3 Modelling procedures to recover slip histories from ^{36}Cl data on fault planes

Different modelling procedures to recover slip histories from ^{36}Cl data on fault planes have been introduced in the last decade (Schlagenauf et al., 2010; Cowie et al., 2017; Beck et al., 2018). Previous codes were based on manual attempts to find best fits of the ^{36}Cl concentrations profiles from temporal sequences of ground displacement (Benedetti et al., 2002; Palumbo et al., 2004; Schlagenauf et al., 2010, 2011; Yildirim et al., 2016). The Schlagenauf et al. (2010) code relies on spotting cusps of ^{36}Cl production before the modelling is performed. In theory, each cusp should identify an earthquake (e.g. Figure 2.10; Palumbo et al., 2004). However, these cusps are unclear even in dense datasets (e.g. Figures 2.13) and not visible at all in sparse datasets (e.g. Figure 2.14). The procedure of

spotting cusps can introduce personal bias in the subsequent modelling. Moreover, the Schlagenhauf et al. (2010) code includes pre-exposure of rocks to the cosmic radiation. This value is again arbitrary, and therefore prone to use of circular reasoning. The modelling is slow and has no Bayesian search method. Hence, this code can introduce several biases into the modelling of the ^{36}Cl concentration measured on the fault plane.

The Cowie et al. (2017) code is based on the Schlagenhauf et al. (2010) basic production code. The Cowie et al. (2017) code improves the calculation of Schlagenhauf et al. (2010) because it does not use pre-exposure and it performs a Bayesian search of the best solution to model the ^{36}Cl concentration measured on the fault plane. However, this code forces constant slip-rate between change points. This operation introduces bias associated with having an algorithm that is not sophisticated enough to perform fast runs, so it has to simplify the search to just looking for change points. This operation can affect the accuracy of the modelled slip histories. In fact, Beck et al. (2018) showed that the Cowie et al. (2017) code missed important earthquakes on the densely sampled Fiamignano fault (Central Italy) (1349 and 847 AD), probably because the code forces constant slip-rate between change points. Other issues associated with the Cowie et al. (2017) code are (1) a prior set of the scarp age (introduces personal bias and does not deal properly with pre-LGM subsurface production), (2) it re-calculates production rates on each model iteration (which makes the modelling much slower), (3) it fixes slip sizes, colluvial densities and production rates, with no iteration allowed, and (4) it has no verification of convergence. Moreover, the code has never been peer-reviewed.

Beck et al. (2018) introduced a new code to recover slip histories from ^{36}Cl data on fault planes that it is not based on the Schlagenhauf et al. (2010) code, but instead uses an

interpolated simulator between calculated values for production. It tabulates all the possible radiation geometries before the runs start and draws from this table from each iteration, rather than calculating the production each time. This operation makes the calculations much quicker. The Beck et al. (2018) code properly deals with the pre-LGM exposure with a Brownian Passage Time (BPT) approach. It also allows the iteration of important parameters such as the slip sizes, the colluvial densities, the attenuation lengths and the production rates. Moreover, the Beck et al. (2018) code has a proper statistical verification of convergence and it can run fast enough to allow convergence. It has been subject to peer review and tested against a synthetic dataset. For these reasons, the Beck et al. (2018) is the one used in this thesis to recover slip histories from ^{36}Cl data on fault planes. The next chapter introduces in detail how the Beck et al. (2018) code works and which are the parameters needed to run it.

2.3.4 Summary of classic field-based measurements of fault slip-rates

Overall, the definition of fault slip-rates is key in order to define the seismic potential of an active normal fault. However, slip-rates alone are not enough to produce seismic hazard assessments. In fact, it is also fundamental to have data that suggest the expected maximum magnitude for an earthquake rupturing the entire area of a fault, and also what the energy budget is for that active normal fault. The next section shows key features that allow to define these parameters.

2.4 Definition of the seismic potential of active faults

This section introduces some key features to identify the seismic potential of an active fault. Fault rupture parameters, such as the fault length or the maximum coseismic displacement (D_{max}), are related to the potential magnitude of an earthquake through empirical fault scaling relationship. Moreover, measurements of the fault length and of the coseismic D_{max} , together with structural measurements of the dip of the fault, allow calculation of the seismic moment of the fault, which is needed to calculate the budget of seismic energy of an active fault given its slip-rate. The next sections describe these features, introducing the problems in using them given slip-rate variations associated with 3D structural complexities.

2.4.1 Empirical fault scaling relationships

A variety of fault rupture parameters can be related to earthquake magnitudes to develop fault empirical scaling relationships. These parameters have been developed based on the collection and analysis of data from coseismic ruptures following surface-rupturing earthquakes, such as the surface rupture length and the coseismic displacement, alongside their comparison with the earthquake magnitude (Figure 2.15).

Empirical fault scaling relationships are commonly used in seismic hazard assessments and in palaeoseismological investigations. For example, the empirical scaling relationship between the surface rupture length and the earthquake magnitude allows one to estimate the potential magnitude of an earthquake that ruptures an active fault for its entire length. Another example is where, in palaeoseismology, empirical scaling relationship between

the displacement per event and the earthquake magnitude are widely used to define the magnitude of palaeoearthquakes. This section highlights the fact that empirical fault scaling relationships do not consider the effect of along-strike fault bends on the value of coseismic displacement. Hence, this thesis aims to explore the effect of fault bends on the scaling relationships involving the D_{max} associated with earthquakes: the D_{max} /surface rupture length and the magnitude/ D_{max} fault scaling relationships.

Several empirical fault scaling relationships have been published through time. Wells and Coppersmith (1994) presented empirical fault scaling relationships based on a worldwide database of 421 historical continental interplate and intraplate earthquakes of magnitude greater than 4.5 (Figure 2.15). For each earthquake, the authors compiled seismologic source parameters and fault characteristics, including magnitude, slip type, surface and subsurface rupture length, maximum and average surface displacement, downdip rupture width and rupture area.

For the fault length measurements, the authors have only included surface ruptures in the regression where surface rupture lengths met the following criteria: 1) uncertainty in the rupture length does not exceed 20% of the total length of the rupture; 2) at least one estimate of the amount of displacement is reported; 3) the lengths of ruptures resulting from individual events in multiple earthquake sequences are known. From the database of coseismic slip per earthquake, the authors derived the D_{max} as the vectorial sum of the slip components (vertical and horizontal) at a single location along the fault. In cases of historical earthquakes, where displacement measurements have been collected many years after the earthquake and multiple measurements are available, in order to avoid and/or minimize the effect of post-seismic slip, the authors selected the first measurements recorded after the earthquake. Moreover, the authors only included data

where the slip occurred primarily on a single fault, as opposed to a zone, or where the total slip across a fault zone is known. What is noteworthy is that both the D_{max} /surface rupture length and the magnitude/ D_{max} scaling relationships exhibit a large scatter in the natural values of D_{max} (Figure 2.15).

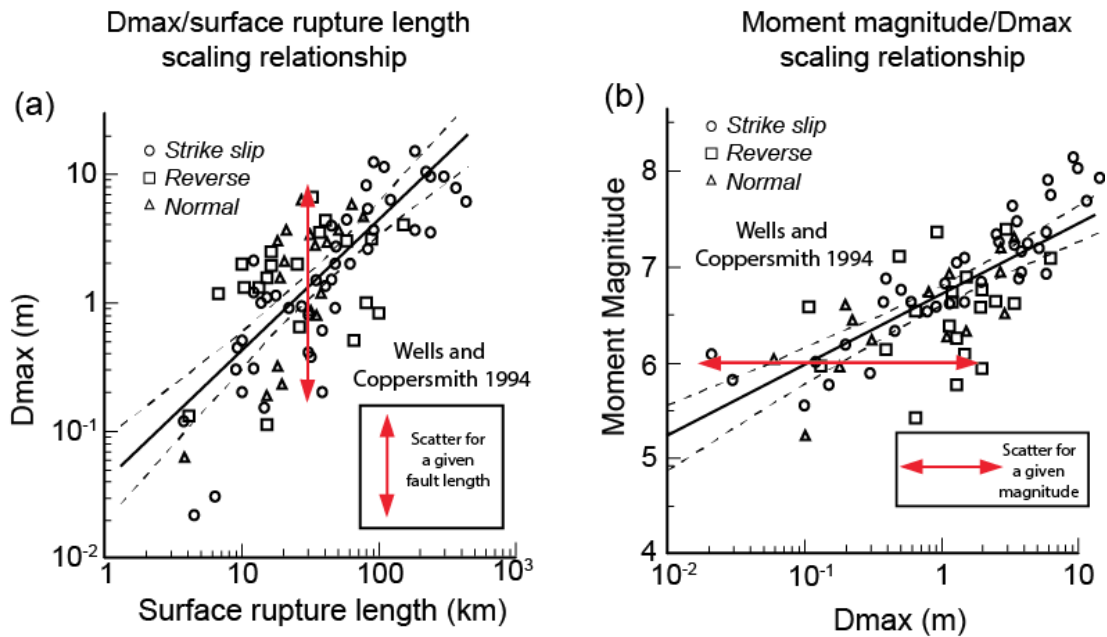


Figure 2.15: Empirical fault scaling relationships from Wells and Coppersmith, (1994). a) D_{max} /surface rupture length scaling relationship. Red arrow highlights the scatter in natural values of D_{max} for a given fault length. b) Moment magnitude/ D_{max} scaling relationship. Red arrow highlights the scatter in D_{max} values given an earthquake magnitude.

Recently new scaling relationships have been proposed, based on reviewed earthquake databases and inclusion of recent earthquakes. Manighetti et al. (2007) examined displacement/fault length data for a set of about 250 continental earthquakes of mixed focal mechanisms, with magnitudes larger than 6 (Figure 2.16a). Data have been collected from earthquakes that occurred in four of the most seismically active regions worldwide: Asia, Turkey, West US, Japan. Wesnousky (2008) based new empirical fault scaling relationships on three dozen worldwide-distributed historical earthquakes (Figure 2.16b). The database in Wesnousky (2008) contains only large surface rupture earthquakes of

length greater than 15 km and for which exist both maps and measurements of coseismic offset along the strike of the rupture.

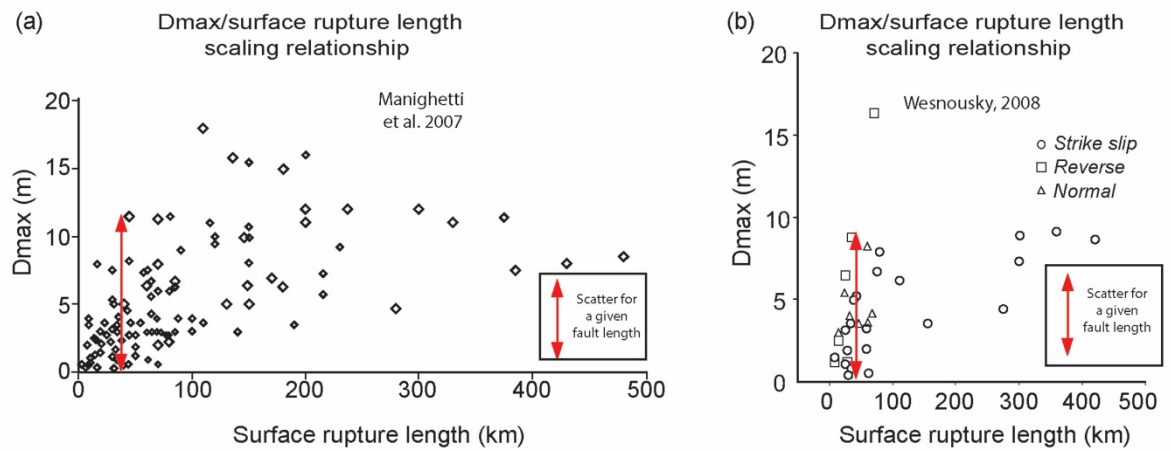


Figure 2.16: D_{max} /fault length empirical fault scaling relationships from Manighetti et al. (2007) (a) and from Wesnousky (2008) (b). These scaling relationships show a large scatter of the natural values of D_{max} for a given fault length, highlighted by the red arrows. Modified after Manighetti et al. (2007) and Wesnousky et al. (2008).

Again, an important point for this thesis is that, independently to the empirical fault scaling relationships used, the natural values of D_{max} shows a large scatter for a given fault length (up to > 10 m of D_{max} variability for fault length; Figures 2.15 and 2.16). Hence, this thesis aims to explore if the control exerted by 3D structural complexities on the values of fault throw is one of the possible explanations of the scatter in these natural values of D_{max} .

2.4.2 Seismic moment of an active fault

The seismic moment of an active fault is a measure of the size of an earthquake, directly related to the energy released during that earthquake. It is commonly defined as $M_0 = \mu AD$, where D is the average coseismic displacement, μ is the shear modulus (commonly considered as 3×10^{10} Pa) and A is the seismogenic area. The latter can be expressed as $A = LW$, where L is the fault length and W is the fault width, intended as the downdip

dimension in the plane of the fault (Kanamori and Anderson, 1975). In other words, seismic moment reveals the connection between the energy budget of an active fault and its geometry, expressed as fault length and width. The seismic moment can be converted in earthquake size through the moment magnitude $M_w = \left(\frac{\log M_0}{1.5}\right) - 6.07$, with M_0 expressed in Nm (Scholz, 2018). Moreover, the seismic moment is thought to be directly related to the stress drop of an earthquake, which represent the amount of stress released by the fault during an earthquake, by the equation $\Delta\sigma = C \frac{M_0}{A^{3/2}}$ (Kanamori and Anderson, 1975; Scholz, 2018). Calculations of the seismic moment do not commonly consider the effect of fault bends on the fault displacement, and therefore the value of average coseismic displacement might be biased if an earthquake ruptures through a fault bend. Hence, this thesis aims to explore the effect of along-strike fault bends on calculations of seismic moment and stress drop. The relationships between structural complexity, slip to length scaling, seismic moment and stress drop will be explored in Chapter 4.

2.5 Geological background of field areas

This section introduces the regional geological background of the field areas within this thesis and outlines the reasons why they have been selected.

2.5.1 Central Apennines, Italy

Active normal faults in the Apennines were chosen for study because they provide the opportunity to study spatial variation in slip across 3D fault complexities, both on the timescale of coseismic slip in recent earthquakes (Chapter 4) and since formation of

cumulative scarps preserved from 15 ± 3 ka (Chapter 5), and on the length scale of active faults that are closely-spaced across strike (< 5 km spacing; Chapter 5).

The Apennines are a fold-and-thrust belt formed during the Alpine orogeny, in response to the collision between the European and the African plates, that is overprinted with extensional faulting in the Quaternary to recent. In general, the Alpine orogeny caused thrusting of Mesozoic and Cenozoic limestones, deposited in the Tethyan ocean, onto Miocene flysch deposits formed during the early stage of the compression, with shortening direction towards NE (Figure 2.17; Anderson and Jackson, 1987; Doglioni, 1993; Vezzani et al., 2010). Since about 2-3 Ma, SW-NE trending extension started to overprint the thrust belt (Cavinato and De Celles, 1999; Roberts et al., 2002), causing the growth of a normal fault system in this new stress field (Patacca et al., 1990; Pizzi and Scisciani, 2000, Cavinato et al., 2002; Pizzi and Galadini, 2009). The shift in tectonic style is constrained by the presence of 2.5 Ma syn-rift sediments in the fault-bound Fucino basin (Cavinato et al., 2002) and the age of fossils found in the basin-filling syn-rift sediments in other basins (e.g. Ficarelli and Silvestrini (1991) for the Colfiorito basin).

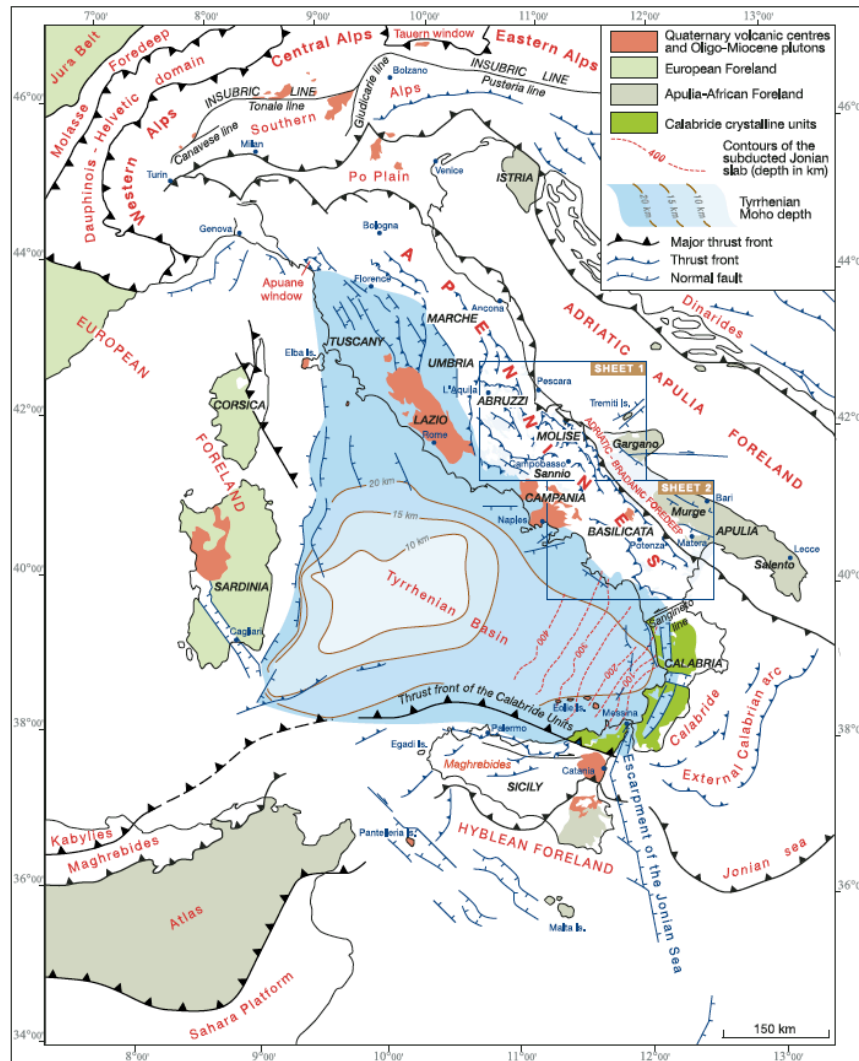


Figure 2.17: Structural map of Italy. The principal active normal faults (in blue) are located in the central portion of the peninsula, meanwhile the front of the thrust belt (in black) is located on the eastern coast. From Vezzani et al., 2010.

The normal fault system consists of an array of dip-slip faults striking ~NW-SE, with lengths of ~20-40 km, total throws less than ~2 km, and both en-echelon and end-on arrangements (Figure 2.18; Pizzi and Scisciani 2000, Roberts and Michetti, 2004). Overall the kinematics of normal faults is dip-slip, with a mean fault slip direction of $222 \pm 4^\circ$ (Roberts and Michetti, 2004). This normal fault system has produced historical seismicity recorded since at least Roman times, including moderate-to-large earthquakes, up to M_w 6.5-7.0 (Catalogo Parametrico Terremoti Italiani 2015, Rovida et al., 2016). Fault-specific earthquake recurrence intervals for surface faulting derived from

paleoseismology are in the order of hundreds to thousands of years (Blumetti et al., 1993; Cello et al., 1997; Galadini & Galli, 2000; Boncio et al., 2004).

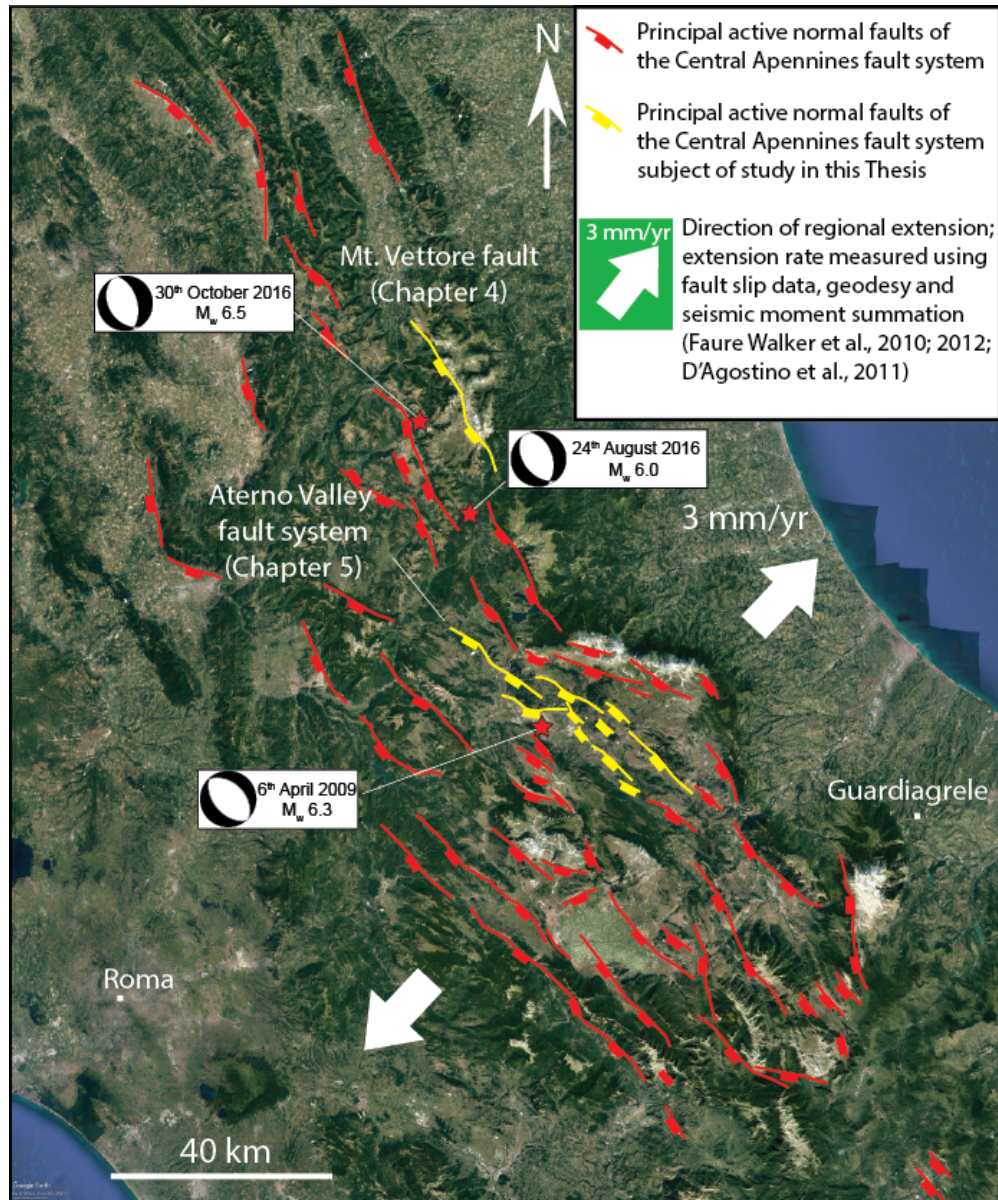


Figure 2.18: Map of the principal active normal faults in Central Italy. In yellow are reported the Mt. Vettore fault and the Aterno Valley Fault System, subject of this study in this thesis. White arrows indicate the direction of regional extension, measured with geodesy (D'Agostino et al., 2011). The extension rate is derived from geodesy, summation of seismic moment and using fault slip data (Faure Walker et al., 2010; 2012; D'Agostino et al., 2011).

Studies of fault scarps on active normal faults that survived since erosion rates decreased during the demise of the LGM (15 ± 3 ka) suggest that these faults have throw-rates up to

1.5 mm/yr (Roberts and Michetti, 2004; Papanikolaou et al., 2005; Faure Walker et al., 2010, 2012). Calculations of the extension rate across the central Apennines using fault slip data show regional horizontal extension occurring at up to ~ 3 mm/yr, matching estimates made with geodesy and seismic moment summations (Figure 2.18; Faure Walker et al., 2010, 2012; D'Agostino et al. 2011).

Calculations of the extension rate since 15 ± 3 ka also prompt the idea that earthquake slip is related to dynamic topographic effects that induce slip on viscous shear zones that form the roots of the upper crustal brittle faults (Cowie et al., 2013). This study showed that rates of slip measured across brittle faults at the surface, when averaged over 15 ± 3 ka and across the strike of parallel faults, imply along-strike variations in horizontal strain-rates that correlate with along-strike elevation changes. The correlation shows a power-law relationship, mimicking power-law viscous flow laws for crustal materials, where strain-rate is proportional to the topographic elevation (stress driver) raised to a power, $n = 3$. This implies that (1) dynamic topographic effects drive the extension by activating slip in underlying viscous shear zones that drive the rates of overlying earthquake slip, and (2) 15 ± 3 ka is a time period that appears long enough to reveal the longer-term behaviour of the fault system.

Within this tectonic framework, two recent earthquakes have struck the Central Apennines fault system: the 2016-2017 Central Italy seismic sequence, which culminated with the 24th August-30th October 2016 M_w 6.0-6.5 earthquakes that ruptured the Mt. Vettore fault, and the 6th April 2009 M_w 6.3 L'Aquila earthquake, which ruptured the Aterno Valley Fault System (Figure 2.18). Details on the earthquakes are provided within Chapters 4 and 5, respectively.

2.5.2 Western Volcanic Zone, Iceland

Active normal faults in the Iceland were chosen for study because they provide the opportunity to study faults at different stages of maturity as 3D complexities develop during propagation of ruptures through relatively-young, Holocene lavas.

Iceland forms part of a plateau generated by the intersection between the Mid-Atlantic Ridge and a mantle plume, which produced relatively thick crust, a broad topographic high and the emergence above sea-level of the oceanic ridge (Figure 2.19a; Wolfe et al., 1997). In Iceland, the Mid-Atlantic Ridge is characterized by two main rift segments: the first one runs on the western side of the island, composed by the Rekyanes Ridge (RR) and the Western Volcanic zones (WNZ); the second one runs on the eastern side of the island, composed by the Eastern Volcanic Zone (EVZ) and the Northern Volcanic Zone (NVZ) (Figure 2.19a). These two main segments are connected by the South Iceland Seismic Zone (SISZ) and the Central Iceland Volcanic Zone (CIVZ) (Figure 2.19a). Those volcanic zones, which represent the centre of spreading across the plate boundary, consist of a complex system formed by central volcanoes, fissure swarms 5-20 km wide and a few tens to more than 100 km long, and rift systems that propagate approximately normal to the spreading direction (Einarsson, 2008). Transform zones, such as the SISZ, are areas where the plate boundary runs parallel to the spreading direction and the deformation is shared within an area of distributed faulting, rather than confined on a single transform fault (Bergerat and Angelier, 2000; Einarsson 2008). GPS observations show that the overall spreading rate across Iceland is about 18-20 mm/yr with the spreading rate not equally distributed across the different Mid Atlantic Ridge segments (Figure 2.19a; LaFemina et al., 2005; Perlt and Heinert, 2006). Spreading rates across the WVZ vary between 3-8 mm/yr, with an overall decrease towards the NE (LaFemina et

al., 2005; Perlt and Heinert, 2006). Spreading rates across the EVZ vary between 11-19 mm/yr, with an overall increase towards the NE (LaFemina et al., 2005).

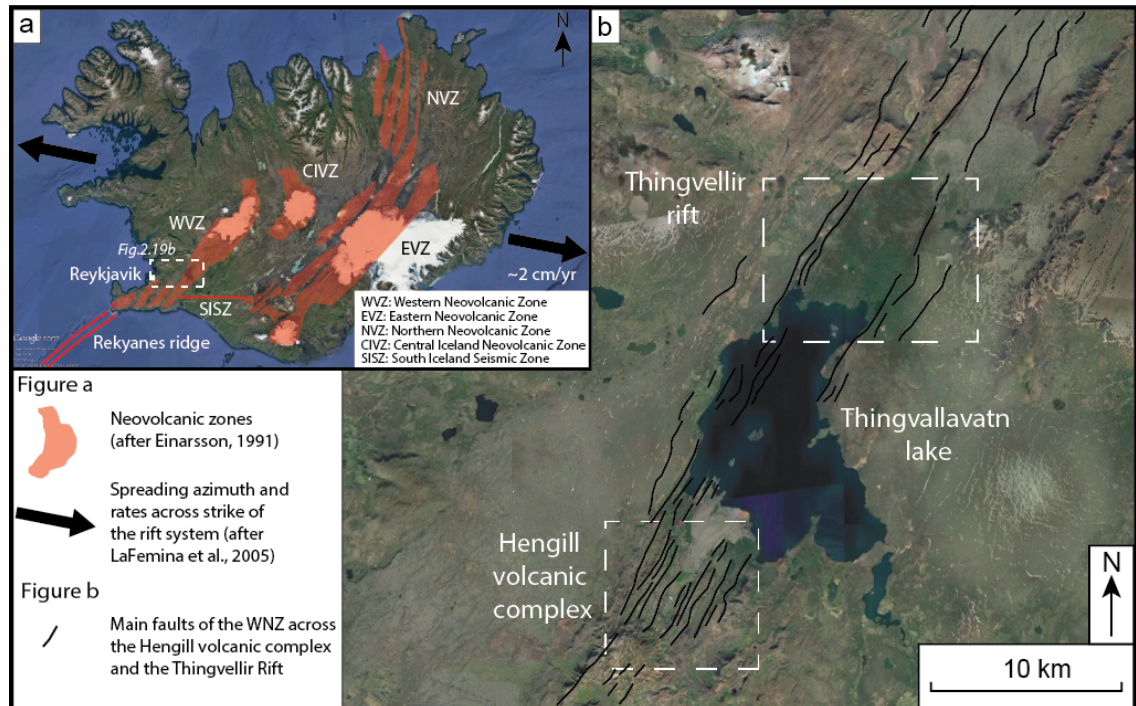


Figure 2.19: Location map of the study areas in Iceland. a) Regional setting of Iceland. In red are highlighted the neovolcanic zones, centre of the continental spreading (modified after Wolfe et al., 1997; Bergerat and Angelier, 2000; Einarsson, 2008). Black arrows indicate the direction of regional extension (after LaFemina et al., 2005). b) Map of the WVZ, with highlighted the Thingvellir rift and the Hengill volcanic complex, subject of study in this thesis.

The opportunity to study faults at different stages of maturity is given by the interplay between lava flows and active normal faults (Figure 2.20; see Podolsky and Roberts (2008) for an example on the Kilauea Volcano, Hawaii). The contemporaneous activity of faults and volcanic centres in Iceland caused the faults to be repeatedly resurfaced by lava flows, even in the Holocene (Figure 2.20a). After a resurfacing event, no throw will be present at the surface if the fault has not ruptured to the surface since the lava flow, meanwhile the throw increases downwards into older volcanic layers, through which the fault propagated earlier in time (Figure 2.20c). The reactivation of the fault at depth will cause propagation of the fault up through the un-faulted lava at the surface (Figure 2.20d).

As a consequence, faults at the surface appear immature because they have to be re-established after each resurfacing event (Figure 2.20d). This interplay between lava flows and fault activity in spreading centres like the WVZ in Iceland causes the faults to present a variety of incipient and recent fault linkage across relay zones that are to become the site of future mature fault bends. This makes the WVZ an ideal field area for studying the role of 3D structural complexities during the process of fault growth.

Interplay between resurfacing lava flows and active faults

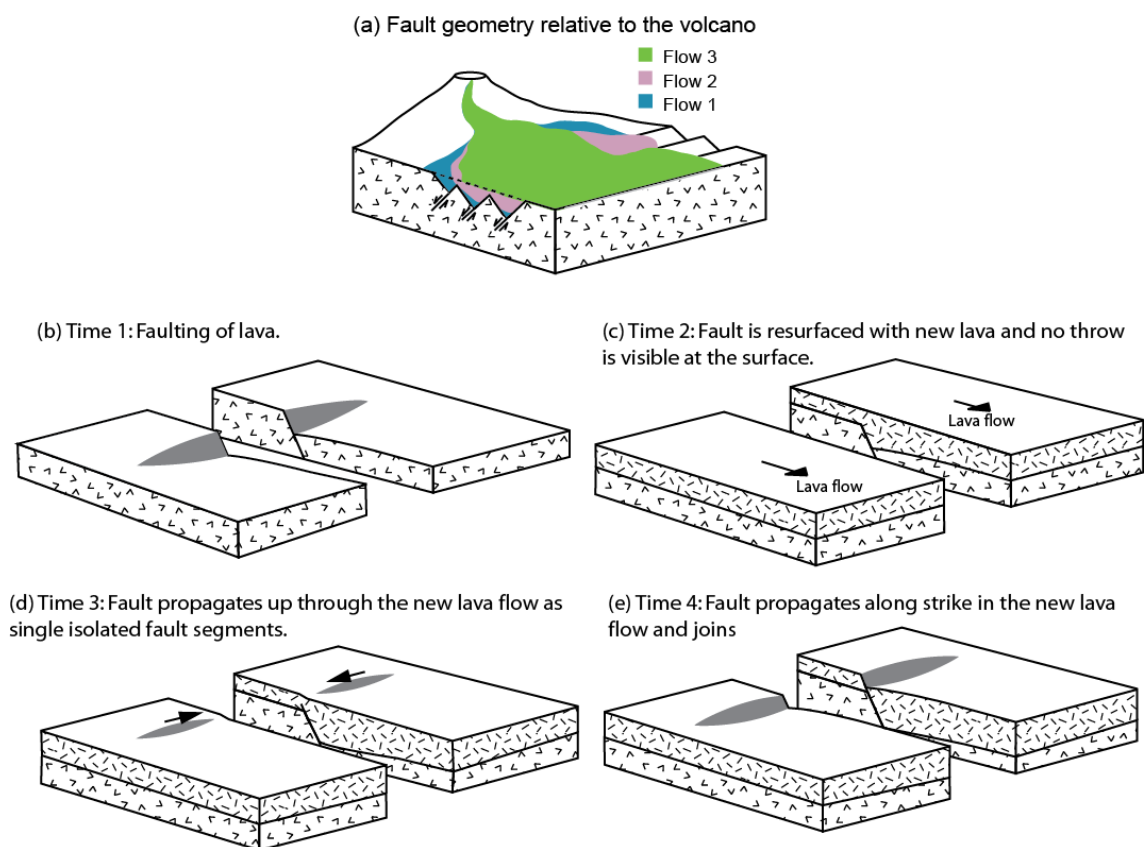


Figure 2.20: Interplay between resurfacing lava flows and active faults. a) Fault geometry relative to the volcano; it is shown how active faults are resurfaced by repeated lava flows. b) Time 1, a fault has produced offsets of a lava flow. c) Time 2, a new lava flow resurfaced the fault, and no signs of faulting are visible at the surface. d) Time 3, the fault starts propagating upward to the surface as two or more segments that begin to propagate along strike towards each other. e) Time 4, two fault segments have linked, and the fault length is re-established. Adapted from Podolsky and Roberts, 2008.

2.5.3 Attica, Central Greece

Central Greece was chosen for study because it is characterised by active normal faults that are located across strike from one another, with well-exposed carbonate fault planes associated with faults scarps. This provides the opportunity to use *in situ* ^{36}Cl cosmogenic exposure dating to assess how faults located across strike from one another share the work of accommodating the regional strain-rate through time, and how the magnitude of any effects compares to those associated with 3D structural complexities such as bends.

Central Greece is characterized by active NNE-SSW directed extension on normal faults, above the Hellenic Subduction Zone in the south, where the Aegean plate is subducting below the Eurasian plate, and also close to the tip of the North Anatolian fault in the north (Figure 2.21a). A compressional phase in late Mesozoic and early Tertiary produced a series of NNW-SSE-trending folds and thrusts involving ophiolites and metamorphic rocks (Jackson et al., 1994). In the Early Miocene, extension started to dominate the geology of the Aegean region, probably due to the rollback of the subduction zone (Jackson et al., 1994; Armijo et al., 1996), causing the development of numerous WNW-ESE striking normal faults. GPS measurements show that the current extension rates for Central Greece have values up to 15 mm/yr (Billiris et al., 1991; Davies et al., 1997; Briole et al., 2000; Chousianitis et al., 2013). Measurements of striae and corrugations from the centres of faults are consistent with both strain directions, derived from GPS campaigns, and from focal mechanisms of large normal-faulting earthquakes (Roberts and Ganas, 2000). The ongoing activity of normal faults in central Greece is testified by the occurrence of more than 170 destructive earthquakes during the last 500 years (Papazachos and Papazachou, 2003). Some of these earthquakes have affected the capital

city, Athens, and this area, characterised by sets of parallel active normal faults forms the focus of the study of Chapter 7.

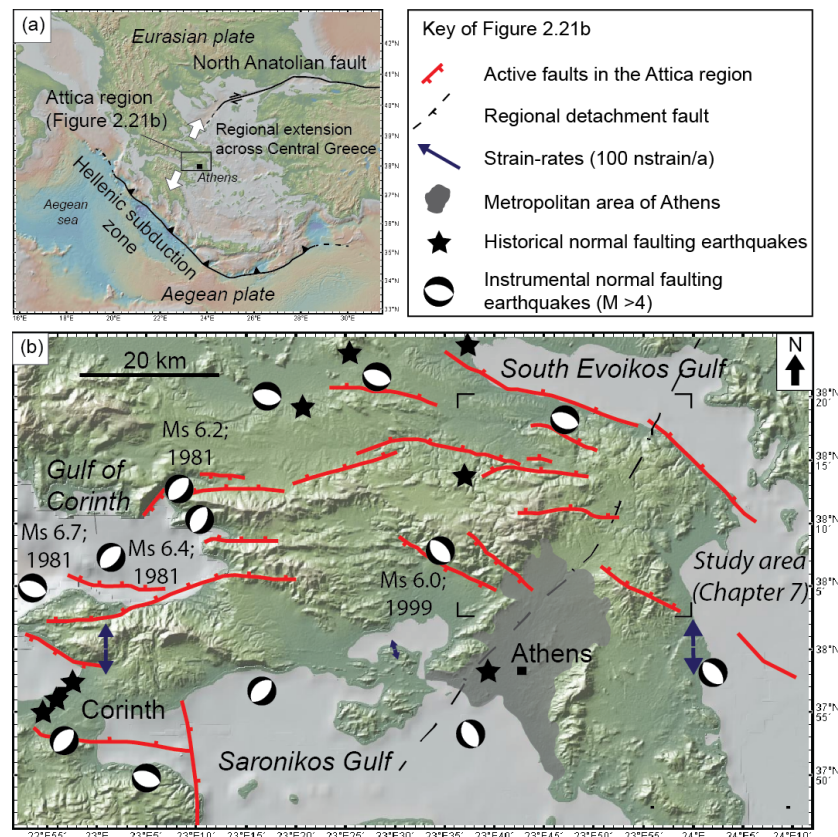


Figure 2.21: Location map of the study area in central Greece. a) Regional setting of Greece. White arrows mark the direction of extension across central Greece, driven by the Hellenic subduction zone to the south and the North Anatolian fault to the north. b) Location map of Attica. Red lines are normal faults, tick marks towards the hangingwall. Fault traces are after Papanikolaou and Papanikolaou, 2007. Historical and instrumental earthquakes, together with the strain-rates, are from Grutzner et al., 2015 and references therein.

2.6 Summary

With the above scientific background in mind, the next chapter will introduce the general methods applied throughout this thesis, in order to explore the relationship between the non-planar fault geometry and the distribution of throw and throw-rates along different active normal faults located in different geodynamic domains.

Chapter 3

Methods

This chapter introduces the principal methodologies used in this PhD thesis to study the relationship between the non-planar fault geometry and the distribution of throw and throw-rates along the fault. Firstly, it describes the methods applied to produce a quantitative analysis of the geometry and kinematics of faulting, explaining the criteria used to define along-strike fault bends. Secondly, this chapter describes the techniques applied to measure throw and throw-rates over different time scales. Thirdly, this chapter presents the procedure to derive fault slip histories from cosmogenic nuclide analysis, describing (1) the criteria followed to collect samples from fault planes, (2) the steps followed during the samples preparation and (3) the computational code used to model the ^{36}Cl concentrations to derive the fault slip history.

3.1 Quantitative analysis of the geometry and kinematics of faulting

This study requires quantitative analysis of the geometry and kinematics of faulting. To accomplish this, structural fault maps have been constructed by combining results from detailed fieldwork, published geological maps, palaeoseismology, structural geology and high-resolution imagery, such as Google Earth[®] and a high-resolution DEM (10 m resolution). During fieldwork, structural fault maps have been annotated on Google Earth[®] basemaps. Structural measurements of fault planes (fault strike, dip, slip vector azimuth and plunge of the slip vector) have been collected using a compass clinometer

($\pm 2^\circ$ error per single measurements) and a hand-held barometric GPS (± 1 m error per single location).

A common problem that was encountered during this study was how to extract and report representative values describing the geometry and kinematics and faults within bends along larger structures. Along-strike fault bends have been defined using strike lines (also known by some as structure contours), horizontal lines joining points of equal elevation on a structure such as the hangingwall cut-off (Figure 3.1). Strike lines are built defining pairs of points where the fault trace crosses the same topographic contour. Strike lines allow to gain strike values that represent the overall character of the principal fault segments for distances of hundreds of meters along the fault. Along-strike fault bends that are small in lateral extent may not be resolved if the spacing of topographic contours is too sparse (Figure 3.1). Moreover, strike lines help to discern whether the trace of the normal fault deviate because of a change in strike or because it crosses a valley or spur, across which the change in fault trace does not reflect a change in fault strike but rather a topographic effect (Figure 3.1).

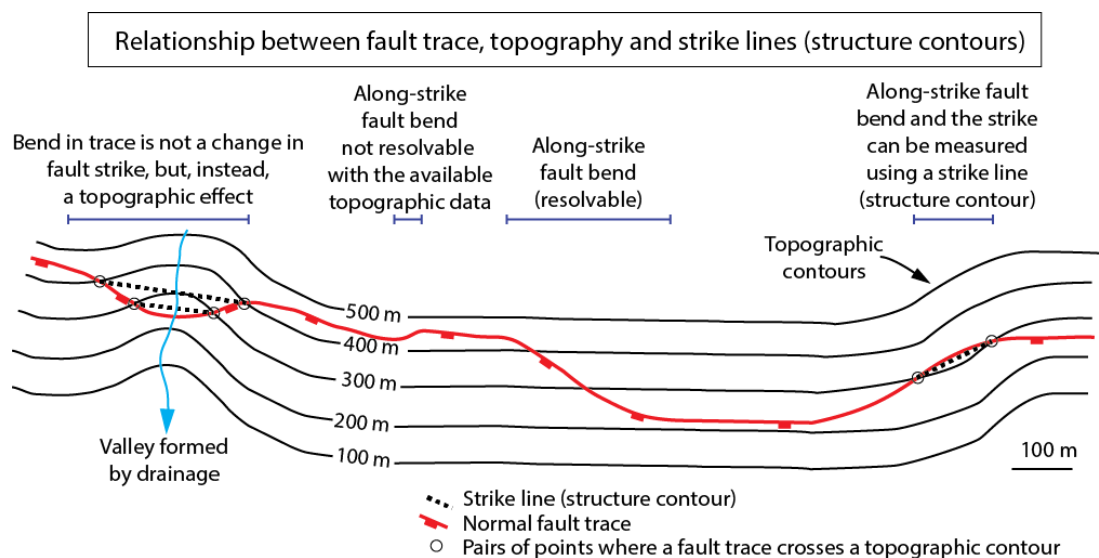


Figure 3.1: Relationship between fault trace and topography and construction of strike lines. This figure describes how to discern along-strike fault bends and topographic effects on a map view of a fault trace by using strike lines. Adapted from Iezzi et al. (2018).

To define the strike of fault bends and of fault segments outside the bend, the use of strike lines is preferred, instead of using single field measurements of fault strike. That is because fault plane orientations are organised so that the fault can accommodate the slip-vector, and this reflects in a large variability of single values of strike of bedrock fault planes where multiple measurements are available to constrain variability (Figure 3.2; Roberts, 2007; Iezzi et al., 2018). Hence, individual compass measurements of fault plane strike are not a good indicator of the overall strike of the fault.

Variability of single field measurements of strike of bedrock fault planes
 Example from the South Alkyonides fault, Greece (from Roberts, 2007)

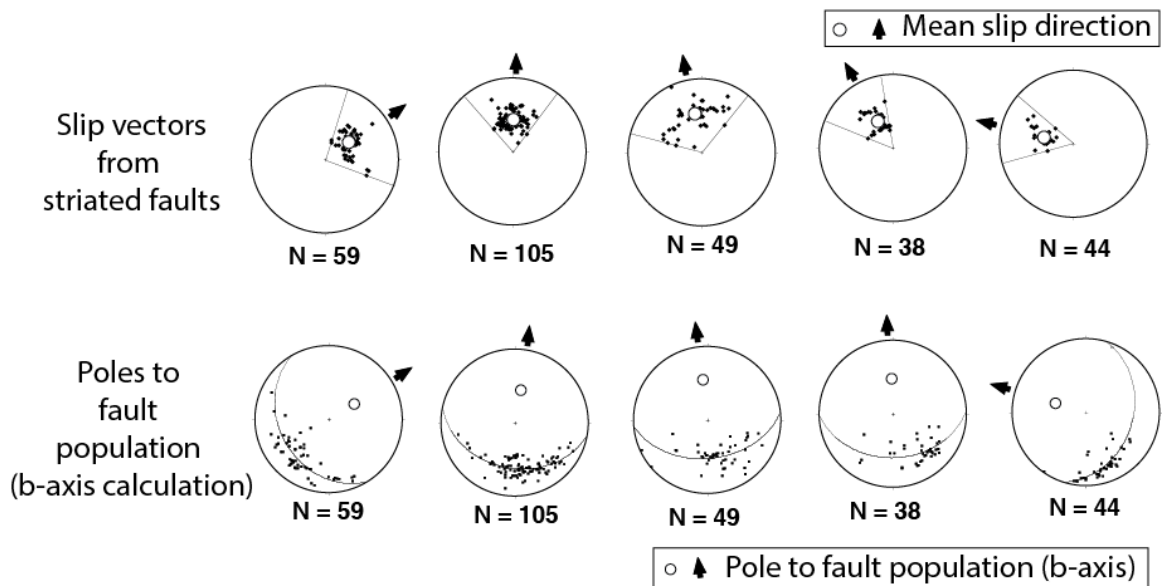


Figure 3.2: Analysis of strike variability of bedrock fault planes and slip vectors for the South Alkyonides fault, Greece. The figure shows the consistency between the slip vectors measured from striated faults and the slip vectors derived as pole to fault populations. This suggests that the fault plane orientations are organised so that the fault can accommodate the slip vector, and this reflects in a large variability of single measurements of throw. Therefore, the mean of single field measurements of strike will not be a good indicator of the overall strike of the fault. Hence, the use of strike lines to derive the overall fault strike is preferred. Adapted from Roberts, 2007.

3.2 Measurements of fault throw over different time scales

Within this PhD thesis, measurements of fault throw accumulated over three different time scales have been collected in order to study the relationship between the fault geometry and the slip-rates variations constrained over different time periods. The methods adopted for each are explained below. Throw values have been measured (1) on coseismic surface ruptures following some of the largest historical normal-faulting earthquakes worldwide, (2) on Holocene fault scarps produced by repeated coseismic surface ruptures, and (3) across geological cross-sections built across pre-faulting strata, to record slip accumulated over the entire history of faulting.

1) Following the M_w 6.0 24th August 2016 and M_w 6.5 30th October 2016 earthquakes of the 2016 Central Italy seismic sequence, coseismic ruptures have been mapped in detail. Measurements of the strike, dip, slip vector azimuth and plunge of the slip vector of the coseismic ruptures have been collected with a compass clinometer. Measurements of displacement, throw and heave associated with the ruptures have been collected in the plane of the slip vector using steel rulers. The locations of the measurements have been recorded using a hand-held barometric GPS. Field measurements of coseismic ruptures of other historical normal-faulting earthquakes are collected from published material.

2) The throw values associated with Holocene fault activity have been constrained during fieldwork by constructing profiles across preserved Holocene fault scarps, with undisturbed upper and lower slopes, parallel hangingwall and footwall cut-offs and no evidences of geomorphic processes affecting the fault scarp (Figure 3.3; see Section 2.3.2 in the previous chapter for details on measurements of throw from fault scarps).

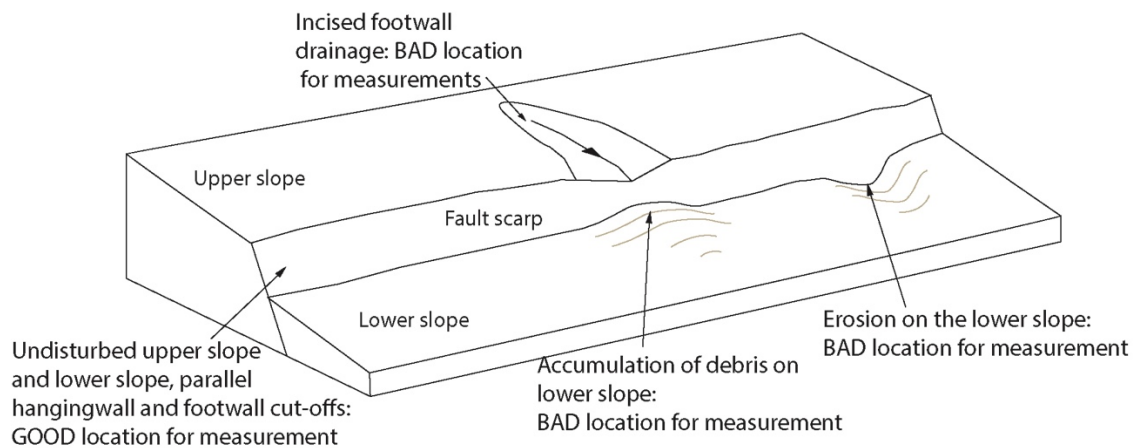


Figure 3.3: Sketch of a fault scarp showing the criteria to measure Holocene fault throw. Modified from Iezzi et al., 2019.

Fault scarp profiles have been built using a hand-held *Trupulse 360R*[®] laser range finder. This allows measurement of the azimuth, the vertical distance and the horizontal distance between the observer and the point of interest within a maximum range of 500 m and an accuracy of ± 30 cm in both distance and elevation (Figure 3.4). Fault scarp profiles were constructed by hitting a dense distribution of clear reflectors with the laser distributed along the same azimuth, recording the relative vertical and horizontal distances of each measurement from the observer (Figure 3.4). The vertical and horizontal distances have been plotted in order to reconstruct a fault scarp profile that allows the fault throw to be measured. The use of a laser range finder allows the building of fault scarp profiles for higher fault scarps and for longer distances away from the fault, compared to the classic technique of using a 1 m steel ruler (e.g. Papanikolaou et al., 2005). The ability to measure for longer distances away from the fault allows also one to overcome the presence of possible degraded upper slopes or accumulation of debris on the lower slope, giving the possibility to constrain both upper and lower slopes for longer distances away from the fault scarp. Furthermore, given the reduced size of the instrument, a hand-held laser finder

is easier to carry and use in different field conditions, compared to LiDAR scanner (e.g. Cowie et al., 2017). The scarp profiles are built normal to the fault strike, so to avoid effects of apparent dip. The throw-rate is constrained by the age of the surface that is offset by the fault scarp.

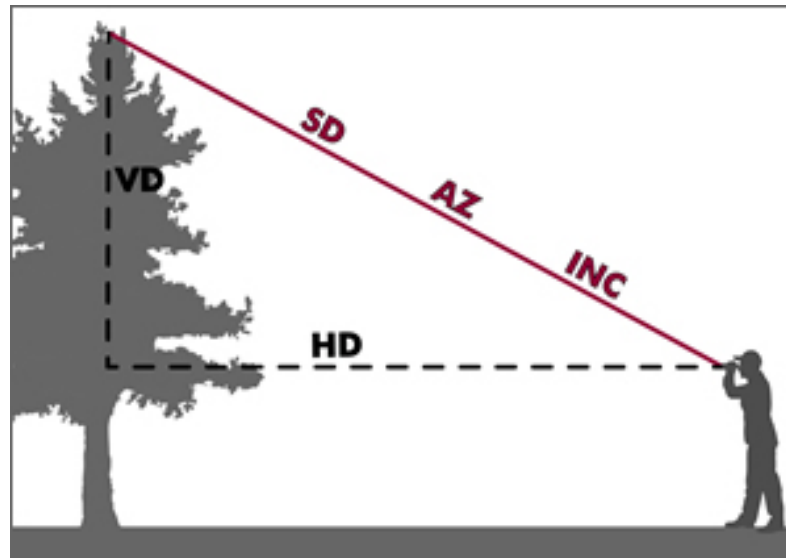


Figure 3.4: Sketch of the measurements collected with the *Trupulse 360R*® laser range finder. VD: Vertical distance; HD: Horizontal distance; SD: slope distance; AZ: azimuth of the measurement; INC: inclination. SD, AZ and INC are measured along the same red line. (from <https://www.lasertech.com/TruPulse-360-Rangefinder.aspx>)

3) Geological cross-sections across pre-faulting strata are used to derive values of throw accumulated over the entire fault history. Geological cross-sections are a graphic representation of the geology along a vertical plane of a certain orientation, and are used to interpret the relationships between different geological bodies. In this thesis, geological cross-sections have been built across the faults of interest via interpretation of published geological maps and observations from fieldwork. The fault throw is measured as the vertical distance between the hangingwall and footwall cut-offs of the same geological body on both sides of the fault. By measuring the offset between geological bodies formed before the onset of the normal faults, this measured offset represents the total slip accumulated by the fault during its entire activity. The cross-sections are built normal to

the faults in order to avoid the effect of apparent dip. The throw-rate is constrained by the age of the initiation of faulting in the region.

3.3 Cosmogenic nuclide analysis to gain information on fault slip

In addition to the 3 timescales described above, recent developments have allowed recognition of millennial slip-rates, that is, the time period between that associated with single earthquakes and the multiple earthquake constrained by post-LGM scarps. Cosmogenic sampling of fault planes has been carried following the criteria of Cowie et al. (2017). Detailed site characterization helped to ensure that the fault surface is exposed only through tectonic exhumation during repeated earthquakes, and it is not disturbed by geomorphological processes (as in Figure 3.3). In addition to this, minimal weathering of the fault plane (<1 mm) is confirmed by preserved frictional wear striae. Fault scarp profiles are constructed as previously described, in order to constrain key parameters for modelling the slip histories: the values of dip of the upper slope (α), the fault dip (β), the dip of the lower slope (γ) and the height of the fault scarp (h) (Figure 3.5).

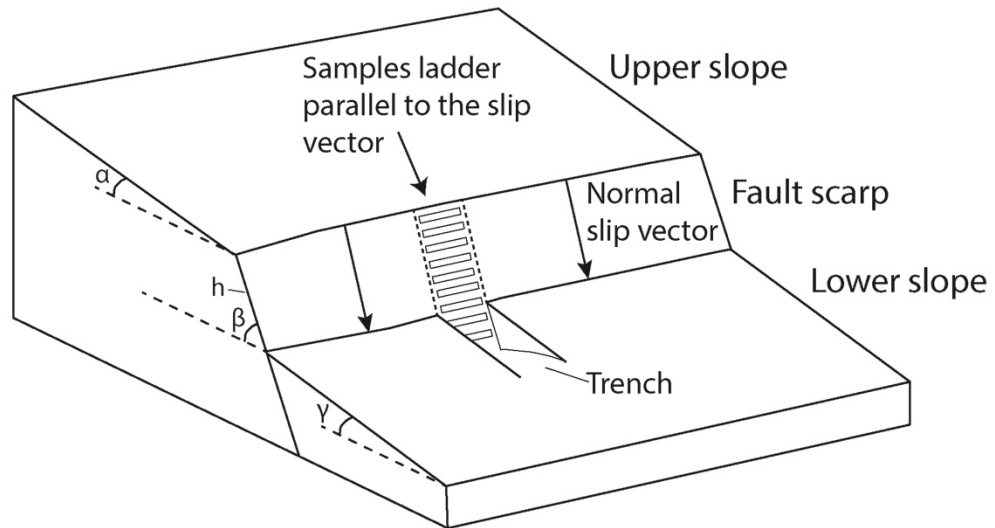


Figure 3.5: Sketch of a field site on a normal fault scarp. The scarp is undisturbed from geomorphological processes, the hangingwall and footwall cut-offs are parallel. The sample ladder is parallel to the slip vector. Samples are collected with equidistance of ~ 30 cm. α : dip of the upper slope; β : dip of the fault plane; γ : dip of the lower slope; h : height of the fault scarp measured along the fault.

3.3.1 Samples collection

Samples have been collected every ~ 30 cm up the fault plane using an angle-grinder rock saw in the vertical plane containing the slip vector (Figures 3.5 and 3.6). Structural data were collected to determine the fault orientation and slip vector using a compass clinometer. Where the fault plane showed weathering, samples were selected to avoid such areas, but to maintain the pattern of sample collection at successively-higher positions on the fault plane. To collect samples below the surface, an approach that provides extra information for modelling of the most recent earthquakes, trenches up to 1 m deep have been dug in front of the fault planes (Figures 3.5 and 3.6). Samples have dimensions of 15 x 5 cm and thickness of 2.5 cm (Figure 3.6). That is because the spallation sensibly reduces for deeper depth within the fault plane (Dunai, 2010).

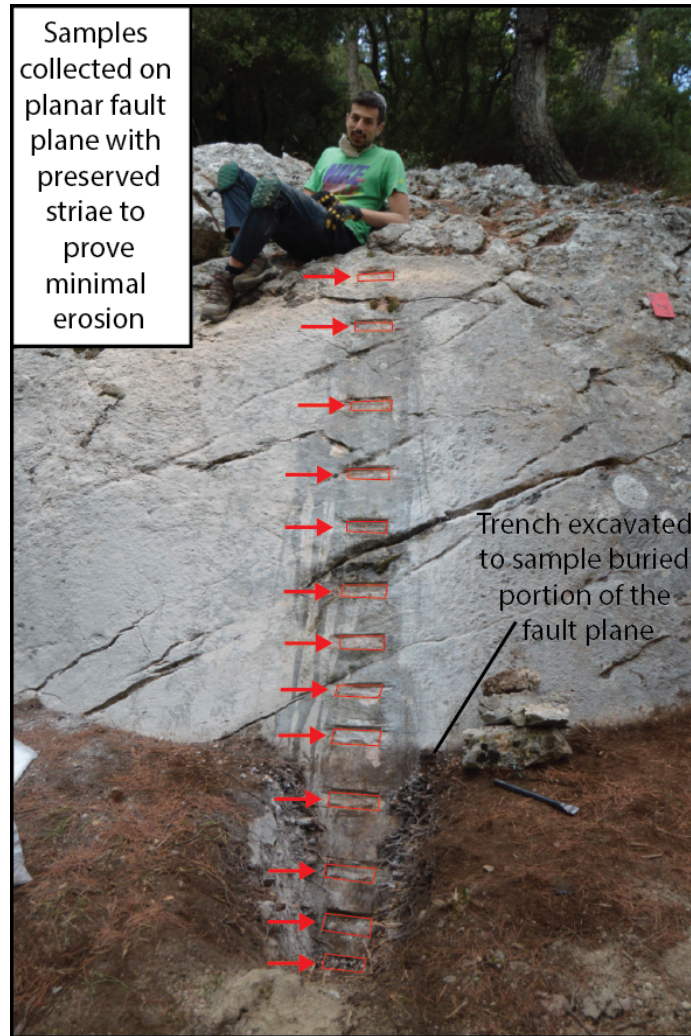


Figure 3.6: Field photo of a sampling location on the Fili fault, central Greece (see Chapter 7 for details). Red arrows mark the samples collected on the fault plane. Samples are collected ~30 cm equidistant, and have dimension of 15 x 5 cm and thickness of 2.5 cm. The trench is excavated in order to collect samples in the buried portion of the fault plane.

Measurements of the topographic shielding, which is due to the presence of additional topography occurring between the field site and the line of the horizon that shields the sampling site from the cosmic radiation, were collected every 20° up to 360° between the site and the line of the horizon, although these were un-necessary as the chosen modelling code (Beck et al., 2018) calculates time-varying shielding during incremental slip. Multiple photographs and videos were collected to constrain the geomorphology of the sample sites.

3.3.2 Samples preparation

All rock samples for ^{36}Cl analysis have been crushed using a jaw-crusher and a disk mill, available at University College London (UCL). This procedure reduced the sample to a grain size between 125-250 μm . Once crushed, the preparation of *in situ* cosmogenic ^{36}Cl AMS (Accelerator Mass Spectrometry) targets from carbonate bedrock samples has been performed at SUERC, Scottish Universities Environmental Research Centre, following the procedure outlined in Schimmelpfennig et al. (2009). The author spent 2 weeks following the entire preparation of a set of samples, from sample dissolution with 2M HNO_3 to the isolation of the cosmogenic ^{36}Cl AMS target, under the supervision of Dr. Delia-Mihaela Gheorghiu. The accelerator mass spectrometry (AMS) was performed at SUERC in East Kilbride, Scotland.

3.3.3 Modelling of ^{36}Cl data

For each fault, the ^{36}Cl concentrations of the samples have been modelled using a flexible Bayesian Reverse Jump Markov-chain Monte Carlo (MCMC) algorithm, published by Beck et al. (2018). Bayesian MCMC methods are a class of algorithms for sampling from a probability distribution. The MCMC code starts from a set of points and performs stochastic chains in order to obtain a sample of the desired distribution by recording states from the chain. The more steps are included, the more closely the distribution of the sample matches the actual desired distribution.

The code proposed in Beck et al. (2018) runs two parallel and independent MCMC chains to avoid premature convergence to local rather than global optima due to lack of explorative capabilities, and it verifies the global convergence of the modelling. Also, it

takes in account uncertainties in important parameters that were held fixed in previous codes (e.g. Schlagenhauf et al., 2010; Cowie et al., 2017), such as the density of the colluvium, ^{36}Cl spallation and muons production rates, and the timing of the moment after which the slip history started to be preserved. The code is available as Electronic Supplements of the Beck et al. (2018) paper.

To run the Matlab code, four files are required. A Matlab file is provided with the code, within which key information need to be reported: the parameters derived from the fault scarp profile (fault scarp height, dip of the upper slope, dip of the fault plane, dip of the lower slope), the depth of the trench dug in front of the fault plane, the mean density of the rock samples, and the maximum displacement per each slip event that the model is allowed to explore. Together with this Matlab file, three further data files are needed: “rock.txt”, “colluvium.txt” and “magfield.txt”. The “rock.txt” file contains the chemical composition of the rock samples, with major elements expressed in oxides and trace elements expressed in ppm, together with the ^{36}Cl concentrations from AMS and measurement uncertainties (atoms/gram), and the elevation of each sample up the fault plane. The “colluvium.txt” file contains the chemical composition of a sample of colluvial deposits in front of the fault plane. The “magfield.txt” contains information on the geomagnetic field to recover the production rates of ^{36}Cl , corrected for the topographic shielding and the elevation of the sample site, using information from Stone et al. (2000).

The next chapters will show the results obtained following the research work carried in the field areas. Each chapter will present a method section in which the methods applied for that specific study are described in detail where appropriate.

Chapter 4

Coseismic throw variation across along-strike bends on well-defined single normal fault segments: implications for displacement versus length scaling of earthquake ruptures.

4.1 Summary

The aim of this chapter is to study the effect of 3D structural complexities such as fault bends on the coseismic geometry, kinematics and slip for surface ruptures from large magnitude normal faulting earthquakes. This chapter presents detailed field measurements of the fault geometry and magnitude of slip in the 2016-2017 central Italy earthquake sequence, alongside three examples from large historical normal-faulting earthquakes in different tectonic settings (1887, Sonora earthquake (Mexico), M_w 7.5; 1981, Corinth earthquakes (Greece), M_w 6.7-6.4; 1983, Borah Peak earthquake (USA), M_w 7.3). All of these earthquakes have ruptured across fault bends in the strike of well-defined single fault segments. Therefore, it became important for this thesis to study the effect of fault bends in the strike of single faults on the distribution of the coseismic throw. The data shows multiple examples where the coseismic throw increases across fault bends, where fault dip also increases beyond what is necessary to accommodate a uniform slip vector. In terms of the underlying theory that needed to be developed to analyse and

interpret the data, this chapter demonstrates that it is possible to estimate the expected change in throw across a bend by applying equations that relate strike, dip and slip vector to horizontal strain conservation along a non-planar fault for a single earthquake rupture. This chapter shows that calculated slip enhancement in bends can explain the scatter in maximum displacement (D_{max}) versus surface rupture length scaling relationships, and suggests that if bends are un-recognized, they can introduce variation in D_{max} that may lead to erroneous inferences of maximum earthquake magnitudes derived from vertical offsets in palaeoseismic datasets, and stress drop variability for earthquakes. The results and contents of this chapter are published in Iezzi et al. (2018) in *Journal of Geophysical Research: Solid Earth*. The data were also used in papers by Civico et al. (2018) and Villani et al. (2018), which the current author, Iezzi, is a co-author, having provided field measurements to the general database; these papers present compilations of data from the so-called “EMERGEO Working group”, an informal association where most scientists working on the earthquakes agreed to compile data into a single data that these papers report.

4.2 Introduction

A key aspect where it was considered that new understanding needed to be developed by this thesis was the area of research involving displacement versus length scaling relationships for earthquake ruptures. Prior to this work the control exerted by local 3D fault complexity had not been considered in terms of its effect on scaling relationships. This is a surprising omission because these scaling relationships are commonly used to infer earthquake magnitudes from palaeoseismic data and measurements of active fault length, and also to calculate stress drops during earthquakes (e.g. Pantosti et al. 1996;

Dolan et al., 1997; Galadini and Galli, 2000, 2003; Villamor and Berryman, 2001; Manighetti et al., 2007; Cinti et al., 2011; Galli et al., 2014; Galli et al., 2017). These displacement versus length scaling relationships (e.g. Wells and Coppersmith, 1994; Stirling et al., 2002; Manighetti et al., 2007; Wesnousky, 2008; Leonard, 2010) are widely cited, yet they contain significant scatter in coseismic maximum displacement (D_{max}) for a given fault length (see Chapter 2, Section 2.4.1 for a detailed review of the fault scaling relationships). This chapter studies this scatter, and point out that (1) normal faulting earthquake ruptures commonly occur on faults with along-strike bends, (2) these bends appear to be characterized by relatively steep fault dips, as suggested by the 5 large normal faulting earthquakes studied in this thesis, and (3) dip increases within the bends will necessitate an increase in the magnitude of the coseismic slip vector, because the coseismic throw and displacement must increase if the coseismic strain is maintained along strike. The main conclusion is that the increase in the magnitude of the coseismic slip vector, if not recognized, can produce scatter in D_{max} values for a given fault length.

A key point that underpins the work in this chapter is that bends in the fault strike appear to be causal in controlling fault dip, and the dip is then causal in controlling local variation in throw and the magnitude of the slip vector in along-strike fault bends. In fact, the dip value for the breach fault, that eventually becomes the fault bend, forms after the formation of the initial en-echelon faults, and, in up-dip and down-dip locations, after the formation of a through-going fault within a bend (see Chapter 2, Section 2.2.1 for details on the growth and propagation of fault bends). In other words, the change in strike across the incipient bend sets up the situation that controls the dip of the eventual fault bend, and the 5 earthquakes described in this chapter suggest that relatively steep dips typify such locations. The formation of a steeply dipping breach fault with an oblique strike

necessitates an increase in throw across the bend if the strain is to be conserved along strike (Faure Walker et al. 2009). Thus, the overall point is that bends in fault strike appear to be causal in controlling fault dip, and the dip is then causal in controlling local increases in throw and the magnitude of the slip vector in along-strike fault bends.

The “Geometry-dependent throw-rate theory” (Faure Walker et al., 2015) suggests that the vertical offset across a given location on an active normal fault is controlled by the regional strain the fault must accommodate and the local non-planar fault geometry; although the theory was developed with longer term offsets in mind, containing multiple earthquake ruptures since the demise of the Last Glacial Maximum (LGM) at 15 ± 3 ka (e.g. Faure Walker et al. 2009), this must also apply to individual earthquake ruptures. For example, in response to the change in obliquity of the slip across an along-strike fault bend, the throw and fault dip must vary locally if the long-term horizontal strain across the fault is to be maintained (see Chapter 1, Section 1.1.2, for details on this relationship; Faure Walker et al., 2009, 2010, 2015). The relationship is confirmed by natural examples of long-term throw-rates across faults (e.g. 15 ± 3 ka) (Faure Walker et al., 2009; Wilkinson et al., 2015), but with only limited study of individual coseismic ruptures with larger coseismic D_{max} within fault bends (Wilkinson et al., 2015; Mildon et al., 2016). The coseismic studies were limited because these authors studied either (a) ancient examples where coseismic slip was clear but the age of the Holocene earthquake(s) unknown and only a small portion of the along strike extent of the rupture studied (e.g. Wilkinson et al. 2015), or (b) an example where the age of the earthquake was known (1997 AD), and the entire rupture extent studied, but the observations were made ~20 years after the earthquake, allowing the possibility that an unknown amount of post-seismic after slip may have obscured the coseismic signal (e.g. Mildon et al., 2016). Field

studies in the days immediately following surface ruptures in 2016 gave the opportunity to circumvent the above problems. The key thing of importance is that if coseismic D_{max} increases in along-strike fault bends with steep fault dips, compared to straight faults, and this phenomenon is not recognized, this chapter hypothesizes that databases such as that in Wells and Coppersmith (1994), and other scaling papers, may contain a mixture of ruptures across along-strike bends and along straight faults, and this may cause scatter in D_{max} for a given fault length. This could lead to erroneous inferences about stress drop and maximum magnitude.

To improve the understanding of coseismic throw variations associated with along-strike fault bends with steep fault dips, this chapter presents measurements and analysis of the surface ruptures to the 24th August 2016 M_w 6.0 and the 30th October 2016 M_w 6.5 earthquakes that both ruptured the southern part of the Mt. Vettore active normal fault in the central Apennines, Italy. The results show that the Mt. Vettore fault exhibits a prominent bend in strike with an associated increase in local fault dip, and a relatively high total finite throw and coseismic throw in this bend. During fieldwork, the coseismic throw, heave and displacement were measured independently within the vertical plane containing the slip vector, with heave derived with trigonometry where it was not possible to measure it directly. The orientation of the slip vector was recorded by mud smears on the fault planes that were striated during coseismic slip, and piercing points in ruptured colluvial deposits. In addition, the along-strike profiles of coseismic throw for these two earthquakes are compared with the structural relief and the long-term throw profile of the fault, constructed through geological cross-sections, to understand how throw in these earthquakes compares with the longer-term throw of the Mt. Vettore fault. Existing quantitative relationships for the conservation of the horizontal extensional strain-rate

across fault bends (Faure Walker et al., 2009, 2015) have been adapted so that they are suitable for single coseismic ruptures, to explain the large coseismic throw within the along-strike bend on the Mt. Vettore fault and within along-strike bends for three other large magnitude normal faulting earthquakes. These observations are used to discuss the observed scatter in D_{max} in displacement versus length scaling data, and the implications of this for calculating stress-drop variability and maximum estimated magnitudes for palaeoearthquakes.

4.3 Geological background of the 2016 Central Italy seismic sequence and of the Mt. Vettore fault.

The 2016-2017 Central Italy seismic sequence began on the 24th August 2016 with a M_w 6.0 earthquake that killed 302 people (Figure 4.1). The earthquake ruptured both the north-western part of the Laga fault and the south-eastern part of the Mt. Vettore fault with reports of surface ruptures confined to the latter (Livio et al., 2016, including the present author, Iezzi, as an author, having provided field measurements and discussed the results). Interesting to notice is that the earthquake ruptured simultaneously two individual fault segments, the Laga fault and the Vettore fault, propagating across a step which has commonly been considered to represent a boundary to the rupture propagation (e.g. Boncio et al., 2004; Figure 4.1). On 26th October 2016, two earthquakes (M_w 5.4, 5.9) ruptured the northern part of the Mt. Vettore fault, but it is unclear if they produced surface ruptures. It is unclear because on the 30th October 2016, before field surveys of the 26th October earthquakes, a M_w 6.5 earthquake ruptured the total length of the Mt. Vettore fault, re-rupturing locations that slipped in the 24th August 2016 earthquake and perhaps those on the 26th October (Figures 4.1, 4.2 and 4.4) (Chiaraluca et al., 2017;

Cheloni et al., 2017; Mildon et al., 2017; Pizzi et al., 2017; Civico et al., 2018; Falcucci et al., 2018; Ferrario and Livio, 2018; Scognamiglio et al., 2018; Verdecchia et al., 2018; Villani et al., 2018a; Villani et al., 2018b; Walters et al., 2018).

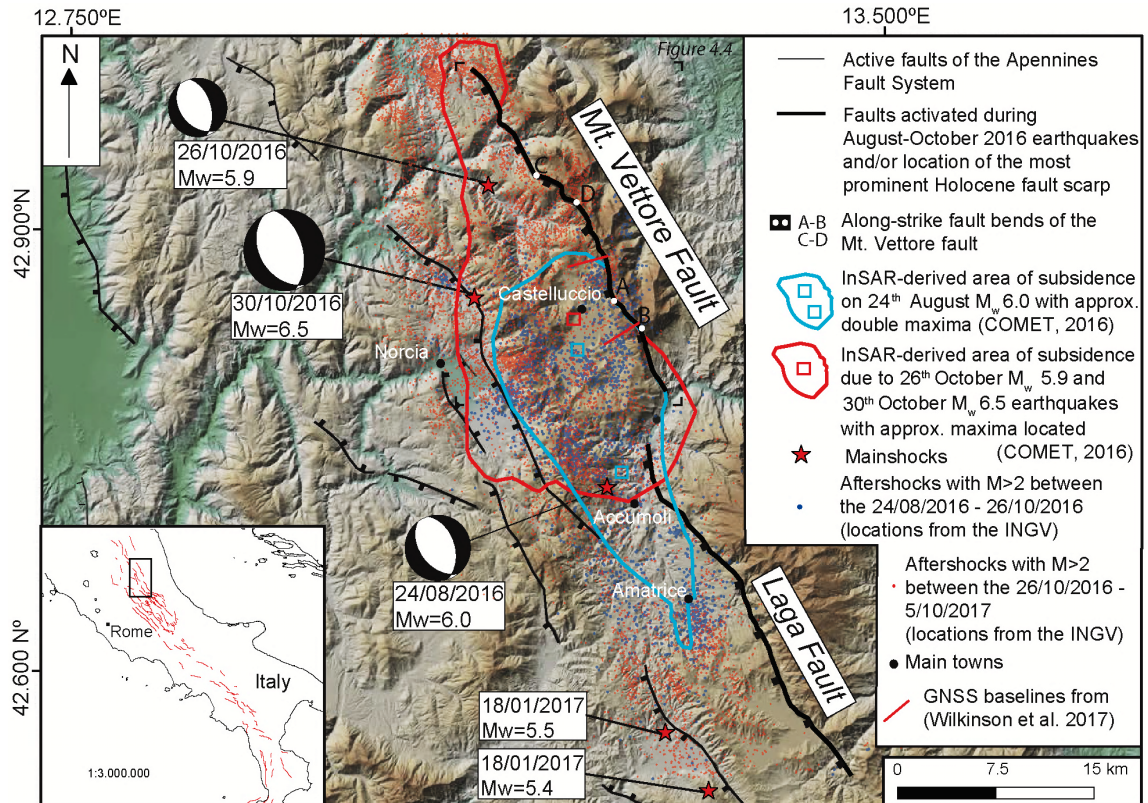


Figure 4.1: Location map of the 2016 central Italy seismic sequence. Black lines are active faults, with tick marks on hangingwall; thick black lines are Mt. Vettore and Laga faults, activated during the seismic sequence; the fault traces represent the location of the most prominent Holocene fault scarp. A-B and C-D are the locations of along strike fault bends of the Mt. Vettore fault. Red stars are the epicentral locations of the mainshocks of the sequence, locations and M_w from INGV (<http://cnt.rm.ingv.it>); focal mechanisms are from CMT catalogue (<http://rcmt2.bo.ingv.it/Italydataset.html>). Blue and red lines are the InSAR-derived area of deformation due to the 24th August M_w 6.0 and to 26th October M_w 5.9-30th October M_w 6.5 earthquakes, respectively (COMET, 2016), with the approximate locations of maximum coseismic subsidence indicated. Blue dots are aftershocks with $M > 2$ recorded between 24th August 2016 and 26th October 2016. Red dots are aftershocks with $M > 2$ recorded between 26th October 2016 and 5th October 2017 (CMT catalogue). From Iezzi et al., 2018.

Metre-scale offset across surface ruptures was measured with near-field 1hz Global Navigation Satellite System (GNSS) for the 30th October ruptures, revealing that the ruptures formed within 2-4 seconds, and before peak ground acceleration, supporting the primary tectonic origin of the ruptures (Wilkinson et al., 2017, including the present author, Iezzi, as 10th author) (Figure 4.1).

The Mt. Vettore fault dissects the western slope of the Sibillini Mountain range (Figures 4.1, 4.2, 4.3 and 4.4). The fault is about 30 km in length, and its 10^6 -year activity has produced an internally draining intramountain basin and lake-bed, and a large footwall escarpment (up to 1000 m of relief) (Figures 4.1, 4.3 and 4.4). Despite clear geomorphic evidence of Holocene active faulting, there is no record of prior historical earthquakes on the Mt. Vettore fault (see Galadini & Galli, 2000). Palaeoseismological analyses of the Mt. Vettore fault suggest a minimum throw-rate of 0.1-0.4 mm/yr, a recurrence interval that could span at least 4690 years and a minimum elapsed time of 1300-1500 years, but possibly up to 4155 years since the last palaeoearthquake (Galadini & Galli, 2003).

4.4 Methods

Field mapping of the surface ruptures was conducted immediately after the 24th August 2016 and 30th October 2016 earthquakes (Figures 4.2 and 4.4). The full extent of the 24th August 2016 surface rupture was mapped within a few weeks after the earthquake, and before the occurrence of the 30th October 2016 earthquake (Livio et al., 2016). For the 30th October earthquake, field mapping for this PhD was focused on constraining the large coseismic throws around a prominent bend near the southern end of the Mt. Vettore fault (bend A-B, Figure 4.4), which also ruptured in the earlier 24th August earthquake. Most of the mapping for the 30th October 2016 earthquake was carried out from the 2nd-6th November 2016, but mapping was completed for a section of the ruptures across the A-B bend in June 2017, due to bad weather after the 6th November 2016; the absence of measured postseismic slip larger than ~5 cm, constrained by re-measuring the offset at given sites in the June campaign, allows the combination of the November and June

datasets. The author of this Thesis has directly collected all the field measurements of coseismic ruptures shown in this Chapter.

The fault trace shows a second prominent along-strike fault bend along its northern half (C-D, Figure 4.4), which also ruptured during the 30th October M_w 6.5 earthquake (Civico et al., 2018; Villani et al., 2018). It was not possible to map ruptures across this fault bend with the detail required for this thesis in the time available, but those ruptures are described by Civico et al. (2018) and Villani et al. (2018) and the present author, Iezzi, is an author on both those publications.

In terms of how data were collected, measurements of the strike, dip, slip vector azimuth, plunge of the slip vector, throw, heave, and displacement associated with the ruptures have been collected using steel rulers, compass-clinometers and hand-held GPS (Figure 4.2a). Measurements were made every 2-10 metres along strike, and every 10-50 metres along strike, following the 24th August 2016 earthquake and the 30th October 2016 earthquake, respectively. These measurements have been plotted as a function of distance along a line oriented parallel to the regional strike (163°) of the Mt. Vettore fault. Where the ruptures occurred directly on the bedrock fault plane, they revealed a freshly-exposed light-coloured stripe in the limestone bedrock (Figure 4.2). In these locations the throw and displacement have been measured in the vertical plane containing the slip vector, defined by striations on mud smears, and the heave was derived with trigonometry. The longer-term slip vector orientation was confirmed by kinematic indicators on the fault plane, such as tool marks and frictional wear striae cut into the limestone fault gouge, and measurements of the strike and dip of fault planes. In places, the ruptures also stepped a few decimetres to metres into the hangingwall of the main bedrock scarp to offset

colluvial deposits (Figure 4.2). To obtain accurate measurements, and avoid the effects of disaggregation on colluvial scarps, two methods have been applied: (1) the slip vector azimuth and the displacement were measured along preserved continuous striae on fault planes cutting through the fine matrix of coarse-grained mixed scree, debris flow and colluvial deposits, and also the magnitude of the slip vector where possible; (2) where striae were not preserved, the slip vector was measured by matching piercing points on the footwall and hangingwall cut-offs defined by clasts and holes left by clasts in the colluvium (see Figures 4.2b.ii and 4.2c.ii).

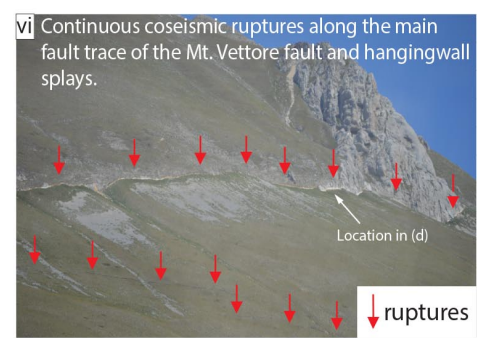
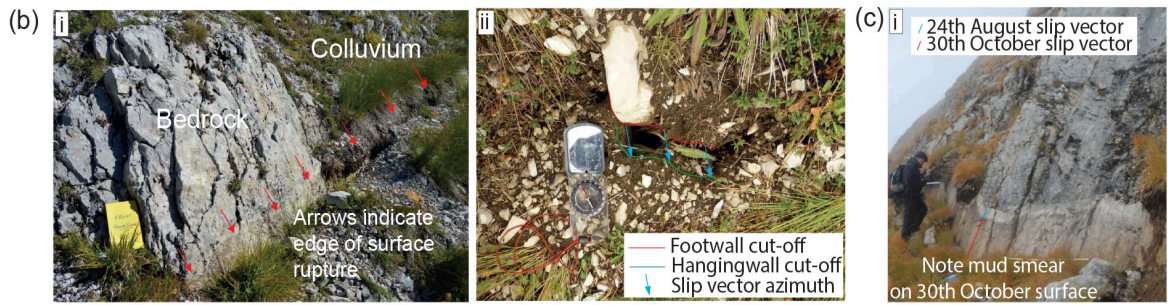
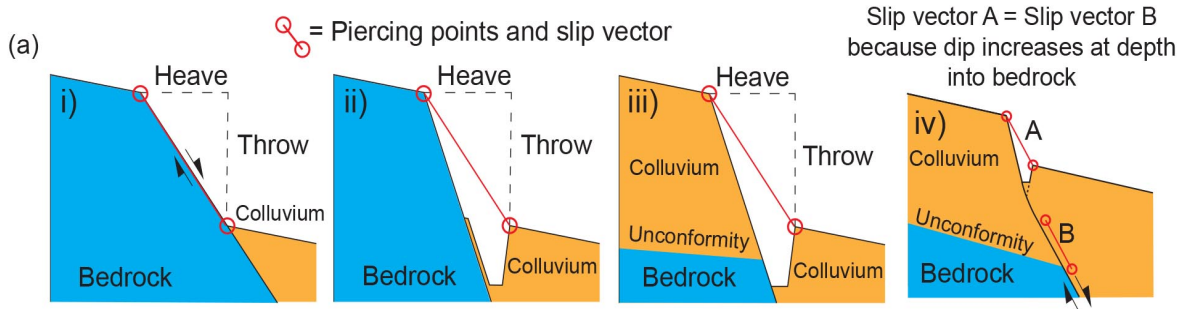


Figure 4.2: Field observations of the surface ruptures along the Mt. Vettore fault. a) Cartoons showing the measurements collected on surface ruptures observed in the field. On bedrock fault planes, the slip vector has been measured along the fault plane, the heave was derived using trigonometry. In colluvium, the slip vector has been measured between piercing points on the hangingwall and footwall. b) Photos of the surface ruptures associated with the 24th August M_w 6.0 earthquake: b.i) coseismic ruptures propagating from bedrock to colluvial deposits without significant variation in slip magnitude; red arrows mark the edge of the rupture on the footwall (notebook for scale, 20 cm tall); b.ii) map view of measurements of the slip vector azimuth from reconstruction of the piercing points in colluvial deposits on ground cracks (compass base is about 18 cm long). c) Photos of the surface ruptures associated with the 30th October M_w 6.5 earthquake: c.i) bedrock fault plane, showing the 24th August rupture (blue line) and the 30th October rupture (red line); c.ii) coseismic surface rupture propagating through colluvium, with the formation of a vertical scarp and an opening at its base; in this cases, the slip vector has been measured by matching piercing points on the hangingwall and footwall cut-offs, to obtain the best representation of the slip vector on fault at depth, below the colluvial deposits; c.iii) striations into a mud smear on the fault plane (red arrows indicate the slip vector); c.iv) maximum offset observed, displacement 2.4 m measured along a single tool track on a mud smear; c.v) coseismic ruptures on an antithetic fault, with exhumation of the fault plane; red arrows indicate the slip vector azimuth, which is consistent between bedrock fault plane and colluvium (plastic bottle as scale, about 20 cm tall); c.vi) panoramic view of the surface ruptures on the Mt. Vettore fault; the ruptures were continuous along the main fault trace of the Mt. Vettore fault, and hangingwall ruptures also formed. d) Ruptures in June 2017, after winter rain and snow cleaned the fault plane of mud; fresh stripes of fault plane following the 24th August M_w 6.0 and the 30th October M_w 6.5 are shown, with pale blue arrows indicating the slip vector for the 30th October earthquake. From Iezzi et al., 2018.

To understand how the offsets produced by these earthquakes compare to offsets that have developed over the long-term history of the Mt. Vettore fault, the along-strike profiles of coseismic throw for the two earthquakes are compared with the long-term throw profile of the fault, constructed from ten serial geological cross-sections across pre-rift strata, based on the geological map published in Pierantoni et al. (2013) and field observations obtained during fieldwork (Figure 4.3). These along-strike profiles are also compared with (1) the large-scale relief associated with the footwall escarpment on the Mt. Vettore Fault obtained using topographic profiles derived from a 10 m resolution DEM (see location of the profiles in Figure 4.4; Tarquini et al., 2012); (2) the location of Middle Pleistocene-Holocene lake deposits in the hangingwall, to ascertain the position and dimensions of areas of maximum subsidence (see location of lake bed in Figure 4.4; from Pierantoni et al., 2013); (3) the locations of maximum coseismic subsidence determined from preliminary InSAR results (see location of maximum subsidence in Figures 4.1 and 4.4; from COMET, 2016).

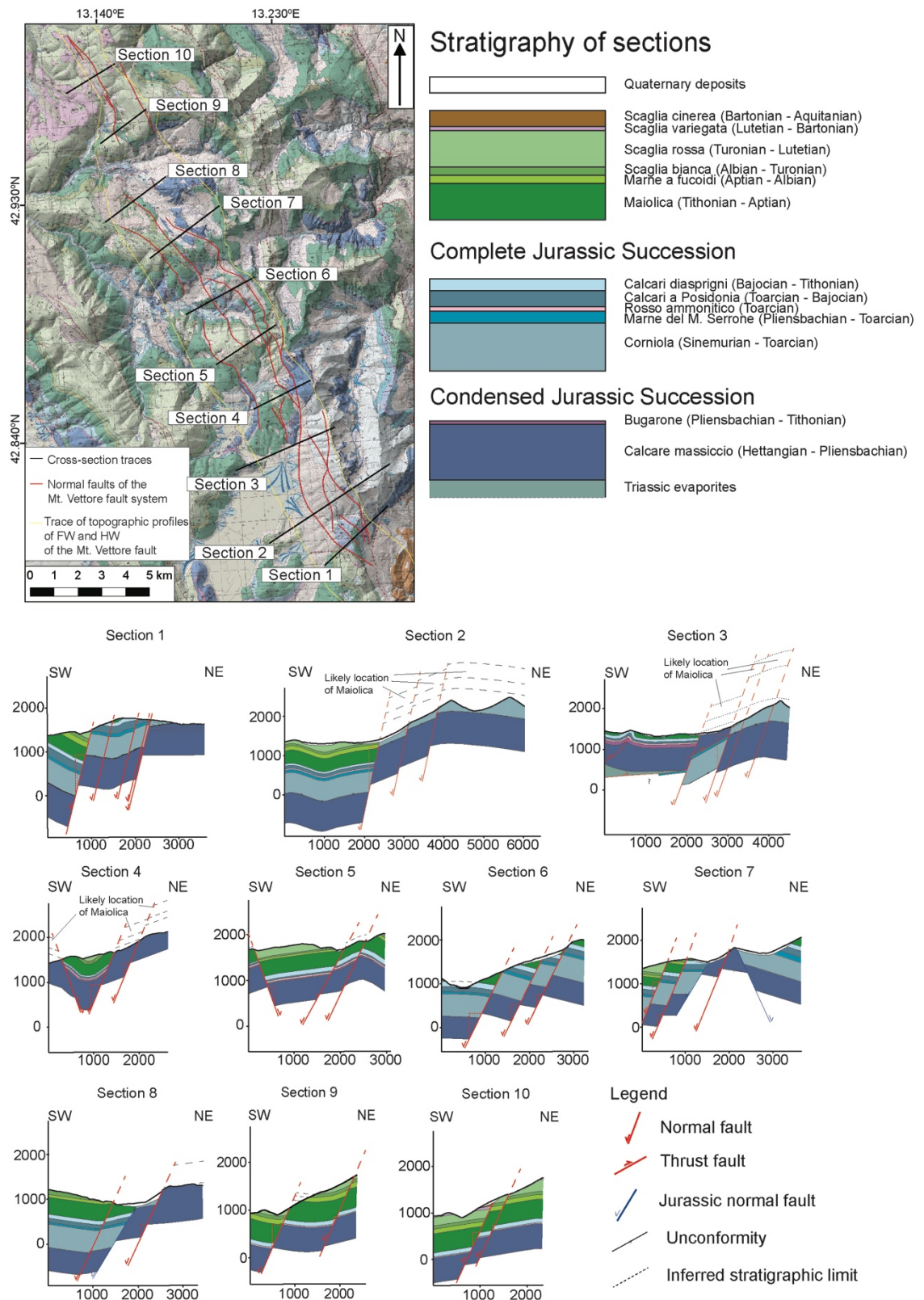


Figure 4.3: Geological cross-sections across pre-rift strata, distributed with an equidistance of about 2.5 km along the length of the Mt. Vettore fault. Stratigraphy and map are based on Pierantoni et al. (2013). In the inset map, in yellow are reported the topographic profiles of the hangingwall and the footwall of the Mt. Vettore fault, used to study the fault-related relief. From Iezzi et al., 2018.

4.4.1 The relationship between strain, fault geometry and coseismic throw

The predicted throws across fault bends have been calculated by adapting the methodology published in Faure Walker et al. (2009) (See Chapter 1, Section 1.1.2 for details), so that it can be used with individual ruptures, using field measurements as input. An “along-strike fault bend” is defined as a portion of the fault where the strike is not perpendicular to the regional extension direction, derived from geodetic measurements (e.g. D’Agostino et al., 2011; Figure 4.4b). The outer faults are portions of the fault either side of the bend with strikes that are perpendicular to the regional extension direction (Figure 4.4b).

The methodology of Faure Walker et al. (2009), when applied to natural examples, shows that the horizontal strain-rate is maintained along strike, even within along-strike fault bends where the dip increases beyond what is necessary to accommodate a uniform slip vector, because variation in fault strike and dip are accompanied by changes in throw and plunge of the slip vector (Faure Walker et al., 2009; 2010; 2015; Wilkinson et al., 2015). This thesis attempts to verify this for individual coseismic ruptures using the 2016 Italian earthquakes and three other large magnitude normal faulting earthquakes that produced surface ruptures reported in the literature.

The horizontal strain is calculated for fault locations outside the bend (the “outer fault segments”). Equation 1, adapted from equations 13-17 from Faure Walker et al. (2010), shows how strain-rate along a specified direction, φ , is calculated using field measurement of strike, dip, slip vector azimuth and coseismic throw.

$$\dot{\epsilon}_{\varphi} = \left(\frac{1}{2at}\right) \sum_{k=1}^K L^k T^k \cot p^k [\sin(\phi^k - \Phi^k) - \sin(\phi^k + \Phi^k - 2\varphi)] \quad (1)$$

$\dot{\epsilon}_\phi$ = strain-rate (/yr), a=area of grid square (m²), t=time (yr), L=fault length (m), T=throw (m), p=plunge (degrees), ϕ =slip vector azimuth (degrees), Φ =fault strike (degrees).

To calculate the expected coseismic throw across the bend, Equation 1 has been rearranged to express throw as a function of strain and field measurements of strike, dip and slip vector azimuth across the bend (Equation 2). In calculations of throw across the bend, the inferred strain magnitude across the fault bend is assumed to be the mean of the strain calculated on the outer faults either side of the bend.

$$T = \frac{\text{mean strain across outer faults per given length}}{\left(\frac{1}{2\alpha}\right)\cot p^B \{ \sin(\phi^B - \Phi^B) - \sin(\phi^B + \Phi^B - 2\alpha) \}} \quad (2)$$

with B representing the value within the bend, α = principal angle of the outer fault segments measured clockwise from north (Fung, 1977; Faure Walker et al., 2010), and p (plunge) is defined as:

$$p = \arctan(\sin(\phi - \Phi) \tan(dip)) \quad (3)$$

Given the values of strain, strike and slip vector azimuth at the bend, the fault dip has been varied over a large number of values (i.e. iterated), in order to obtain a coseismic throw consistent with the field measurements of throw across the bend.

To obtain strike values that represent the overall character of the fault bend and of the outer faults, for distances of hundreds of metres along the fault, strike lines were constructed (Figure 4.4b; See Chapter 3, Section 3.1, Figure 3.1 for details on the use of strike lines to determine the orientation of the fault). The dip is obtained from field measurements.

To assess whether results for the 2016 Mt. Vettore ruptures also explain aspects of other examples, published structural data are used to study coseismic throw across along-strike fault bends for other active normal faults ruptures (1887, Sonora earthquake, Mw 7.5 (Suter, 2008a; 2008b; 2015); 1981, Corinth earthquake, Mw 6.7-6.4 (Jackson et al., 1982; Morewood & Roberts, 2001); 1983, Borah Peak earthquake, Mw 7.3 (Crone et al., 1987). Additional data were collected for the Corinth earthquake during fieldwork carried by the author of this thesis. The above data were used to predict the coseismic throw in along-strike fault bends for comparison with measurements of the same, as was done for the Mt. Vettore earthquake sequence studied herein.

The reader should note that the above calculations apply only once a rupture is through going and has crossed a bend. This is emphasized because there are natural examples of normal faulting ruptures that terminated at along strike fault bends. Biasi and Wesnousky (2017) shows that earthquake ruptures can either terminate at fault bends or propagate through them. It is beyond the scope of this thesis to discuss further the reasons why earthquake ruptures can be halted by fault bends or propagate across them. This PhD Thesis explores the consequences of fault ruptures propagating within fault bends.

4.5 Results

4.5.1 Field observations

For the 24th August 2016 earthquake, surface ruptures formed either on the bedrock fault scarp, forming a freshly exposed stripe on the fault plane, or a few metres into the

hangingwall, for a length of about 5 km along strike, propagating across a prominent along-strike fault bend (Figures 4.1, 4.2 and 4.4). Surface ruptures were identified on the Mt. Vettore fault with a footwall made of competent limestone, whereas there are few clear signs of surface ruptures on the Laga fault, which has a footwall made mainly by less competent siliciclastic flysch (Livio et al., 2016). On the Mt. Vettore fault, the ruptures were continuous for about 2 km across the fault bend. The rupture was less continuous towards the SE and NW terminations of the overall rupture. The surface ruptures were organized as sets of well-defined partially-overlapping traces, tens of metres in length, each with a local *Dmax*. Rupture traces were arranged with both right and left-stepping en-echelon relay zones placing overlapping tip zones a few decimetres to metres apart across strike. Ruptures could be traced along strike from fault traces within colluvial deposits onto bedrock fault planes and vice versa (Figure 4.2b).

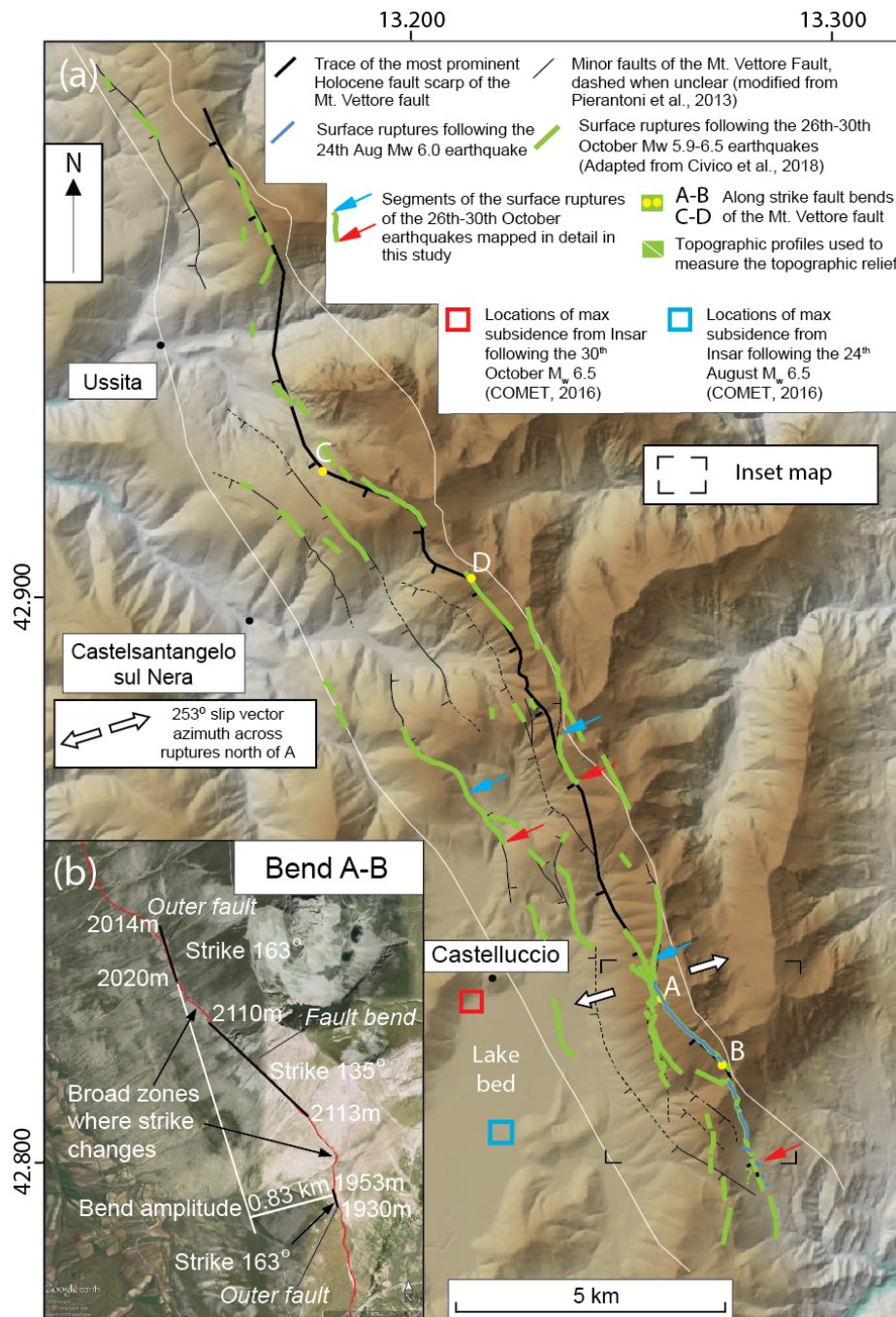


Figure 4.4: Map of the Mt. Vettore fault. a) Summary map of the surface ruptures associated with the 2016 central Italy earthquakes, adapted from Civico et al. (2018) and field mapping carried by the author. Fault traces are from the geological map published in Pierantoni et al. (2013). Thick black lines mark the trace of the most prominent Holocene fault scarp of the Mt. Vettore fault. Thin black lines are minor faults of the Mt. Vettore fault system, dashed where not clearly evident at the surface. Pale blue traces are the total coverage of the surface ruptures that occurred after the 24th August earthquake. Green traces are the distribution of the surface ruptures associated with the 30th October earthquake (adapted from Civico et al., 2018). Pale blue and red arrows mark the traces of the surface ruptures following the 30th October earthquake that were mapped and described in detail in this thesis. White lines are topographic profiles built to derive the topographic relief of the Mt. Vettore fault. Red and blue squares are depocenters of the InSAR-derived area of deformation following the 30th October earthquake and the 24th August earthquake, respectively. b) Characterization of the fault bend marked as A-B. Red line is the main fault trace of the Mt. Vettore fault. Black lines are strike lines. The figure shows that within the fault bend the strike changes by about 28°, producing an amplitude of the bend of about 0.83 km. This figure also shows that both earthquakes ruptured across the along-strike fault bend. From Iezzi et al. (2018).

After the 24th August 2016 M_w 6.0 earthquake, the combined effect of the 26th October 2016 M_w 5.4 and 5.9, and the 30th October 2016 M_w 6.5 earthquakes appear to have ruptured the entire Mt. Vettore fault, reactivating the locations that exhibited surface ruptures produced by the 24th August M_w 6.0 earthquake (Figures 4.2 and 4.4). Given the location of the mainshock, the 26th October M_w 5.9 earthquake appears to have ruptured only the northern part of the fault (Figure 4.1). Due to the short temporal interval between the 26th October and 30th October events, it was not possible to determine whether the surface ruptures of the northern part of the fault were in part caused by the 26th October M_w 5.4 and 5.9 earthquakes or if the measured surface rupture was formed entirely by the larger 30th October M_w 6.5 earthquake, so these northern parts of the rupture were not included in this study. The surface ruptures in the central and southern parts of the fault, on which the field mapping has been focused, were all attributable to the 30th October M_w 6.5 earthquake, based on the magnitude of slip and observations concerning their timing of formation (Civico et al., 2018; Villani et al., 2018).

The 30th October surface ruptures were significantly longer and more continuous, with more slip for each rupture trace, than ruptures associated with the 24th August earthquake. The ruptures mainly occurred on bedrock fault planes, and as synthetic ruptures in colluvial deposits adjacent to the main Mt. Vettore fault escarpment. However, in places, synthetic and antithetic ruptures occurred a few tens to a few thousand metres into the hangingwall (Figure 4.4). Where it ruptured on bedrock, the coseismic slip produced a second freshly-exposed stripe on the fault plane (Figure 4.2c.i, 4.2c.iv, 4.2c.v and 4.2d). The presence of a mud smear covering the fault plane (Figure 4.2c.iii) allowed recognition of portions of the fault plane exhumed by the 24th August (white stripe, no mud smear due to wind and rain since 24th August) and the 30th October earthquakes (mud

smear deformed by tool tracks and frictional wear striae observed a few days after the event). By June 2017, mud smears on the fault planes were no longer preserved, but it was still possible to recognize two generations of light-coloured stripe on the fault planes, belonging to the two different earthquakes (Figure 4.2c.i and 4.2d).

All the parameters measured in the field show high variability along strike, even over a few tens of metres (Figures 4.5 and 4.6). This is because individual rupture traces were as short as a few metres to tens of metres, and thanks to dense sampling it was possible to capture changes in parameters along each individual rupture trace. Despite the small-scale variability revealed by field measurements, four overall features can be identified:

1) The range of strike values for the surface ruptures is similar between the two different earthquakes. Measurements of both the coseismic ruptures in colluvium and the strike of the bedrock fault planes show a large variability of values: the strike ranges between N110° - N210° for ruptures in colluvium (Figures 4.5a and 4.6a), and between N110° - N178° for bedrock fault planes (Figure 4.6h and 4.7). Such variation is common on bedrock fault scarps where multiple measurements are available to constrain variability (Figure 4.7; Roberts, 2007; Iezzi et al., 2018). Strike lines are a better way to gain the overall strike of the fault over along-strike distances of hundreds to thousands of metres and show that the fault strike is ~N163° to the north-west and south-east of the bend and N135° within it (Figure 4.4b).

2) The dip of the bedrock fault plane is steeper in the fault bend, where it ranges between 70° - 88°, compared with ranges between 50° - 70° on the outer faults (Figure 4.6i).

3) The slip vector azimuths are very similar for both earthquakes: they range between N210° - N270°, which is consistent across the mapped fault strands (Figures 4.5b and 4.6b), and consistent with the regional stress field and 2016 focal mechanisms (σ^3 is orientated NE-SW; Mariucci and Montone, 2016). The overall azimuth of the slip vector across the fault bend and the outer faults is derived by combining measurements of the coseismic slip vector azimuth with calculations of the best fit to poles of fault planes (Figure 4.7). This shows that the slip vector azimuth is relatively constant along the fault trace (Figures 4.5, 4.6 and 4.7). The overall coseismic slip vector azimuth is thought to be best-represented by measurements close to the centre of mapped ruptures (Roberts, 2007), and field measurements suggest a value of $\sim 253^\circ$ (Figures 4.4 and 4.7), perpendicular to the overall fault strike, and oblique to the bend A-B. The value of $\sim 253^\circ$ is consistent with the regional NE-SW orientated extensional stress field and 2016 focal mechanisms (Mariucci and Montone, 2016). The plunge of the slip vector is also similar between the two earthquakes, with values increasing within the fault bend, where it ranges between 60° - 80°, compared to values along the outer faults, where it ranges between 40° - 70° (Figures 4.5c and 4.6c). The change in the plunge of the slip vector within the fault bend suggests that the Mt. Vettore fault is not a perfectly corrugated fault surface, in fact exhibiting a non-cylindrical geometry (see Roberts, 2007, for explanation).

4) Values recording the magnitude of slip appear to increase across the bend for both surface-rupturing earthquakes (Figure 4.5d, e, f and 4.6d, e, f). The throw for the 24th August earthquake is less than 12 cm along the southern outer fault, and increases to a maximum of 29 cm within the bend (Figure 4.5f). For the 30th October earthquake, throw is less than 90 cm along the southern outer fault, increases within the fault bend to a maximum of 234 cm, and decreases across the northern outer fault to less than 150 cm

(Figure 4.6f). Similar patterns are evident for field measurements of displacement (Figures 4.5d and 4.6d). Evidence for along-strike variability for heave is less marked, suggesting that the magnitude of horizontal extension was, in general, conserved across the bend, away from the tips of the overall ruptures (Figures 4.5e and 4.6e). Also, values for offset do not appear to be affected by propagating through different materials (e.g. colluvial deposits and carbonate bedrock) with similar values where ruptures propagated from one material to the other (Figure 4.2b.i).

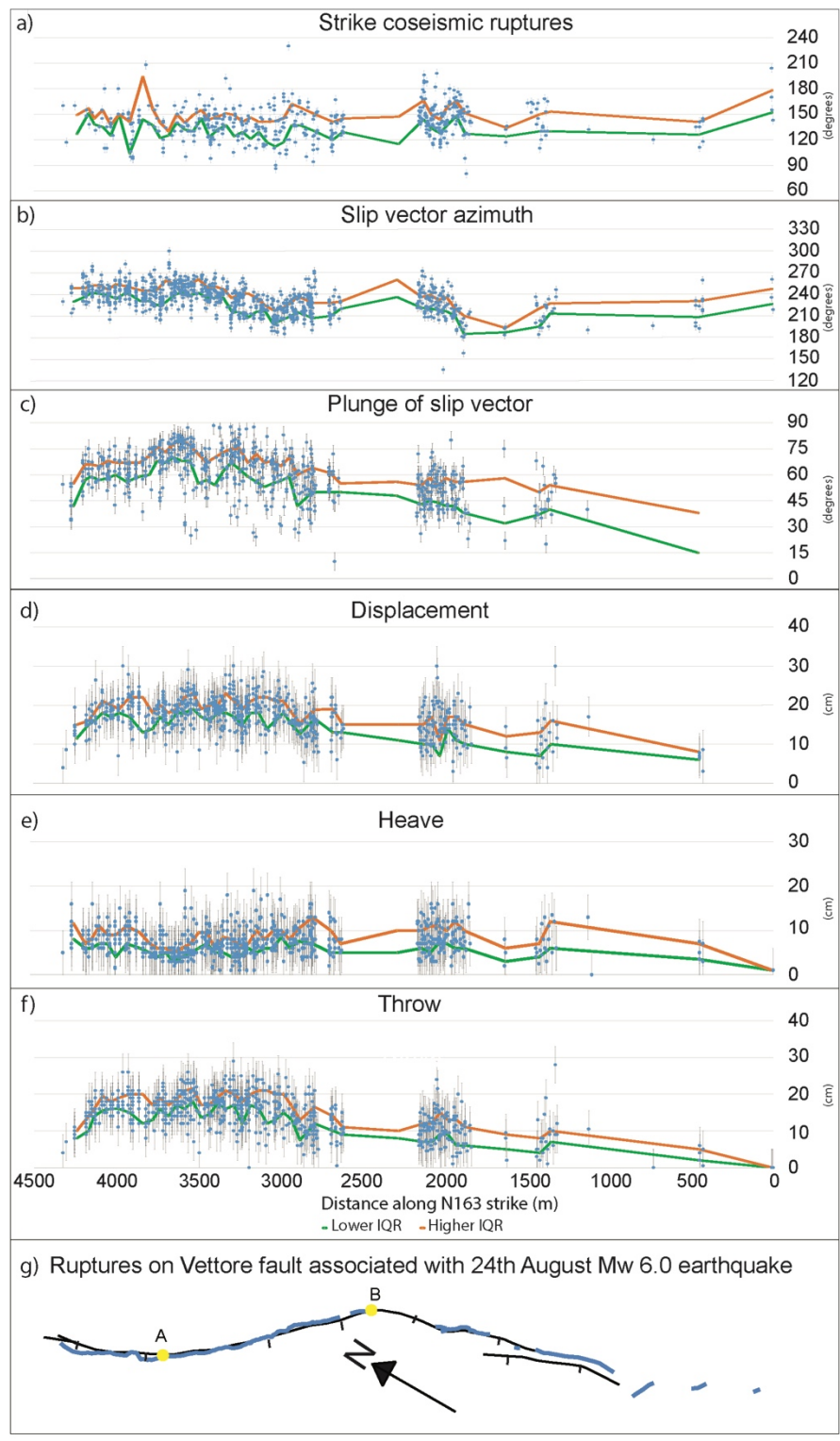


Figure 4.5: Field data following the 24th August 2016 M_w 6.0 earthquake. In grey are reported error bars of ± 5 degrees for strike, slip vector azimuth and plunge of slip vector, ± 5 cm for displacement, heave and throw. In orange and green are reported the Interquartile ranges (IQR) of the measurements, calculated every 50 m along the strike of the fault. This show how throw and displacement profiles are skewed towards the fault bend A-B. Modified from Iezzi et al., 2018.

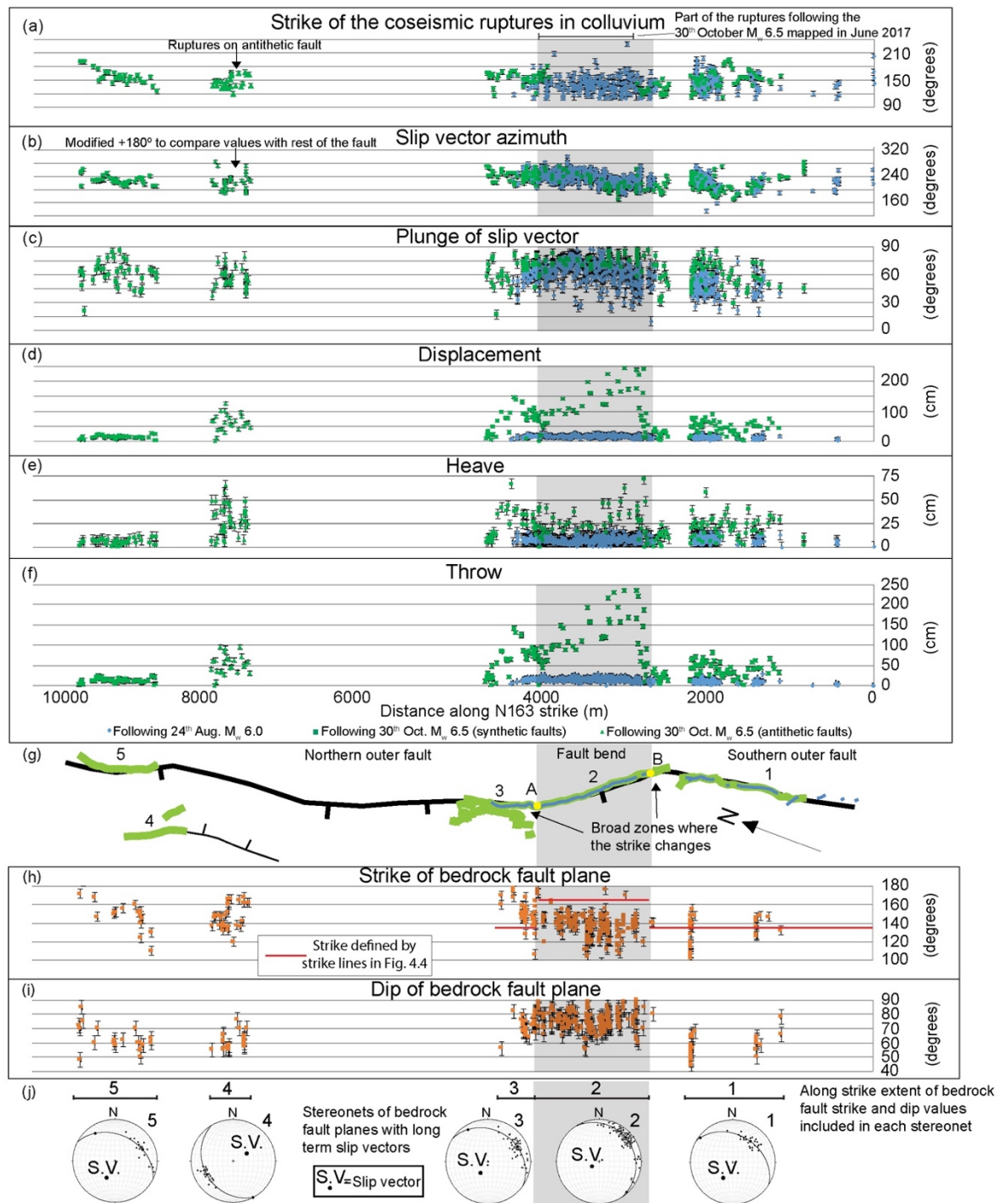
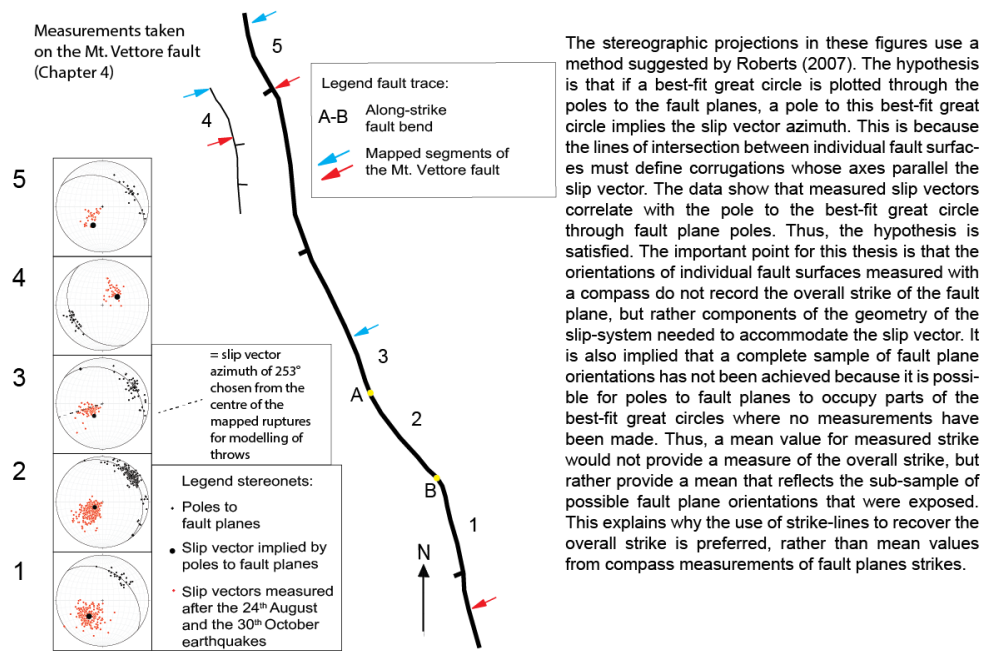


Figure 4.6: Field data following the 24th August and 30th October earthquakes collected during this PhD. Panels a-f are measurements of the coseismic surface ruptures: in blue are measurements of the coseismic ruptures following the 24th August M_w 6.0 earthquake, in green are measurements of the coseismic ruptures following the 30th October M_w 6.5 earthquake. Panels h-j are measurements of the bedrock fault plane. Horizontal black bar in (a) highlights the part of the ruptures following the 30th October event mapped in June 2017. Error bars of $\pm 5^\circ$ for strike, slip vector azimuth and plunge of slip vector and of ± 5 cm for displacement, heave and throw are reported as grey lines for field measurements, although errors as large as ± 6 cm are plausible for throw for some of the largest values. Panel g shows the fault map of the sector of the Mt. Vettore fault mapped in detail; in blue are the surface ruptures mapped following the 24th August M_w 6.0 earthquake; in green surface ruptures mapped following the 30th October M_w 6.5 earthquake. Panel j presents stereonets of different sectors of the fault (numbers coded as in g)), showing the long-term slip vectors derived from calculation of the best fit of poles to measured bedrock fault planes. From Iezzi et al., 2018.

Variability of single field measurements of strike of bedrock fault planes



Example of corrugated bedrock fault plane, with high local variability of strike measurements

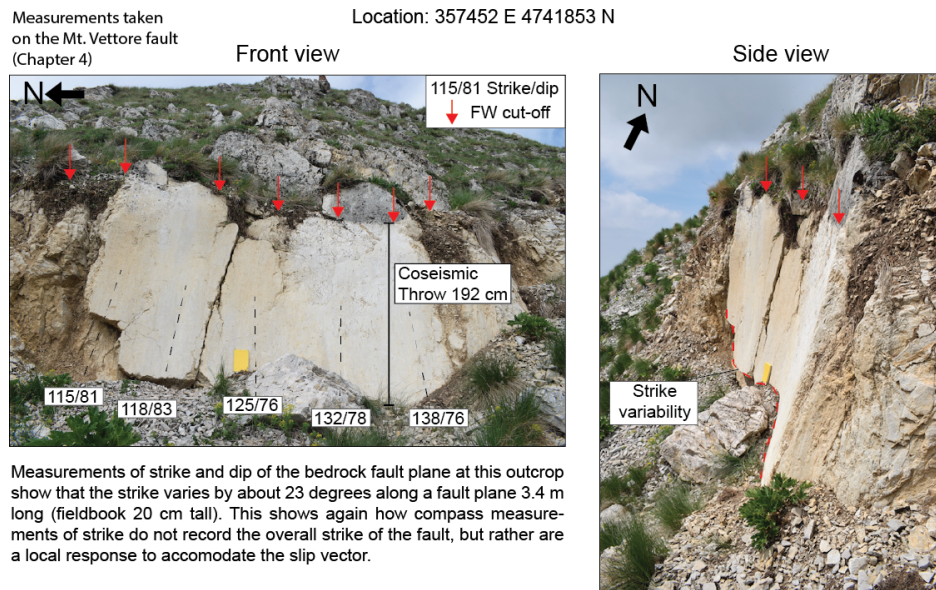


Figure 4.7: Analysis of strike variability of bedrock fault planes and slip vectors. Stereonets represents fault planes and slip vectors orientations for the Mt. Vettore fault. Black dots are poles of bedrock fault planes, big black dot is the mean slip vector, derived by the best-fit of the poles. Red dots are the measured slip vectors following the 24th August 2016 and the 30th October 2016 earthquakes. The stereographic projections show that the mean slip vector is consistent with the measured slip vectors. Stereonet 3 shows measurements of the slip vector azimuth in the central part of the map trace of the ruptures, which is the most representative of the overall slip as recorded from focal mechanisms (see Roberts, 1996; Roberts, 2007); therefore, 253° has been chosen as the coseismic slip vector of the Mt. Vettore fault, derived as best fit of the measured coseismic slip vector azimuths in stereonet 3. The analysis of the different stereonets along the fault trace shows that the long-term slip vector across the bend is more oblique to the strike of the fault, compared to the slip vectors across the outer faults. Photos of one outcrop show how strike varies of about 23° in about 3 m long distance. These two observations confirm that all the measured fault planes work to accommodate the fault slip vector. From Iezzi et al., 2018.

To assess whether the observed scarps could be related to shallow gravitational motions (e.g. Huang et al., 2017, for the 24th August 2016 earthquake) instead of coseismic slip, the azimuth of slip vectors measured across the ruptures is compared with slope dip directions, derived from a 10m resolution DEM (Tarquini et al., 2012, Figure 4.8). The slip vector azimuths associated with the two earthquakes appear to be independent of the slope dip direction. In particular, the coseismic slip vector azimuth points across the slope or upslope in some locations, especially near the southern end of the rupture trace. The overall uphill-facing scarp geometry near its southern termination, and the lack of correlation between slip vector azimuths on the faults and the dip direction of the local slope suggest a primary tectonic origin of the surface ruptures. This implies that coseismic slip from depth propagated upwards to offset the ground surface, consistent with very rapid formation of the ruptures (2-4 seconds) measured with GNSS results (Wilkinson et al., 2017, with the present author, Iezzi, an author on this paper).

Overall, the key observation is that the fault bend A-B was the site of anomalously large throw and displacement in both the 24th August and 30th October earthquakes; this is where the fault strike changes by about 25° and the dip steepens by about 20°.

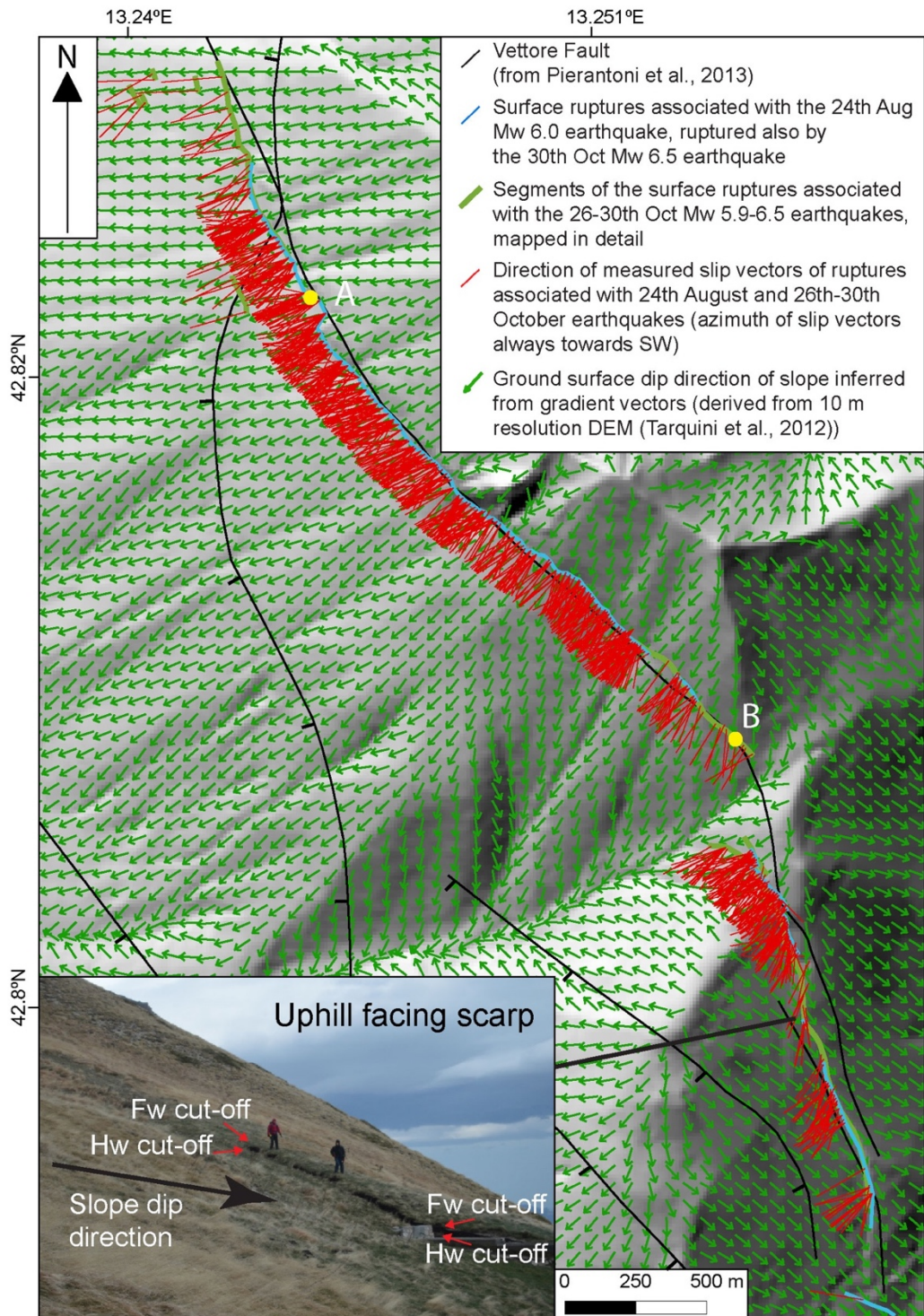


Figure 4.8: Comparison between the measured slip vector azimuths from both earthquakes (red lines) and the slope dip directions (green arrows). The slope dip directions are derived from a 10 m resolution DEM (Tarquini et al., 2012). The photo in the inset shows an uphill-facing rupture with slip vectors across and/or almost opposite to the slope dip direction (two people provide scale). The direction of the measured slip vectors does not correlate with the slope dip directions; hence this does not support the hypothesis that gravitational processes generate the surface ruptures. From Iezzi et al., 2018.

4.5.2 Comparison between long-term and coseismic activity of Mt. Vettore fault

In order to see if the spatial variation of coseismic offsets from the 2016 earthquakes are representative of past earthquakes, and hence the longer-term slip across the faults, offsets of the pre-rift strata and geomorphology were undertaken. The results indicate that long-term fault offset varies along the strike of the Mt. Vettore fault, with local maxima evident within the along-strike fault bends (Figure 4.9). The maximum total throw for the Mt. Vettore fault is ~1400 m since the initiation of faulting at 2-3 Ma (Roberts et al., 2002; Roberts and Michetti, 2004) and is located within the fault bend A-B (Figure 4.9a). A second local maximum abuts the fault bend C-D (Figure 4.9a). Also, the fault-controlled relief, which developed at least partially since 2-3 Ma, reaches a maximum value of ~1000 m within the fault bend A-B, again with a second maximum close to the bend C-D (Figure 4.9b). Where the hangingwall profile is higher than the footwall profile, this indicates uphill facing scarps (south-eastern termination, see Figure 4.8 inset) or erosion of the footwall by fluvial drainage. Additionally, the maximum fault-related subsidence since the Middle Pleistocene is centred opposite fault bend A-B indicated by the local presence of fluvio-lacustrine sediments in the hangingwall (Figure 4.9e); this is consistent with the notion that rates of vertical motion are relatively high within the fault bend since the middle Pleistocene, including the incremental offset of post-LGM units within the valley (Villani and Sapia, 2017). Moreover, the maximum coseismic subsidence indicated by preliminary InSAR results for both earthquakes show maxima located near the lake bed (Figure 4.9e).

Overall, Figure 4.9 suggest that the along-strike fault bend A-B, and perhaps also C-D, have been persistent features which have influenced the development of vertical motions

across the Mt. Vettore fault for a time period encompassing hundreds to thousands of earthquakes.

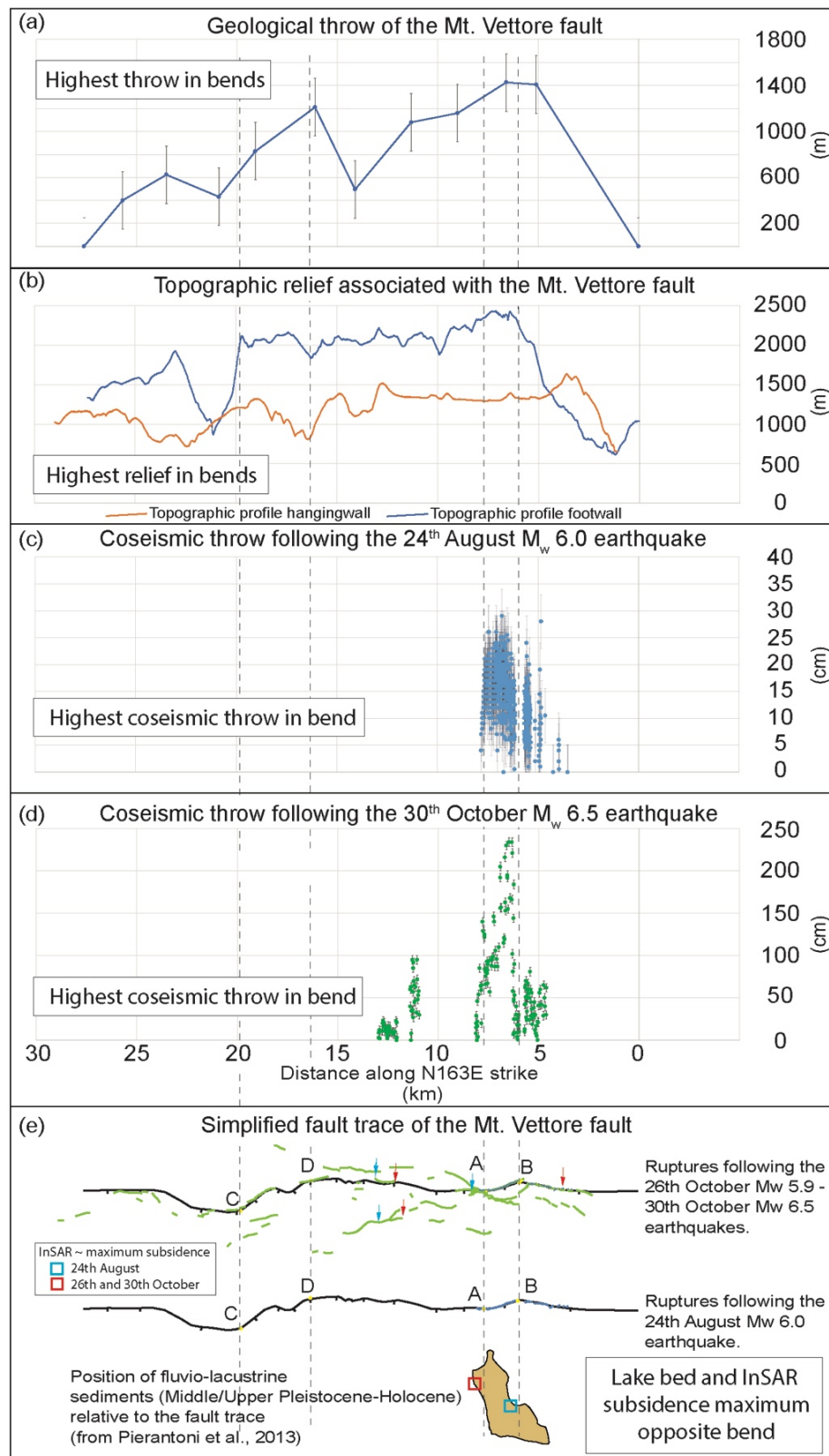


Figure 4.9: Comparison between (a) the geological throw profile of the Mt. Vettore fault, obtained from geological cross-sections, (b) the fault-related relief of the Monti Sibillini range (footwall of the Mt. Vettore fault), (c) the coseismic throw profile for 24th August M_w 6.0 earthquake, (d) the coseismic throw profile for the 30th October M_w 6.5 earthquake, and (e) the along strike extent of the ruptures, the lake bed location and preliminary InSAR measurements of maximum subsidence. All the measurements are projected across strike onto a line with N163° strike, parallel to the overall strike of the Mt. Vettore fault. Error bars of ± 5 cm for coseismic throw, ± 250 m for geological throw are reported in grey. Two along-strike fault bends marked as A-B and C-D are shown in (e). The figure shows that the maxima in coseismic throws for the two earthquakes, the maximum in geological throw and the largest topographic relief are located adjacent to the along-strike fault bend A-B. Moreover, the lake-bed and the maximum of subsidence in preliminary InSAR are located adjacent the bend A-B. Other maxima in the geological throw and in the topographic relief are also located within the along-strike fault bend C-D. Overall, the figure shows that the along strike bends have influenced both long-term and coseismic throw along the Mt. Vettore fault. From Iezzi et al., 2018.

4.5.3 Modelling the expected throw within fault bends

4.5.3.1 Earthquakes on the Mt. Vettore fault

In order to investigate whether the field observations from the 2016 earthquakes can be related to 3D complexity in the geometry and kinematics of faulting across the fault bend, whilst conserving horizontal strain, Equations 1 and 2 were applied to the field measurements of the Mt. Vettore earthquakes (Figure 4.10). The fault strike values, derived from strike lines for the Mt. Vettore fault, are N163° for the outer fault segments and N135° for the bend (Figure 4.4b). A dip of 60° is set for the outer fault segments, which is the arithmetic mean of the measured dips. A slip vector azimuth to N253° is set on the entire fault, consistent with field measurements (Figures 4.5, 4.6 and 4.7). Values for coseismic throws for the outer fault segments are set using the arithmetic means of the field measurements for each earthquake. Those parameters are used to constrain the outer faults, in order to calculate the modelled throw and dip within the bend.

For the 24th August earthquake, a value of 9 cm is used for the throw on the southern outer fault, and 14 cm for the northern outer fault. An iterated fault dip value in the bend of 77° produces a modelled throw of 29 cm. The iterated dip across the bend, which is

necessary to model a throw value consistent with field measurements (maximum measured throw 29 ± 5 cm), is consistent with field measurements of dip across the bend (mean of measured dip $75^\circ \pm 6^\circ (\pm 1\sigma)$) (Figure 4.10a).

For the 30th October earthquake, throws across the outer faults are set as 39 cm and 46 cm. An iterated fault dip in the bend of 84° produces a modelled throw of 233 cm, which is consistent with the maximum measured throw of 234 ± 6 cm. The 84° dip is a value consistent with field measurements of dip at locations of maximum throw, with arithmetic mean of $86^\circ \pm 3^\circ (\pm 1 \sigma)$ (Figure 4.10b).

Overall, for the Mt. Vettore earthquakes the model iterations suggest throw values consistent with field measurements of throw across the bend, and field measurements of fault dips within the bend, given the theory explained in equations (1), (2) and (3). This indicates that the conservation of the strain across along-strike fault bends influences the coseismic throw values (Figure 4.10), and that the 29 cm and 234 cm coseismic throws across the fault bend for the two earthquakes are required to preserve the extensional strain along the strike of the studied portion of the Mt. Vettore ruptures. This also further supports the interpretation that the observed offsets are due to primary tectonic faulting which propagated to the surface from seismogenic depths, rather than resulting from shallow gravitational processes (c.f. Huang et al. 2017 for the 24th August 2016 earthquake).

(a) 24th August 2016 Mt. Vettore (Italy), M_w 6.0 earthquake (b) 30th October 2016 Mt. Vettore (Italy), M_w 6.5 earthquake

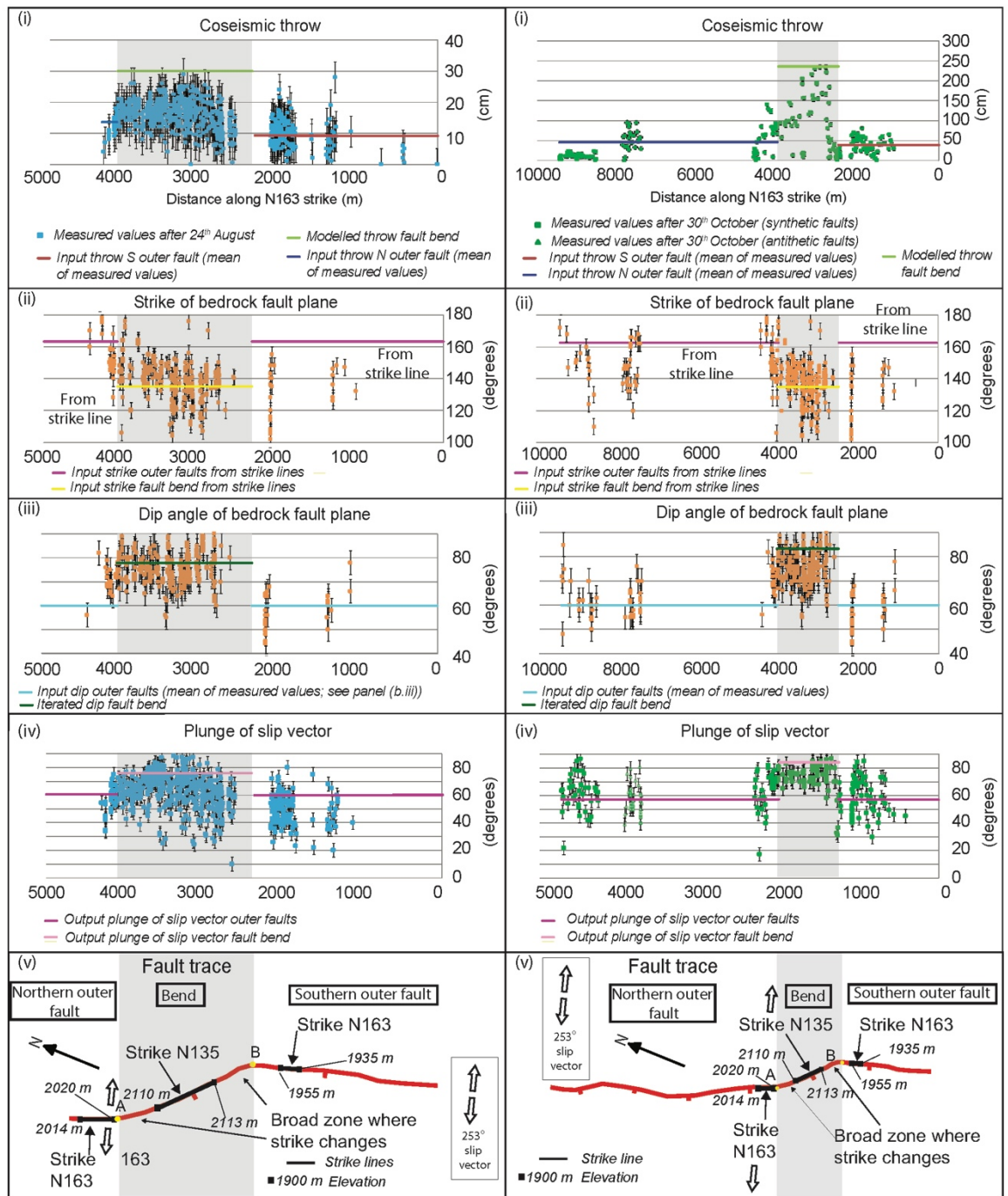


Figure 4.10: Modelling the 24th August M_w 6.0 (a) and 30th October M_w 6.5 earthquakes (b). Field measurements of coseismic throw are reported for each of the earthquakes (panels a.i and b.i), measurements of the strike of the bedrock fault plane (panels a.ii and b.ii), measurements of the dip of bedrock fault plane (panels a.iii and b.iii), measurements of the plunge of the slip vector (panels a.iv and b.iv), and the relative fault traces (panels a.v and b.v). In every panel the straight, horizontal lines represent the input value used within the calculations for the outer faults and the iterated values for the fault bend. See text in Section 4.5.3.1 for details in the calculations. From Iezzi et al., 2018.

4.5.3.2 Coseismic offsets for other large normal faulting earthquakes

To evaluate whether bends influence offsets elsewhere, again in agreement with the relationships in equations (1), (2) and (3), displacement data from surface ruptures for the 1887 M_w 7.5 Sonora earthquake (Suter, 2008a; 2008b; 2015); 1981 Corinth M_w 6.7-6.4 earthquake (Jackson et al., 1982; Roberts 1996; Morewood & Roberts, 2001) and the 1983 M_w 7.3 Borah Peak earthquake (Crone et al., 1987) are examined (Figures 4.11 and 4.12). In addition, new fieldwork on the 1981 Corinth ruptures was carried out in 2017 to supplement values from Roberts (1996) (Figure 4.11).

Observations show that fault traces for these earthquakes show prominent along-strike fault bends, 2-10 km long, whose presence are confirmed by the construction of strike lines (Figure 4.12, panels iii, vi, ix). Other smaller bends may exist, but it was not possible to verify these because of the spatial distribution of the field measurements of throw (average spacing of measurements along-strike for the Sonora earthquake is 528 m, for the Corinth earthquake is 1070 m, for the Borah Peak earthquake is 426 m). It is only possible to resolve variation in throw across bends with along-strike length longer than the along-strike spacing of the field measurements of throw, so this work concentrated on the larger, recognisable along-strike fault bends, which are constrained using strike lines (Figure 4.12, panels iii, vi, ix). These bends exhibit localized maxima in coseismic throw for the surface ruptures (Figure 4.12, panels i, iv, vii) and increases of fault dip, as confirmed by published data for the Sonora earthquake (Suter, 2008a; 2008b; 2015) and from fieldwork for the Corinth earthquake. It was not possible to identify detailed fault dip data for the Borah Peak earthquake, although published photos suggest that dip may be relatively steep within the fault bend (e.g. Figure 6 of Crone et al., 1987).

(a) Sonora (Mexico), 1887, Mw 7.5 (b) Corinth (Greece), 1981, Mw 6.4-6.7

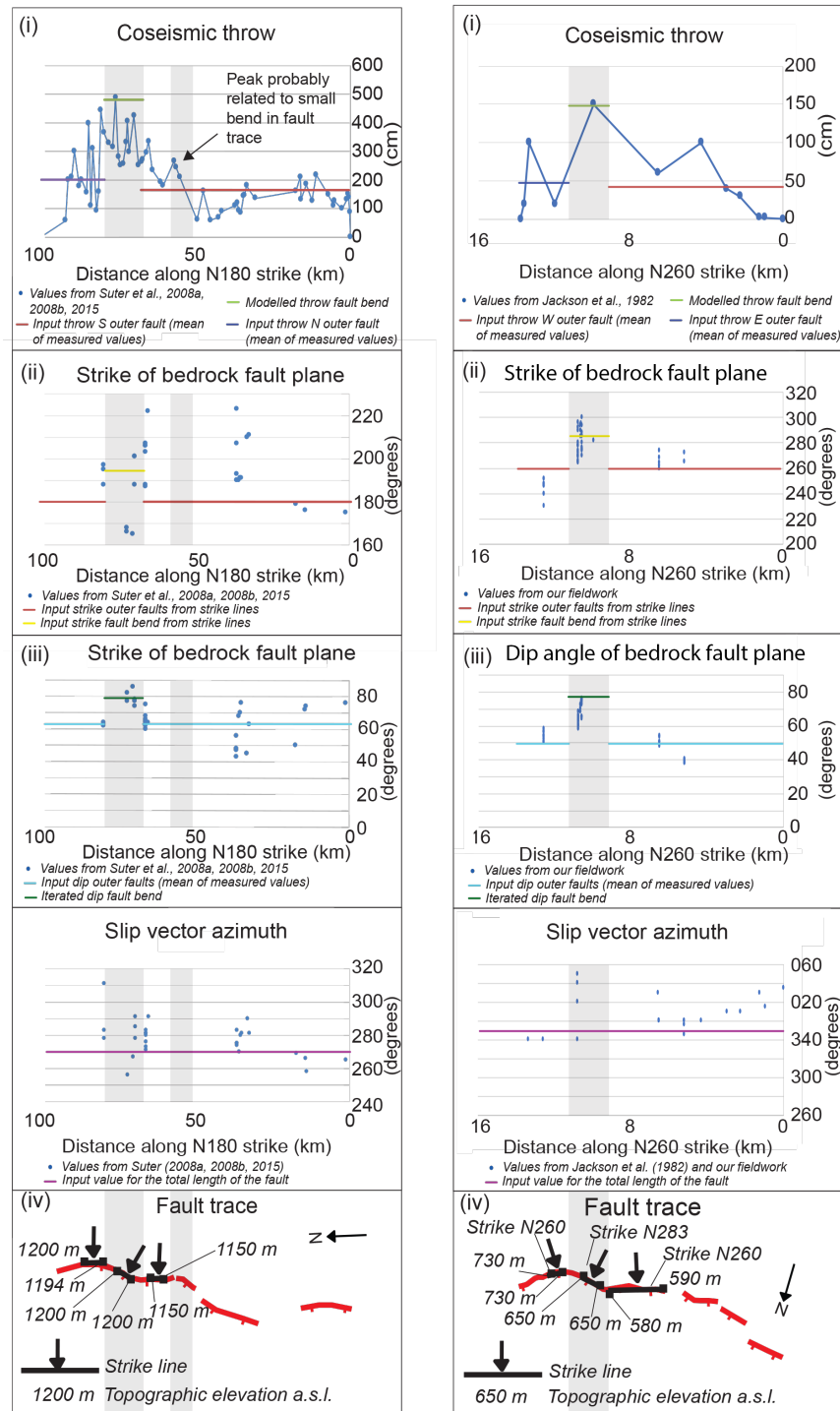


Figure 4.11: Modelling the 1887 M_w 7.5 Sonora (a) and the 1981, M_w 6.4-6.7 Corinth (b) earthquakes. For the Sonora earthquake, every measurement is from Suter (2008a; 2008b; 2015). For the Corinth earthquake, the throw profile is from Jackson et al. (1982); values of strike and dip have been measured during fieldwork in 2017; slip vector azimuth measurements are from Jackson et al. (1982) and fieldwork. The input values of throw and dip for the outer faults are obtained as the arithmetical mean of the measured values. The input values of strike are derived from strike lines. The iterated dip across the fault bend is reported as green line in panels a.iii and b.iii. The modelled throw at bend is reported as pale green line in panels a.i and b.i. Iterated dip and modelled throw across the bends are consistent with measured values in the field, and therefore this suggests that the fault bends can be an explanation of the large measured D_{max} . From Iezzi et al., 2018.

The methodology explained in Section 4.4.1 has been applied to investigate whether the observed offsets at fault bends can be explained by the relationships in equations (1), (2) and (3). As for the Mt. Vettore earthquakes, for each earthquake fault strike values are derived from strike lines, and fault dips and throws for the outer faults are derived as the arithmetical means of field measurements reported along the entire fault traces outside the bends, and the slip vector azimuth from field measurements. The fault dip angles are iterated within the bends, in order to derive modelled throws across the fault bends to check for consistency with field measurements (Figures 4.11, 4.12 and Table 4.1). For the Borah Peak earthquake, given the lack of field measurements of fault dip available, the dip of the outer faults is set at 60° , common value for normal faults.

For the Sonora earthquake, where ruptures outside the bend show a D_{max} of about 400 cm, the iterated fault dip value of 79° produces a modelled throw across the bend of 498 cm; these values are consistent with field measurements (arithmetic mean of dip 79° , maximum measured throw 495 cm, from Suter et al., 2008a; 2008b; 2015; Figures 4.11a, 4.12 and Table 4.1).

For the Corinth earthquake, where ruptures outside the bend show a D_{max} of about 100 cm, the iterated dip value of 76° produces a modelled throw across the bend of 148 cm, consistent with field measurements (maximum measured dip across the bend of 77° , from field measurements; maximum measured throw at bend 150 cm, by Jackson et al., 1982; Figures 4.11b, 4.12 and Table 4.1).

For the Borah Peak earthquake, where ruptures outside the bend show a D_{max} of about 200 cm, the iterated dip value of 79° produces a modelled throw across the bend of 270

cm, consistent with the maximum field measurements of 270 cm by Crone et al., 1987 (Figure 4.12 and Table 4.1). The 79° dip is similar to that shown by a field photo within the bend (see Figure 6 of Crone et al., 1987), and agrees with measurements of fault dips between 60° and 90° mentioned in Crone et al. (1987).

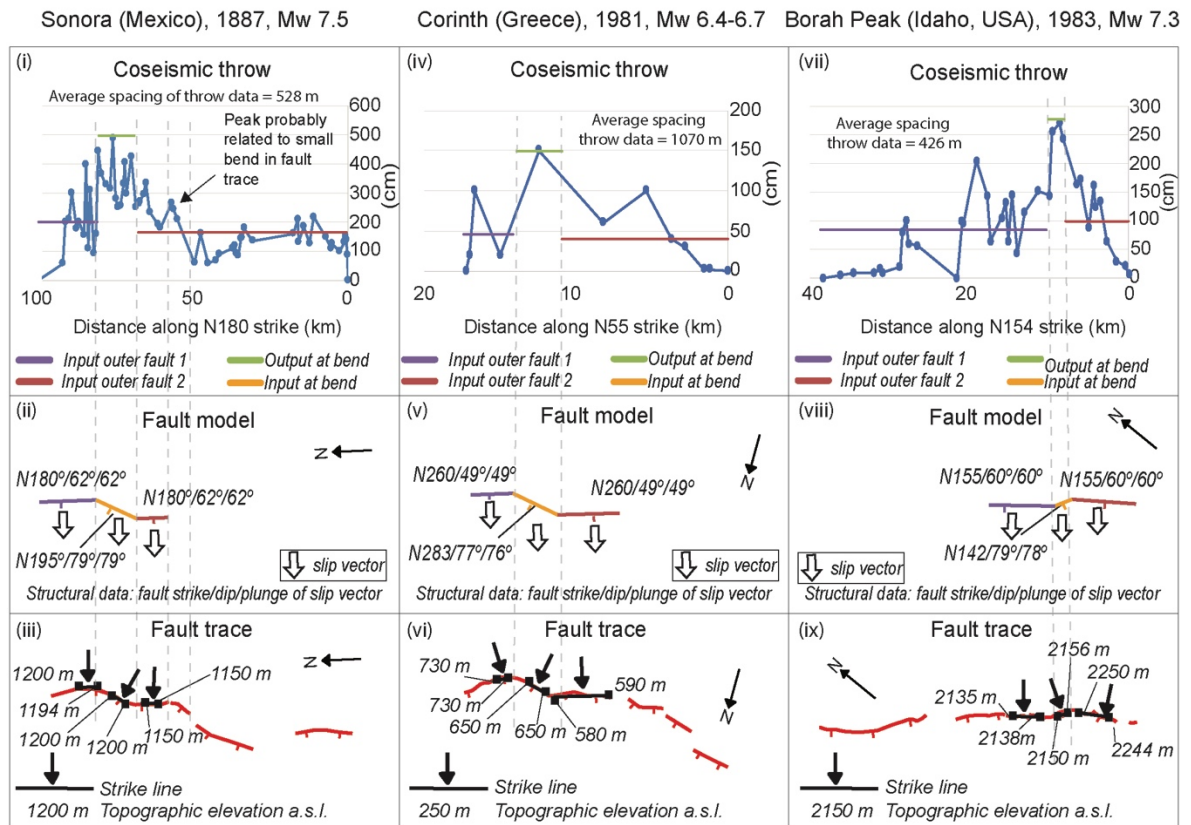


Figure 4.12: Modelling of historical earthquakes that ruptured across along-strike fault bends. Datasets for the coseismic slip and fault trace are from Suter (2008a, 2008b, 2015), for the 1887, Sonora earthquake, M_w 7.5; Jackson et al. (1982) and Morewood & Roberts (2001), and fieldwork for the 1981, Corinth earthquake, M_w 6.7-6.4; Crone et al. (1987), for the 1983, Borah Peak earthquake, M_w 7.3. It is used the same approach shown in Figure 4.9. Coseismic throw panels (i, iv, vii, x) reports along-strike throw profiles for each earthquake. For each of these panel, the average spacing of measurements reported is the average distance between the field measurements of throw for each earthquake, which represents the lower limit of spatial resolution for the identification of fault bends. Fault model panels (ii, v, viii, xi) reports the input parameters of strike, dip and plunge of the slip vector used to model the throw across the bends, as well as the slip vector azimuth used for the earthquakes. Colours are coded to input values of throws in the panels above. Fault trace panels (iii, vi, ix, xii) show simplified fault traces of the earthquakes, on with strike lines defining the along-strike fault bends. Adapted from Iezzi et al. (2018)

Parameters used to model the studied earthquakes

Earthquakes	Measured outer fault sections strike (from strike lines)	Measured fault bend sections strike (from strike lines)	Measured outer fault sections dip (arithmetical mean of measured values)	Measured outer faults throws (arithmetical mean of measured values) (cm)	Measured fault bend maximum throw (cm)	Iterated fault bend dip	Modelled fault bend throw (cm)	Slip vector azimuth along the length of the fault (consistent with field measurements)
24th August M_w 6.0, Mt. Vettore (central Italy)	N163°	N135°	60°	9-14	29	77°	30	N253°
30th October M_w 6.5, Mt. Vettore (central Italy)	N163°	N135°	60°	39-46	234	84°	240	N253°
1887, M_w 7.5 Sonora (Mexico)	N180°	N195°	62°	163-201	495	79°	498	N270°
1981, M_w 6.4-6.7 Corinth (Greece)	N260°	N283°	49°	39-46	150	76°	148	N350°
1983, M_w 7.3 Borah Peak (Idaho, USA)	N155°	N142°	60°	99-83	270	79°	280	N245°

Table 4.1: Parameters used to apply the equations 1-2-3 on the five earthquakes studied.

Thus, for the 1981 Corinth M_w 6.7-6.4 and for the 1887 Sonora M_w 7.5 earthquakes, the results suggest that the required fault dip angles across the bends are consistent with field measurements. The required fault dip across the bend for the 1983 Borah Peak M_w 7.3 earthquake is a plausible value for normal faults that represents a testable hypothesis given further fieldwork, but we note that the required dip value is similar to that shown in a field photo. Hence, it appears that along-strike fault bends may be a key control on coseismic offset. The major implication is that fault bends, in turn, will control how *D_{max}* relates to rupture length and magnitude if coseismic throws from bends are converted to displacement and/or reported as *D_{max}* and included in calculations to gain the average displacement (*D_{average}*).

A note on the modelling is that the results for modelled throw replicate the measured values very well ($R^2 = 0.999$), but the results are highly sensitive to the iterated dip, and less sensitive to the input strike (Figure 4.13). This highlights the importance of dip measurements; future rupture-mapping and palaeoseismic studies should report the dip of the fault as fully as possible if the approach advocated here is to be used. Also, it is important to note that the modelling is applied for bends with changes in strike angle of less than 28° (compare with Biasi and Wesnousky 2017). The author is unaware of natural examples of bends with greater angles up to a case-limit of a transform fault connecting two normal faults.

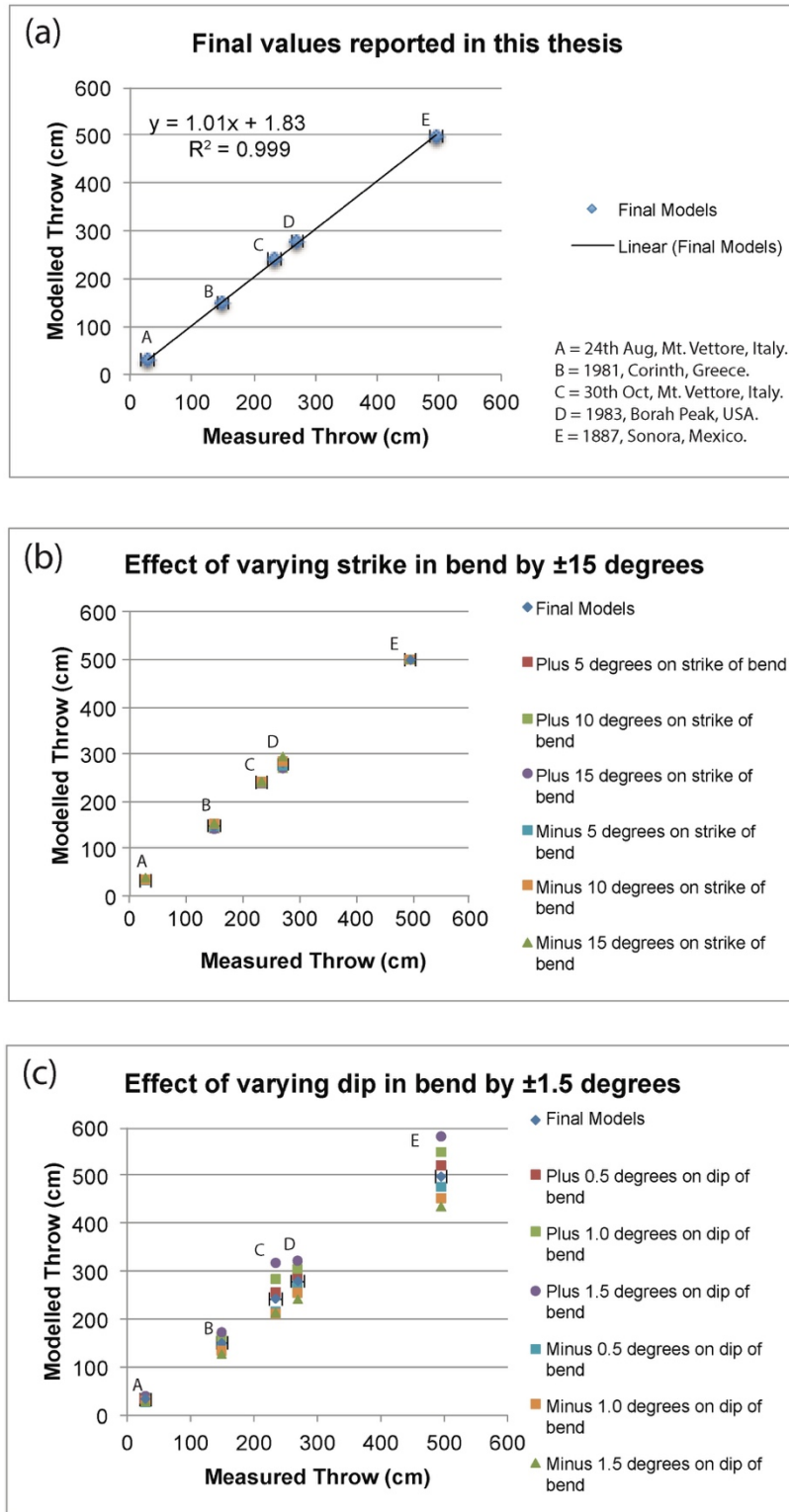


Figure 4.13: Analysis of the sensitivity of varying strike and dip in modelling the five earthquakes presented in this thesis. (a) shows the correlation between the modelled throws and the measured throws across the bend. (b) and (c) show the variation of the modelled throw because of the variation of fault strike and fault dip across a fault bend. In (b), for each earthquake the values of fault dip on the outer faults and the fault bend have been maintained constant, obtained with field measurements, and the value of fault strike across the bend has been varied. In (c), for each earthquake the values of fault strike on the outer faults and the fault bend have been maintained constant, obtained with strike lines, and the value of fault dip across the bend has been varied. From Iezzi et al., 2018.

4.5.3.3 Comparison between field measurements and predictions of D_{max} from existing scaling relationships

To investigate whether existing, empirically-derived scaling relationships (e.g. Wells and Coppersmith, 1994) adequately predict measured displacement values for faults with along-strike bends, the D_{max} and M_w for the two Mt. Vettore earthquakes, and the Sonora, Borah Peak and Corinth earthquakes are compared with the same values implied by existing scaling relationships of D_{max} versus surface rupture length ($\text{Log}D_{max} = -1.38 + 1.02 \times \text{log}(L)$) and M_w versus D_{max} ($M = 6.61 + 0.71 \times \text{log}(D_{max})$), published in Wells and Coppersmith (1994) (Figure 4.14). Both the “all kinematics” and “normal” scaling relationships expressed in Wells and Coppersmith (1994) are used in this chapter. The “all kinematics” D_{max} versus fault length scaling relationship is used because it covers the full range of fault lengths of the examples herein presented, including those from the literature (the range of surface rupture length in the examples is 5-100 km, the “normal kinematic” scaling relationship from Wells and Coppersmith (1994) is valid for cases within a range of 3.8-75 km). The normal kinematics M_w versus D_{max} scaling relationship is used in agreement with the kinematics of the earthquakes on the Mt. Vettore fault and of the historical earthquakes. For the two Mt. Vettore earthquakes the D_{max} derived from field measurements are used; for the other historical earthquakes studied the D_{max} is calculated from measured throws at bends, on a fault plane with value of dip given by the iterated dip at bends obtained from the modelling.

The measured D_{max} values shown in Figure 4.14a for the five studied earthquakes with fault bends are consistently higher than the D_{max} predicted from their lengths using the Wells and Coppersmith (1994) D_{max} versus surface rupture length scaling relationship.

The M_w predicted from the observed D_{max} for the five studied earthquakes are overall larger than the M_w predicted based on the D_{max} predicted from the surface rupture length, although error bars overlap for some examples (Figure 4.14b). Although slip for the earthquakes in the Wells and Coppersmith (1994) database may well be influenced by a variety of parameters (e.g. depth of moment centroid, fault strength, seismogenic thickness etc.), these results suggest that fault bends may form an important part of the explanation for the ~ 1 order of magnitude scatter in D_{max} for a given fault length (Wells and Coppersmith, 1994).

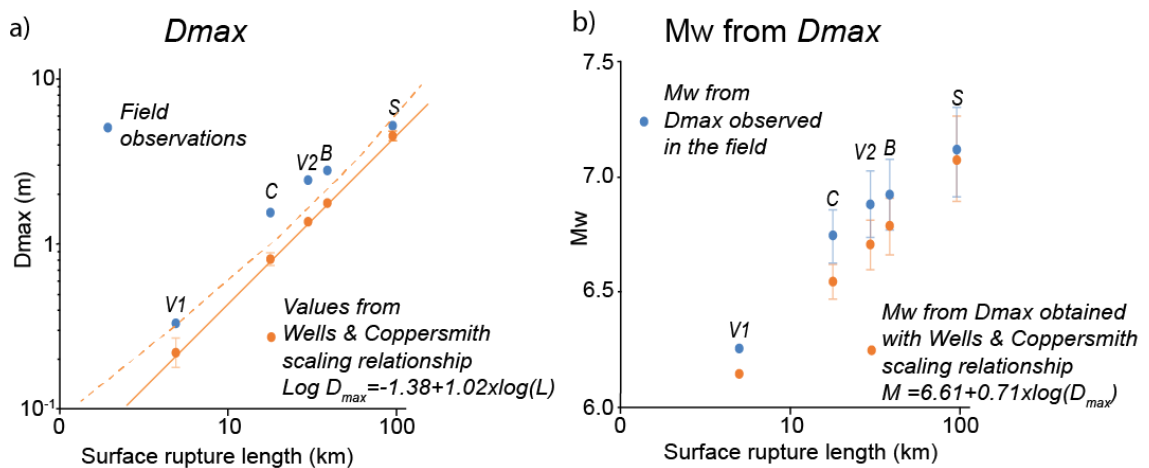


Figure 4.14: Comparison between D_{max} (a) and the expected M_w for D_{max} (b) for given fault lengths from field data obtained from the scaling relationships in Wells and Coppersmith (1994). Field measurements of D_{max} for the Mt. Vettore are used; for the historical earthquakes, D_{max} are calculated from maximum throws, using the value of iterated fault dip. V1= M_w 6.0 24th August 2016 Mt. Vettore earthquake; V2= M_w 6.5 30th October 2016 Mt. Vettore earthquake; C= M_w 6.4-6.7 Corinth earthquake; B= M_w 7.3 Borah Peak earthquake; S= M_w 7.5 Sonora earthquake. For values derived from the Wells and Coppersmith (1994) scaling relationships, error bars, derived from standard errors reported in their Tables 2b and 2c, are reported. When the error bar is not visible, it is smaller than the symbol. In a), the dashed line is the upper 95% confidence interval of the D_{max} versus fault length scaling relationship (Wells and Coppersmith, 1994) Overall, the figure shows a preponderance of higher values for the observed D_{max} versus fault length relationship compared to those predicted from Wells and Coppersmith (1994). Modified from Iezzi et al., 2018.

To explore whether fault bends can produce the high values and scatter seen in D_{max} versus surface rupture length scaling, Equations 1 and 2 are used to calculate the expected throw across a bend for a variety of fault lengths and increasing fault dips within the bend,

in agreement with field observations of steeper fault dips at bends, as shown by the five examples from the two Mt. Vettore earthquakes, and the Sonora, Corinth and Borah Peak earthquakes, following the methodology outlined in Section 4.4.1. For each fault rupture length, the strain across the outer faults is calculated with an assigned 40° fault dip, pure dip slip kinematics and a value of coseismic throw calculated using the D_{max} versus surface rupture length scaling relationship in Wells and Coppersmith (1994) ($\text{Log}D_{max} = -1.38 + 1.02\text{Log}(L)$) (Figures 4.15 and 4.16). Again, the “all kinematics” scaling relationship is used because it covers the total range of rupture length explored. Across the bend, the strain and slip vector azimuth are maintained as constant, and the predicted throw is calculated by varying the fault dip in the bend in 5° increments from 40° - 85° (Figures 4.15 and 4.16). The range of dips explored (40° - 85°) represents the range of dips that have been documented in databases containing many thousands of measurements from normal faults (e.g. Roberts, 2007). From each of the modelled throws, the expected D_{max} is calculated on a fault plane dipping with the value used in the calculation, and it is compared with the D_{max} versus surface rupture length scaling relationship from Wells and Coppersmith (1994). The above is calculated also for the scaling relationship in Wesnousky (2008) (Figure 4.17).

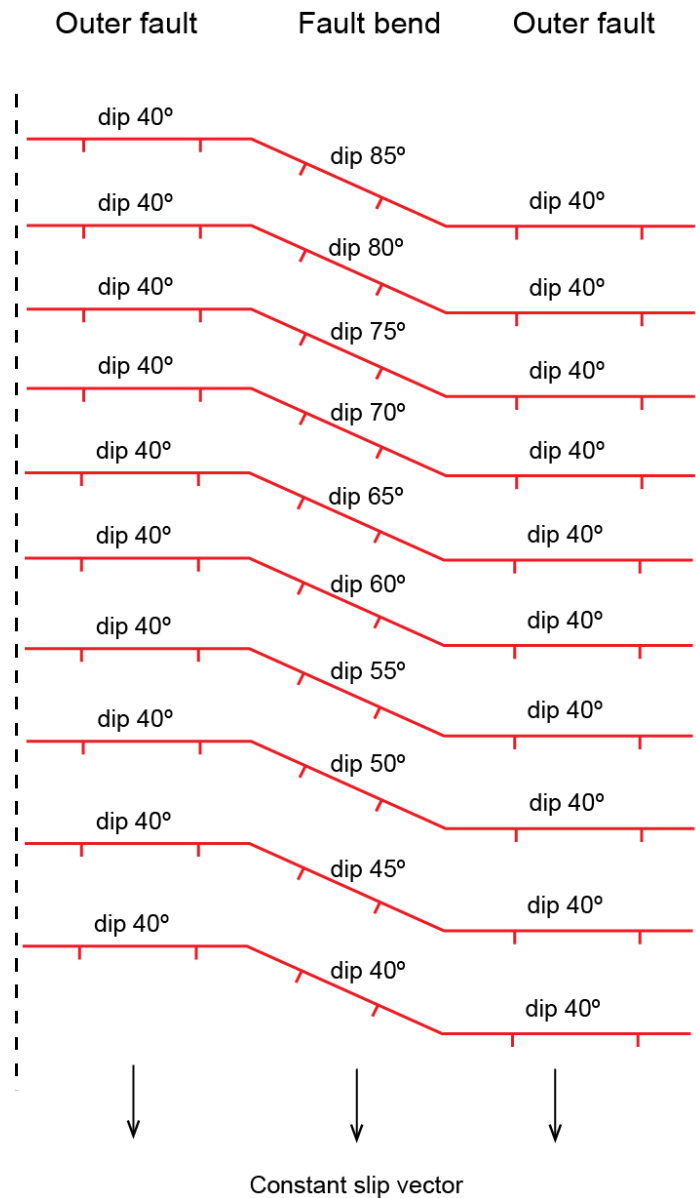


Figure 4.15: Fault model used to analyze the effect of fault bends on scaling relationships shown in Figures 4.16 and 4.17. For each fault length, the throw is calculated across the outer faults using Wells and Coppersmith (1994) $D_{max}/\text{fault length } (L)$ scaling relationship $\text{Log}D_{max} = -1.38 + 1.02 \times \text{Log}(L)$. This is used as input in the Equation 1, together with 40° dip and dip slip kinematic, to calculate the strain-rate across the outer faults. Maintaining the strain-rate constant across the bend, as well as the azimuth of the slip vector, the predicted throw is calculated across the bend by varying the value of fault dip from 40° to 85° , for a given variation of 20° of fault strike across the bend.

The results show that changing the fault dip can produce dramatic variability in the coseismic D_{max} within the fault bend (Figures 4.16a and 4.17a). The value of D_{max} can increase by ~ 1 order of magnitude for a fault bend with dip angle of 85° compared to one with a dip of 40° . A comparison between these results and measurements for normal

faulting earthquakes in Wells and Coppersmith (1994) shows a similar range in D_{max} for a given fault length (~ 1 order of magnitude; Figure 4.16b). This suggests that the effect of fault bends is a likely contributor to the scatter in coseismic throw for a given fault length recorded in natural datasets.

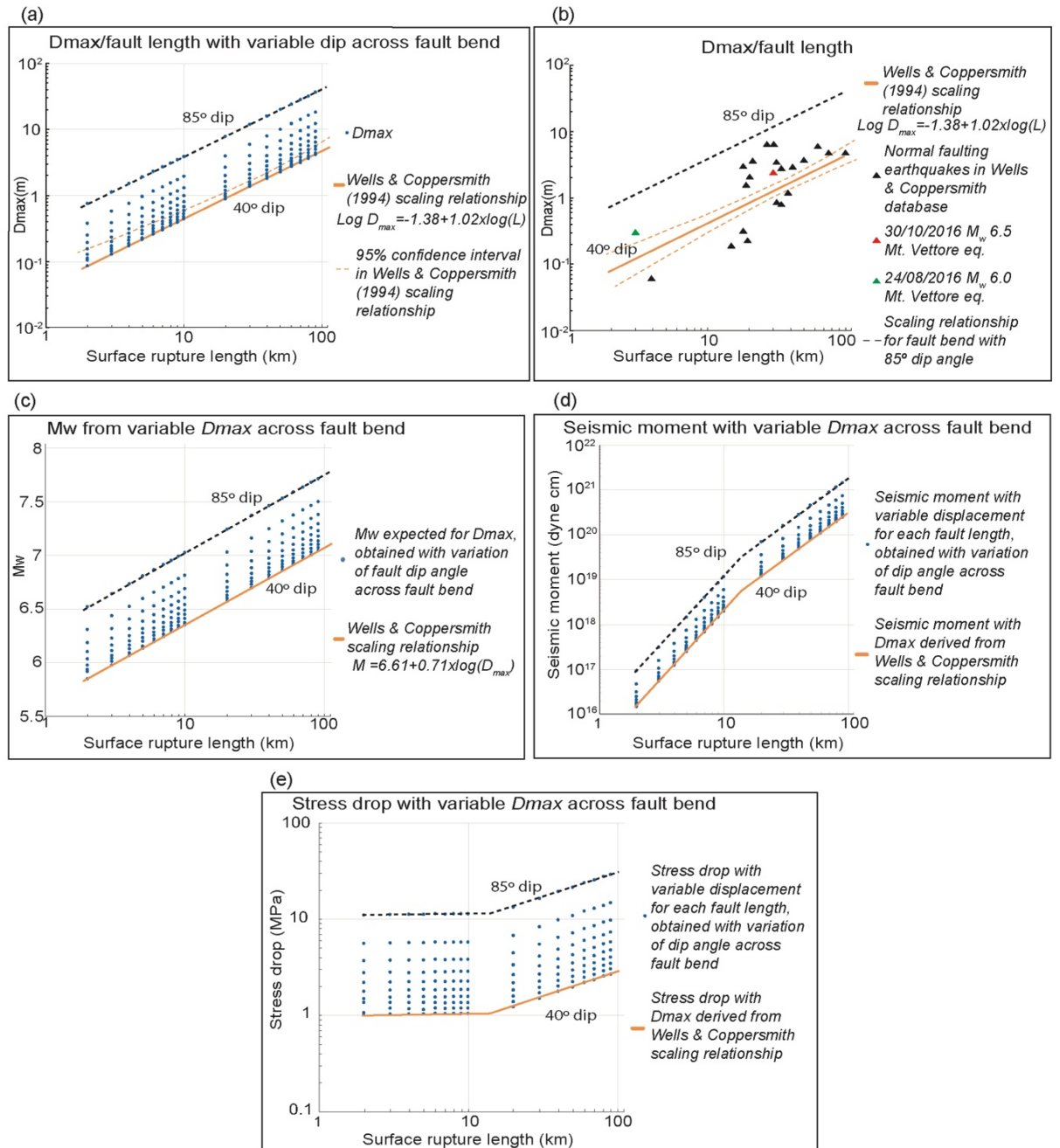


Figure 4.16: (a) D_{max} versus surface rupture length scaling relationships obtained by varying the fault dip angle from 40° to 85° across an along-strike fault bend. Each D_{max} value has been calculated from modelled throws across an along-strike fault bend. To model throws across bends, values for throw on the outer faults are set as the D_{max} value calculated with the Wells and Coppersmith (1994) D_{max} versus surface rupture length scaling relationship for each fault length, and a fault dip of 40° . Throw at the bend is calculated by varying values of fault dip every 5° between 40° and 85° (see Figure 4.15). The continuous orange line represents the Wells and Coppersmith (1994), relationship. Dashed orange line is the upper 95% confidence interval of the Wells and Coppersmith (1994) relationship. Dashed black line represent values of throw for a bend with 85° fault dip angle. (b) Superposition of the normal faulting earthquakes reported in Wells and Coppersmith (1994), D_{max} versus surface rupture length graph, and related scaling relationship (continuous orange line) and 95% confidence interval (dashed orange lines), with plots of expected D_{max} with variable dip angle across along-strike fault bend at 85° . (c) M_w derived from each D_{max} calculated in Figure 4.16a. For each fault length, the expected M_w is calculated from the modelled values of D_{max} showed in Figure 4.16a using the M_w versus D_{max} scaling relationship from Wells and Coppersmith (1994). Results are plotted with fault length on the x-axis to show that, for each fault length, the variability of D_{max} given by the fault bend causes a large variability in the expected M_w , when it is derived with Wells and Coppersmith (1994) M_w versus D_{max} scaling relationship. The orange line is the regression for M_w calculated from D_{max} obtained with the Wells and Coppersmith (1994) D_{max} versus surface rupture length regression. (d) Seismic moment expected for each D_{max} calculated in Figure 4.16a. For each fault length the seismic moment is calculated using the values of D_{max} across a fault bend calculated in Figure 4.16a. The thickness of the seismogenic layer is set at 15 km; for fault length <15 km it is assumed a circular fault geometry. It is shown that for given fault lengths, variable displacement across fault bends can produce ~ 1 order of magnitude of variability in seismic moment estimations. The orange line shows the regression of seismic moment values calculated from D_{max} obtained with Wells and Coppersmith (1994) D_{max} versus surface rupture length scaling relationship. (e) Stress drop expected for each D_{max} calculated in Figure 4.16a. The stress drops are obtained using the M_0 calculated in Figure 4.16d. The graph shows that variable displacement across a fault bend can induce a variability of ~ 1 order of magnitude for the stress drop value, for given fault lengths. The orange line is the regression of stress drop calculated from D_{max} obtained with Wells and Coppersmith (1994) D_{max} versus surface rupture length scaling relationship.

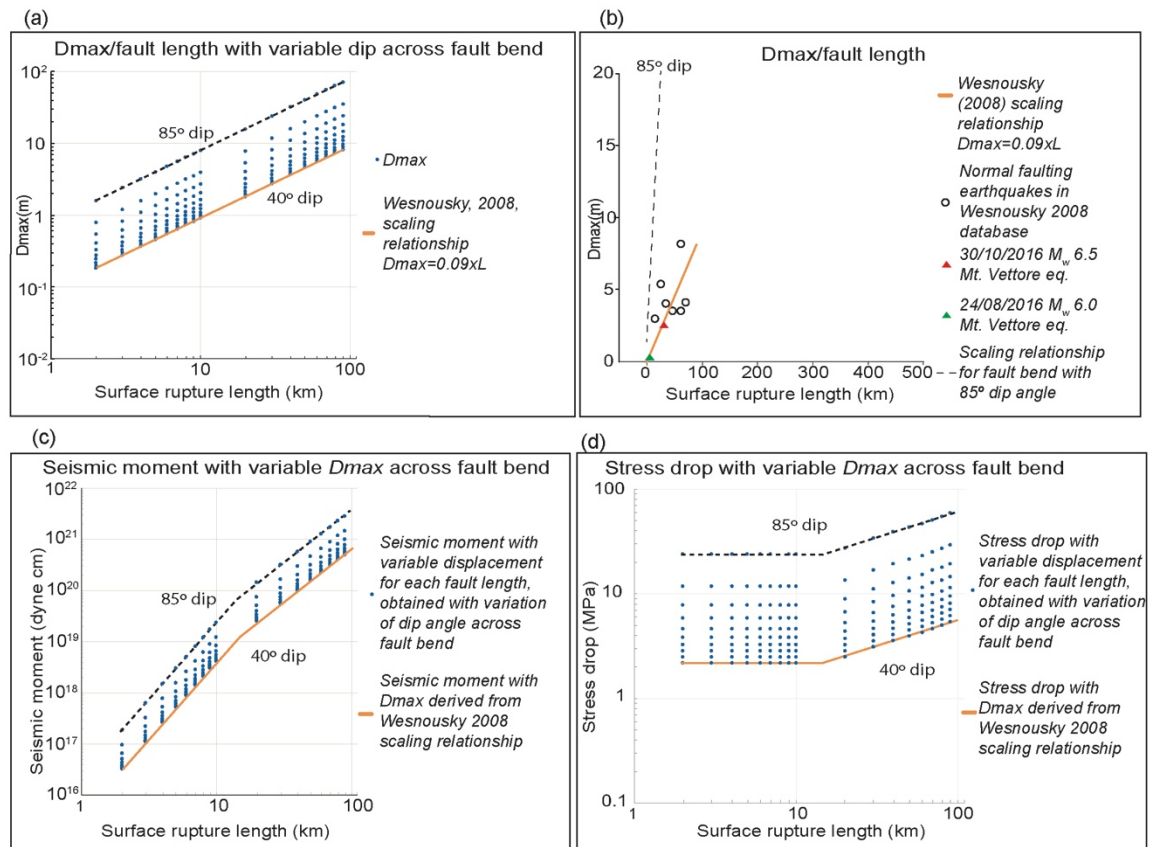


Figure 4.17: Application of the modelling in Figures 4.15 and 4.16 to the D_{max} /surface rupture length scaling relationship from Wesnousky, 2008. The normal kinematic scaling relationship $D_{max}=0.09 \times L$ (km) has been used to derive the D_{max} across the outer faults, and then applied the same approach as Figure 4.14 to derive throws and D_{max} across the bend.

4.6 Discussion

The along-strike throw profiles of five different coseismic surface ruptures associated with normal faulting earthquakes show that the coseismic throw, and therefore the coseismic D_{max} , increases where ruptures propagate across along-strike fault bends characterized by steep fault dips. Quantitative relationships can explain these larger throws in terms of conservation of strain across the fault bend, where the fault dip becomes steeper.

Note that in these examples ruptures propagate across bends, and do not terminate at these structural anomalies, as is the case for examples in the literature (e.g. Biasi and Wesnousky, 2017). Biasi and Wesnousky (2017) suggest that stiffening of mechanical resistance for dip slip ruptures occur for bends with change in strike angle of about 50° . The author of this thesis hypothesizes that the approach advocated herein is perhaps only applicable for ruptures that do propagate across fault bends up to a change in strike of about 45° , corresponding to the limiting point at which the bend would be classified as a normal fault, rather than an oblique-slip or strike-slip fault. However, the model has been tested only for examples where propagation of ruptures across fault bends occurs, and where the change in strike angle is up to 28° .

In terms of the relevance of the results to databases that have compiled D_{max} and rupture length (e.g. Wells and Coppersmith, 1994; Manighetti et al., 2007, Wesnousky 2008, Leonard 2010), it is unfortunately uncommon for the data sources that support these compilations to report whether data were collected from fault bends with strikes oblique to the extension direction or portions of faults striking perpendicular to the extension direction. In general, they do not report the geometry and kinematics of the faulting for each measurement. This is important because the observed scatter in D_{max} for a given fault length (see Chapter 2, Section 2.4.1 for a review) has been interpreted as indicating significant variation in implied stress drop (Manighetti et al., 2007), but the results in this thesis suggest caution regarding the interpretation of variation in stress drop. Values of D_{max} are also used in some examples to infer palaeoearthquake magnitudes from palaeoseismic studies, (e.g. Pantosti et al., 1996; Dolan et al., 1997; Galadini and Galli, 2000; 2003; Villamor and Berryman, 2001; Cinti et al., 2011; Galli et al., 2014; Galli et al., 2017). Although some palaeoseismological studies have carefully considered

uncertainties (e.g. Working Group on Utah Earthquake Probabilities (WGUEP), 2016), it is not a ubiquitous practice to consider if measurements are impacted by the effect of along-strike fault bends. The results in this chapter are important because they reveal that local variations in fault geometry and kinematics can produce variations in coseismic throw values, and therefore in the coseismic displacement associated with the earthquake. This leads to uncertainty in palaeoearthquake magnitudes and implied variations of stress drops for a given fault length if the effect of fault bends is not recognized.

It is important to consider alternative explanations of high slip magnitudes at the surface on surface ruptures. For example, it might be possible that high slip patches occur at depth, possibly propagating to the surface without the influence of fault bends; however, this is difficult to prove with direct measurements at depth. The analysis of five surface-rupturing normal fault earthquakes shows that fault bends are a plausible explanation for patches of high slip measured at the surface and that the detailed characterization of fault bend geometry allows prediction of the magnitude of the slip anomaly. Fault bends are also likely to exist at depth and these may even be responsible for suggested high slip-patches at depth. This suggests that: (1) non-planar fault geometry may be an alternative explanation of high spatial variability within slip distributions for finite fault inversions of major normal faulting earthquakes; (2) finite fault inversions, that is, for example, where sub-surface slip distributions are recovered through inversion of geodetic measurements of surface deformation or seismology, should include variable fault geometry at depth, to derive the best representation of the slip distribution along the fault.

This chapter also addresses how variable coseismic throws across fault bends impact calculations of M_w from D_{max} . If the reported D_{max} value comes from a fault bend with

a high dip value, and this is not recognized, by how much might the M_w be overestimated compared to a straight fault? To answer this question, for each fault length the expected M_w is calculated for all the plausible D_{max} for values within the fault bend (shown in Figure 4.16a), using the M_w versus D_{max} scaling relationship in Wells and Coppersmith (1994) ($M=6.61+0.71\log(D_{max})$) (Figure 4.16c). The graph shows that for a given fault length, the variability of D_{max} across fault bends leads to a large variability of M_w estimates if M_w is derived using the M_w versus D_{max} scaling relationship in Wells and Coppersmith (1994). This is important because fault bends, and their associated fault dip angles, are not commonly considered when using displacements measured in paleoseismic trenches to infer M_w for palaeoearthquakes. It appears that this can introduce a large uncertainty of M_w into palaeoseismic estimates of past seismicity.

The effect of the variability of D_{max} on the estimation of the M_w also raises the question of how the variability in D_{max} due to fault bends affects calculations of seismic moment and stress drop associated with normal faulting earthquakes. It is known that seismic moment and stress drop should be calculated using the $D_{average}$ (Kanamori and Anderson, 1975; Scholz, 1992). It is also known that $D_{max} \sim 2 * D_{average}$ for most large earthquakes (e.g. Manighetti et al., 2005), and the presence of fault bends on normal faults contributes to D_{max} being larger than $D_{average}$. Therefore, this chapter suggests that the presence of fault bends may produce bias in calculation of $D_{average}$ for two reasons. Firstly, given limitations in the field due to accessibility and quality of exposure, it is possible that measurements may be focused in locations where the ruptures are more impressive and have larger offsets, which may be located within fault bends. Thus, the derived $D_{average}$ may contain sampling bias and overestimate the true $D_{average}$ if bends with high dip angles are included, but not recognized. Secondly, as fault bends with high

dip angles produce higher values of throw, the calculated *Daverage* for a dataset where measurements have been made at regularly-spaced intervals along strike will contain values influenced by the high dip angles in the fault bend. Therefore, a fault with an along-strike bend with high dip angle, sampled at regular distances along strike, would have higher *Daverage* compared to that for a straight fault. Thus, claimed *Daverage* values could be biased and affect calculation of seismic moment and stress drop if the effect of bends and high dip angles are not recognized. To investigate this, the worst-case scenario is examined herein, where *Daverage* equals *Dmax*, a scenario that could be approached if fault bends have not been considered at all, and a relatively large portion of the rupture occurs within a bend like the 24th August Mt. Vettore example.

The scalar seismic moment is calculated using the equation: $M_0 = \mu AD$, where μ is the shear modulus (considered herein as 3×10^{10} Pa, as in Boncio et al., 2004), A is the seismogenic area and D is the *Dmax* across fault bend, derived from values in Figures 4.16a and 4.17a (Figures 4.16d and 4.17c). The thickness of the seismogenic layer is set to be 15 km. A circular fault is assumed when the fault length (L) is < 15 km, and rectangular faults with increasing aspect ratio for faults with L values progressively larger than 15 km. The fault width (down-dip dimension in the plane of the fault) has been corrected for different dip angles. For each fault length, the seismic moment is calculated for each displacement associated with variable fault dip. Variable displacement across fault bends can produce almost 1 order of magnitude of variability in the seismic moment estimations (Figures 4.16d and 4.17c).

To calculate stress drops, equation (4) is used:

$$\Delta\sigma=c(M_0/A^{(3/2)}) \quad (4)$$

(Kanamori & Anderson, 1975; Scholz, 2002) (Figures 4.16e and 4.17d), where c is a non-dimensional shape factor (~ 1 from Kanamori and Anderson, 1975).

The M_0 values shown in Figures 4.16d and 4.17c are used to evaluate the effect of variable D_{max} across fault bends. The results show that the variable displacement across a fault bend can produce ~ 1 order of magnitude of variability in stress drop values for each fault length (Figures 4.16e and 4.17d). Although this effect may be overestimated, because the worst case where D_{max} equals $D_{average}$ is considered, this result is important because information on the geometry and kinematics of faulting are not commonly considered when using D values to calculate stress drop.

Overall, this work suggests that along-strike fault bends, where the fault strike becomes oblique to the slip vector azimuth and the fault dip steepens beyond what is required to maintain the slip vector, strongly influence values of coseismic throw and displacement within the bend, and thus D_{max} . This influences the estimation of M_w from palaeoseismic studies and stress drop from field data on surface ruptures. Furthermore, these findings suggest that D_{max} to length scaling datasets are even more valuable than previously envisaged because it appears that the scatter of D_{max} for a given length provides information about how earthquake strain and moment release are partitioned along the strike of non-planar faults.

4.7 Conclusions

The 24th August 2016 M_w 6.0 and 30th October 2016 M_w 6.5 earthquakes ruptured the Laga and Mt. Vettore faults, in the central Apennines, Italy, producing anomalously large coseismic surface ruptures within an along-strike fault bend with steep fault dips on the Mt. Vettore fault. The bend has an amplitude of 0.83 km, which changes the fault strike and dip by $\sim 25^\circ$. Detailed field mapping was carried out to characterize the surface ruptures across the bend. The fault bend and its steep dip appear to have produced (1) a local maximum in total finite slip across the fault from offset of pre-rift strata, (2) a local maximum in fault-related relief, and (3) internal drainage on the hangingwall, all three of which developed over several million years, testifying to the long-term influence of the fault bend on the coseismic throw during earthquakes.

The application of the quantitative relationships (Faure Walker et al., 2009; 2010, 2015) on field data related to these two earthquakes, shows that the relatively large coseismic throw observed across the bend (29 cm and 234 cm for the 24th August M_w 6.0 and 30th October M_w 6.5 earthquakes, respectively) are required by the geometry and kinematics of the faulting to maintain the horizontal extensional strain along strike and across the fault bend with its high fault dip (Figure 4.9).

Increases of coseismic throws in fault bends are also investigated for some of the largest historic normal faulting earthquakes (1887, Sonora earthquake, M_w 7.5; 1981, Corinth earthquake, M_w 6.7-6.4; 1983, Borah Peak earthquake, M_w 7.3). The same equations can explain the anomalously-large coseismic D_{max} values in terms of conservation of the horizontal extensional strain along-strike and across the fault bends with their high fault

dips. Thus, this chapter provides for the first-time multiple examples from different normal faulting regions showing that coseismic throw depends on fault geometry. Furthermore, it is possible to quantify and explain changes in observed coseismic throws across fault bends in addition to longer-term changes in throw-rates across fault bends.

These results imply that along-strike fault bends are a plausible explanation of the scatter of D_{max} values for normal faulting earthquakes in D_{max} versus surface rupture length scaling relationships (e.g. Wells and Coppersmith, 1994). Thus, if the role of bends and high dips in those bends are not considered, this can produce misleading interpretations of (1) M_w from D_{max} values gathered during palaeoseismological studies, (2) seismic moments and (3) stress drops influenced by D_{max} . This study should prompt further investigation into the role of fault bends and their dips in influencing the magnitude of coseismic displacements associated with surface ruptures because it appears that the scatter of D_{max} for a given length provides information about how earthquake strain and moment release are partitioned along the strike of non-planar faults.

This chapter shows that well-established along-strike fault bends on single fault segments can produce coseismic throw enhancements within the fault bend. Less is known about the effects of along-strike fault bends affecting highly-segmented normal fault systems, where the change in strike affects different fault segments. The next chapter examines this situation, studying in detail the Aterno Valley Fault System, Central Apennines, Italy, an highly-segmented normal fault system which ruptured the 6th April 2009 during the M_w 6.3 L'Aquila earthquake.

Chapter 5

Occurrence of partial and total coseismic ruptures of segmented normal fault systems: Insights from the Central Apennines, Italy.

5.1 Summary

The previous chapter shows that an along-strike fault bend on a single fault segment causes throw enhancements within the bend, demonstrating that such enhancements occur on the timescale of individual earthquakes as well as over longer term 15 ka timescales as has been previously demonstrated (Faure Walker et al., 2009; Wilkinson et al., 2015). This chapter explores the effect of fault bends affecting multiple faults within a segmented normal fault system, where strike variations along individual faults are located in a similar along-strike location producing an overall curvature to the trace of the fault systems. Thus, this chapter extends existing studies of individual faults to a larger scale of fault systems.

The study area for this chapter is the Aterno Valley Fault System, located in Central Italy, which hosted the 6th April 2009 M_w 6.3 L'Aquila earthquake. The fault system comprises a dense array of normal faults, and exhibits a multi-fault along-strike fault bend in its central part. This chapter presents studies of the offsets for this fault system produced in a single earthquake, since the demise of the LGM (15 ± 3 ka) and since the initiation of

faulting (2-3 Ma) to show that: 1) individual faults within a segmented fault system behave as a single interacting fault segment over time periods including multiple earthquake cycles (e.g. 2-3 Ma or 15 ± 3 ka), with single earthquakes causing either partial or total ruptures of the entire system; 2) an along-strike bend causes throw and throw-rate enhancements within the bend throughout the seismic history of the fault system. This chapter discusses the synchronised and geometrically controlled activity rates on these faults in terms of the propensity for so-called “floating earthquakes”, multi-fault earthquakes, and seismic hazard. The findings of this chapter are published in Iezzi et al. (2019) in *Journal of Structural Geology*.

5.2 Introduction

Normal faulting earthquakes occur commonly within fault systems that consist of multiple closely-spaced fault surfaces, both along and across strike (Jackson et al., 1982; Crone et al., 1987; dePolo et al., 1991; Suter, 2015; Civico et al., 2018; Villani et al., 2018). The summed slip across all the faults that developed over the entire history of faulting (herein defined as long-term slip, also known as total or finite slip) commonly displays a coherent pattern with a slip maximum decreasing along strike to zero at the overall tips of the system (e.g. Roberts and Michetti, 2004). However, some earthquakes are said to “float” along a single fault within the system, rupturing either small portions or the entire length of the fault (Visini et al., 2019), whilst others rupture several faults during a single seismic event producing multi-fault earthquakes (also known as multi-rupture or multi-segment earthquakes) (Caskey and Wesnousky, 1996; Morewood and Roberts, 2001; Suter, 2015; Brozzetti et al., 2019). This wide variety of slip distributions means that it can be unclear how the coseismic slip distribution in one earthquake relates

to the summed long-term slip distribution. This uncertainty in the relationship between coseismic slip and longer-term slip is important because it limits the ability to plan for specific coseismic slip distributions and expected earthquake magnitudes during seismic hazard assessment given knowledge of the longer-term faulting. This chapter attempts to show some key features involved in this process, relating long-term slip magnitudes to fault geometries such as along-strike bends, highlighting the fact that coseismic ruptures do not necessarily inhabit the whole fault length or reflect the location of maximum strain accumulation in the longer term.

For example, during the 2016-2017 Central Italy seismic sequence two large earthquakes with different magnitudes, the 24th August 2016 M_w 6.0 and the 30th October 2016 M_w 6.5 earthquakes, ruptured the Mt. Vettore fault producing surface ruptures for ~18% and what appears to be the entire fault length, respectively (see Chapter 4 for details). The key observations from the 2016 Mt. Vettore examples are that (1) the longer-term slip is asymmetric, with the largest offset (~1400 m) within an along-strike fault bend (Iezzi et al., 2018; see Chapter 4); (2) the coseismic throw profiles for both earthquakes were also asymmetric, but with opposite senses (either skewed to the NW or SE), with the largest offsets (~30 cm and ~234 cm) located within the same along-strike fault bend (Iezzi et al., 2018; see Chapter 4); (3) multiple fault strands were activated in single earthquake (e.g. the 30th October 2016 M_w 6.5 earthquake; Ferrario and Livio, 2018; see Chapter 4), contributing to the long-term throw. Thus, the along-strike fault bend, and associated multiple fault strands, appear to be a recurrent control on slip that produces the long-term slip distribution. Although bends are commonly considered locations where the propagation of ruptures stop (Biasi and Wesnousky, 2017), the Mt. Vettore example shows that in some cases, propagation of coseismic ruptures across fault bends produces

enhancement of slip along the fault bend (Iezzi et al., 2018; see Chapter 4), in agreement with previous findings and theory (see Chapter 1, Section 1.1.2 for details). Less is known about slip enhancement across along strike bends where multiple faults are involved.

This chapter investigates whether activation of multiple faults during single earthquakes and the largest long-term and coseismic offsets within fault bends, as described for the Mt. Vettore earthquakes (see Chapter 4), can be identified for other normal faulting examples where multiple faults were involved. This chapter studies the 6th April 2009 M_w 6.3 L'Aquila earthquake that occurred 50 km to the SW of the 2016 earthquakes on the Mt. Vettore fault. This chapter shows that (1) the long-term slip is again asymmetric, (2) the strike of the multiple fault strands in the area change across a zone defining an along-strike bend in the fault system, (3) the long-term slip maximum is located within the fault bend, (4) in contrast to the 2016 earthquakes, the 2009 ruptures occurred outside the bend so that the location of maximum coseismic slip does not match the location of longer-term maximum fault slip, and (5) a previous earthquake on this fault system in 1703 AD appears to have had an alternative geometry and spatial extent, rupturing across the bend. This chapter discusses the complexity exhibited by the 3 modern earthquake ruptures in April 2009, August 2016 and October 2016, and that in 1703 AD, to investigate if rupture extent in one earthquake can be a good guide to the ruptures that may occur in the longer-term history of an individual fault. Moreover, this chapter discusses how this complexity, in particular with regard to along-strike fault bends, should be taken in account for seismic hazard assessments and when attempting to study the growth of normal faults.

5.3 Geological background of the 6th April 2009 M_w 6.3 L'Aquila earthquake

The 2009 L'Aquila earthquake ruptures occurred in the Aterno Valley, a narrow NW-SE trending tectonic depression located in the central part of the Apennines chain, central Italy (Figure 5.1). On the 6th April 2009, the Aterno Valley was struck by a M_w 6.3 earthquake, which caused severe damage to the city of L'Aquila and surrounding villages, with 309 fatalities, followed on the 7th April 2009 by a M_w 5.6 aftershock (Figure 5.2; Chiaraluce et al., 2011).

Seismological and geodetic data suggest that the 2009 earthquake had a slip distribution with a SE-striking, SW-dipping, 12-19 km long rupture extent at depth (Atzori et al., 2009; Walters et al., 2009; Cheloni et al., 2010; Cirella et al., 2010; Papanikolaou et al., 2010; D'Agostino et al., 2012; Lavecchia et al., 2012). Coseismic surface ruptures showed that the Paganica fault was the fault that ruptured in the earthquake, with maximum measured coseismic offset of about 10 cm at the surface (Figures 5.1 and 5.2; Falcucci et al., 2009; Boncio et al., 2010; Emergeo Working Group, 2010; Galli et al., 2010; Wilkinson et al., 2010; Vittori et al., 2011). DInSAR analysis exhibited a distributed coseismic slip of 25 cm, possibly including the contribution of the 7th April event to the deformation field (Papanikolaou et al., 2010). DiNSAR analysis also demonstrated that 66% of the deformed area subsided whereas 34% was uplifted, with an overall footwall uplift versus hangingwall subsidence ratio of about 1/3 (Papanikolaou et al., 2010).

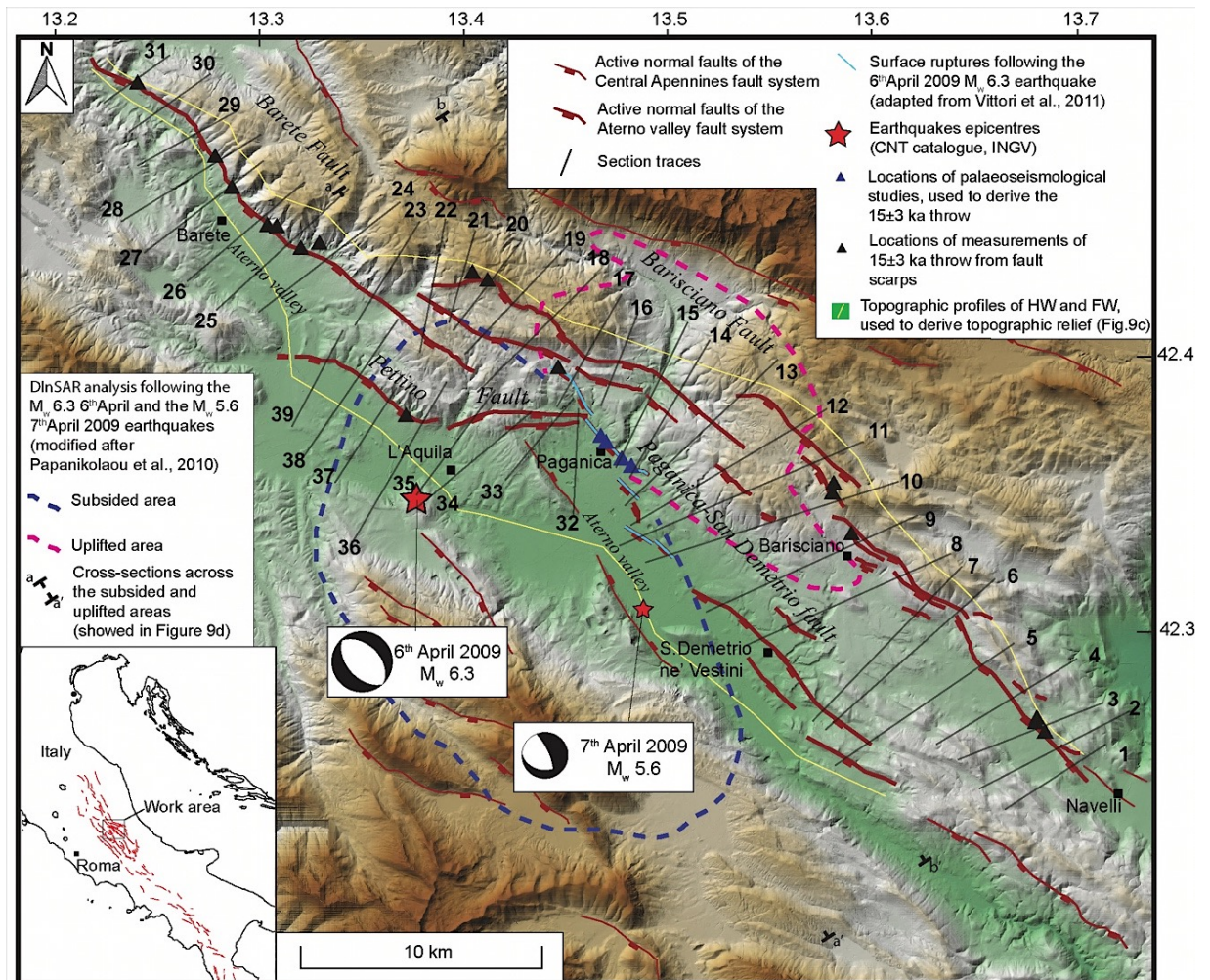


Figure 5.1: Location map of the Aterno Valley Fault System, central Apennines, Italy. Thick red lines are normal fault segments part of the Aterno Valley Fault System, thin red lines are other active normal faults part of the Central Apennines Fault System. Black lines are traces of the geological cross sections. Black triangles are locations of measurements of post 15±3 ka fault throw obtained from fault scarp measurements (from Roberts and Michetti, 2004; Papanikolaou et al., 2005; Galli et al., 2011; new measurements); blue triangles are locations of measurements of post 15±3 ka fault throw derived from throw-rates obtained with palaeoseismological analysis, assuming these throw-rates constant within the last 15±3 ka (from Galli et al., 2010; 2011; Cinti et al., 2011). Red stars are the epicenters of the 6th April 2009 M_w 6.3 L'Aquila earthquake mainshock and of the 7th April 2009 M_w 5.6 aftershock. Pale blue lines are the traces of the coseismic surface ruptures following the 6th April 2009 M_w 6.3 L'Aquila earthquake (modified from Vittori et al., 2011). Blue and pink dashed lines define the areas of subsidence and uplift, respectively, derived from DiNSAR analysis (Papanikolaou et al., 2010). a-a' and b-b' are traces of profiles across the deformed areas (see Figure 5.9). Yellow lines are topographic profiles used to derive the topographic relief associated with the Aterno Valley Fault System (showed in Figure 5.9c). From Iezzi et al., 2019.

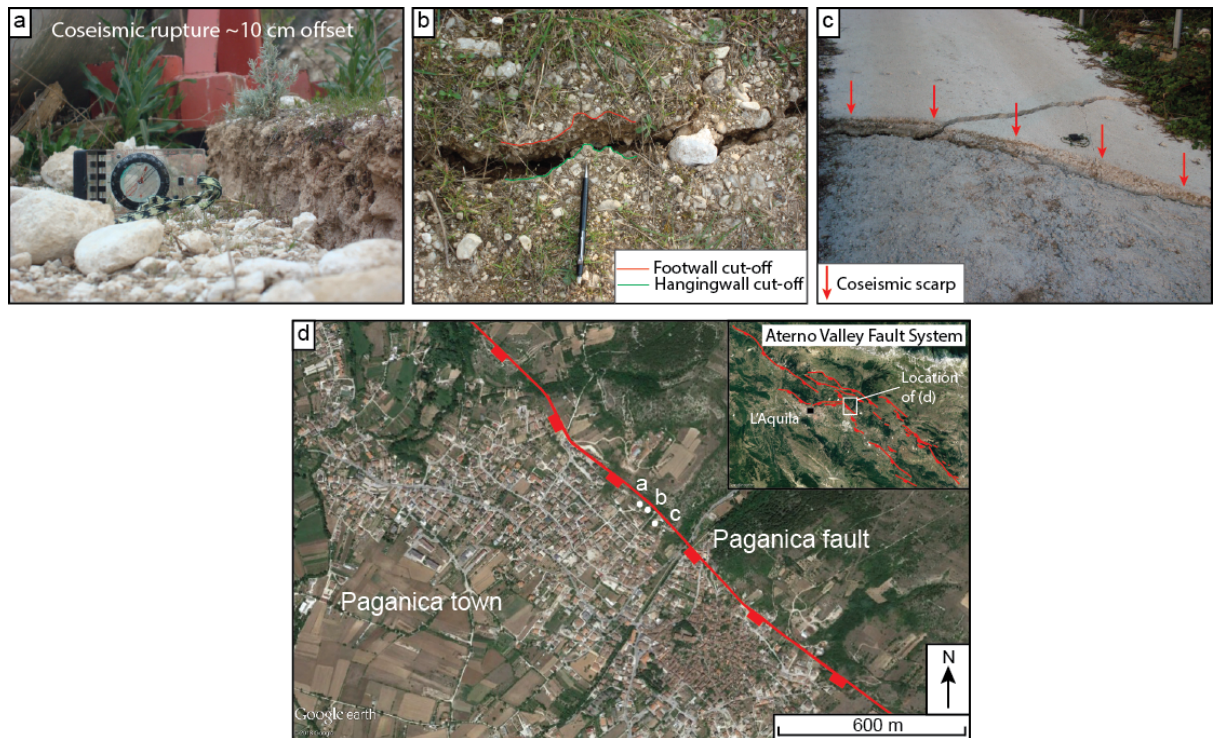


Figure 5.2: Coseismic ruptures following the 2009 L'Aquila earthquake. a) Coseismic scarp in eluvial-colluvial deposits, with vertical offset of ~10 cm. b) Opening cracks on the ground surface. c) Surface rupture on concrete, with vertical offset of ~10 cm. d) Location map of the surface ruptures showed in a), b) and c). From Iezzi et al., 2019.

The Paganica fault is characterized by several smaller fault segments that juxtapose Cenozoic limestones and calcarenites with Pleistocene-Holocene deposits (Vezzani and Ghisetti, 1998; ISPRA, 2009; Pucci et al., 2015). Different studies agree that the slip-rate in the Holocene is ~ 0.4 mm/yr (Galli et al., 2010; Roberts et al., 2010; Cinti et al., 2011; Moro et al., 2013). However, the Paganica fault is only one of a number of faults that deform the region, controlling the geomorphology and contributing to the summed long-term fault slip. In fact, following compilation of palaeoseismic results from trench studies conducted on a number of the faults, Galli et al. (2011) suggested that previous earthquakes, such as the 1703 A.D. M_w 6.7 event, may have ruptured multiple faults within the system (Figure 5.3). The question arises as to which rupture scenario (compare Figure 5.3 a and b) should be used to plan for future coseismic slip distributions and expected earthquake magnitudes during seismic hazard assessment. Measurements of the

long-term slip, accumulated over the entire activity of the faults, can provide information on whether the faults are interacting over a time span which encompasses all the seismic cycles that the faults have experienced, and therefore it may provide insights into the occurrence of multi-fault earthquakes in the Aterno Valley Fault System. In order to assess whether information on the long-term slip can help with this question, this work presents (1) 39 geological cross-sections across the Aterno Valley Fault System to quantify the along-strike long-term throw profile for the entire fault system (Figure 5.4); (2) new measurements of post-LGM throw and throw-rates, collated with published values, and projected onto an along-strike profile of the values (Figures 5.5 and 5.6); (3) the large-scale relief associated with the footwall escarpment of the Aterno Valley Fault System, obtained with topographic profiles derived from 10 m resolution DEM; (4) the along-strike arrangements of faults, in order to observe how the fault strike varies along the fault system (Figure 5.7); (5) a comparison of the longer term throw profile with the distribution of the coseismic ruptures following the 2009 L'Aquila earthquake (Figure 5.8).

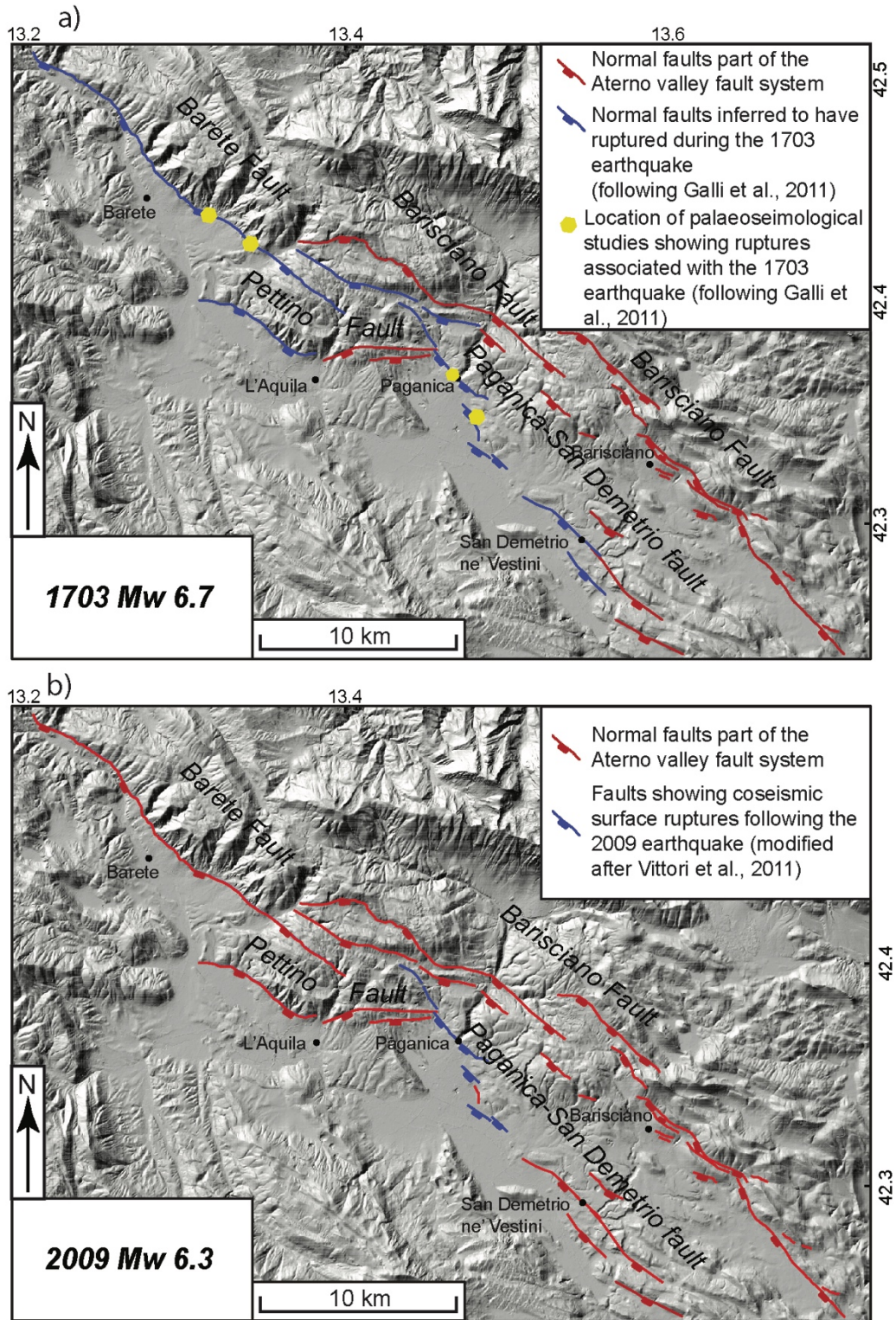


Figure 5.3: Palaeoseismological hypothesis of the occurrence of multi-fault earthquakes across the Aterno Valley Fault System. (a) shows in blue fault segments inferred to have ruptured during the 1703 M_w 6.7 earthquake, following Galli et al., 2011. Yellow polygons are locations of palaeoseismological studies with evidences of rupture ascribable to the 1703 earthquake (from Galli et al., 2011). (b) shows in blue surface ruptures following the 6th April 2009 M_w 6.3 earthquake, modified after Vittori et al., 2011. It is shown that palaeoseismological studies suggest that the 1703 M_w 6.7 earthquake may have ruptured several fault segments at the same time, across the total extent of the fault system, suggesting the occurrence of multi-fault earthquakes. From Iezzi et al., 2019.

5.4 Methods

Fault segments showing evidence of post-LGM and Holocene activity (Figure 5.1) have been identified by combining results from fieldwork, published geological maps, palaeoseismology, structural geology and high-resolution imagery such as Google EarthTM and a 10 m resolution DEM (opendata.regione.abruzzo.it).

A set of 39 approximately serial geological cross-sections across pre-rift strata have been constructed along the strike of the Aterno Valley Fault System, based on published geological maps and field mapping (Figures 5.4; Vezzani and Ghisetti, 1998; ISPRA, 2009; Pucci et al., 2015). These cross-sections were used in order to define the long-term slip of the analysed faults, stretching back to 2-3 Ma, the time when extension is thought to have initiated (Cavinato and De Celles, 1999; Roberts et al., 2002). The cross-sections were constructed perpendicular to the fault traces, in order to avoid measurements of apparent fault dip. The cross-sections were chosen in order to avoid effects of inherited throw associated with cross faults with pre-Quaternary tectonic history (e.g. Pizzi and Galadini, 2009). The long-term throw has been measured as the vertical distance between the hangingwall and footwall cut-offs of the Meso-Cenozoic bedrock formations that were in place before the onset of the extension across the Apennines, and therefore record all the slip accumulated by the faults (since 2-3 Ma). The bedrock formations exhibit significant variability in thickness across the fault system (Vezzani and Ghisetti, 1998). Therefore, to incorporate uncertainty in the thickness of a formation, for example under the sedimentary fill of the Aterno Valley, the maximum stratigraphic thickness provided by Vezzani and Ghisetti (1998) has been assigned, but local geological observations were also incorporated to gain appropriate values where appropriate. In places where the fault

trace is complex, formed by both synthetic and antithetic fault segments, the total throw was considered as the sum of the single measurements of throw on each fault segment. Some faults present in the geological map have not been included in the Aterno Valley Fault System because a lack of evidence of Holocene or post-LGM activity. Also, some faults with Holocene or post-LGM activity, as revealed by geomorphology and palaeoseismology, may not have been resolved by the geological maps in cases where the thickness of the Meso-Cenozoic units is larger than the fault offset, and therefore there is no evidence of offset of geological units on the fault.

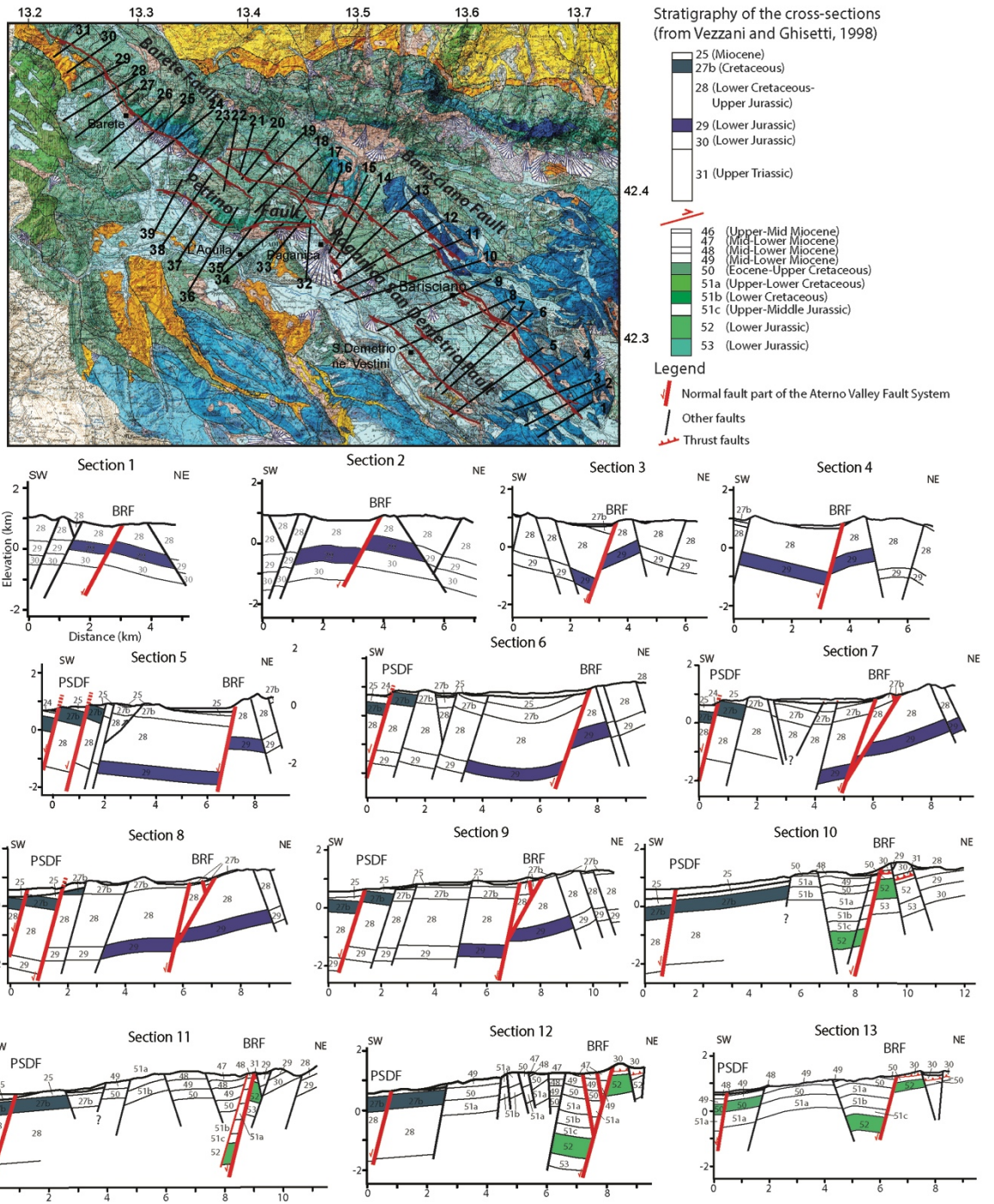


Figure 5.4: Geological cross-sections built across the Aterno Valley Fault System. From Iezzi et al., 2019. (Continued).

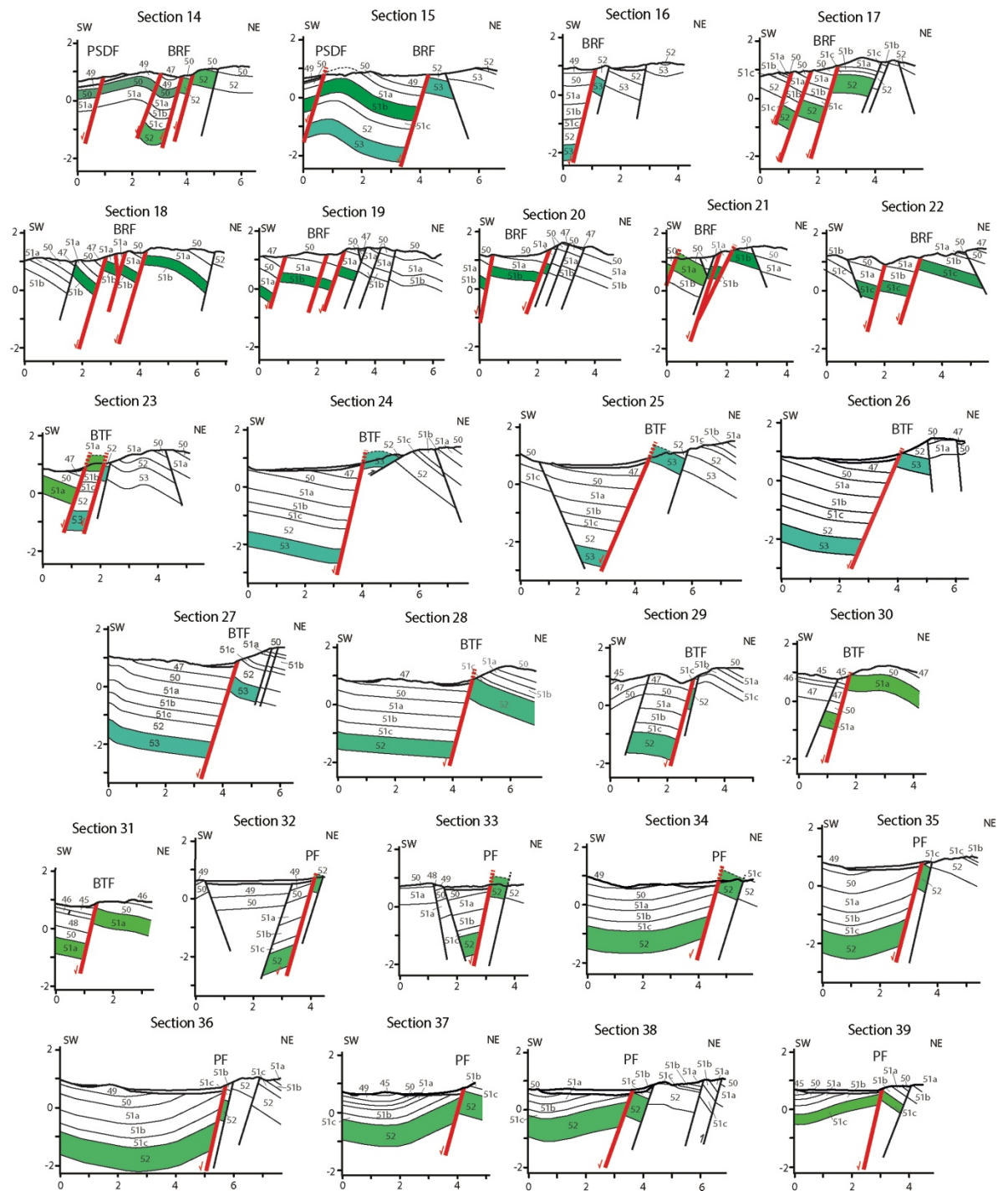


Figure 5.4: Geological cross-sections built across the Aterno Valley Fault System. The geological map of the Aterno Valley Fault System is modified from Vezzani and Ghisetti, 1998. In red are faults part of the Aterno Valley Fault System, in black traces of the cross-sections. In the cross-sections, the stratigraphy is derived from Vezzani and Ghisetti, 1998, map; colours are in agreement with the ones reported in the map, and used to highlight the offset on fault. BRF: Barisciano fault; PSDF: Paganica-San Demetrio fault; BTF: Barete fault; PF: Pettino fault. When it was not possible to establish the thickness of a formation, it has been assigned the maximum thickness provided by the legend of the map. From Iezzi et al., 2019.

Measurements of the throw accumulated since the demise of the Last Glacial Maximum (15 ± 3 ka; LGM throw) have been collated from published values (Roberts and Michetti, 2004; Papanikolaou et al., 2005; Faure Walker et al., 2010; Galli et al., 2010; Cinti et al., 2011; Galli et al., 2011) and new field measurements, collected and provided for this thesis by Gerald Roberts (Figures 5.5 and 5.6). The LGM was a time of high erosion and sedimentation due to the cold climate and freeze-thaw activity (Tucker et al. 2011). This means that slip in the LGM has not been preserved, and only slip after the climate changed during the demise of the LGM has been preserved as fault scarps. In particular, this thesis uses throw values for periglacial slopes from the LGM offset across the faults (see Roberts and Michetti (2004) for a review).

To gain values for the throw-rates on the active fault scarps, this work combines (1) measurements of fault scarp offsets (Roberts and Michetti, 2004; Papanikolaou et al., 2005; Faure Walker et al., 2010; Galli et al., 2011), (2) palaeoseismological analysis (Galli et al., 2010; Galli et al., 2011; Cinti et al., 2011), assuming that the throw-rate measured in the trench is constant during the last 15 ± 3 ka, and (3) new field measurements across LGM scarps (Figure 5.6). The post-LGM throw values have only been collected from locations free of significant Holocene erosion and sedimentation, following the approach of Cowie et al. (2017), where the periglacial surfaces in the footwall and hangingwall are planar and undisturbed by post-Holocene erosion, evidenced by parallel hangingwall and footwall cut-offs (see Chapter 3 for details). With these characteristics, it is reasonable to assume that the fault scarp has been exhumed only by repeated coseismic surface ruptures, and therefore its height represents a measurement of the throw accumulated since 15 ± 3 ka.

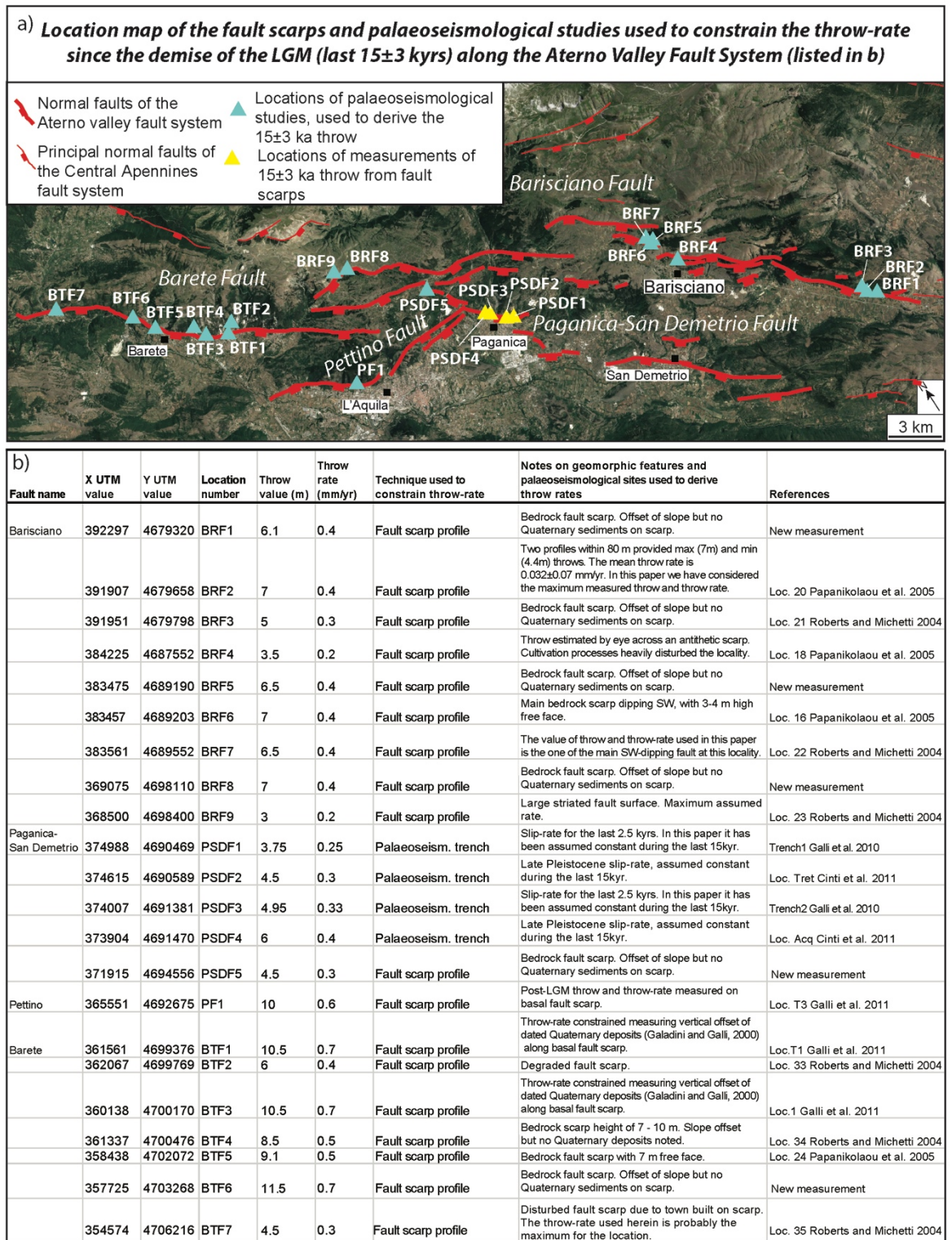


Figure 5.5: Measurements of throw since the demise of the Last Glacial Maximum (15 ± 3 ka). a) Location map of the fault scarps and palaeoseismological studies used to constrain the throw-rates since the demise of the LGM along the Aterno Valley Fault System, comprehensive of published and newly collected data. Location numbers are coded in agreement with the name of the fault to which they belong: BRF=Barisciano fault; PSDF=Paganica-San Demetrio fault; PF=Pettino fault; BTF=Barete fault. b) Database of measurements of throw and throw-rates shown in a). Adapted from Iezzi et al., 2019.

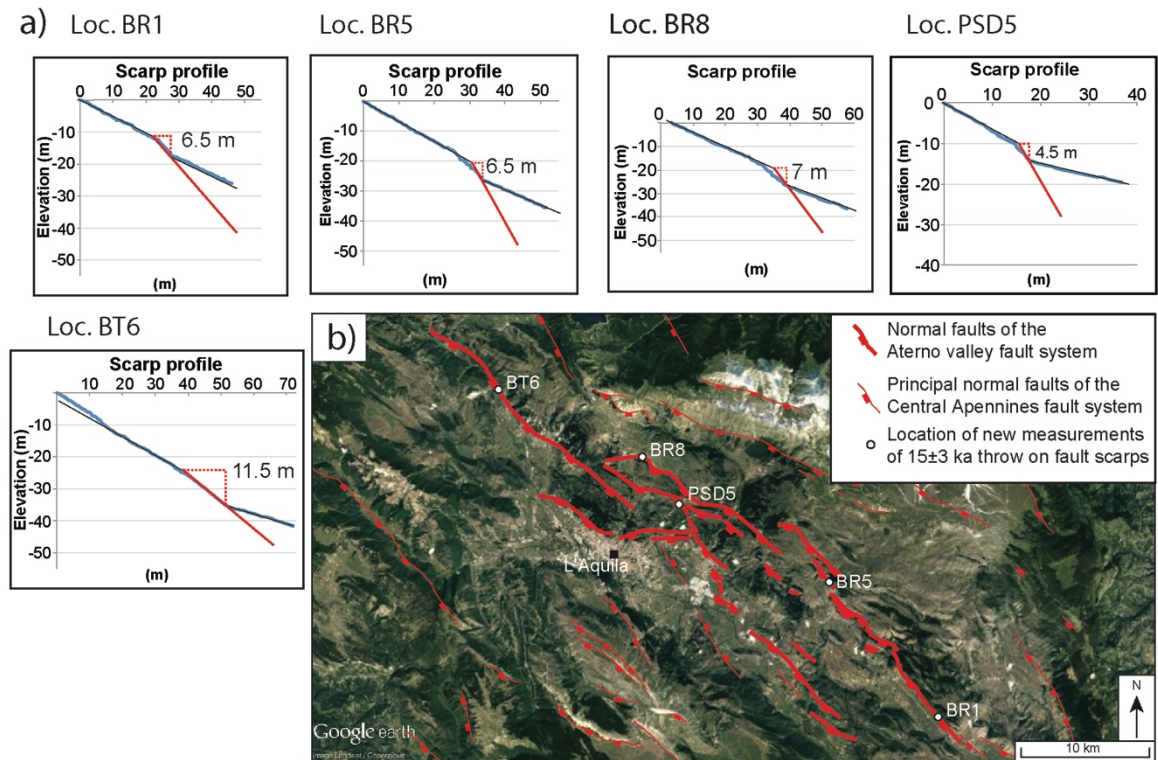


Figure 5.6: New field measurements of throw and throw-rates since the demise of the Last Glacial Maximum (15 ± 3 ka) from fault scarps located along the Aterno Valley Fault System (collected and provided for this thesis by Gerald Roberts). a) Interpreted scarp profiles showing the measured throw associated with the fault scarp. Scarp profiles have been built through chain surveying techniques using a 1 m ruler and a clinometer. Location numbers are coded in agreement with the database shown in Figure 6b. b) Location map of the field locations in a). From Iezzi et al., 2019.

The along-strike arrangements of faults have been also studied, and strike lines were constructed for the principal fault segments in order to understand how the fault strike varies along the fault system (Figure 5.7).

To compare all the above data, along-strike profiles for the long-term throw from offsets of pre-rift strata (Figure 5.8a), and offsets since the LGM (Figure 5.8b) have been constructed. These profiles, together with the analysis of the fault trace arrangement, the topographic relief associated with the Aterno Valley Fault System (Figure 5.8c) and the presence of N-S striking cross faults (e.g. Pizzi and Galadini, 2009; Figure 5.4), allow the identification of the tips of the fault system and to reconstruct the segmentation of the main faults of the system (Figure 5.8f). The long-term activity of the Aterno Valley Fault

System has been compared also with the coseismic activity following the 6th April M_w 6.3 L'Aquila earthquake and 7th April M_w 5.6 aftershock, herein referred to as (1) the coseismic surface deformation derived from DiNSAR analysis (Figure 5.8d; Papanikolaou et al., 2010), and (2) five different published geodetic and seismological models of the coseismic slip distribution at depth of the earthquake (Figure 5.8e; Atzori et al., 2009; Walters et al., 2009; Cheloni et al., 2010; Cirella et al., 2010; D'Agostino et al., 2012).

5.5 Results

5.5.1 Analysis of the geometry of the Aterno Valley Fault System

The Aterno Valley Fault System is composed of several fault segments of variable length, with both en-echelon and end-on arrangements (Figure 5.7). Overall, the south-eastern part of the fault system is highly segmented, characterized by relatively short fault traces. The north-western part appears to be characterized by relatively more continuous fault traces, with significant overlaps between fault segments. The distance between the tips of neighbouring faults is relatively small, and in most instances is less than 5 km.

Strike-lines drawn along the fault system show that the fault system contains a bend in its strike (Figure 5.7). While the fault segments outside the bend (outer faults) have an average strike of N131°, with values ranging between N130° and N133°, across the bend the strike gradually change, with values ranging between N083° and N122°, with an average strike of N106°. This along-strike bend, resulting from a variation of fault strike of ~25°, produces an overall left en-echelon arrangement of the fault system (Figure 5.7).

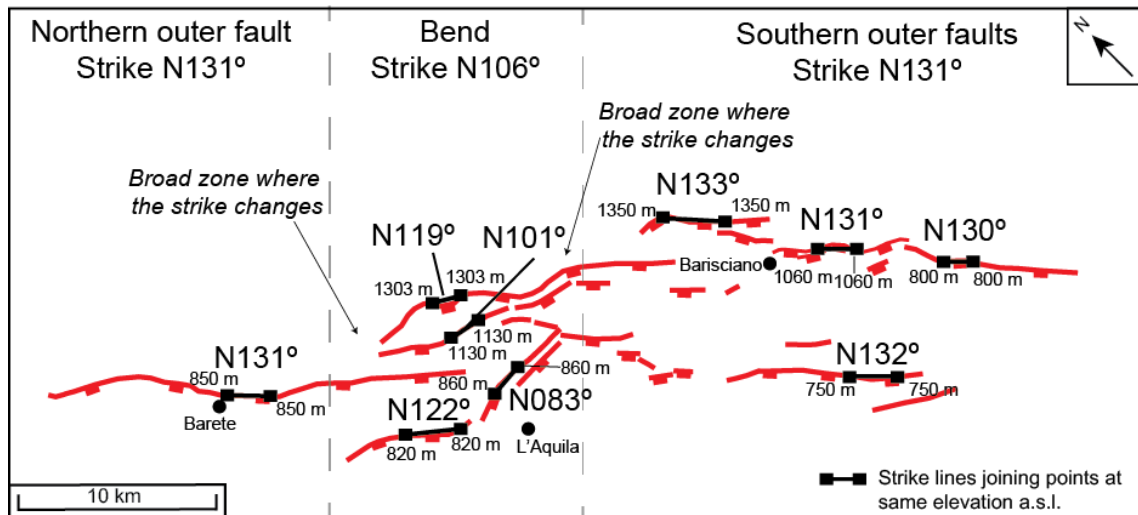


Figure 5.7: Analysis of the geometry of the Aterno Valley Fault System. In black are reported strike lines built on the main fault segments of the fault system. It is shown that the fault system presents a wide along-strike bend, across which the strike of different fault segments changes, with an overall shift of $\sim 25^\circ$ from the strike of the fault segments outside the fault bend (outer faults). From Iezzi et al., 2019.

5.5.2 Analysis of the throw profiles of the Aterno Valley Fault System

By combining the measured along-strike throw distributions and the fault trace arrangements, the segmentation and the length of the four main faults of the Aterno Valley Fault System has been reconstructed: the Barisciano fault, the Paganica-San Demetrio fault, the Pettino fault and the Barete fault (Figure 5.8). The Barisciano and the Paganica-San Demetrio faults at the surface appear to be characterised by many relatively short, discontinuous fault segments (Figure 5.8f), organised with en-echelon arrangements and the presence of mostly synthetic faults with a few short antithetic strands. However, the lengths of individual faults are in places hard to determine due to limited exposure and Quaternary sediments; it may be that faults are more connected than shown in Figure 5.8f. The multi-humped throw profiles, with numerous maxima and minima along strike, are consistent with the notion that the faults grew by linkage of relatively short segments (green and pale blue lines in Figure 5.8a; see Cowie and Roberts, 2001). The Pettino and Barete faults are characterized by what appear to be

longer and more continuous fault segments, although again this may be due to more continuous exposure rather than any difference in fault connectivity compared to faults to the SE (Figure 5.8f). However, greater connectivity may be reflected in their long-term throw profiles, which show a single maximum and a decrease of values towards the fault terminations (purple and orange lines in Figure 5.8a). The cumulative long-term throw profile across all the faults in the Aterno Valley Fault System (dark blue line in Figure 5.8a) shows that the overall throw is asymmetric, with the maximum summed throw located in the NW half of the overall fault trace, within the along-strike bend of the Aterno Valley Fault System defined by strike lines (Figure 5.7).

The throw that has accumulated since the demise of the LGM (dark blue line in Figure 5.8b), constructed using measurements from fault scarp heights (squares in Figure 5.8b) and palaeoseismology (triangles in Figure 5.8b), shows that the cumulative post-LGM throw is again asymmetric, with the post-LGM maximum throw located in the NW half of the overall fault trace, within the along-strike bend of the Aterno Valley Fault System defined by strike lines (Figure 5.7).

The topographic relief associated with the Aterno Valley Fault System agrees with the findings obtained with the study of the longer-term offsets (Figure 5.8c). The relief achieves a maximum within the bend (~1000 m) and decreases towards zero at the tips of the fault system (Figure 5.8c). A local minimum within the fault bend is produced by a prominent incised drainage system that cuts through the fault system (see Figure 5.1).

Overall, the similarity between the long-term and post-LGM throw profiles (Figures 5.8a and 5.8b), together with the study of the topographic relief (Figure 5.8c), indicates that

this group of faults behave as a single interacting fault segment over multiple earthquake cycles, and that the repetition of slip during several earthquake cycles, like that occurred since the demise of the LGM, built the long-term throw. This is also suggested by the observation of the slip vector azimuths measured along the fault system (from Roberts and Michetti, 2004; Papanikolaou et al., 2005; Faure Walker et al., 2010), which show a convergent pattern towards the hangingwall, with dip-slip kinematic in the central part and oblique slip towards the tips of the fault system (Figure 5.8f). Converging slip vector azimuths like this have been used as a criterion to define the length of single interacting segments because they form due to the lateral continuity of differential uplift between the hangingwall and footwall, which causes asymmetry between the extensional strains in both hangingwall and footwall (Ma and Kuszniir, 1995; Roberts 1996a, Roberts and Ganas 2000, Roberts and Michetti 2004, Roberts 2007; Hampel et al., 2013).

5.5.3 Comparison between the longer-term activity of the Aterno Valley Fault System and the M_w 6.3 L'Aquila Earthquake

The key question is whether the single interacting segment defined above ruptures in its entirety or partially in single earthquakes. The comparison between the long-term and the post-LGM throw profiles with the coseismic slip profiles of the 6th April 2009 M_w 6.3 L'Aquila earthquake shows that the earthquake only ruptured a relatively small portion of the Aterno Valley Fault System (~20 km; compares Figures 5.8a-c and 5.8d-f), comprising only ~ 40% of its overall ~50 km along strike length. This is consistent with the mapped traces of the coseismic ruptures, which are localized in a small part of the fault system (Figure 5.8f). Note that the surface rupture formed mostly outside of the

overall fault bend in the Aterno Valley Fault System, where the maximum cumulative post LGM throw and longer-term throw was observed (Figure 5.8f).

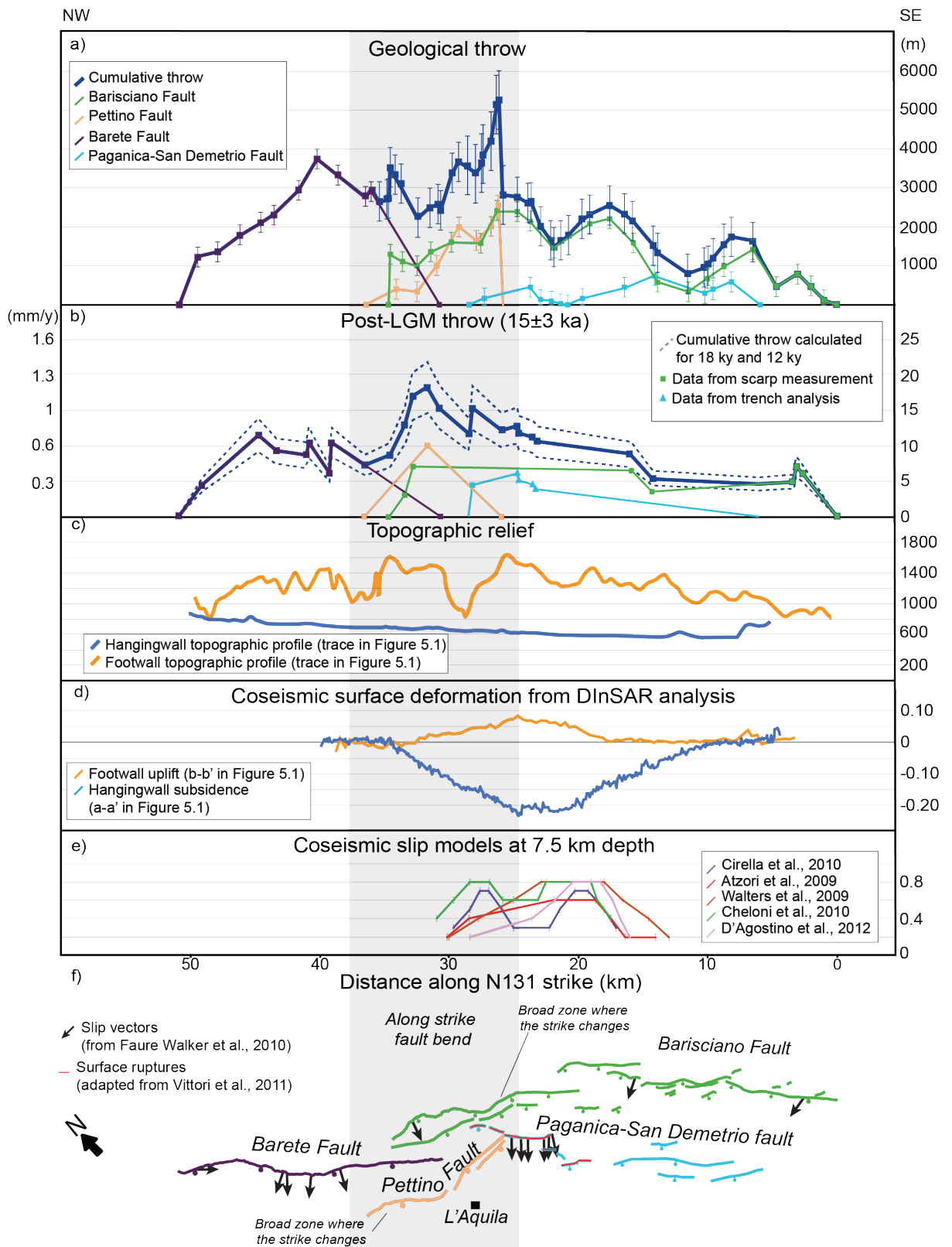


Figure 5.8: Throw profiles of the Aterno Valley Fault System. a) Long-term throw profiles of the main faults of the fault system. Values of throw are derived from geological cross-sections shown in Figures 5.4. In blue is reported the cumulative throw profile of the fault system, calculated by summing up the throw values across each fault segment. b) Profiles of the throw accumulated since the demise of the Last Glacial Maximum (15 ± 3 ka) across the fault system. Squares are values of throw derived from fault scarp measurements (Roberts and Michetti, 2004; Papanikolaou et al., 2005; Galli et al., 2011; fieldwork), triangles are values of throw derived from palaeoseismological analysis (palaeoseismological throw rate times 15 ± 3 ka; Galli et al., 2010; 2011; Cinti et al., 2011). In blue is the cumulative LGM throw profile of the entire fault system. Throw-rates, reported on the left-hand side, are calculated assuming a constant throw-rate within the last 15ka. c) Topographic relief associated with the footwall escarpment of the Aterno Valley Fault System. In orange is the topographic profile of the footwall, in blue of the hangingwall, derived from 10m DEM. d) Profiles of coseismic deformation areas of uplift and subsidence following the 6th April 2009 M_w 6.3 mainshock and the 7th April 2009 M_w 5.6 aftershock, derived from DInSAR analysis (profile traces a-a' and b-b' in Figure 5.2; adapted from Papanikolaou et al., 2010). e) Along-strike profiles of the coseismic slip of the 6th April 2009 M_w 6.3 L'Aquila earthquake, derived from different geodetic and seismological fault models (Atzori et al., 2009; Walters et al., 2009; Cheloni et al., 2010; Cirella et al., 2010; D'Agostino et al., 2012). Profiles have been drawn at 7.5 km depth. F) Reconstruction of the segmentation of the principal faults forming the Aterno Valley Fault System. This figure shows that 1) the 2009 earthquake ruptured only a small part of a complex fault system, 2) faults within the Aterno Valley Fault System are interacting over several earthquake cycles, with potential to release multi-fault earthquakes, 3) maximum throws are localized within a fault bend, which is a persistent feature influencing the throw distribution over the history of the fault system. From Iezzi et al., 2019.

5.5.4 Comparison between the long-term and post-LGM throw-rates along the

Aterno Valley Fault System

To understand how the post-LGM throw-rates compare with the long-term history of the fault system, the predicted long-term throw profile of the Aterno Valley Fault System is calculated assuming constant post-LGM throw-rates during the entire fault activity (last 3 Ma; Roberts et al., 2002). This is a valid assumption when slip-rates are averaged over normal fault systems (e.g. Roberts and Michetti, 2004). The predicted long-term throw profile is compared with the long-term throw profile derived from the geological cross-sections (Figure 5.9). The comparison shows that the predicted long-term throw is overall consistent with the measured long-term throw profile given the above assumptions, and reveals how the post-LGM fault throw-rates are working in a way that mimics the long-term behaviour of the fault system. In fact, local discrepancies between the predicted and the measured throw profiles suggest that faults are working in order to produce a throw profile consistent with one for a single interacting fault segment, with relatively low post-

LGM throw-rates localized where the long-term throw profile presents local maxima (for example at ~40 km distance along strike, Figure 5.9) and relatively fast post-LGM throw-rates localized where the long-term throw profile presents minima (at ~33km distance along strike, Figure 5.9). The short wavelength variation in throw shown in both profiles is most likely due to the effect of the local segmentation of the faults.

Thus, the overall finding from this and the previous section is that faults studied herein behave as a single interacting fault segment over time periods containing multiple earthquake cycles (e.g. over 15 ± 3 ka or 2-3 Ma), with the position of the maximum offset controlled by a bend in the strike of the system, producing an asymmetric throw profile. Individual ruptures, if typified by the 2009 earthquake, float within the fault system, rupturing only part of the along strike extent of the system. Other ruptures, such as those in 1703 AD, if the palaeoseismic reconstruction is correct, have a greater along strike extent. Thus, an important new insight is suggested where different rupture scenarios can occur through time on the same fault. Moreover, rupture locations since the demise of the LGM may exhibit a propensity to fill displacement deficits that have developed over 2-3 Ma. Palaeoseismic results from Galli et al. (2011) suggest that in some earthquakes multiple faults may be ruptured with rupture extent approaching that of the length of the entire fault system.

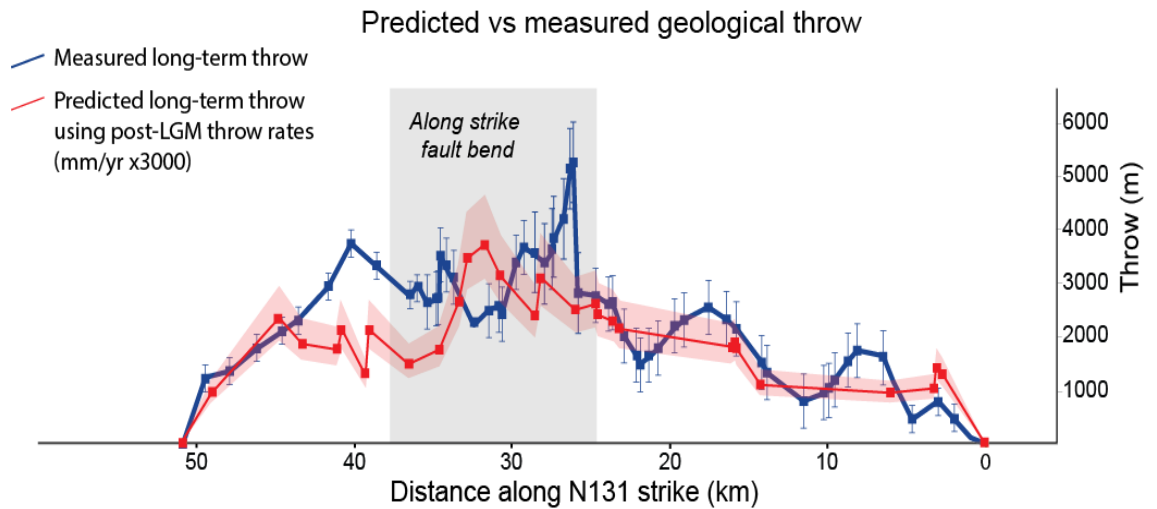


Figure 5.9: Comparison between the measured long-term throw profile (blue line) and the predicted long-term throw profile (red line), assuming constant post-LGM throw-rates during the last 3 Ma. It shows that the two profiles are overall consistent, which suggest that the post-LGM throw-rates can be representative of the throw-rates averaged over the entire faults activity. Local discrepancies prompt the idea that post-LGM throw-rates are working in order to produce a throw profile which reflect the long-term throw profile. From Iezzi et al., 2019.

5.6 Discussion

The results show that the 2009 L’Aquila M_w 6.3 earthquake shared several of the attributes observed for the 2016 Mt. Vettore M_w 6.0 and M_w 6.5 earthquakes: the overall long-term throw profile is asymmetric, as is the post-LGM throw profile, with maxima located within a fault bend, and numerous across-strike fault strands combine to produce these asymmetries. However, the coseismic throws in the 2009 L’Aquila earthquake occurred mostly outside of the overall fault bend, in contrast to the Mt. Vettore earthquakes. Overall, these three earthquakes show that the locations of coseismic offsets can define either complete or partial rupture of the overall fault system. The “partial” earthquakes float within the structure in the way described for other earthquakes on normal faults (e.g. Roberts, 1996b; Roberts and Koukouvelas, 1996; DuRoss et al., 2016),

with frequent surface-faulting earthquakes rupturing the central part of the fault system and more slip accumulated within the fault bend through time. These observations imply that the along strike extent of single coseismic ruptures are not a good guide to describe the lengths of fault segments that develop over multiple seismic cycles, or the potential rupture lengths and earthquake magnitudes for future events.

The relative short distance between fault segments of the Aterno Valley Fault System (mostly < 5 km across strike) is interesting to compare with maximum distance for the definition of multi-fault earthquakes on other fault systems such as the San Andreas fault system in California (e.g. UCERF 3 model, Field et al., 2014; 2015; 2017) where 5 km steps in the fault system are thought to define individual rupture segments. Also, empirical studies have shown that normal faulting earthquakes are capable of rupturing steps in the fault strike that can reach up to 5-7 km (Wesnousky, 2008), and that for dip slip ruptures 30% of the observed ruptured steps are larger than 5 km (Biasi and Wesnousky, 2016). Moreover, there are examples of normal faulting earthquakes that ruptured simultaneously parallel faults spaced about 5 km (e.g. the M 7.2-6.8 1954 Fairview Peak-Dixie Valley and the M 7.5 1959 Hebgen Lake earthquakes; dePolo et al., 1991). Therefore, the relatively small across strike spacing within the Aterno Valley Fault System may indicate that ruptures can cross between fault strands. Given these considerations, it appears that seismic ruptures are able to jump from one fault to another within the Aterno Valley Fault System, rupturing more than one fault during the same seismic event and producing multi-fault earthquakes, as is suggested by palaeoseismological studies (Galli et al., 2011; see Figure 5.3a), although palaeoseismological data for the Barisciano fault is lacking. It follows, therefore, that ruptures within the bend may lead to relatively large throws, for example related to larger

coseismic throw, as was the case for the 2016 Mt. Vettore ruptures (Iezzi et al., 2018; Chapter 4).

If ruptures join along strike linking separate faults, earthquake magnitudes larger than the M_w 6.3 of the 2009 L'Aquila earthquake may occur (e.g. the 1703 earthquake). The worst-case scenario, in which the fault system ruptures for its entire length of about 50 km, would imply that the fault system has the potential to release a M_w 7 earthquake, according to empirical M_w /surface rupture length scaling relationship (Figure 5.10; Wells and Coppersmith, 1994). More work is needed to assess whether the above is true of other parts of the overall Central Apennines Fault System, but faults are commonly interconnected and close to each other within the fault system (Roberts and Michetti 2004). This chapter suggests that the occurrence of multi-fault earthquakes should be investigated for other localities along the fault system, and that study of the structural geology of active faults, as demonstrated in this chapter, should form part of future studies aimed at ascertaining the propensity for multi-fault earthquakes.

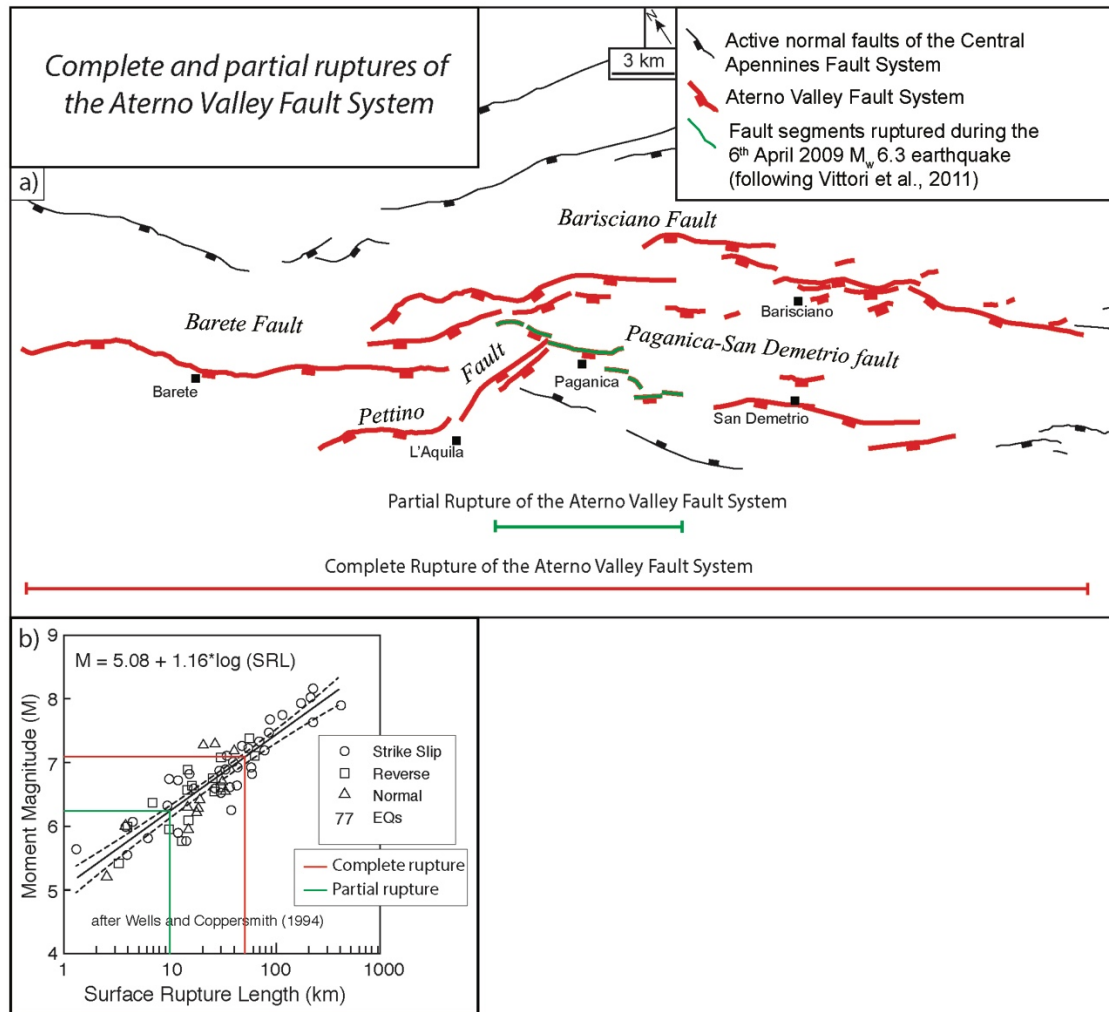


Figure 5.10: Complete and partial ruptures of the Aterno Valley Fault System. a) Fault map of the Aterno Valley Fault System showing that it can experience complete ruptures, involving all its fault segments (red bar), and partial ruptures, as is the case of the 2009 M_w 6.3 L'Aquila earthquake (green bar). b) Moment Magnitude versus Surface Rupture Length scaling relationship (Wells and Coppersmith, 1994), with reported partial and total ruptures of the Aterno Valley Fault System. From Iezzi et al., 2019.

The propensity of the post-LGM throw-rates to fill the displacement gaps developed in the last 2-3 Ma suggests that the fault interaction occurred later during the history of faulting, with faults of the Aterno Valley Fault System that firstly worked as individual segments and subsequently started interacting. A detailed analysis of the sedimentary architecture of the Quaternary deposits in the hangingwall basins might help to understand the timings of the onset of the fault interaction. In fact, before faults started interacting, syntectonic sediments would have been localised in the hangingwall basins associated with the individual faults. As the faults started interacting, the syntectonic

hangingwall basins would tend to merge, and therefore the sediments would tend to be widespread along the entire Aterno Valley. Hence, a detailed analysis of the distribution of the Quaternary syntectonic sediments (e.g. Pasquarè et al., 2004; Guerrieri et al., 2006; Cosentino et al., 2014; Cosentino et al., 2017) would help to understand the timings of the onset of the fault interaction within the Aterno Valley Fault System.

Furthermore, the results for the 2016 Mt. Vettore earthquakes and the 2009 L'Aquila earthquake have implications for how to interpret palaeoseismic results. They show that maximum throw values are found within the bends in both fault systems: examples include the 2009 L'Aquila earthquake in both the long-term throw and the post-LGM throw profiles, and the 2016 Mt. Vettore earthquakes in both the long-term and coseismic throw profiles. This is similar to results from other studies which show that anomalously large throws are located within along-strike fault bends on single fault segments (Faure Walker et al., 2009; Wilkinson et al., 2015; Mildon et al., 2016; Iezzi et al., 2018). If high values for throw-rates in the long-term are produced by large values of coseismic throw, rather than more frequent earthquakes, as suggested by the Mt. Vettore example, then palaeoseismic throws reported from trench sites within bends may overestimate the palaeoearthquake magnitude if that value of coseismic throw is used within the scaling relationships between maximum displacement and magnitude, such as that in Wells and Coppersmith (1994), and Manighetti et al. (2007) (Iezzi et al., 2018). In fact, this may well be a common feature for normal fault systems because the consistency of the locations of the maxima in both the long-term and LGM throw profiles may indicate that the effect of the along-strike fault bend persists through time (see Faure Walker et al., 2009).

Overall, these results suggest that the 2009 M_w 6.3 L'Aquila earthquake represents a partial rupture of a more complex fault system. Therefore, this chapter recommends that future studies of the Aterno Valley Fault System, and other fault systems with similar geometry, should investigate whether it has the potential to release larger earthquakes. If this typifies other active normal faults, the occurrence of partial and complete rupture of the overall fault length will produce ambiguity in the outputs of palaeoseismology for seismic hazard. Detailed palaeoseismological studies within segmented fault systems, concentrating on whether multiple faults rupture simultaneously, should be given high priority.

5.7 Conclusions

This chapter presents studies of the fault geometry and the slip history of the Aterno Valley Fault System (Central Apennines) that ruptured during the 6th April 2009 M_w 6.3 L'Aquila earthquake, in order to understand 1) how coseismic slip magnitudes in one earthquake relate to the summed slip across all the faults of the fault system that have developed over the entire history of faulting and 2) if prominent along-strike bends within a fault system has consistently halted earthquake ruptures or promoted high values of slip.

The comparison between the offset measured since initiation of faulting at 2-3 Ma, since the Last Glacial Maximum at $\sim 15 \pm 3$ ka and during the 2009 M_w 6.3 L'Aquila earthquake, together with the analysis of the geometry of the fault system and the comparison between long-term and post-LGM throw-rates, suggest that: 1) faults within a segmented fault system can behave as a single interacting fault segment over time periods containing multiple earthquake cycles (e.g. over 15 ± 3 ka or 2-3 Ma), with

maxima values of throw within a bend in the strike of the fault system, across which the strike shifts of $\sim 25^\circ$; 2) single earthquakes can float within the fault system, rupturing either part or all the along strike extent of the system; 3) the along-strike bend seems to exert a persistent control on the distribution of throw within the fault system, promoting high values of throw and throw-rates within the bend and large coseismic throw when seismic ruptures propagate within it; 4) the close proximity between mapped fault segments indicates that for the Aterno Valley Fault System seismic ruptures may be able to jump from one fault to another, producing multi-fault earthquakes, which can release earthquakes with magnitudes up to M_w 7. Given the structure of the Central Apennines Fault System, where faults are commonly interconnected and close to each other, these results imply that the occurrence of multi-fault earthquakes should be investigated for other parts of the fault system. Hence, this chapter suggests that study of the structural geology of active faults should be included in assessments of the propensity for the occurrence of multi-fault earthquakes.

Overall, this chapter shows that along-strike fault bends affects the distribution of throw and throw-rates over different time scales also for segmented normal fault systems, following what is shown in Chapter 4, where a fault bend affects one single fault segment. However, both the studies in Chapter 4 and Chapter 5 have been carried out in the Central Apennines, Italy. Prior to this thesis, there were no detailed studies of the relationships between the local non-planar fault geometry and the along-strike throw distribution outside the Central Apennines. Hence, the next chapter focuses on normal faults in the Western Volcanic Zone, Iceland, to study if this relationship is applicable also in a geodynamic context of a mid-oceanic rift.

Chapter 6

Throw-rates variation within linkage zones during the growth of a normal fault: case studies from the Western Volcanic Zone, Iceland.

6.1 Summary

The previous two chapters showed that along-strike fault bends can produce coseismic throw, long-term throw-rates and total throw enhancements within bends along a single fault segment and along a segmented normal fault system. However, the examples shown in the previous chapters are located in the Central Apennines, Italy, an area of active continental extension; at the time of writing there are no detailed studies of the relationship between the local non-planar fault geometry and throw and throw-rate variations in other geodynamic domains. In addition, little is known on how these relationships evolve during the process of fault growth and linkage. To address these questions, this chapter presents a study of normal faults in the Western Volcanic Zone (WVZ), Iceland. This field area includes faults that are repeatedly re-surfaced by lava flows, even in the Holocene, so that their geometry at the surface is immature because it has to be re-established after each resurfacing event (See Chapter 2, Section 2.5.2 for details on the interplay between lava flows and active faults). Therefore, faults in the WVZ show a variety of examples of incipient and recent fault linkage across relay zones that are to become the site of future mature fault bends. The faults have been mapped,

and along-strike throw profiles have been constructed in order to understand how the throw-rates relate to the local fault geometry along faults at different stages of linkage. The results show that throw-rates increase within linkage zones and propagating fault bends independently from the stage of maturity of the fault bend. The implication of these findings for fault evolution, in particular on the process of fault growth by linkage and coalescence of separate faults, and palaeoseismological results are discussed. The results presented in this chapter demonstrate that existing models showing increased co-seismic and throw-rates within fault bends and sites of fault linkage found in continental extensional settings are valid in a geodynamic context of a mid-oceanic rifts and for zones with incipient fault linkage and immature fault geometries. The findings of this chapter are published in Iezzi et al. (2020) in *Journal of Structural Geology*.

6.2 Introduction

The growth of along-strike fault bends along normal faults has been shown to be dominated by the linkage of originally isolated fault segments (e.g. McLeod et al., 2000; Manfield and Kattenhorn, 2001; Jackson et al., 2002; Walsh et al., 2002; Gawthorpe et al., 2003; Nicol et al., 2005; Rotevatn et al., 2018). Fault growth models show that once en-echelon fault segments are linked, and a fault bend is established to link the faults, the throw-rates along the newly formed fault increase to re-establish the displacement-length scaling following the length increase (e.g. Cowie and Roberts, 2001; See Chapter 2, Figures 2.2 and 2.3).

Moreover, the previous chapters have highlighted the occurrence of throw and throw-rate enhancements within along-strike fault bends that form at sites of fault linkage in

response to local anomalies in strike and dip within the bend, especially where the fault dip value is relatively high and the horizontal strain-rate is maintained (see Chapters 1, 4 and 5; Faure Walker et al., 2009; Wilkinson et al., 2015; Mildon et al., 2016; Iezzi et al., 2018; Iezzi et al., 2019). However, there is a lack of studies describing in detail how the throw-rate varies within the linkage zones during the propagation of the fault bends. To expand knowledge on how faulting develops within along-strike fault bends, it is important to study how the throw and the throw-rate within fault bends evolve during the propagation and establishment of fault bends throughout the process of fault growth by linkage.

The Western Volcanic Zone (WVZ) in Iceland (Figure 6.1) is one of the most studied regions in terms of understanding the mechanisms of fault growth because it is characterised by the continuous propagation of active faults upwards through subsequent lava flows (Gudmundsson, 1987; 1992; 2000; Saemundsson, 1992; Acocella et al., 2000; Bull et al., 2003; Grant and Kattenhorn, 2004; Sinton et al., 2005; Friese, 2008; Sonnette et al., 2010; Villemin and Bergerat, 2013; Trippanera et al., 2015). Different models of growth of the fault bends in this region have been proposed, explaining the development of bends as fault segments growing to connect two principal en-echelon faults (e.g. Acocella et al., 2000), and as a response to local perturbations of the stress field in the region of the bend (Grant and Kattenhorn, 2004). However, none of the previously published models have explored how the throw-rate within the fault bend evolves during the onset and development of bends in zones of fault linkage. Furthermore, although normal faults within the WVZ have been widely studied (e.g. Gudmundsson, 1987; Friese, 2008; Sonnette et al., 2010), none of them have analysed the relationship between

the local fault geometry and the distribution of throw and throw-rates along the strike of the fault.

This chapter studies faults in the Thingvellir rift and the Hengill volcanic complex, located in the Western Volcanic Zone (WVZ) in Iceland (Figure 6.1). Due to ongoing propagation through young lavas occurring at different rates, given by different fault slip rates, these faults preserve a variety of different stages of fault linkage maturity. In fact, longer faults with higher slip rates propagate faster than shorter faults with lower slip rates. Therefore, at the surface faults with higher slip rates would appear more mature than faults with lower slip rates. This framework allow investigation of a spectrum of cases ranging from cases where the principal fault segments are not physically connected at the surface (soft-linkage) to cases where the principal fault segments are connected at the surface with well-established fault bends (hard-linkage). This chapter describes observations of these different geometries and discuss what is implied for how the throw and throw-rates evolve during the development of along-strike fault bends. This chapter then discusses the broader implications of these findings for the process of fault growth by linkage and for how these should guide us with interpretations of palaeoseismological studies. Furthermore, study of the faults in Iceland's WVZ allows us to test whether local non-planar fault geometry exerts a control on the along-strike distribution of throw in the geodynamic context of a plate boundary, the Mid Atlantic Ridge, as has been demonstrated within zones of continental extension (Faure Walker et al., 2009; 2015; Iezzi et al., 2018; Chapters 4 and 5).

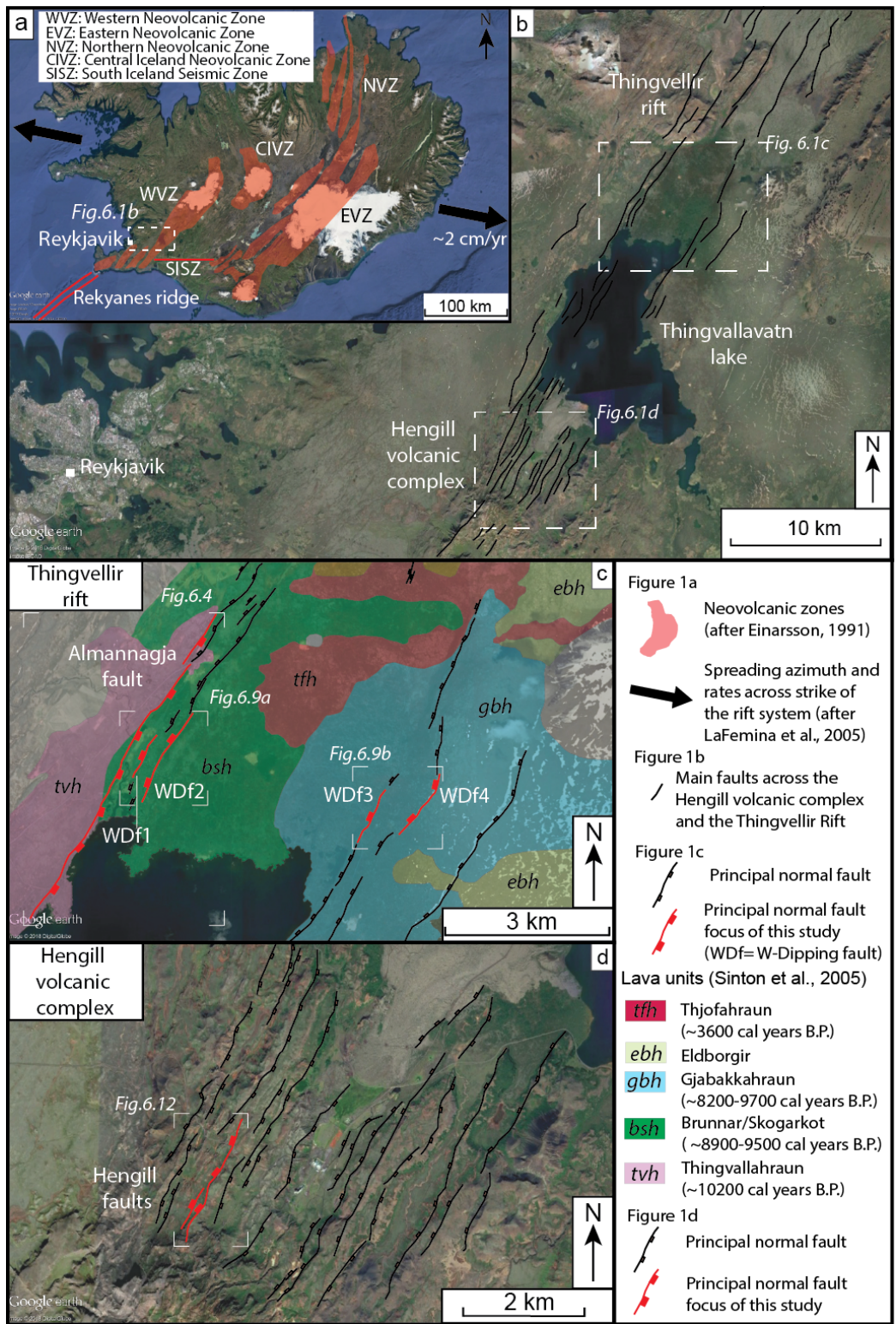


Figure 6.1: Location map of the study areas. a) Regional setting of Iceland. In red are highlighted the neovolcanic zones, centre of the oceanic spreading (modified after Wolfe et al., 1997; Bergerat and Angelier, 2000; Einarsson, 2008). Black arrows indicate the direction of regional extension (after Lafemina et al., 2005). b) Map of the WVZ, with highlighted the Thingvellir rift and the Hengill volcanic complex. c) Map of the Thingvellir rift. In red are the faults subject of this study, in black are other principal faults of the Thingvellir rift (defined with our fieldwork and modified after Gudmundsson, 1987; Saemundsson, 1992; Sinton et al., 2005; Sonnette et al., 2010). Lava units are after Sinton et al., 2005. d) Map of the Hengill volcanic complex. In red are the faults studied within this thesis, in black are other principal faults. From Iezzi et al., 2020.

6.3 Geological background of Thingvellir rift and Hengill volcanic complex

The Thingvellir rift and the Hengill volcanic complex, which are both part of the WVZ, occur north and south of the Thingvallavatn lake, a large catchment produced by extensive subsidence within the rift zone (Figure 6.1b; Saemundsson, 1992; Bull et al., 2003). The Thingvellir rift is a narrow rift system trending about N30°, expressed at the surface by a series of normal faults and extension fractures striking mostly semi-parallel to the trend of the WVZ on both sides of the rift (Figure 6.1c; Gudmundsson, 1987; Grant and Kattenhorn, 2004; Friese, 2008; Sonnette et al., 2010). At Thingvellir, faults propagate through post-glacial Holocene lava flows which have filled the rift valley in the last ~10 ka (Figures 6.1c; Saemundsson, 1992; Sinton et al., 2005). The Hengill Volcanic complex is characterized by a central volcano and a dense set of normal faults striking about N30° and dissecting Pleistocene basaltic lava flows and hyaloclastite deposits, with extensive activity during the Holocene (Figure 6.1d; Friese, 2008). The area is characterized by distributed seismicity, with focal mechanisms of larger events in Hengill displaying both normal and strike-slip faulting (Foulger, 1988a; 1988b; Feigl et al., 2000; Clifton et al., 2002; Li et al., 2019). Two faulting episodes are reported to have produced normal-faulting surface ruptures: the 1789 earthquake, which have ruptured faults in both Hengill and Thingvellir (Saemundsson, 2006), and an earthquake occurred between 1973 and 1977, which have caused a localised displacement of up to 9 cm on the Almannagja fault (Tryggvason, 1990).

6.4 Methods

Detailed field mapping (Figures 6.1 and 6.2) of the Almannagja fault was carried in order to produce structural fault maps and densely-spaced along strike throw and throw-rate data, together with a study of the evolution of the footwall drainage following fault linkage (Figures 6.3, 6.4, 6.5, 6.6 and 6.7). During detailed field mapping, structural fault maps and densely-spaced along-strike throw and throw-rate profiles were also constructed for four W-dipping faults distributed within and on the eastern flank of the Thingvellir rift (thereafter called WDf1, WDf2, WDf3 and WDf4; Figures 6.1c, 6.8, 6.9 and 6.10). Within the Hengill volcanic complex, 3 faults were mapped, and in particular a map of the offsets of a glacial erosion surface preserved during the demise of the glaciation was constructed (Figures 6.1d, 6.11, 6.12, 6.13). In all cases, along-strike profiles were built to show how throw and throw-rates vary approaching bends, compared to values of throw and throw-rates immediately outside bends. It was possible to make such measurements across a variety of fault bends at various stages of maturity.

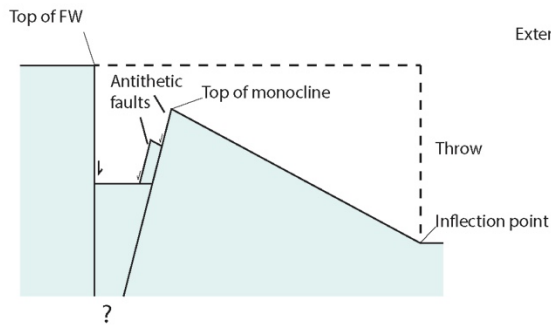
Structural fault maps from Thingvellir (Figures 6.4, 6.5 and 6.9) and Hengill (Figure 6.12) have been produced combining published maps (Gudmundsson, 1987; Saemundsson, 1992; Sinton et al., 2005; Sonnette et al., 2010), Google Earth imagery and original fieldwork led by the current author. Fault scarp profiles were constructed using a *Trupulse 360R*® laser range finder (See Chapter 3 for details on this methodology) (Figure 6.2).

In Thingvellir, most faults and extension fractures present a dilatational component between the footwall and hangingwall (Figures 6.2a, 6.2b, 6.2c, 6.3 and 6.8), so measurements of the vertical component of slip have been used to differentiate between

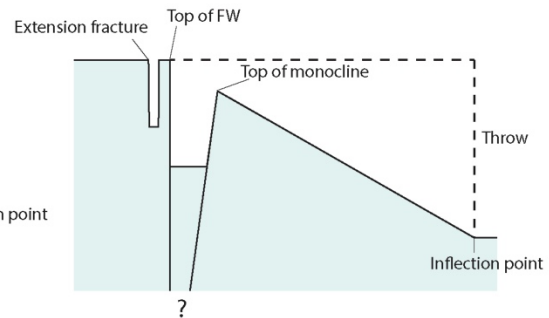
faults and extensional fractures. Faults are defined as fractures with more than 1 m of vertical slip; extension fractures are defined as fractures with a vertical slip less than 1 m. For the Almannagja fault, which shows a prominent monocline in the hangingwall (Figures 6.2a, 6.2b, 6.3a, 6.3b, 6.3c, 6.3e, 6.4 and 6.5), serial fault scarp profiles have been constructed with an along-strike spacing of about 50 m to define the geometry of the monocline (Figure 6.6). Where it was not possible to take measurements across the monocline, measurements of the distance between the observer and (1) the inflection point at the base of the monocline (i.e. the point where the hangingwall starts to bend towards the footwall), (2) the top of the monocline and (3) the top of the footwall were collected (Figures 6.2a, 6.2b, 6.5 and 6.6). The throw is defined as the vertical distance between the inflection point at the base of the monocline and the top of the footwall (Figures 6.2a, 6.2b and 6.6). Offsets across the southern part of the fault could not be measured because the inflection of the monocline is below the lake level (Figures 6.3e, 6.4 and 6.5). For the Almannagja fault, the evolution of the drainage system during fault linkage has also been investigated (Figure 6.7).

Almannagja fault

a) Section of the Almannagja fault with multiple antithetic faults

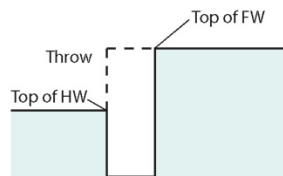


b) Extension fractures at tips of the principal fault segments of the Almannagja fault



W-dipping and Hengill faults

c) W-Dipping faults 1, 2, 3



d) W-Dipping fault 4 and Hengill faults

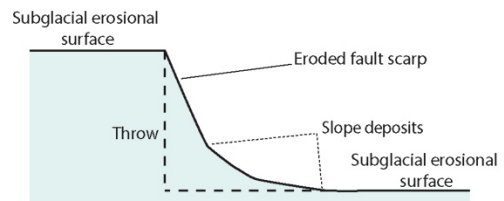


Figure 6.2: Cartoons of the field measurements. a) Cartoon of the Almannagja fault. It shows the presence of an inner graben and a prominent monocline connecting footwall and hangingwall. The throw has been measured as the vertical distance between the inflection point and the top of the footwall. b) Cartoon of the extension fractures located within the footwall of the fault in the linkage zones between the principal fault segments of the Almannagja fault. c) Cartoon of the field measurements on Wdf1, Wdf2, Wdf3. It shows that these faults are characterized by a dilatational component between hangingwall and footwall. The throw has been measured as the vertical distance between the hangingwall and the footwall. d) Cartoon of the field measurements on Wdf4 and Hengill faults. The faults present a prominent fault scarp with slope deposits on it. The throw has been measured reconstructing the geometry of the erosional surfaces on the hangingwall and footwall. From Iezzi et al., 2020.

For the Wdf1 and Wdf2, the throw was defined as the vertical offset between the top of the hangingwall and the top of the footwall (Figures 6.2c, 6.8a, 6.8b, 6.8c, 6.8d, 6.10a and 6.10b). For the Wdf3, which is part of the Hrafnagja fault (*sensu* Gudmunsson, 1987), given the difficulty of the field survey along the fault due to dense vegetation, the throw profile has been derived by building along-strike topographic profiles of the top of the hangingwall and of the top of the footwall from one observation point and then measuring the relative vertical distance between the two profiles (Figures 6.2c, 6.8e, 6.8f and 6.10c). The Wdf4, which is part of the Gildruholtsgja fault (*sensu* Gudmundsson,

1987), does not show a dilatational component between the footwall and hangingwall, and the throw is measured with fault scarp profiles using the vertical offset of the footwall and the hangingwall surfaces across the fault scarp (Figures 6.2d, 6.8g, 6.8h and 6.10d). For the Thingvellir rift, throw-rates are calculated using time constraints from ages of the lava flows dislocated by the faults (Figures 6.1b, 6.4 and 6.9; from Sinton et al., 2005). The age constraints of the lava flows are derived combining ^{14}C -dating, tephrochronology and chemical analyses from major and trace elements (see Figures 6.1, 6.4 and 6.9; Sinton et al., 2005).

For Hengill, a set of W-dipping normal faults has been mapped in detail, together with a dissected subglacial erosional surface, produced by the erosive action of glaciers on the underlying landforms (Figures 6.11 and 6.12). Serial fault scarp profiles have been constructed across the normal faults, and the throw in each profile has been constrained measuring the offset between subglacial erosional surfaces in the hangingwall and footwall (Figures 6.2d, 6.11a, 6.11b, 6.11e, 6.12 and 6.13). For Hengill, the ^3He cosmogenic exposure ages of these erosional surfaces were used as a constraint to calculate the throw-rate of the faults. This is possible because it is assumed that the erosive process of a moving glacier would not have allowed preservation of fault scarps, and therefore these started to be preserved only once the deglaciation occurred, causing the exposure of the eroded surfaces. Measurements of the cosmogenic ^3He concentrations in olivine phenocrysts, collected from different erupted basaltic lava caps of table mountains located within the WVZ, show that the exposure age of these lava flows occurred when the ice melted during the deglaciation between 7.2 ka and 13 ka (from Licciardi et al., 2007). Hence, the exposure age of the subglacial erosional surfaces in Hengill can be inferred to be comprised between 7.2 ka and 13 ka (note this is comparable

to the 15 ± 3 ka time range studied in the central Apennines). This time range is used to constrain the fault throw-rates for Hengill.

Along-strike throw and throw-rate profiles for each fault have been constructed projecting the throw measurements along the principal strike of the fault, obtained using strike lines (Figures 6.6, 6.10 and 6.13). The along-strike profiles are compared with the fault traces to study if the local fault geometry affects the distribution of throw and throw-rates along the fault.

6.5 Results

6.5.1 Thingvellir rift

6.5.1.1 Almannagja fault

The so-called Almannagja fault is a complex fault system about 7.1 km long with a dip towards the SE and strike of $N033^\circ$ (Figures 6.3, 6.4 and 6.5). It is formed by the linkage of smaller fault segments, up to 1 km long, arranged with end-on and en-echelon distributions (Figures 6.3, 6.4 and 6.5). The fault system dissects Holocene lava flows dated to $\sim 10,200$ and $\sim 9,000$ years BP (Figures 6.3 and 6.4; Sinton et al., 2005). The Almannagja fault is characterized by a vertical footwall scarp and a broad monocline which connects the footwall with the rift valley (Figures 6.2a, 6.2b, 6.3a, 6.3b, 6.3c, 6.3e, 6.4 and 6.5). An inner graben-like structure developed between the footwall and the monocline with minor antithetic faults that delimit the SE flank of the graben (Figures 6.2a, 6.2b, 6.3a, 6.3d, 6.3e, 6.4 and 6.5). In some places along the fault, the monocline is dissected by multiple antithetic faults (Figures 6.2a, 6.3a, 6.3d, 6.4 and 6.5). The fault

segments distributed with en-echelon arrangements are, in most cases, linked by extension fractures propagating through the footwall of the fault (Figures 6.2b, 6.3a, 6.3d, 6.4 and 6.5). Those fractures are interpreted as the palaeoterminations of the principal fault segments prior to fault linkage (palaeo-tips, *sensu* McLeod et al., 2002).

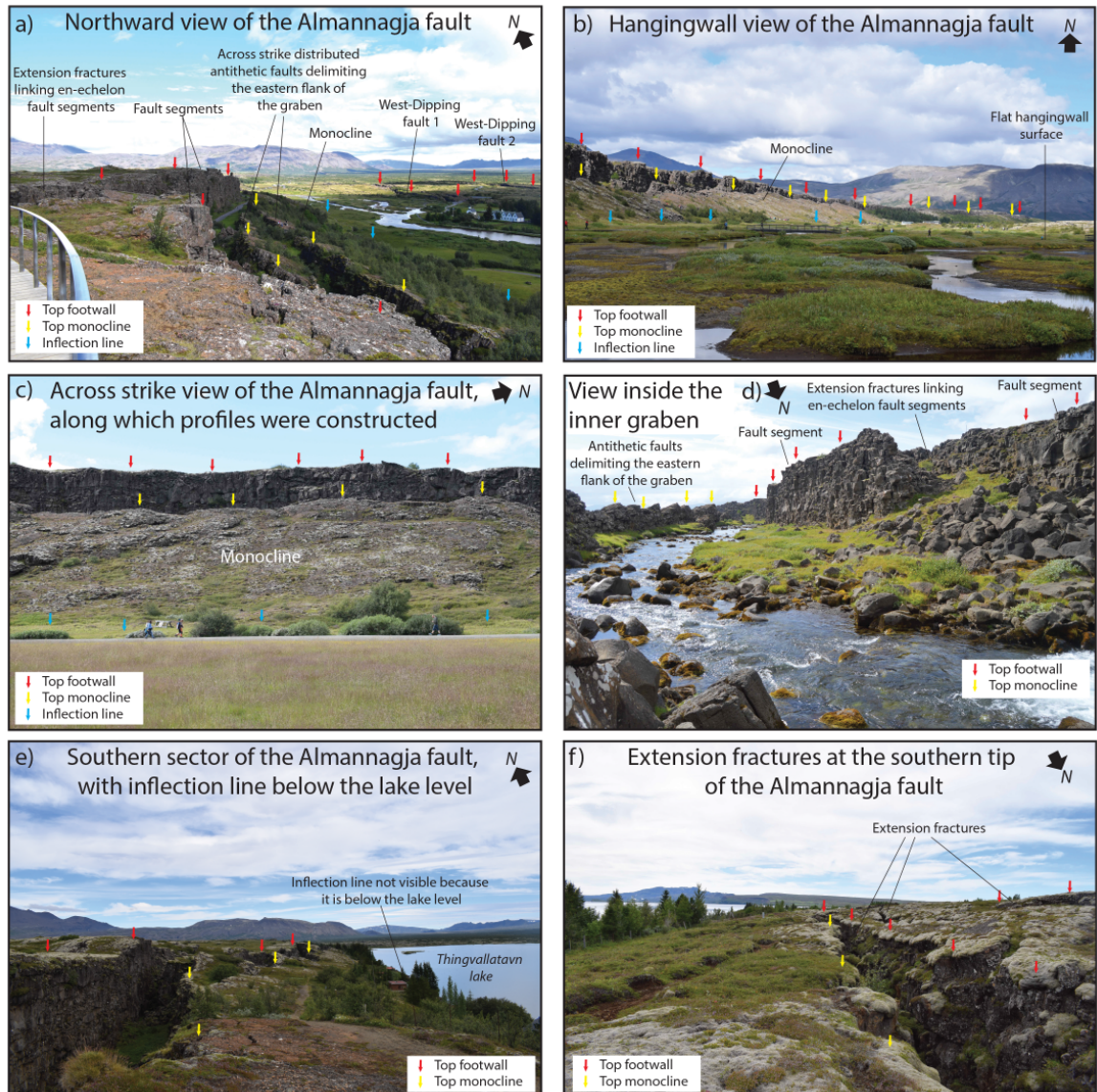


Figure 6.3: Field photos of the Almannagja fault. a) Northward view of the fault. It shows the presence of different fault segments, linked by extension fractures in the footwall; the presence of an inner graben-like structure, delimited westward by sets of antithetic faults; a prominent monocline which connects the footwall to the hangingwall. b) Hangingwall view of the Almannagja fault. It shows how the fault and the monocline are continuous along the fault strike. c) Across-strike view of the Almannagja fault showing the direction across which the profiles were constructed. d) View inside the inner graben. It highlights the presence of extension fractures linking en-echelon principal segments and the presence of antithetic faults. e) View of the southern sector of the Almannagja fault. It shows that the inflection line is below the lake level, and therefore it was not possible to collect measurements in this sector of the fault. f) View of the southern tip of the Almannagja fault. It shows how the fault is characterized by extension fractures, across which the vertical offset is less than 1 m. From Iezzi et al., 2020.

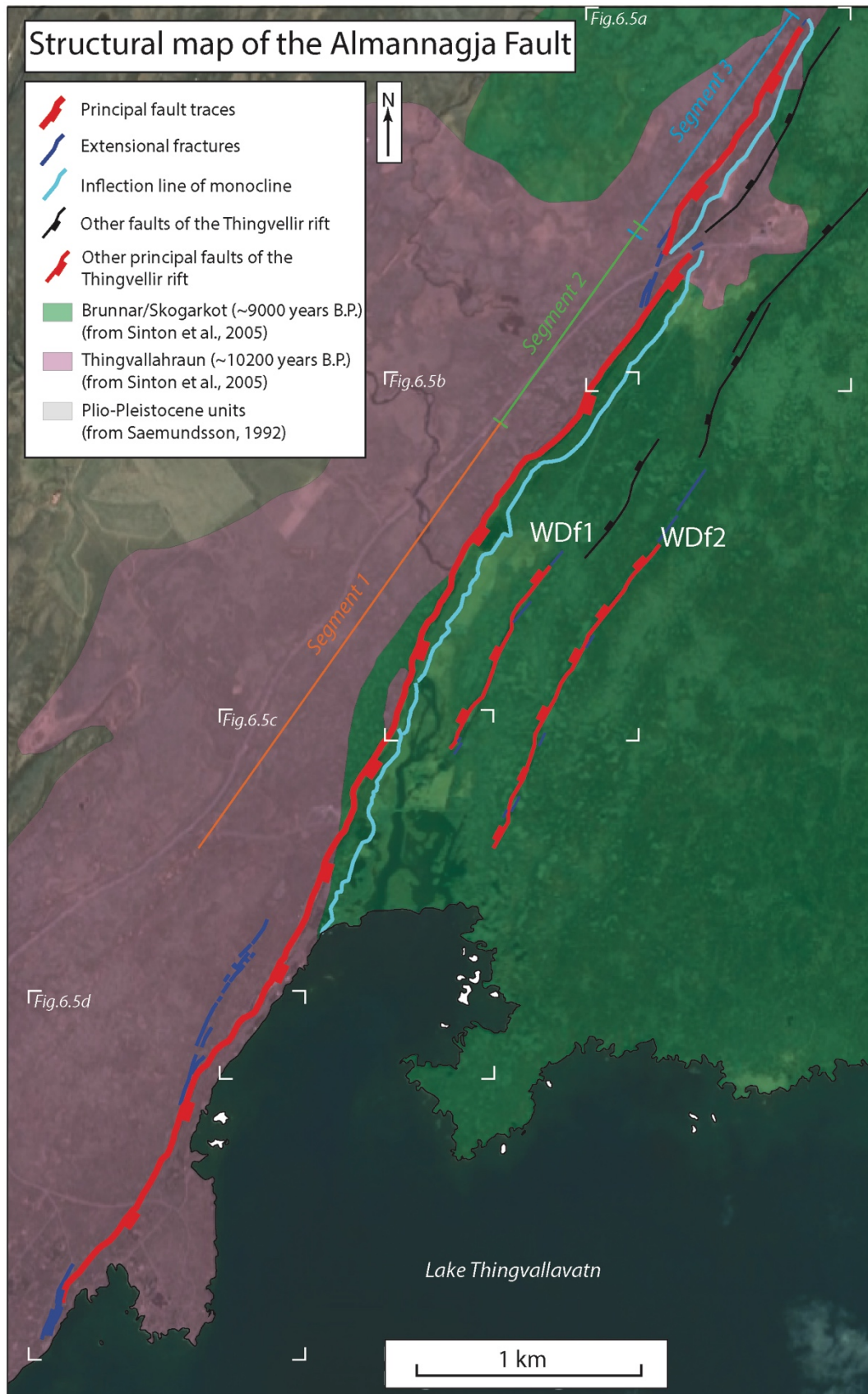


Figure 6.4: Structural map of the Almannagja fault. In red is the principal trace of the Almannagja fault. In blue are extension fractures, in pale blue is the inflection line of the monocline. The location of the Wdf1 and Wdf2 (thinner red and blue lines) are shown. In black are other faults of the Thingvellir rift. Geological units are from Saemundsson, 1992, and Sinton et al., 2005. From Iezzi et al., 2020.

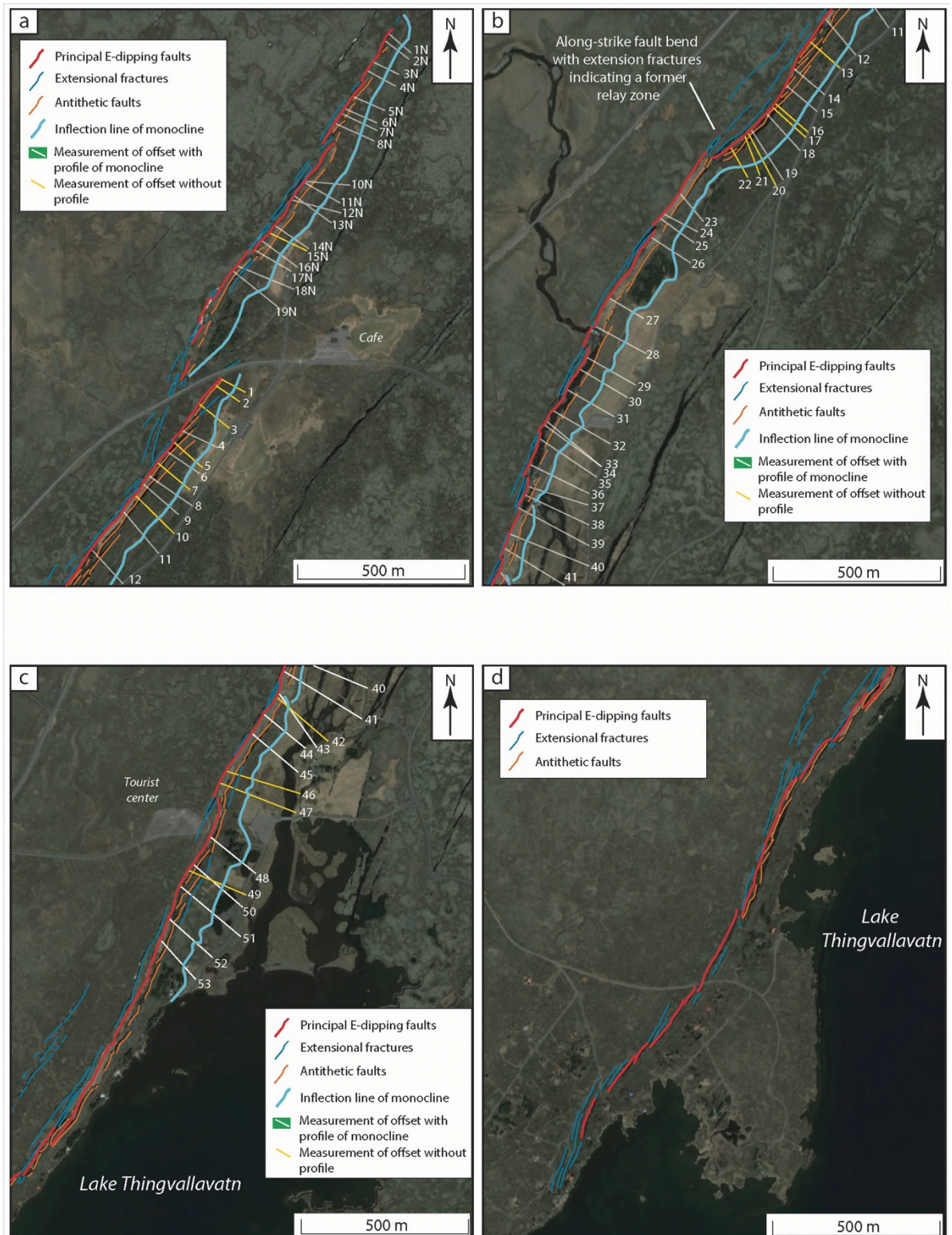


Figure 6.5: Detailed structural maps of the Almannagja fault. This figure shows in detail the geometry and the structure of the Almannagja fault. Locations of a), b), c) and d) are shown in Figure 6.4. In red are the principal fault segments, in blue are the extension fractures, in orange are the antithetic faults, and in pale blue is the inflection line of the monocline. In white are the offset measurements with a complete profile of the monocline. In yellow are offset measurements without a profile of the monocline. From Iezzi et al., 2020.

Field observations suggest that the shape of the monocline reflects the segmentation of the Almannagja fault. Where the fault segments of the Almannagja fault are longer and more continuous, the inflection line of the monocline is continuous and consistent along the strike of the fault (Figures 6.4, 6.5 and 6.6). Where the single faults are shorter and less continuous, the inflection line becomes less regular and moves closer to the fault trace (Figures 6.4, 6.5 and 6.6). The tips of the Almannagja fault are characterized by the base of the monocline inflection line approaching or joining the fault, a decrease of the height of the vertical fault scarp and of the monocline and by a predominance of extension fractures (Figures 6.3f, 6.4 and 6.5).

The along-strike throw profile of the Almannagja fault has a multi-humped shape, with an overall increase of throw towards the south (Figure 6.6). The maximum measured throw is about 39 m, located in what appears to be the central part of the entire Almannagja fault. The comparison between the multi-humped throw profile and the fault geometry allows one to identify three principal fault segments of the overall Almannagja fault (Figure 6.6). A well-defined along-strike fault bend links two of the main segments of the Almannagja fault, herein called Segment 1 and Segment 2, accommodating an overall right step of the fault trace in a position where a palaeo-tip indicates the presence of a former relay zone (Figures 6.4, 6.5b and 6.6). Within the fault bend the throw anomalously increases, causing the throw profile of Segment 2 to have a double peak of about 31 m (Figure 6.6). The Segment 2 and Segment 3 are soft-linked in a left en-echelon arrangement (Figure 6.4, 6.5 and 6.6). Because of the vegetation, it was not possible to obtain measurements across the southern part of Segment 3, and therefore it is not clear how the throw varies in that location. Other smaller bends exist along the fault, connecting single small fault segments, but the resolution of the throw measurements (every ~50 m

along strike) does not allow study of variations of throw for bends shorter than this distance. The width of the monocline confirms the principal segmentation of the Almannagja fault. The monocline tips out in the relay zone between Segment 2 and Segment 3, in agreement with the soft-linkage between the two fault segments (Figures 6.4, 6.5 and 6.6). At the same time, the monocline does not tip out in correspondence of the fault bend linking Segment 1 and Segment 2, but does narrow, reflecting the hard-linkage between the two fault segments (Figures 6.4, 6.5 and 6.6).

In summary, the Almannagja fault consists of a normal fault that grew via linkage of several single faults. The comparison between the fault geometry and the multi-humped throw profile allows subdivision of the fault into three principal fault segments. A prominent along-strike fault bend links two of these principal fault segments, within which the throw and the throw-rates anomalously increase if compared with the values of throw and throw-rate outside the fault bend.

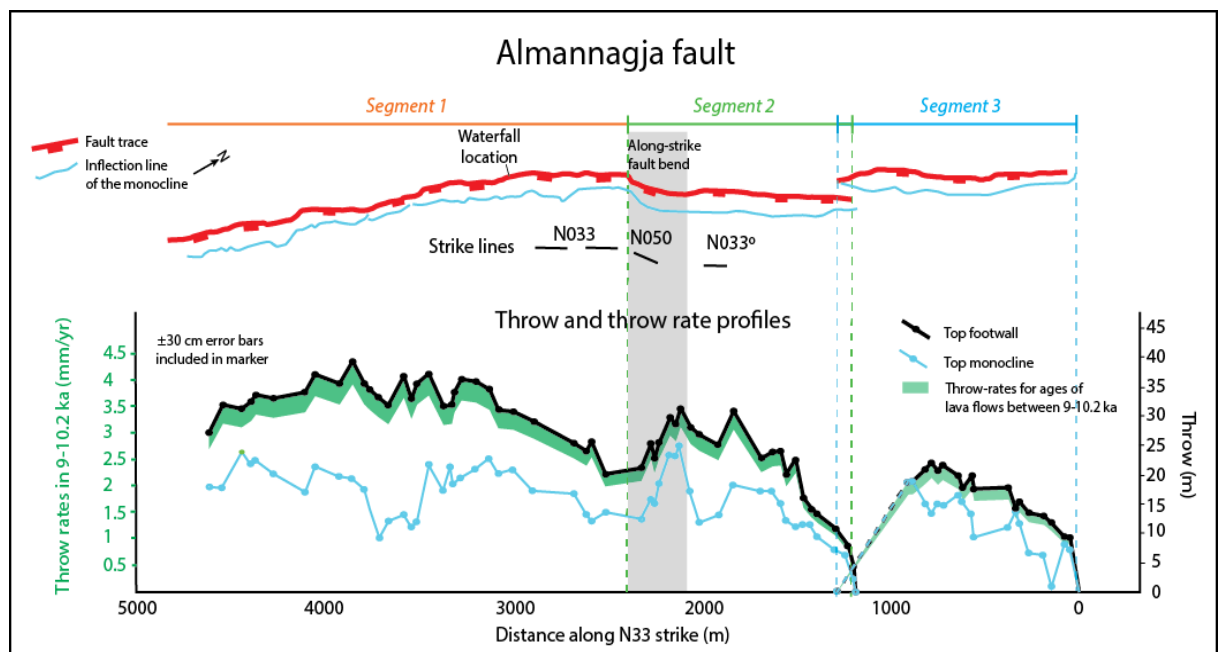


Figure 6.6: Along-strike throw profile of the Almannagja fault. Measurements of the top of the footwall and of the top of the monocline have been normalized for the inflection line. Therefore, measurements of the top of the footwall represent the throw of the fault. In green is the range of the throw-rates of the fault, calculated for the time constraint of 9 and 10.2 ka (from the age of dissected lava units, Sinton et al., 2005). The suggested principal segmentation of the Almannagja fault is shown. Note that the throw and throw-rates increase within an along-strike fault bend. From Iezzi et al., 2020.

6.5.1.1.1 Influence of the fault linkage on the drainage system.

The drainage system in the footwall of the Almannagja fault has been studied to observe how the fault evolution has influenced the river flow through time (Figure 6.7). This provides important insights to understand the timings (1) of the fault linkage and (2) of the propagation of fault bends at the surface. The footwall of the fault is marked by the presence of a river flowing south-eastwards and towards the rift valley (Figure 6.7a and 6.7b), crossing the Almannagja fault at a spectacular waterfall (Figures 6.7c and 6.7d). The waterfall lies in the position of a former en-echelon step between two faults, now marked by a fault bend and preserved palaeo-tip (Fig. 6.7b and 6.7c). Both the river bed and the waterfall are located to the north of the maximum peak in throw of the Almannagja fault (see location of the waterfall in the throw profile in Fig. 6.6). As shown in Fig. 6.7b, an abandoned river bed is located to the southwest of the present river.

The combination of these observations suggest that the fault linkage has influenced the drainage in the footwall of the Almannagja fault, causing a northward migration of the river bed. The linkage of the Almannagja fault caused an increase of the throw-rates along the entire fault, with faster throw-rates located within the central part of the fault (e.g. Cowie and Roberts, 2001). This is proposed because the initial river course flowed through the en-echelon step, with recent linkage to form a bend occurring rapidly so that the waterfall formed, and the river has not had time to produce an incised slot gorge due to headward erosion (*sensu* Whittaker et al., 2007). Therefore, an increase of the throw-rates during linkage allowed footwall uplift to outpace headward erosion and incision by the river, with off-fault footwall uplift diverting the course of the river to NE away from the growing uplift at the fault centre, SW of the river. In summary, the northward

migration of the river bed can be interpreted as a response of the drainage system to the increased uplift in the centre of the fault following fault linkage.

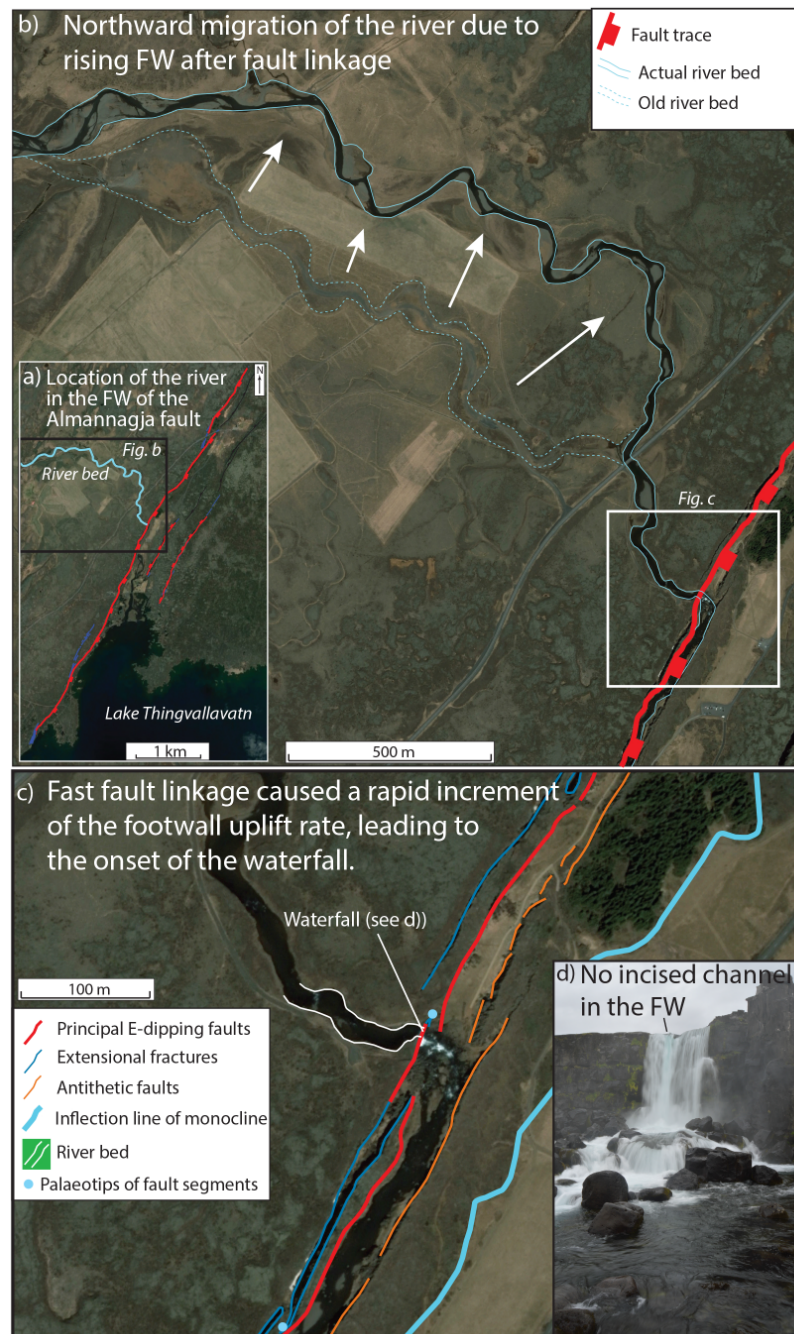


Figure 6.7: Study of the drainage in the footwall of the Almannagja fault. a) Location map of the river bed in the footwall of the Almannagja fault. b) Northward migration of the river bed in relationship to the increased uplift following the fault linkage. c) Blockage of the river and production of the waterfall following fast footwall uplift and fault linkage. d) The photo shows that the waterfall does not present an incised channel in the footwall, which reflects a recent formation of the waterfall. Overall this figure shows that the fault linkage processes are influencing the drainage across the fault. From Iezzi et al., 2020.

6.5.1.2 *W-dipping faults*

Several W-dipping faults are accommodating the regional extension across the Thingvellir rift. This work focused the attention on two faults located in the immediate hangingwall of the Almannagja fault (Wdf1 and Wdf2), and on two faults bounding the eastern flank of the rift valley (Wdf3 and Wdf4; Figures 6.1c, 6.8, 6.9 and 6.10).

The Wdf1 and Wdf2 are both formed by mostly subparallel small fault segments with a dilatational component, organized in en-echelon and end-on arrangements, dissecting lava flows dated to ~9000 years BP (Figures 6.8a, 6.8b, 6.8c, 6.8d and 6.9a; Sinton et al., 2005). Extensional fractures accommodate the deformation within the relay zones of the en-echelon distributed segments (Figures 6.8a, 6.9a, 6.10a and 6.10b). Both the along-strike throw profiles are multi-humped, reflecting an immature stage of the fault growth (Figures 6.10a and 6.10b). However, both faults display maxima in throw and throw-rates across relay zones and incipient fault bends linking fault segments (Figures 6.10a and 6.10b). Thus, the structures are at an early stage of fault linkage, during which the throw has started to increase within the newly formed linkage zone (Figure 6.10a and 6.10b). Again, other local maxima might exist across smaller relay zones and incipient bends, but it is not possible to study these because of the resolution of the field measurements.

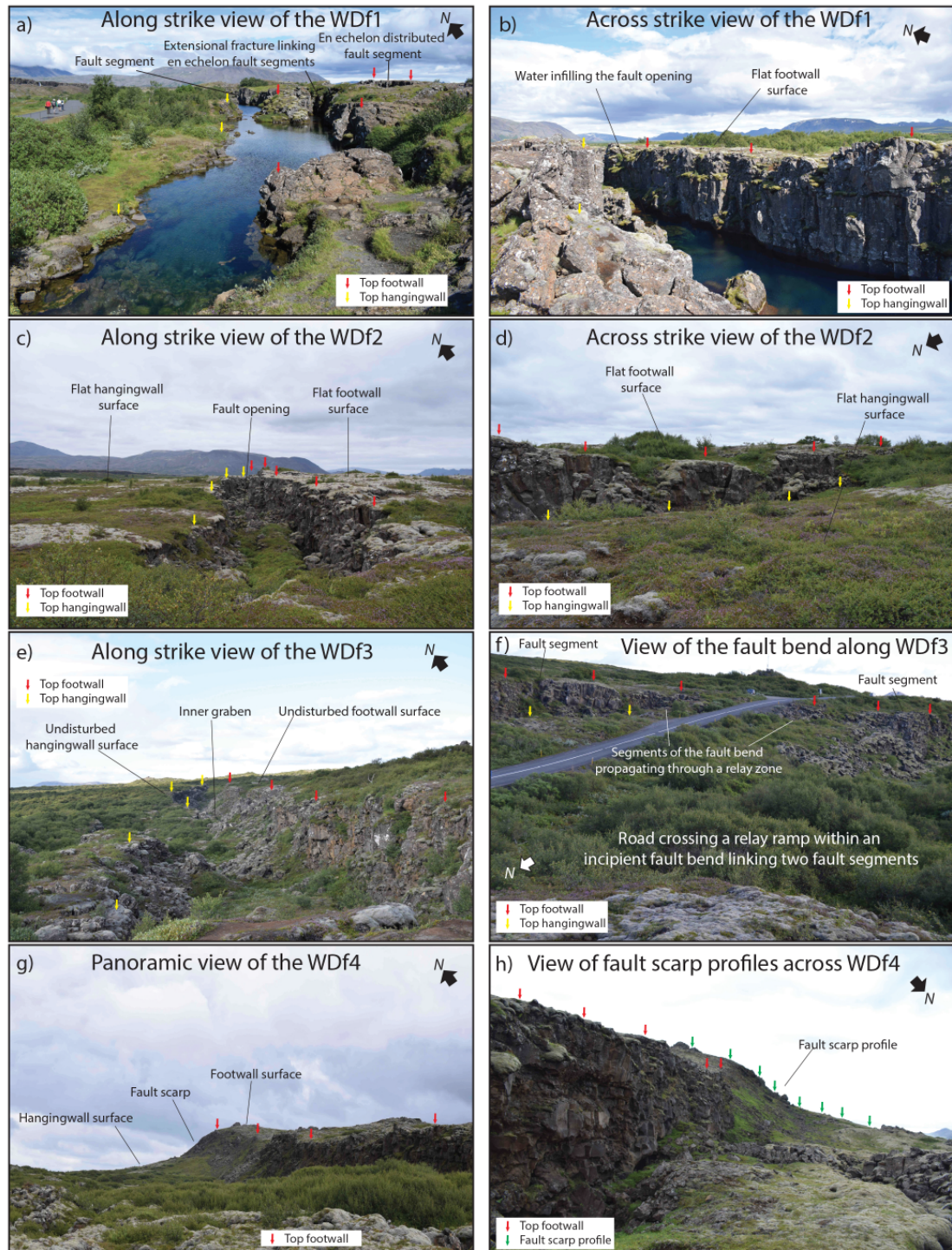


Figure 6.8: Field photos of the W-Dipping faults in the Thingvellir rift. a) Along strike view of the Wdf1. It highlights the presence of multiple fault segments and of the extensional fractures linking these en-echelon faults. b) Across strike view of the Wdf1. It highlights the dilatational component of the fault and the presence of water infilling the inner graben. c) Along strike view of the Wdf2 showing the flat hangingwall and footwall surfaces and the dilatational component of the fault. d) Across strike view of the Wdf2 highlighting the vertical offset between the hangingwall and the footwall of the fault. e) Along strike view of the Wdf3. It shows the undisturbed hangingwall and footwall surfaces and the dilatational component of the fault. f) View of the fault bend along Wdf3. An incipient fault bend is propagating through a relay ramp connecting two principal fault segments. A road is located across the relay ramp. g) Panoramic view of the Wdf4 showing the continuity of the prominent fault scarp. h) View of the fault scarp profiles across Wdf4. Green arrows mark a fault scarp profile collected across the fault. From Iezzi et al., 2020.

The fault traces of Wdf3 and Wdf4 are more continuous than Wdf1 and Wdf2, and both present along-strike fault bends in their traces (Figures 6.8e, 6.8f, 6.8g, 6.8h, 6.9b). The two faults dissect lava flows dated to ~8200-9700 years BP (Figures 6.1c and 6.9b; Sinton et al., 2005). The Wdf3 is formed by fault segments with a dilatational component, with two small antithetic faults accommodating the deformation in the hangingwall (Figures 6.9b and 6.10c). In the southern part of the fault trace an incipient along-strike fault bend is propagating through a relay zone connecting two en-echelon fault segments (Figures 6.8f, 6.9b and 6.10c). The throw profile shows an increase of the throw within the fault bend compared with the values of throw immediately outside the bend (Figure 6.10c). The Wdf4 has a more continuous fault trace, characterized by a classic fault scarp without an obvious dilatational component (Figures 6.8g, 6.8h, 6.9b and 6.10d). The fault trace presents a mature along-strike fault bend, within which the throw and throw-rates profiles have relative maxima, when compared to values of throw and throw-rates immediately outside the bend (Figure 6.9b and 6.10d).

In summary, normal W-dipping faults distributed within the Thingvellir rift are characterized by different stages of the process of fault growth and linkage, which is reflected in different stages of maturity of relay zones and fault bends. Independently to the stage of maturity of the fault bend, all the studied faults present relative throw and throw-rate enhancements within fault bends.

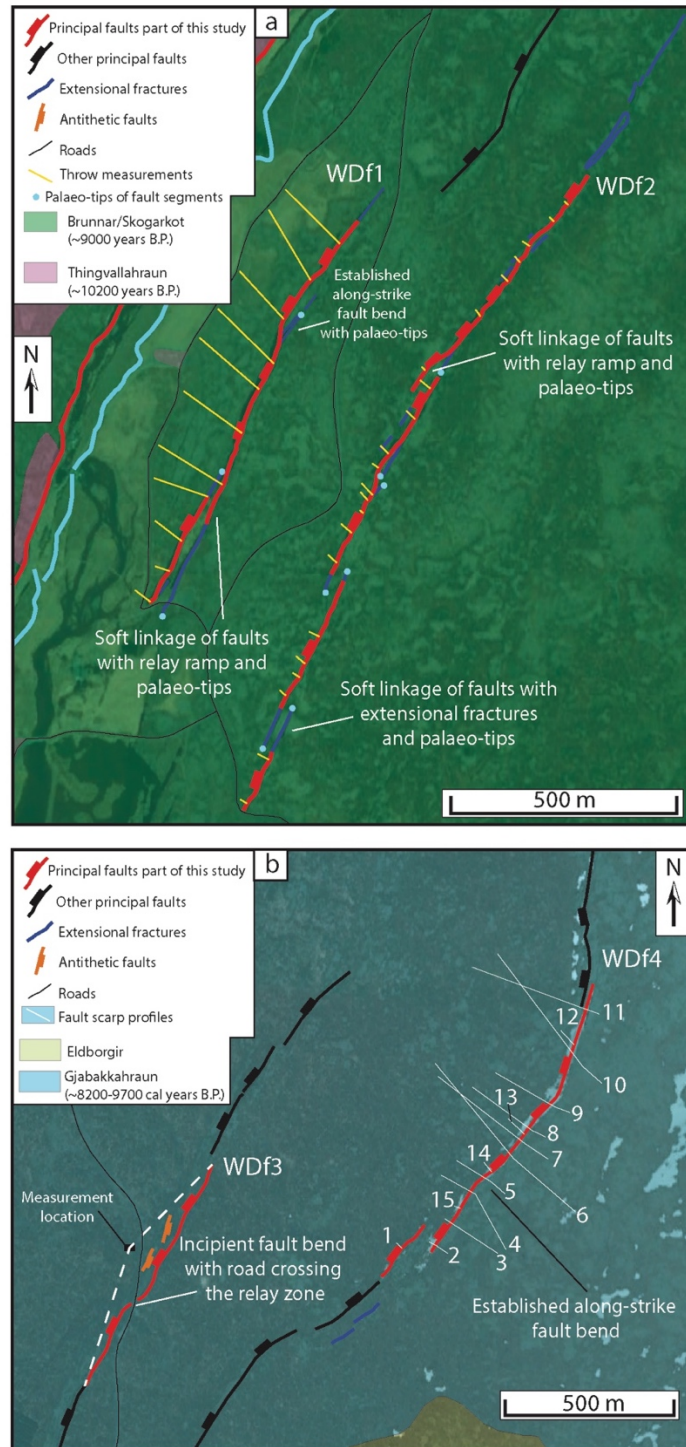


Figure 6.9: Structural maps of the W-Dipping faults. a) The structural fault maps of the Wdf1 and Wdf2, located immediately in front of the Almannagja fault. In red are the principal fault traces, in blue are the extension fractures, in black are other fault traces. In yellow are the location of the measurements of the throw. b) Structural fault maps of the Wdf3 and Wdf4, located on the eastern flank of the Thingvellir rift. In red are the principal fault segments mapped, in blue are the extension fractures, in orange are antithetic faults, in black are other principal faults, not mapped in detail in this study. For Wdf3, the dashed lines mark the sector of the fault along which field measurements have been collected from the measurement location (see text for details). For Wdf4, fault scarp profiles used to measure the throw are shown in white. Geological units are from Sinton et al., 2005. From Iezzi et al., 2020.

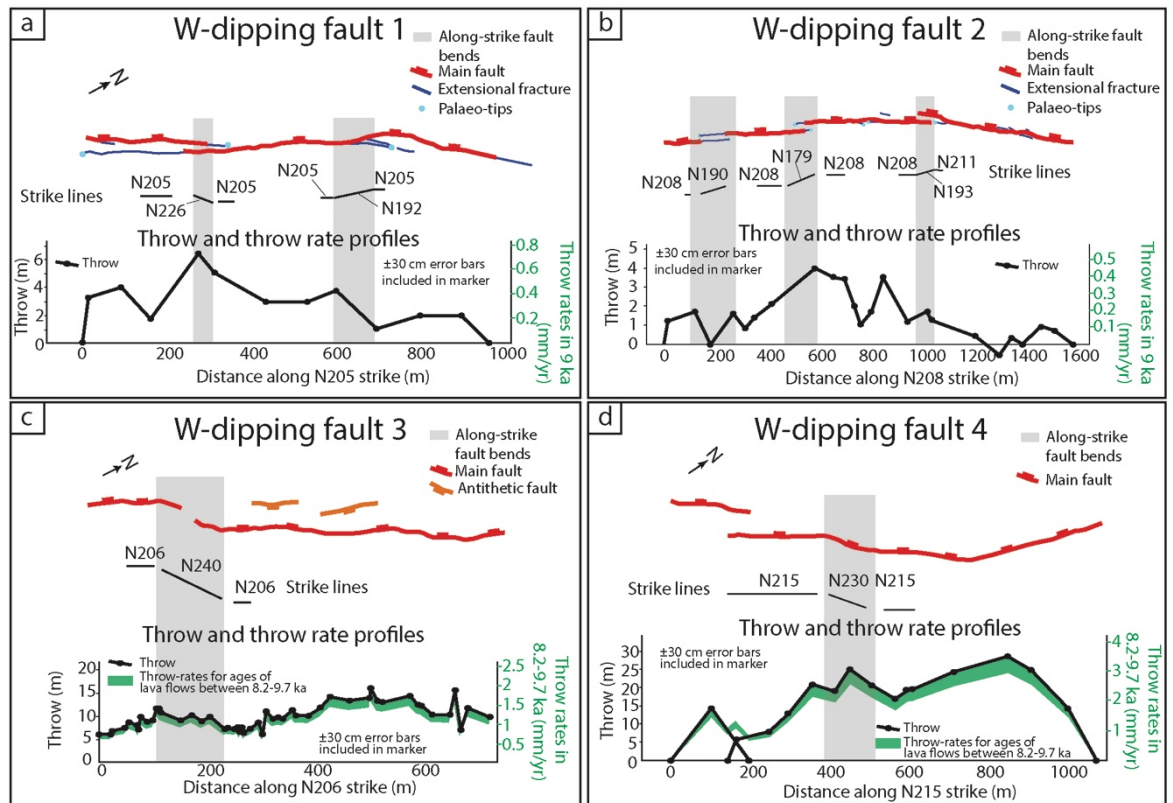


Figure 6.10: Along-strike throw profiles of the W-Dipping faults. In black are the measurements of throw. In green are the range of the throw-rate values, constrained using the age of the lava flows which the faults are propagating through (see Figure 6.9). For the Wdf1 and Wdf2, the throw-rate profiles coincide with the throw profile because of the single value for the age of the lava flows. From Iezzi et al., 2020.

6.5.2 Hengill volcanic complex

Faults in the Hengill volcanic complex appear with prominent fault scarps, often with slope deposits at the base of the scarp, propagating through hyaloclastites and basaltic lava flows (Figures 6.2d, 6.11a, 6.11b, 6.11d, 6.11e and 6.12). In two locations, outcrops of striated fault planes show dip-slip kinematics (Figures 6.11d and 6.12). Subglacial flat erosional surfaces, the products of the erosional activity of the moving glacier on the volcanic deposits, are located on both the hangingwall and the footwall of the faults (Figures 6.11a, 6.11b, 6.11c, 6.11e and 6.12). The glacial origin of these surfaces is confirmed by the presence of erratic boulders on top of them (Figure 6.11c).

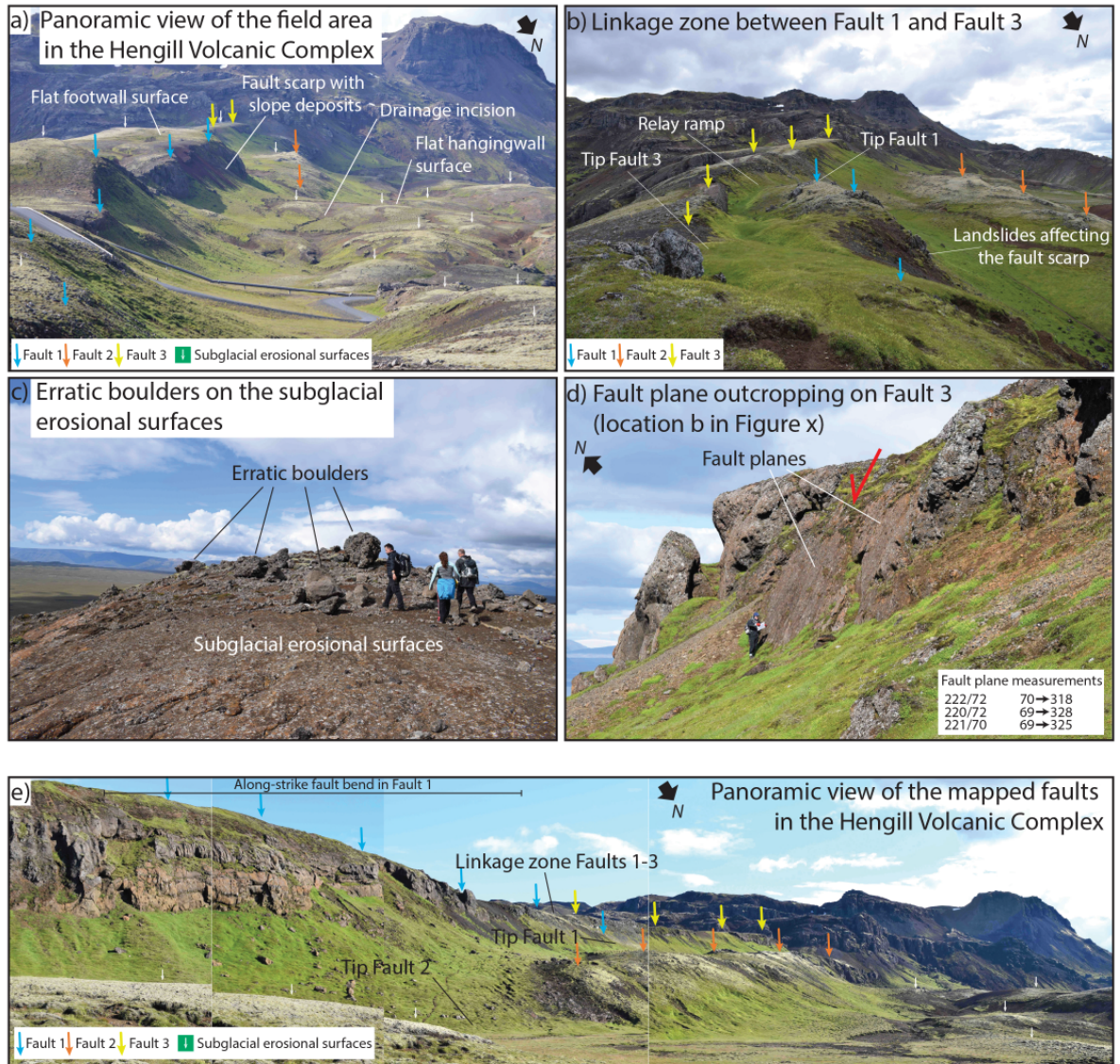


Figure 6.11: Field photos of the Hengill volcanic complex. a) Panoramic view of the study area. The three principal fault segments identified in the area are marked with the different coloured arrows. The white arrows mark the subglacial erosional surfaces used to constrain the throw across the faults. b) Linkage zone between Fault 1 and Fault 3, with a relay ramp located between the two. It is also evidenced the presence of a landslide affecting the fault scarp. Measurements have not been collected in the presence of landslides. c) Erratic boulders on the subglacial erosional surfaces, confirming the glacial origin of the surfaces. d) Outcrop of a fault plane along Fault 3. Field measurements show dip slip kinematics for the fault. e) Panoramic view from the hangingwall of the studied faults. The coloured arrows show the principal faults, with the subglacial erosional surfaces shown in white. The along-strike fault bend in Fault 1 is shown. From Iezzi et al., 2020.

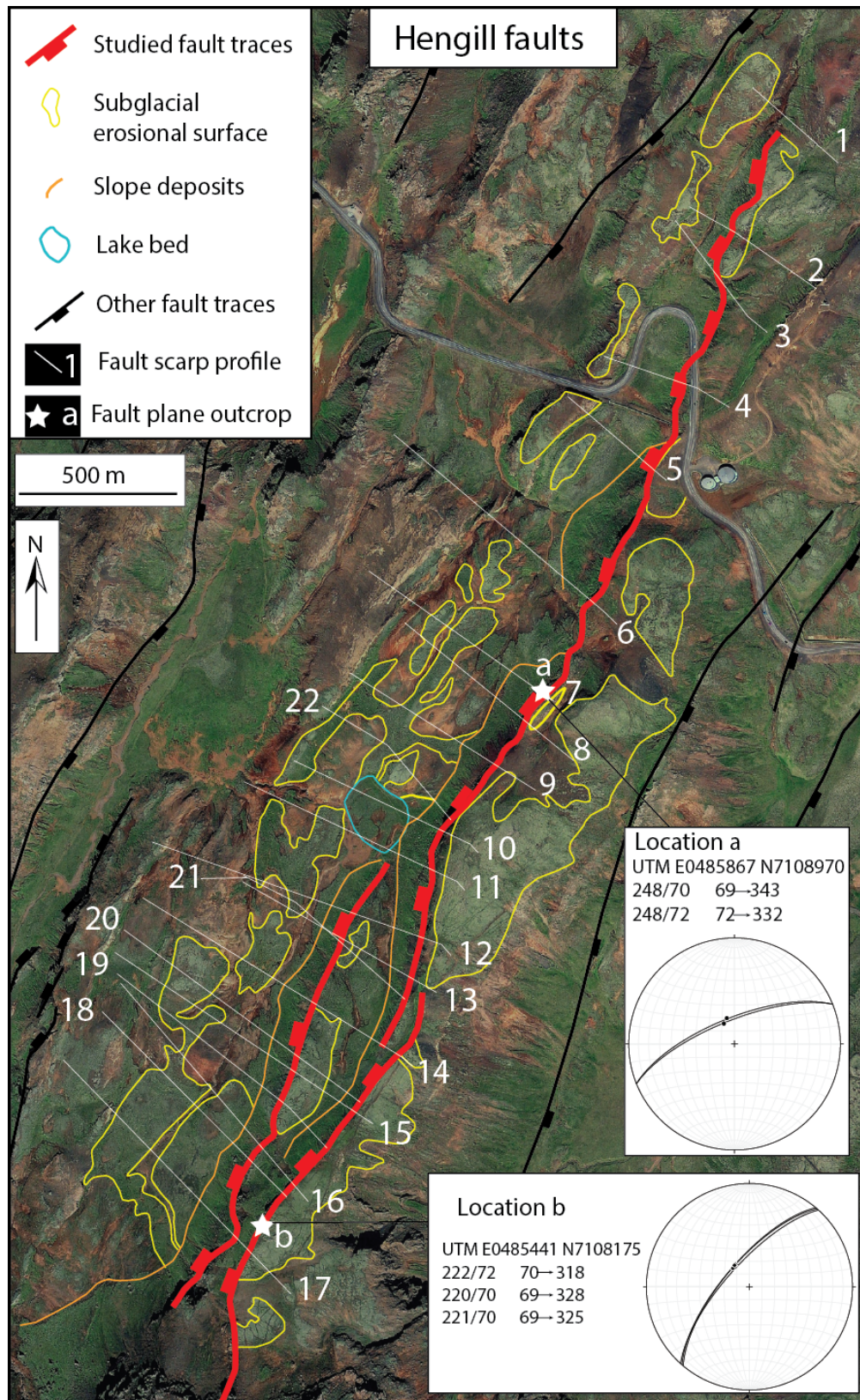


Figure 6.12: Structural fault map of the faults studied in the Hengill volcanic complex. In red are the principal faults studied, in black are other principal faults. Yellow indicates the subglacial erosional surfaces, orange indicates slope deposits on the fault scarps, blue indicates a lake bed in the hangingwall of the fault. White lines show the traces of the fault scarp profiles. White stars mark the locations of outcrops of the fault plane. From Iezzi et al., 2020.

The comparison between the along-strike throw profiles and the fault traces identifies three principal fault segments (Figure 6.13). Fault 1 has a skewed along-strike throw profile, with maxima in throw values located within a fault bend in the strike of the fault (Figure 6.13). Fault 2 has a fault bend towards its northern mapped extent, across which the throw profile of Fault 2 achieves a relative maximum (Figure 6.13). Overall, these two fault bends define a broad fault bend for the mapped set of faults (Figure 6.13). The cumulative throw and throw-rate profiles have maxima located within the broad fault bend (Figure 6.13). Moreover, it is interesting to notice that a lake bed is located in the hangingwall of the broad fault bend, in correspondence of the maximum measured throw and between the two fault bend segments identified on Fault 1 and Fault 2 (Figure 6.13). This suggests that the fault bend has influenced the drainage system in the hangingwall of the fault, causing a maximum subsidence in front of the bend, where the maximum offset is accumulated. Hence, these results suggest that the local fault geometry can affect the spatial distribution of throw and throw-rates along normal faults in this example.

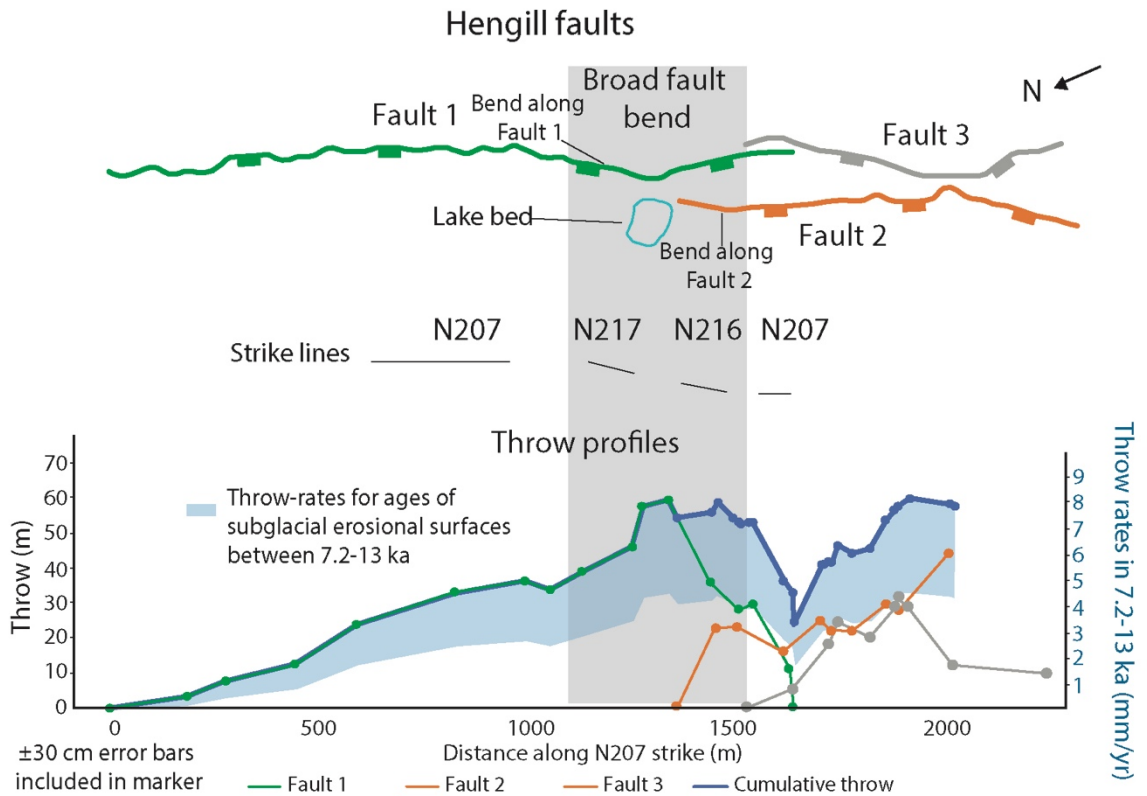


Figure 6.13: Along-strike throw profiles for the faults in the Hengill volcanic complex. It shows the presence of along-strike fault bends along Fault 1 and Fault 3, across which the throw increases. The shaded blue area in the profile is the range of throw-rates for the faults, constrained with the age of deglaciation and exposure of the subglacial erosional surfaces (from Licciardi et al., 2007). The presence of a lake bed in the hangingwall of the fault is of note, located in front of the fault bend, in the location where the maximum throw has been measured. This shows that the fault bend has influenced the drainage system in the hangingwall of the fault. From Iezzi et al., 2020.

Overall, the study of the faults in the Thingvellir and Hengill regions suggests that faults within the Western Volcanic Zone in Iceland are characterized by different stages of fault growth, and this is reflected in different stages of maturity of the linkage zones and of the along-strike fault bends. The comparison between the local fault geometry and the spatial distribution of throw and throw-rates shows that, independently to the stage of maturity of the fault bends, the throw and throw-rates anomalously increase within the bends. These findings imply that the relationship between the non-planar fault geometry and the conservation of the strain-rate across the bend described by Faure Walker et al. (2009;

2015), Iezzi et al. (2018; 2019) and Chapters 4 and 5, also applies in the context of a mid-oceanic ridge.

6.6 Discussion

Normal faults within the Western Volcanic Zone in Iceland are characterized by different stages of fault growth by linkage and coalescence of previously isolated fault segments, and this is reflected in different stages of maturity of along-strike fault bends. The results presented herein show that throw and throw-rates increase anomalously within the fault bends independently to the stage of maturity of the fault bend.

These findings can improve the knowledge on the progressive development of faulting within fault bends, because previous studies of throw and throw-rate enhancements within fault bends have been focussed on well-established fault bends at the surface (Faure Walker et al., 2009, 2015; Wilkinson et al., 2015; Mildon et al., 2016; Iezzi et al., 2018; 2019; Chapters 4 and 5). Here, for the first time, it is shown that throw-rate enhancements occur also in incipient fault bends, where the propagation and the establishment of the fault bend is incomplete. This suggests that the relationship between the non-planar fault geometry and the conservation of the strain-rate along the fault, might be driven from processes occurring on the fault at depth, where the fault bends are established and propagate towards the surface (e.g. see Iezzi et al. 2018, their Figure 2; Chapter 2, Section 2.2.1, Figure 2.7 in this thesis).

These findings can also help to improve the knowledge of the process of fault growth by linkage of previously isolated fault segments (Figure 6.14). If the variation of strike and

dip in an incipient bend promotes high throw-rates due to conservation of heave (Fig. 6.14a), local throw and displacement maxima may develop (Fig. 6.14b). As the fault linkage proceeds, throw-rates along the entire fault work to create an along-strike profile consistent with a single longer fault, but local maxima in throw-rates will be located within the fault bends. However, the development of such maxima depend on the relative values of strike and dip in the fault bend and along intervening segments, and also, presumably, the magnitude of rotations about horizontal axes in relay zones (e.g. see Walsh et al. 2003; their Fig. 4); note that it was not possible to resolve such rotations due to the short time window recorded by the deformation measured (<10-12 ka) and the resultant low magnitude of the rotations. This suggestion is consistent with classic models of fault growth by linkage, where the fault length is established early followed by accumulation of the finite fault slip (McLeod et al., 2000; Manfield and Kattenhorn, 2001; Walsh et al., 2002; Nicol et al., 2005), but here it is emphasised that local maxima may develop in fault bends. Throw enhancements within incipient fault bends can also represent one possible explanation of the wide scatter in natural values of displacement accumulation during fault lengthening (10-60% of faults displacement accumulated during faults lengthening; Rotevatn et al., 2019). In fact, if the measurements of maximum displacement, obtained at different stages of fault lengthening and used to constrain displacement versus fault length diagrams, were collected across fault bends, this might create a scatter of the values of maximum displacement used to study the fault evolution through time.

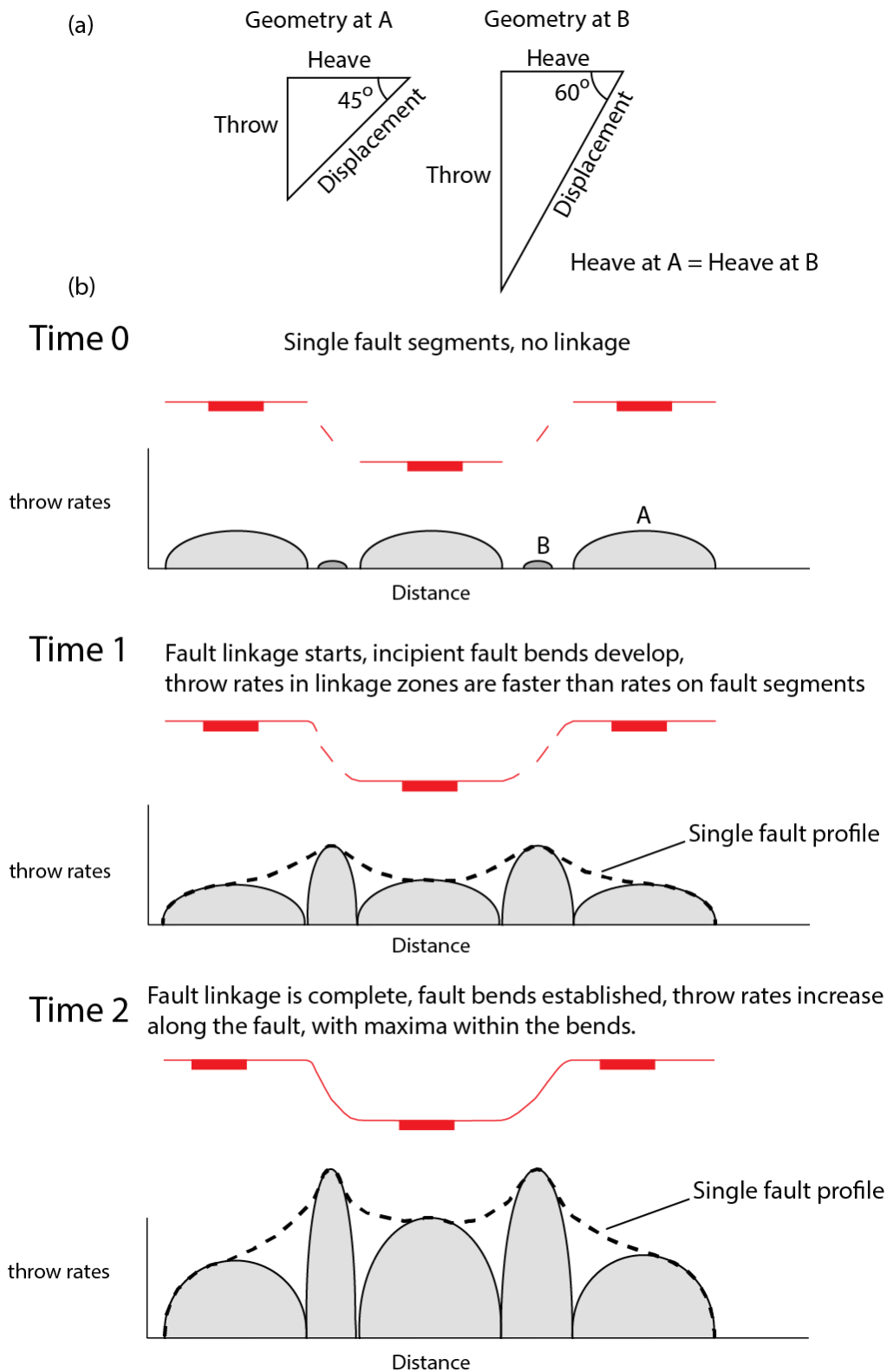


Figure 6.14: Fault growth model showing that fault bends present faster throw-rates, compared to the throw-rates on faults immediately outside the bend, since the onset of the fault linkage processes. From Iezzi et al., 2020.

The increases of throw-rate within incipient fault bends has implications for palaeoseismology. Previous studies show that fault bends may be the site of anomalously high coseismic throws (e.g. Iezzi et al., 2018; Chapter 4) which if not recognised as the result of bends with strike and dip values that promote high throw-rates, could lead to overestimates of palaeoearthquake magnitudes from palaeoseismological trenches. This chapter points out that also incipient fault bends can affect measurements of D_{max} obtained with palaeoseismological trenches.

Overall, this study suggests that the throw and throw-rate distributions along faults within the WVZ are influenced by the local fault geometry and the strain that the fault must accommodate in that location, following the model first presented in Faure Walker et al. (2009). This implies that the relationship between the non-planar fault geometry and the conservation of strain along the fault and across fault bends, which causes throw-rate enhancements within the bends, is valid also in an extremely fast-deforming geodynamic domain such as the Mid-Atlantic Ridge. Therefore, this work highlights the importance of including the effects of non-planar fault geometry on the seismic behaviour of normal faults in seismic hazard assessments located in geodynamic contexts different from the Central Apennines, where the first examples have been identified (Faure Walker et al., 2018).

6.7 Conclusions

Detailed fault mapping and serial fault scarp profiles were carried out along 5 normal faults in the Thingvellir rift and 3 normal faults in the Hengill Volcanic Complex, both located in the WVZ, Iceland. Normal faults within the WVZ in Iceland present different

stages of fault growth, which is reflected in a variety of stages of maturity of along-strike fault bends connecting the principal fault segments. Along-strike throw and throw-rate profiles show that, independently to the stage of maturity of the fault bends, the throw and throw-rates increase within the fault bends, compared to the values on the fault segments immediately outside the bends.

These findings imply that: 1) the relationship between the local fault geometry and the conservation of the strain-rate, which causes throw and throw rate enhancements within the bend in response to local changes in strike and dip within the bend with constant horizontal strain, might be driven by processes occurring in the deeper part of the fault; 2) during fault growth, fault bends in linkage zones are propagating faster than the slip accumulation of the principal fault segments, implying that during the process of fault growth by linkage and coalescence the fault works in order to first establish the fault length and then to accumulate slip; 3) palaeoseismological studies must take in account the effect of incipient fault bends on the throw-rates of a fault, in order to avoid misleading interpretations of results obtained from palaeoseismological trenches located in proximity of incipient bends. Overall, this work shows that the previously observed relationship between the non-planar fault geometry and the conservation of strain-rate along a fault affects the seismic behaviour of a normal fault also in a geodynamic domain of a mid-oceanic ridge, implying that this relationship is indeed valid also in geodynamic contexts different from the Central Apennines, where the first examples of this relationship have been identified.

This chapter, together with the previous Chapters 4 and 5, shows that throw-rates are influenced by the local non-planar fault geometry for different types of normal faults and

in different geodynamic domains. Moreover, results in Chapter 5 suggests that the throw-rate varies along the strike of a densely-spaced fault system, where normal faults are distributed both along-strike and across-strike. This suggests that faults within a fault system interact, influencing their activity rates through time. However, although the interaction between along-strike distributed faults have been shown previously (e.g. Roberts and Michetti, 2004), there are no detailed studies demonstrating how faults distributed across the strike of a fault system interact.

The next chapter will present measurements of *in situ* cosmogenic ^{36}Cl concentrations performed on three faults distributed across-strike within the fault system in Attica, central Greece. This allows reconstruction of the slip histories of faults since the demise of the LGM (15 ± 3 ka), and the comparison between the three different slip histories will allow to study the interaction processes through time between across-strike distributed faults.

Chapter 7

Across-strike variations of fault slip-rates constrained using *in situ* cosmogenic ^{36}Cl concentrations.

7.1 Summary

The previous chapters have shown that slip-rates vary along the strike of normal faults due to the presence of 3D structural complexities. Moreover, Chapter 5 showed that multiple adjacent faults distributed both along and across the strike of a fault system, and spaced $\leq \sim 5$ km across strike, work together to accommodate the regional deformation. However, less is known about the interaction between faults distributed > 5 km across the strike of a fault system. To increase the knowledge in the dynamics of normal fault systems, this chapter presents measurements of *in situ* cosmogenic ^{36}Cl concentrations performed on three faults distributed 6-15 km across-strike within the fault system in Attica, central Greece. The ^{36}Cl approach allows slip histories, including scarp age, slip-rates, elapsed time since the last earthquake, slip sizes, and changes in slip-rate, to be recovered since the time when an outcropping fault plane that forms part of a fault scarp was exposed by tectonic slip, usually since the demise of erosion in the last glacial maximum (see Chapter 2, Section 2.3.3 and Beck et al. (2018) for a review). This chapter shows the characterization of the sample sites and the parameters used as input in the Matlab code for recovering slip histories from ^{36}Cl data provided by Beck et al. (2018).

The fault slip histories are analysed and compared to each other in order to understand how the slip-rate varies through time and how distant across-strike faults interact. This chapter shows that the three faults exhibit clustered behaviour, with alternation of earthquake clustering and anti-clustering through time, and with individual faults dominating the strain accumulation at different times rather than showing simultaneous activity.

7.2 Introduction

The identification of slip-rates on active faults is vital to quantify recurrence intervals for PSHA. When active faults are part of dense fault systems, the interaction between adjacent faults influences the fault slip-rates (e.g. Cowie and Roberts, 2001; Bennett et al., 2004). Different studies have shown that faults distributed along the strike of a fault system interact to accommodate the regional deformation (Cowie and Roberts, 2001; Roberts and Michetti, 2004; Papanikolaou et al., 2005; Papanikolaou and Roberts, 2007; Faure Walker et al., 2012; Iezzi et al., 2019). However, it is equally important to understand the relationships between faults distributed across the strike of a fault system. Iezzi et al. (2019) (Chapter 5) showed that adjacent faults arranged across the strike of a narrow fault system (faults spaced ~ 5 km across strike or less) are working together to accommodate the regional deformation. However, less is known about the interaction between more distant across-strike faults.

Cowie et al. (2013; 2017) suggested that parallel sets of faults interact through time, with activity switching back and forth across-strike yet maintaining the regional strain-rate. This is supported by observation of post 1349 AD historical seismicity localized on

specific sets of faults on the NE flank of the Apennines, yet earlier Holocene strains, constrained by observations of offsets across post-LGM scarps, are distributed across the entire width of the orogen, including earthquakes in 1349 AD and earlier times that were clearly located on the SW flank of the orogen causing severe damage in Rome (Cowie et al., 2017; Figure 7.1; see also Beck et al. 2018). To explain this, the authors suggested that the switching activity between faults, on a millennial timescale, may be due to (1) elastic interaction during stress-transfer associated with earthquakes or due to (2) alternating uplift and subsidence produce by faults sited on opposite sides of an orogen, which alters the location where least work against gravity is needed to accommodate the extension in a system driven by dynamic topography (Cowie et al., 2017; Figure 7.1). However, at the time of writing there are no direct observations of the switching activity between faults arranged across strike, on a timescale less than the age of the LGM.

The fault system in Attica, central Greece, provides an ideal opportunity to study the temporal relationships between activity on parallel sets of faults, over the required timescale, in order to provide observations of the characteristics of across-strike switching of activity. The Attica region contains sets of parallel active faults located in a densely-populated area around Athens (Figure 7.2). These faults have already revealed themselves as highly dangerous, for example during the 7th September 1999 M_w 6.0 earthquake, which caused severe damage in the northwest part of Athens and 143 deaths due to building collapse (Pavlidis et al., 2002; Ganas et al., 2004). Thus, studying the evolution of the slip histories for faults in Attica could provide key information on the dynamics of fault systems with parallel faults and on the mitigation of the seismic hazard for the city of Athens.

Comparison between strain rates, topography and historical earthquakes in central Italy

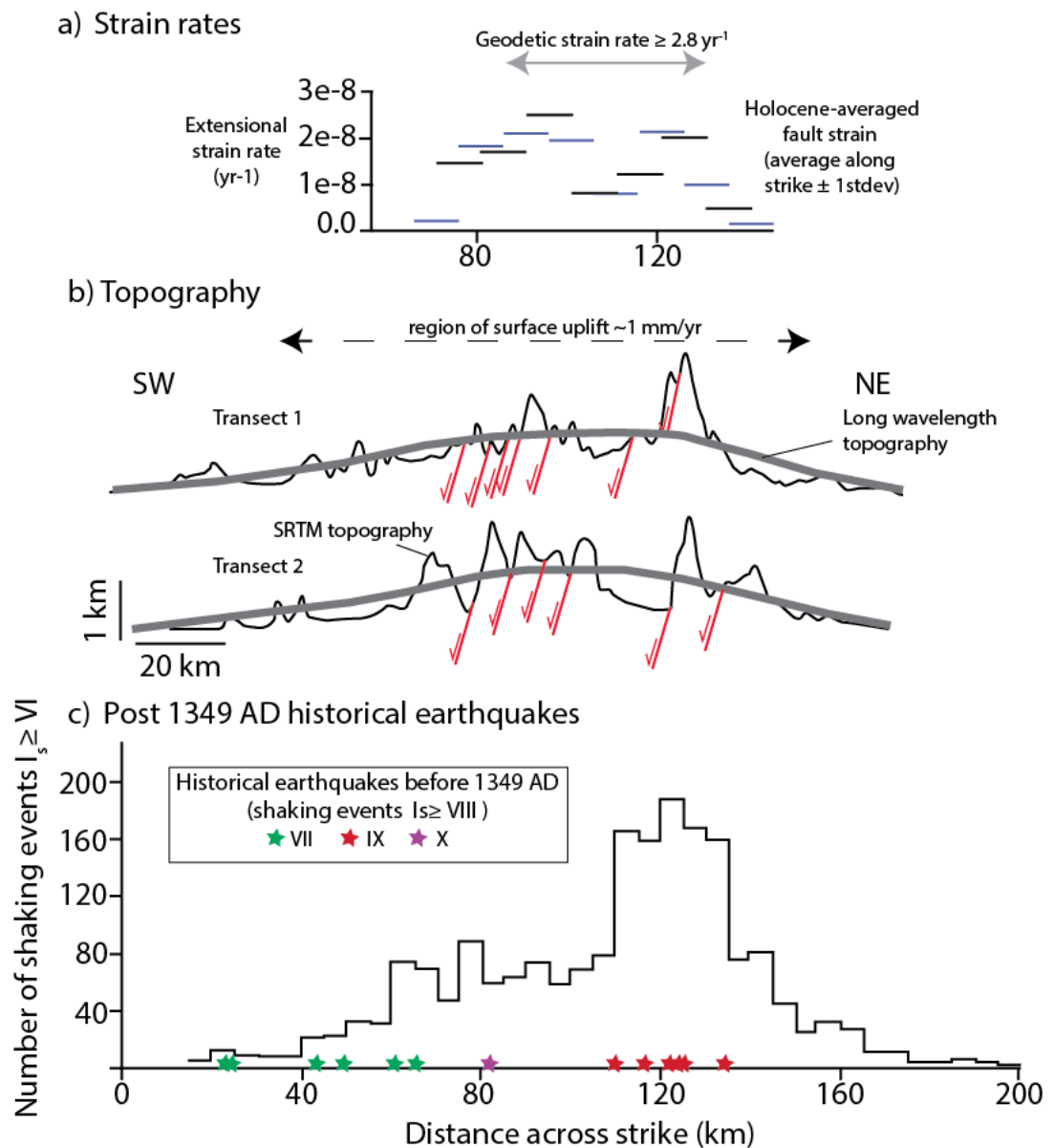


Figure 7.1: Regional strain-rates, topography and location of faults, and historical earthquakes across central Italy, adapted from Cowie et al. (2017). a) Extensional strain-rates across Central Italy; the grey arrow is the geodetic strain-rate (from D'Agostino et al., 2004); blue and black bars are strike-averaged Holocene rates, calculated in two sets of 10km-wide transects offset by 5 km across strike to avoid sampling bias (from Faure Walker et al., 2010;2012). b) Two transects across central Italy, showing the SRTM topography (Shuttle Radar Topography Mission; Jarvis et al., 2008) and the location of the principal faults within the Central Apennines; in grey is reported the long-wavelength topography (from D'Agostino et al., 2004). c) Macroseismic shaking intensities ($I_{MCS} \geq VI$; $M \geq 5.8$) from 1350 – 2016 AD (Rovida et al., 2016; Galli et al., 2016). Stars are location of historical shaking events with $I_{MCS} \geq VIII$ occurred before 1350 AD (Rovida et al., 2016). This shows that, although most of the seismicity is localised on the NE flank of the Central Apennines, damaging historical earthquakes occurred also within the SW flank of the Central Apennines, supporting the idea of switching activity between parallel faults.

To do so, this chapter presents measurements of the exposure ages of three faults distributed across strike in the Attica fault system using *in situ* ^{36}Cl cosmogenic exposure dating of fault planes exhumed since the demise of the erosional processes associated with the last glaciation. The three faults have been chosen given the presence of good sampling sites along their traces. Other faults do not present suitable field sites for sampling. Cosmogenic dating of the exposure ages of fault planes has been proven to be a powerful tool to constrain the slip history of a normal fault since the timing of onset of the fault scarp (see Chapter 2, Section 2.3.3 for a review of the theory and of the literature about cosmogenic dating). Moreover, the modelling of cosmogenic ^{36}Cl concentrations up the fault plane provides fundamental information on some key inputs for seismic hazard calculations: (1) the slip-rate on active faults; (2) the timing of the last earthquake (T_{elap}); (3) the mean recurrence interval for maximum magnitude earthquakes (T_{mean}) and (4) the variability in recurrence (CV), that is the standard deviation of recurrence intervals divided by the mean recurrence interval (Pace et al., 2016). The understanding of these parameters could help in the mitigation of the seismic hazard of Athens, and little information is available of this kind to date (see Deligiannakis et al., 2016).

This chapter describes the site characterizations for the three faults and the parameters used as input in the Beck et al. (2018) code to model the slip histories. The results show that the three faults exhibit clustered behaviour, with alternation of earthquake clustering and anti-clustering through time, and with individual faults dominating the strain accumulation at different times rather than showing simultaneous activity. In other words, this chapter shows that earthquake clusters and anti-clusters are alternating between the three faults, supporting the idea of switching activity between across-strike faults. This

chapter discusses these findings in terms of activity of fault systems and for the mitigation of the seismic hazard in Athens.

7.3 Geological background of Attica

The geology of Attica is characterized by the presence of two main tectonic units, divided by a major NNE-SSW trending, NW dipping, detachment fault (Figure 7.2a). The latter separates Meso-Cenozoic limestones at low metamorphic to diagenetic grades to the west from metamorphic marbles and other siliciclastic to the east (Figure 7.2a; Papanikolaou & Papanikolaou, 2007). Although the activity of the detachment fault was probably concentrated in Miocene to Early Pliocene times, and it appears not to be active nowadays (Papanikolaou & Papanikolaou, 2007; Papanikolaou et al., 2008), it seems to exert a control in the current neotectonics. In fact, most of the principal active normal faults in Attica are located west of the detachment fault, dissecting the Meso-Cenozoic limestones, and only one principal fault is located east of the detachment fault (Figure 7.2b; Papanikolaou & Papanikolaou, 2007; Deligiannakis et al., 2016).

The active fault system west of the detachment consists in a set of across-strike distributed normal faults striking mainly E-W to NW-SE. These faults have lengths of 10-18 km, average slip-rates that do not exceed 0.5 mm/yr, constrained by offsets across scarps that have been assumed to post-date the LGM (15 ± 3 ka), and the potential to release earthquakes with magnitudes up to M_w 6.6 (Figure 7.2b; Deligiannakis et al., 2016). Although the active faults are clear in the geology and geomorphology, with fault scarps offsetting Holocene landforms providing clear evidence of recent activity, the completeness of historical and instrumental seismic catalogues does not provide detailed

information about the activity rates of faults, so slip-rates and T_{mean} are poorly known whilst T_{elap} and CV are unknown (Ganas et al., 2004; Deligiannakis et al., 2016). Yet, defining the seismic hazard associated with these faults is crucial, given the proximity of a densely-populated city like Athens. One fault, the Fili fault, may extend into the Athens metropolitan area raising the concern about earthquake ground-rupture within the city.

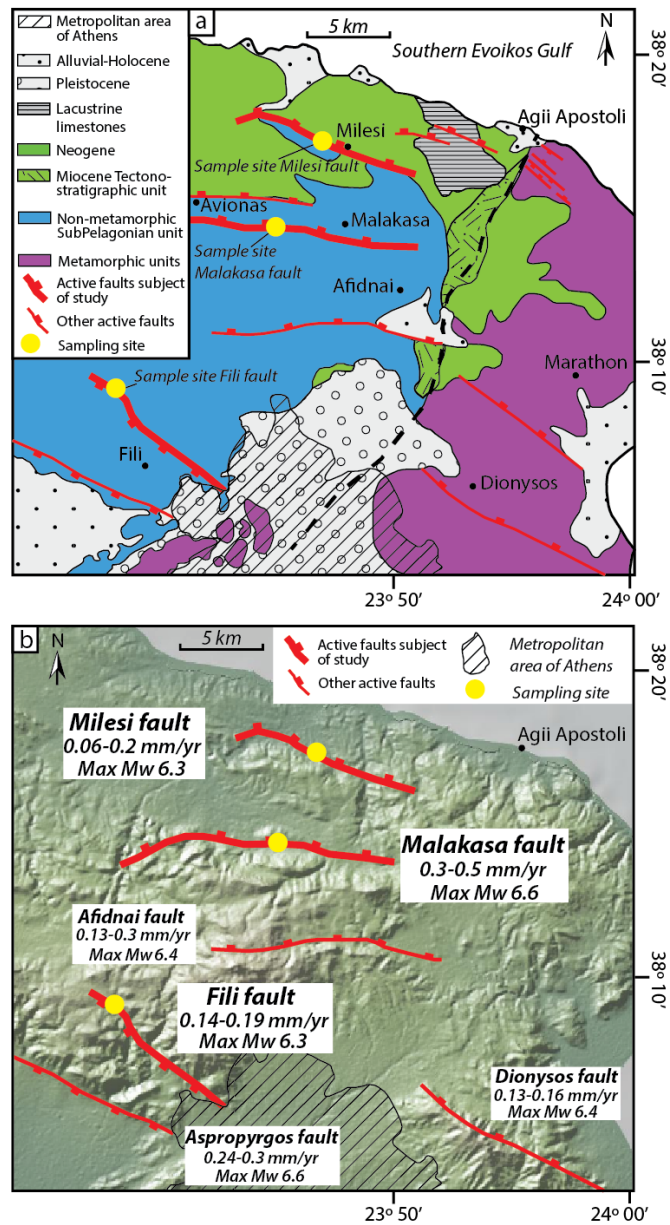


Figure 7.2: Maps of Attica. a) Geological map of Attica (modified from Papanikolaou and Papanikolaou, 2007). Thick red lines are principal faults subject of study in this thesis, thin red lines are other active faults. b) Map of the principal active normal faults in Attica. Fault traces are modified from Papanikolaou and Papanikolaou, 2007; thick red lines are faults subject of study in this thesis, thin red lines are other principal faults. With fault names are reported slip-rates (derived from offsets across scarps that have been assumed to post-date the LGM (15 ± 3 ka)) and expected maximum magnitudes derived from fault length (from Deligiannakis et al., 2016).

7.4 Site characterizations

Samples have been collected on the Milesi fault, the Malakasa fault and the Fili fault (Figure 7.2). These faults had the best sampling sites available from among the candidate faults, following the criteria shown in Chapter 3. Other across-strike faults could not be sampled because of lack of acceptable sampling locations. Following is a description of the sampling sites for each fault, ordered from north to south (Figure 7.2).

7.4.1 Milesi fault

The Milesi fault sampling site is located in the central part of the fault map trace (Figure 7.2). The sampling site is distant from drainage incisions, has planar, and hence probably undisturbed upper and lower slopes, and has horizontal and parallel hangingwall and footwall cut-offs (Figures 7.3a and 7.3b). It is characterized by a planar fault plane, with constant dip along the outcrop and preserved striae proving minimal erosion of the fault plane through time (Figure 7.3).

A scarp profile was constructed perpendicular to the strike of the fault using a hand-held laser range finder (see Chapter 3, Section 3.3 for a review of the methodology). The interpretation of the fault scarp profile indicates a throw of 4.25 m and an on-fault slip of 6.53 m, with a dip for the upper slope of 28° and dip of the lower slope of 27° (Figure 7.3h). The dip of the fault plane, constrained with field measurements, is 40° (Figures 7.3e and 7.3g).

A trench ~0.6 m deep was dug in front of the fault plane in order to collect samples below the surface (Figures 7.3c and 7.3f). The stratigraphic succession exposed in the trench shows Holocene dark, organic-rich deposits in contact with light-coloured sediments,

mainly formed by angular scree clasts, deposited during glacial-periglacial conditions associated with the last glaciation (Figure 7.3f). This contact indicates the change in climate conditions due to the demise of the last glaciation, and therefore it has been used to mark the sample of elevation 0 metres. Samples have been collected ~30 cm approximately equidistant up the fault plane and downdip within the trench (Figure 7.3c). In the upper part of the fault plane, samples have been collected on a parallel ladder, tied to the elevations of lower sample using a spirit level and ruler, in order to sample the preserved higher portion of the fault plane (Figure 7.3c). In total, 14 samples of the fault plane were collected: MIL-60, MIL-30, MIL0, MIL+30, MIL+68, MIL+112, MIL+135, MIL+180, MIL+200, MIL+227, MIL+250E, MIL+250W, MIL+400, MIL+430.

Milesi Fault

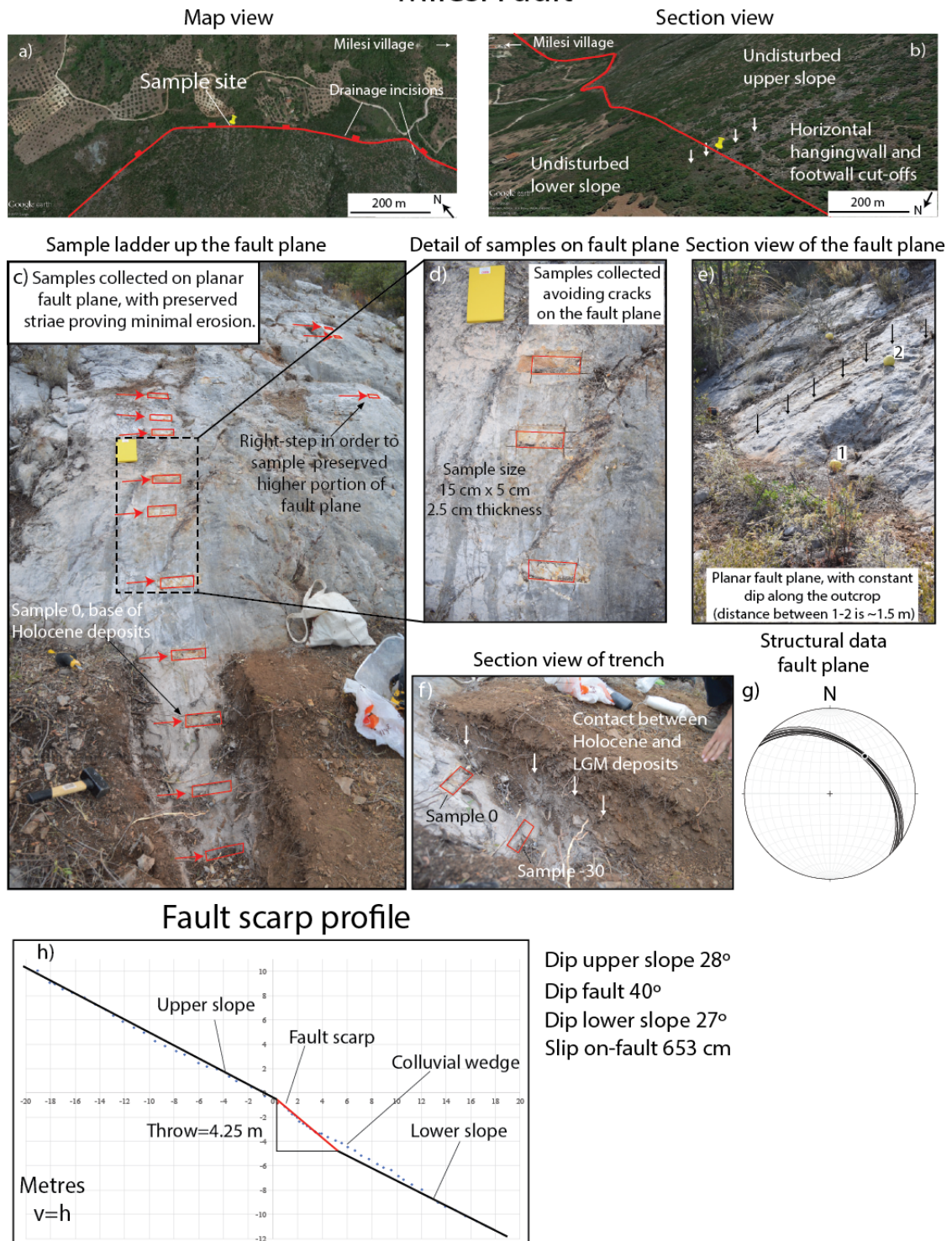


Figure 7.3: Site characterization of the Milesi fault. a) and b) are location maps of the sample site. The site is distant from drainage incisions, presents undisturbed upper and lower slopes and has parallel hangingwall and footwall cutoffs. c) Sample ladder up the fault plane. Samples have been collected with ~30 cm equidistance; sample 0 is at the base of the Holocene deposits; the parallel ladder is to sample preserved higher portion of the fault plane. d) Details of samples on the fault plane. e) Section view of the fault plane. f) Section view of the trench, with exposed the stratigraphic contact between Holocene deposits and periglacial deposits. g) Structural data of the fault plane, showing dip slip kinematics. h) Fault scarp profile, with parameters derived. Blue dots mark the original scarp profile built across the sample site; black line are the interpreted upper and lower slope profiles; red line is the fault. The slip on-fault is measured as the distance between the upper and lower slopes cut-offs measured along the fault.

7.4.2 Malakasa fault

As with the Milesi fault, the Malakasa fault sampling site is located approximately in the central part of the fault map trace. The sampling site is distant from drainage incisions along the slope, has undisturbed upper and lower slopes, and presents horizontal and parallel hangingwall and footwall cutoffs (Figures 7.4a and 7.4b). The fault plane is planar, with constant dip along the fault plane and preserved striae proving minimal erosion of the fault plane (Figure 7.4c, 7.4d and 7.4e).

The interpretation of the fault scarp profile indicates a throw of 4.15 m and an on-fault slip of 6.12 m, with a dip for upper slope of 29°, dip of the lower slope of 22°, and dip of the fault 43°, constrained with field measurements (Figure 7.4f).

A trench ~0.4 m deep was dug in front of the fault plane to collect samples below the surface (Figure 7.4d). The stratigraphic succession exposed in the trench shows Holocene dark, organic-rich deposits in contact with light-coloured sediments, mainly formed by angular scree clasts, deposited in a glacial-periglacial environment during the last glaciation (Figure 7.4d). This contact is used to identify the sample of elevation 0 metres. Samples have been collected every ~30 cm approximately equidistant up the fault plane and downdip within the trench (Figure 7.4c). The upper part of the fault plane has been sampled in a parallel ladder, again tied to lower elevation samples using a spirit level and ruler, in order to collect samples on an undisturbed portion of the fault plane (Figure 7.4c). In total, 15 samples have been collected on the fault plane of the Malakasa fault: MAL-42, MAL-21, MAL0, MAL+32, MAL+59, MAL+84, MAL+110, MAL+140, MAL+168, MAL+194, MAL+257, MAL+316, MAL+360, MAL+420, MAL+468.

Malakasa Fault

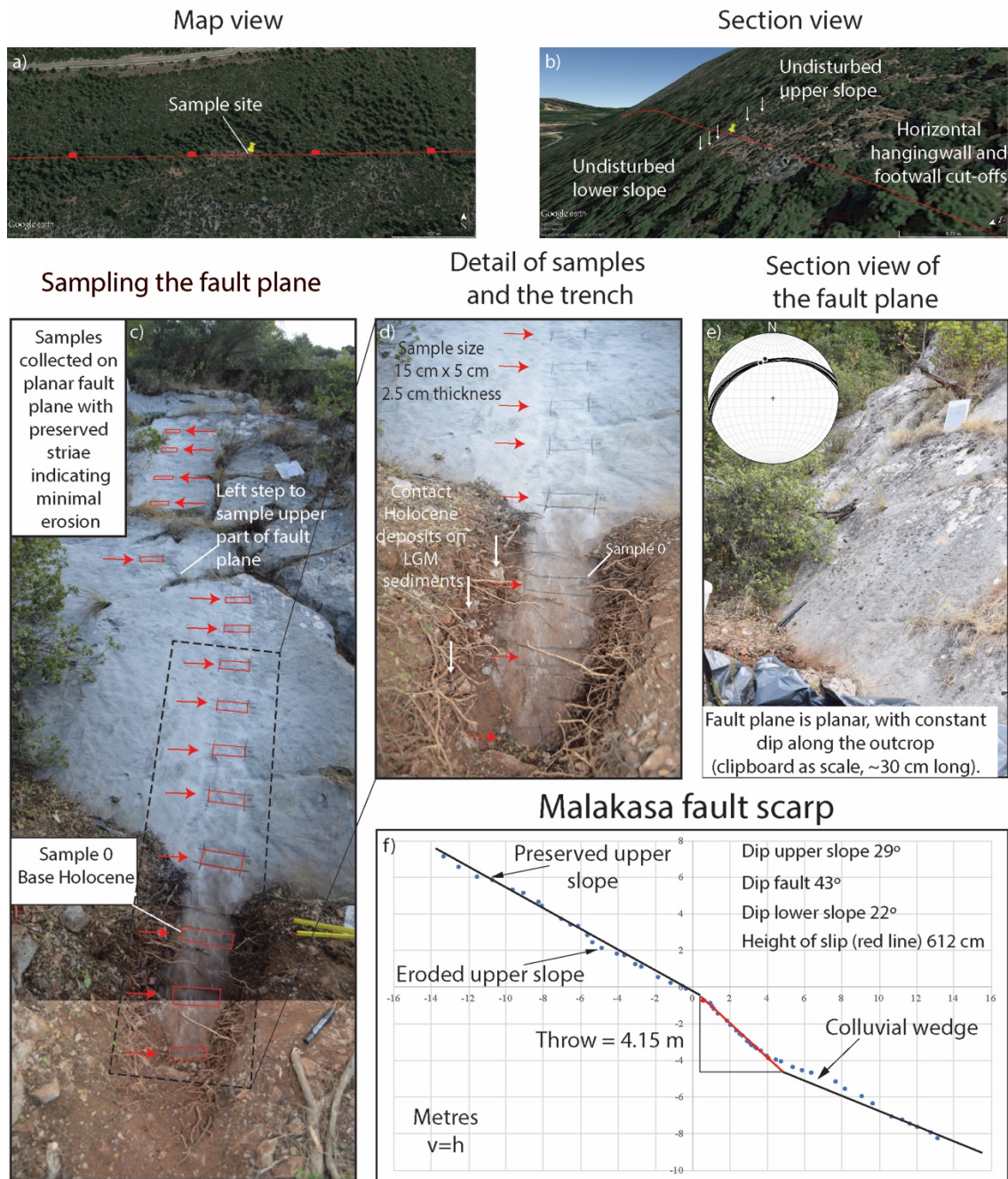


Figure 7.4: Site characterization of the Malakasa fault. a) and b) are location map of the sample site. The site is distant from drainage incisions, presents undisturbed upper and lower slopes and parallel hangingwall and footwall cutoffs. c) Sample ladder up the fault plane. Samples have been collected with about 30 cm equidistance; sample 0 is at the base of the Holocene deposits; the parallel ladder is to sample preserved higher portion of the fault plane. d) Details of samples on the fault plane and of the trench; Red arrows mark the samples; white arrows indicate the contact between Holocene deposits and sediments associated with the last glaciation. e) Section view of the fault plane; the fault plane is planar, with preserved striae indicating minimal erosion; the stereonet reports the structural data collected on the fault plane, indicating a dip-slip kinematics. f) Fault scarp profile used to characterize the fault scarp. Blue dots mark the original scarp profile built across the sample site; black line are the interpreted upper and lower slope profiles; red line is the fault. The slip on-fault is measured as the distance between the upper and lower slopes cut-offs measured along the fault.

7.4.3 Fili fault

Unlike the Milesi and Malakasa fault sample sites, the Fili sample site is located towards the north-western tip of the fault (Figure 7.2). The sampling site is distant from drainage incisions along the slope, has undisturbed upper and lower slopes and presents horizontal and parallel hangingwall and footwall cutoffs (Figures 7.5a and 7.5b). The fault plane is planar, with constant dip along the fault plane and preserved striae proving minimal erosion of the fault plane (Figure 7.5e).

The interpretation of the fault scarp profile indicates a throw of 3.05 m and an on-fault slip of 3.98 m, with dip of the upper slope of 14°, dip of the lower slope of 7° and dip of the fault of 53°, constrained with field measurements (Figure 7.5h).

A trench ~20 cm deep was dug in front of the fault plane to collect samples below the surface (Figure 7.5g). The stratigraphic succession exposed in the trench, as for the other sites, again shows Holocene dark, organic-rich deposits in contact with light-coloured sediments, mainly formed by angular scree clasts, deposited in a glacial-periglacial environment during the last glaciation (Figure 7.5e). This contact is used to identify the sample with 0 elevation on the fault plane.

Samples have been collected every ~30 cm, approximately equidistant moving up the fault plane and downdip within the trench. In total 13 samples of the fault plane have been collected: FIL-20, FIL-16, FIL0, FIL+28, FIL+45, FIL+67, FIL+80, FIL+100, FIL+127, FIL+150, FIL+184, FIL+226, FIL+256 (Figure 7.5c).

At this site, the sampling exposed a peculiar rock texture characterized by matrix-supported and clast-supported, poorly-sorted angular clasts surrounded by a fine red matrix that resemble cave collapse and infill deposits from an ancient and long abandoned karst system. To better understand the composition of these features and the implications

that this would have on the cosmogenic dating, two thin sections have been obtained from two samples located at different elevations on the fault plane (FIL-16 and FIL+256). The thin sections have been analysed with an electron microprobe, available at Birkbeck, University of London, in order to identify the chemical composition of the angular clasts and of the fine red matrix. The analysis shows that the angular clasts are predominantly rich in Ca and Mg. This agrees with the chemical composition of a dolomitic limestone, which is the predominant rock type of the area (Figure 7.2a; Papanikolaou and Papanikolaou, 2007). In contrast, the analysis of the red matrix shows a composition of almost entirely pure calcite. Given the chemical composition and the rock texture, the angular clasts are interpreted as formed by the collapse of karstic caves or tunnels formed within Triassic dolomitic limestones, and the red matrix is interpreted as a vadose silt that sedimented from interstitial water flowing between the clasts. The peculiar composition of this rock type does not affect the cosmogenic dating of the fault plane, because both clasts and matrix are enriched in Ca and poor in other elements that can produce cosmogenic ^{36}Cl (e.g. potassium). Therefore, during the sample preparation and modelling/analysis, the production rate of cosmogenic ^{36}Cl is calculated based on the total amount of ^{40}Ca measured in the rock sample, independently if it comes predominantly from a dolomitic limestone or a pure calcite (see Schimmelpfennig et al., 2009).

Fili fault

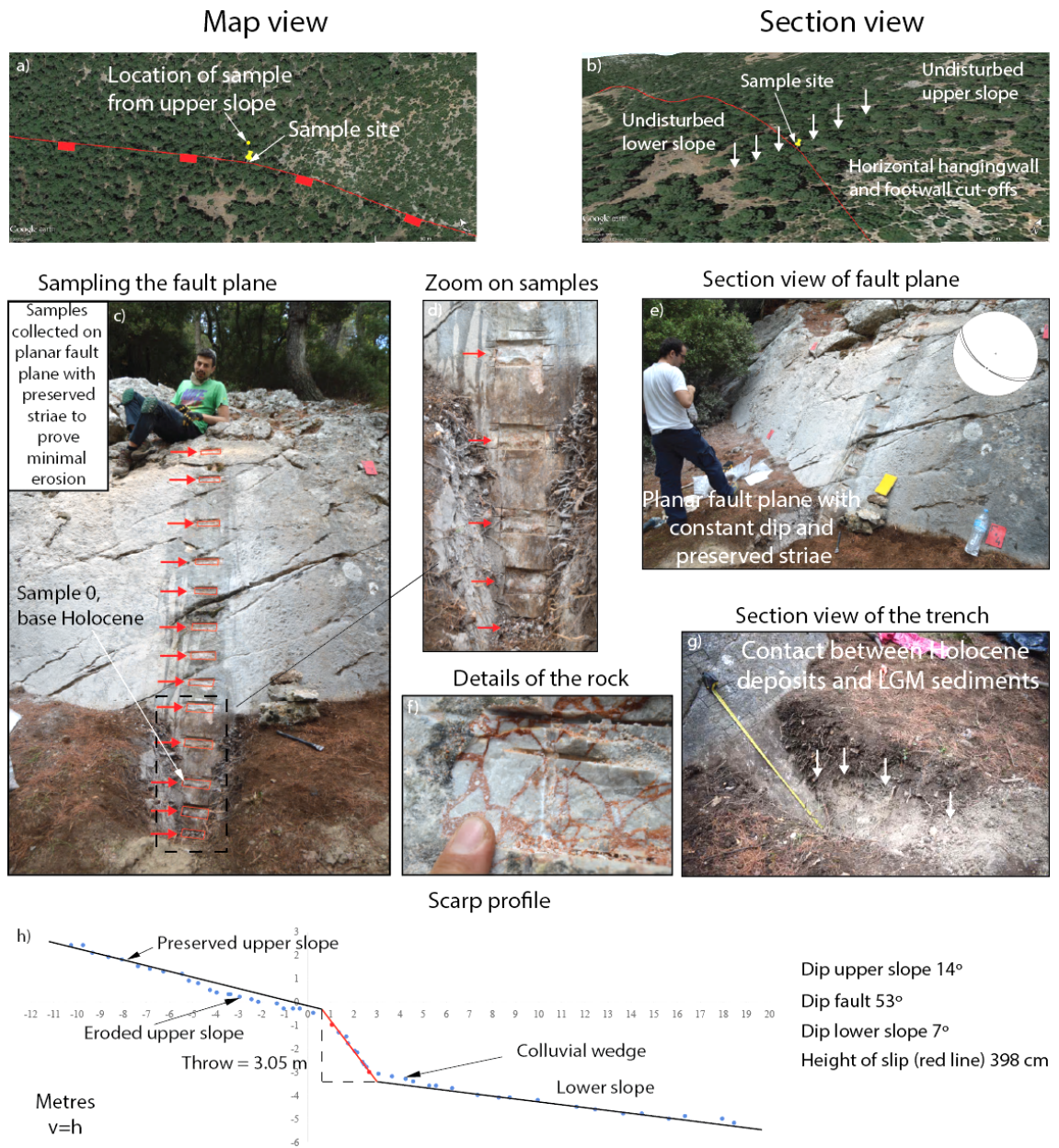


Figure 7.5: Site characterization of the Fili fault. a) and b) are location map of the sample site. The site is distant from drainage incisions, presents undisturbed upper and lower slopes and parallel hangingwall and footwall cutoffs. c) Sample ladder up the fault plane. d) Zoom on samples on the fault plane. e) Section view of the fault plane. It is planar, with constant dip and have striae showing minimum erosion. The stereonet with structural measurements of the sampling site is shown. f) Details of the rock sampled, characterized by angular clasts surrounded by a fine red matrix. g) Section view of the trench. It exposes the contact between the Holocene deposits and sediments associated with the last glaciation, used to find the sample 0. h) Scarp profile used to characterize the fault scarp. Blue dots mark the original scarp profile built across the sample site; black line are the interpreted upper and lower slope profiles; red line is the fault. The slip on-fault is measured as the distance between the upper and lower slopes cut-offs measured along the fault.

7.5 Modelling the measured ^{36}Cl concentrations

The measured ^{36}Cl concentrations per each sample have been modelled using the Beck et al. (2018) Matlab code (see Chapter 3, Methods, for details).

Data obtained from the fault scarp profiles (dip of the upper slope, dip of the fault scarp, dip of the lower slope, amount of slip on-fault) have been used as input for modelling.

The maximum slip per event that the code has been allowed to explore is 300 cm, a value about a factor of 3 higher than that expected for faults of these lengths (e.g. Wells and Coppersmith, 1994). The time window within the code has been allowed to model the potential slip histories is set up to 120 ka, a time period that allows iteration of the age of the initial production after any climate change and erosion rate change within the code, in case the expected value (15 ± 3 ka) was not applicable.

For each sample the “rock.txt” file contains the concentrations of the major elements expressed in oxides (Al_2O_3 , Fe_2O_3 , MnO , MgO , CaO , Na_2O , K_2O , TiO_2 , P_2O_5), the natural content of ^{35}Cl , the content in ^{40}Ca , the concentration of ^{36}Cl AMS and the uncertainty in ^{36}Cl values.

The “colluvium.txt” files contains the chemical composition of a sample of colluvium collected in central Italy, where data are available and the climate conditions and the parental rocks are similar to central Greece (provided by Prof. Gerald Roberts).

The “magfield.txt” contains scaling factors for spallation and muons capture due to the latitude and the elevation of each field site, following Stone et al. (2000).

A burn in of 50% has been applied to the modelling of each fault so as to remove initial results produced before the MCMC code had started to converge on a least-squares solution. Convergence was achieved as confirmed by a Geman-Rubin (GR) test (see Beck et al. 2018 for details).

7.6 Results

The measured ^{36}Cl concentrations have been modelled in order to recover the slip histories of the three faults (Figure 7.6). For the Milesi fault, 1,349,962 MCMC iterations for each of two Markov chains have been performed (Figure 7.6a.i). For the Malakasa fault, 1,203,366 MCMC iterations of each of two Markov chains have been performed (Figure 7.6b.i). For the Fili fault, 1,624,196 MCMC iterations of each of two Markov chains have been performed (Figure 7.6c.i). Per each fault, the modelling has been interrupted when the two Markov chains have converged on a least-squares solution, which validity was confirmed by the GR convergence diagnostic (Figures 7.6a.ii, b.ii and c.ii).

The modelled slip histories reveal that the three faults have episodic behaviour, with alternating periods of rapid accumulation of slip and periods of quiescence (Figures 7.6a.iii, b.iii and c.iii). The Milesi fault scarp started recording slip since ~ 44 ka, and the fault slip history shows two phases of rapid accumulation of slip; the first occurred at ~ 30 ka and the second occurred between ~ 10 and ~ 7 ka (Figure 7.6a.iii). The Malakasa fault scarp started recording slip since ~ 22 ka, and the fault slip history presents three periods of rapid accumulation of slip; these occurred at ~ 22 ka, ~ 18 ka and at ~ 6 ka (Figure 7.6b.iii). The Fili fault scarp started to record slip since ~ 18 ka, and the fault slip history shows that periods of rapid accumulation of slip occurred at ~ 18 ka, ~ 4 ka and at ~ 1 ka-present time (Figure 7.6c.iii). Note that these pulses of rapid accumulation of slip are not interpreted as single earthquakes, but rather as time periods during which the fault experienced repeated earthquakes in a short time interval.

Modelling of ^{36}Cl concentrations on fault planes

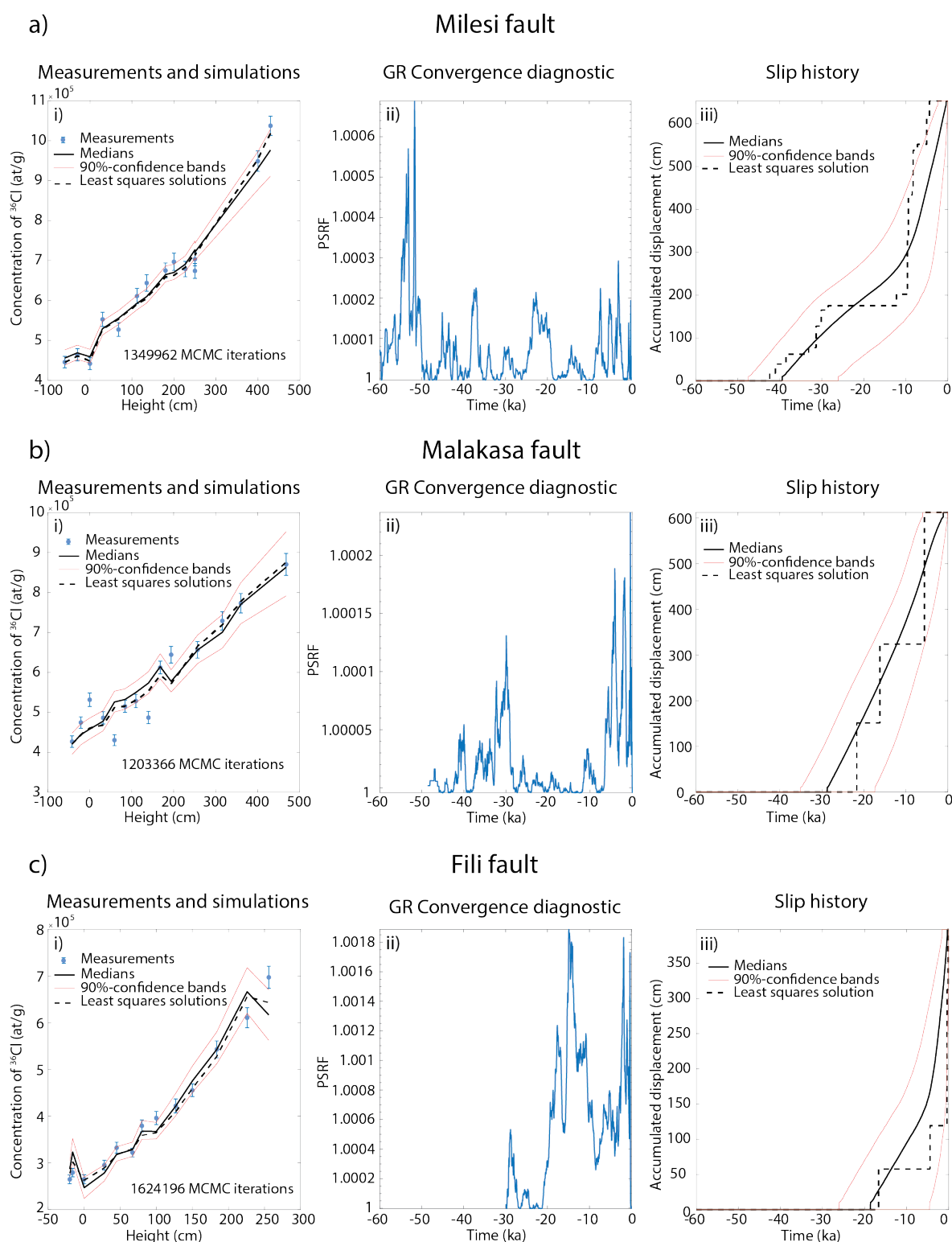


Figure 7.6: Modelling the ^{36}Cl concentrations measured on the Milesi fault (a), Malakasa fault (b) and Fili fault (c). Figures a.i, b.i and c.i report the measurements and simulations of the concentrations of ^{36}Cl . Figures a.ii, b.ii and c.ii are the convergence diagnostic of the modelling, following Gelman and Rubin (1992). Figures a.iii, b.iii and c.iii are the recovered slip histories of the three faults. Red lines are the bands constraining 90% confidence bounds, black dashed lines are the least squares solutions, which are the solutions for the faults slip histories discussed herein.

To have a better and more detailed understanding of the fault behaviour in recent times, the slip histories of the faults during the last 15 ka have been plotted and compared to each other (Figure 7.7). The comparison shows that the periods of rapid slip accumulation and quiescence are alternating through time on the three faults (Figure 7.7): the Milesi fault accumulated most of the slip between ~ 10 ka and ~ 7 ka; the Malakasa fault accumulated most of the slip at ~ 6 ka; the Fili fault accumulated most of the slip at ~ 1 ka-present time. During these peaks of activity, the other faults were experiencing phases of quiescence (Figure 7.7a). The plot of the slip intensities through time confirms the alternation of fault activity through time (Figure 7.7b). As the slip on the Milesi fault increases at ~ 10 ka, the slip intensity increases through time, overtaking the values of slip intensities for the other two faults. After ~ 4 ka, the rapid increase of activity on the Fili fault corresponds with a rapid increase of its slip intensity, which eventually overtakes the slip intensities of the other two faults. Overall, these results suggest that the fault activity switches between across-strike distributed faults, with alternating periods of rapid slip accumulation and quiescence on the three faults.

Combined fault slip histories and intensities during the last 15 ka

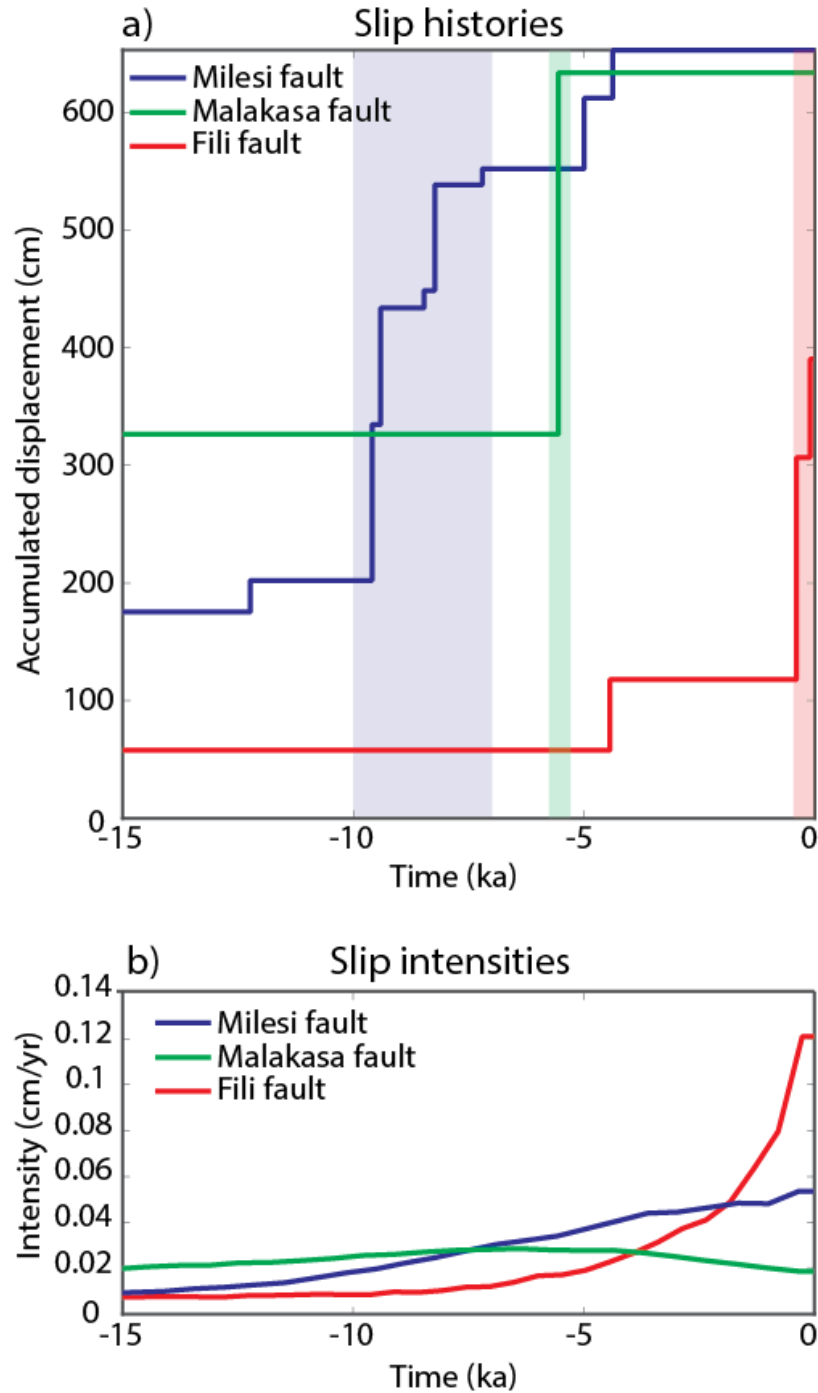


Figure 7.7: Slip histories (a) and slip intensities (b) for the three faults within the last 15 ka. Shaded areas in a) highlight phases of rapid accumulation of slip on one fault, during which other parallel faults are quiescent; colours are coded in agreement with the colour of the predominant fault in that time interval. The graph shows how the periods of rapid slip and maximum intensity are alternating on each fault.

The retrieved slip histories highlight a difference in the ages since the three fault scarps started to be preserved. It is commonly accepted that fault scarps are preserved since the demise of the LGM (see Chapter 3, Methods, for details), and in the Mediterranean area this occurred at about 15 ± 3 ka (e.g. Roberts and Michetti, 2004; Cowie et al. 2017; Beck et al. 2018). However, the modelled slip histories show that the Malakasa and Milesi fault scarps started recording slip before this time. To understand what may have caused this earlier preservation of the fault scarps, the ages since the scarps started to be preserved have been compared with the topographic elevations of the sample sites (Figure 7.8). This comparison shows that there is a correlation between the two parameters: the lower the elevation of the fault scarp, the older is the age since the scarp started to be preserved. Presumably this is because erosion, related to frost-shattering, increases with elevation. The lower elevation sites have less frost-shattering and hence preserve a longer portion of the scarp history. This feature was revealed because, as mentioned above, the time window within the code has been allowed to model the potential slip histories is set up to 120 ka, a time period that allows iteration of the age of the initial production after any climate change and erosion rate change within the code, in case the expected value (15 ± 3 ka) was not applicable.

Correlation between the age of preserved fault scarps and elevation

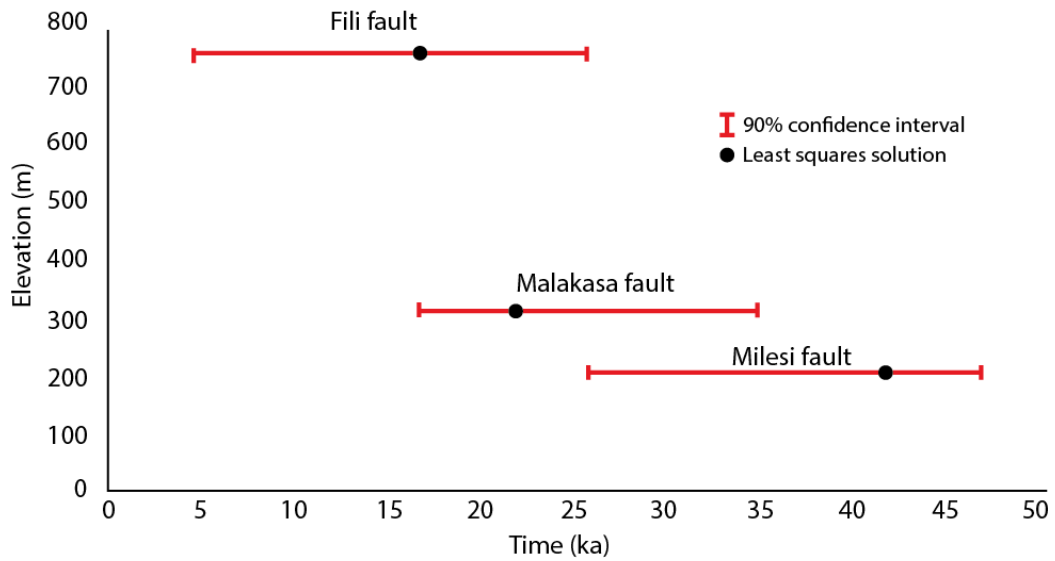


Figure 7.8: Comparison between the age since the fault scarps started to be preserved, as estimated through the cosmogenic exposure modelling, and their elevation at which they are exposed at the surface. The red bar shows the range of possible values for the 90% best results of the suitable modelling. The black dot marks the age for the least square solution. This shows that there is a correlation between the two parameters: the lower the elevation of the fault scarp, the older the age since it starts to be preserved.

Overall, the measurements and modelling of the concentrations of cosmogenic ^{36}Cl on fault planes in Attica provide a unique set of information to understand the fault behaviour. The results herein presented show that (1) the faults have an episodic behaviour, with alternating periods of rapid accumulation of slip and quiescence through time; (2) the activity switches between faults distributed across the strike of a fault system, with the alternance of periods of rapid slip and quiescence on the three faults; (3) there is a correlation between the age since the fault scarps started to be preserved and the elevation of the fault scarps, with older scarps preserved at lower elevations. In the next section these findings will be discussed, and their implications analysed.

7.7 Discussion

The episodic behaviour of the studied faults in Attica suggests that the sampled fault scarps have not been built with constant slip-rates through time, but they rather formed during specific time intervals over which several surface-rupturing earthquakes occurred. This behaviour indicates that the fault slip is clustered in time (Figure 7.9a).

The alternation of earthquake clustering and anti-clustering over the three faults prompts the idea that parallel faults interact through time. The contemporaneous occurrence of earthquake clustering on one fault and anti-clustering on the other faults suggests that the faults are working together to accommodate the deformation, maintaining the regional strain-rate, but this cooperation is only revealed over time periods longer than several earthquakes. These findings are in agreement with the observations of localised seismicity on specific sets of faults proposed in Cowie et al. (2017; Figure 7.1). Hence, it is possible to speculate that elastic interaction during stress-transfer associated with earthquakes might be the cause of the switching activity between faults in Attica, or alternatively the least-work hypothesis may apply; the importance of the results herein is that they, for the first time, present observational evidence that these alternative hypotheses should be investigated further.

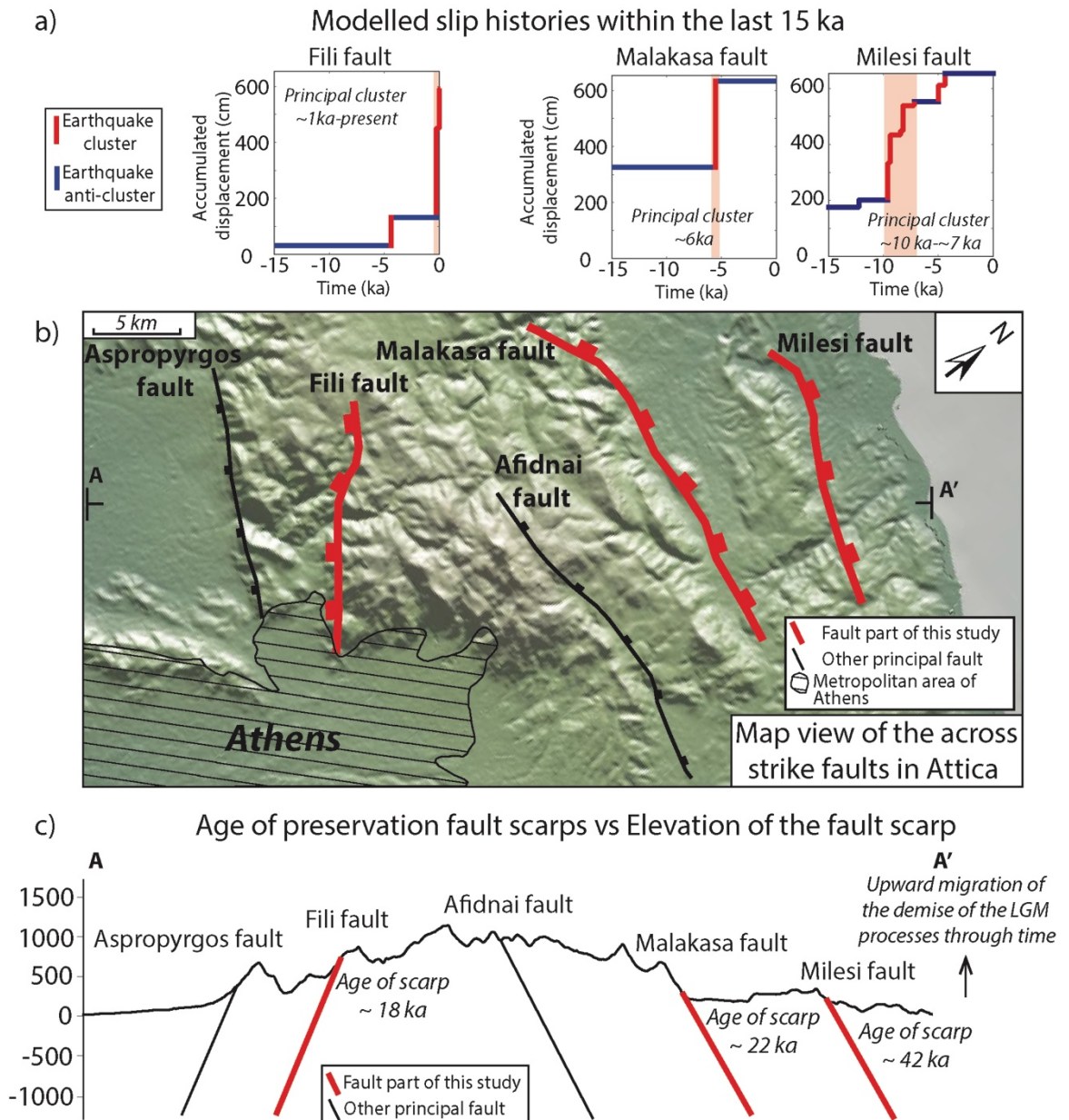


Figure 7.9: Summary of the principal findings. a) Modelled slip histories of the three faults, with highlighted earthquake clusters and anti-clusters. It is shown how the principal clusters occur on faults in different times. b) Map view of the across-strike distributed faults in Attica; in red are reported faults studied in this work, in black are other principal faults of the fault system; A-A' marks the trace of the topographic profile shown in c). c) Topographic profile across the Attica fault system, with reported the principal faults. In red are the faults studied in this work, in black are other principal faults. It is shown how the preservation of the fault scarps is related to its elevation.

The clustered behaviour of faults in Attica raises important issues for the definition of the seismic hazard in complex fault systems. The high variability of the slip-rate through time implies a high variability of the recurrence interval of faults and of the elapsed time since the last earthquake. The problem in the identification of the recurrence interval leads to

large values of CV per each fault. The Beck et al. (2018) code iterates the values of CV for the retrieved slip histories: the iterated CV for the Milesi fault is 1.24; for the Malakasa fault is 1.15; for the Fili fault is 1.19. Values of CV larger than 1 imply that the variability of the recurrence interval is larger than the mean recurrence interval of the fault, and the slip is highly clustered in time. This suggests that high CV values should be included in calculations of seismic hazard. For example, Pace et al. (2006) use values of CV between 0.15 and 0.94, but generally around 0.3-0.4, for faults in central Italy (see the values for α in their Table 3), where parallel faults exist, and this value appears low given the results of this chapter for Attica. Overall, these findings evidence that the fault behaviour into dense fault systems is complicated, and the interpretation of key parameters like the T_{mean} , T_{elap} and the CV requires more work in order to produce accurate seismic hazard assessments.

The retrieved slip histories for the Attica faults also show that there is a correlation between the age since the fault scarp started to be preserved and the elevation of the fault scarp. This correlation suggests that the lower the elevation of the fault scarp, the older the age since the scarp started to be preserved. This implies that, at these latitudes, the elevation above the sea level plays a role in the dynamics of the erosion processes occurring during the last glaciation (e.g. freeze-thaw erosion and frost-shattering). The results herein presented suggest that in central Greece at lower elevations the demise of the erosional processes associated with the last glaciation gradually migrated towards higher elevations; the processes are diachronous with regard to elevation. The gradual upward migration of the demise of these erosional processes would allow the preservation of older fault scarps at lower elevations. Note that these findings apply for Attica, meanwhile multiple sample locations at different elevations in central Italy did not show

preservation of fault scarps older than 15 ± 3 ka (e.g. Cowie et al., 2017; Beck et al., 2018). This suggests that the preservation of older fault scarps was favoured at lower latitudes (such as in Attica), where the erosion processes associated with the last glaciation were less intense, meanwhile at higher latitudes (such as in Central Italy) the erosion processes associated with glacial-periglacial conditions were intense enough to not to be influenced by the elevation of the fault scarps. In addition to this, given the proximity of the lower fault scarps with the sea coast (e.g. the Milesi fault, Figure 7.2), it is possible that the influence of the Mediterranean sea into the climate conditions might have mitigated the erosion processes, and therefore facilitated the preservation of older fault scarps. Overall, the preservation of older fault scarps raises possible issues for seismic hazard assessments in Attica. Fault slip-rates, when measured across fault scarps (e.g. Deligiannakis et al., 2016, and references therein), are commonly calculated over 15 ± 3 ka, which is thought to be the age of the last glacial maximum in Mediterranean area (e.g. Roberts and Michetti, 2004). However, if the fault scarps are low in elevation, it is possible that they started to be preserved before that age, and therefore the calculated slip-rates might be lower than expected. This might have implications for seismic hazard assessments of the city of Athens. Hence, the correlation between elevation and age of the scarp recommends that more care should be taken in constrain the age of fault scarps at lower latitudes. For example, appropriate stratigraphic and dating analyses of the slope deposits sequences in the coastal area of N Attica and Southern Evoikos Gulf (e.g. pedostratigraphy, soil data, tephrocronology) should be performed in order to further constrain the age of the fault scarps at lower latitudes.

A final question that arises must be how the variation in slip-rate that occurs during the passage from an anti-cluster to a cluster in time compares with the variation from low to

high slip-rate spatially across the type of fault bends discussed in earlier chapters. Previous chapters have shown that the slip-rate can double into a fault bend, associated with larger coseismic slip magnitudes. The ^{36}Cl results show that slip-rates can go from zero to a finite value within a few hundreds of years. This means that the type of slip-rate increase across a bend may not be recognised unless temporal earthquake clustering exists, but this is not recognised, for example in a palaeoseismic study of duration shorter than a typical cluster. The ^{36}Cl results show clusters last only a few millennia (e.g. 4.3 m slip in 2-3 millennia for Milesi) compared to many millennia for anti-clusters (e.g. zero metres slip between ~30 and 12 ka, again for Milesi). Given these values, it is clear that studies of spatial variation of slip and slip-rate cannot be conducted over time periods shorter than many millennia in a fault system with faults interacting across strike, as an apparently inactive fault may re-awaken due to its transition from an anti-cluster to a cluster on this timescale.

Overall, the measurements and modelling of cosmogenic ^{36}Cl concentrations on fault planes on three faults arranged across the strike of a fault system in central Greece provides fundamental insights on (1) the dynamics of normal fault systems, on (2) the mitigation of the seismic hazard of a densely-populated city like Athens and on (3) the interplay between the erosion processes associated with glacial-periglacial conditions and elevation on the preservation of fault scarps.

7.8 Conclusions

The measurements and modelling of cosmogenic ^{36}Cl concentrations up to fault planes on three principal faults with approximately parallel strikes within the Attica fault system

(central Greece) show that earthquakes on these faults are clustered, with a non-systematic alternance of periods of rapid slip accumulation (i.e. earthquake clustering) and periods of quiescence (i.e. earthquake anti-clustering). The comparison between the modelled slip histories shows that the activity switches between faults, with earthquake clusters alternating on the different faults. Earthquake clustering on one specific fault is accompanied by low rates of activity on the other faults. These results show that parallel faults interact in terms of sharing the regional strain-rate, with switching activity that affects the slip-rate on a single fault. The clustered behaviour of parallel faults implies that the definition of key parameters for seismic hazard assessments (T_{mean} , T_{elap} and CV) is complicated in fault systems with across-strike distributed faults. Moreover, this work suggests that the preservation of a tectonic fault scarp is strictly related to the elevation above the sea level, with older fault scarps preserved at lower elevations, implying a gradual migration of the demise of the erosional processes associated with the last glaciation towards higher elevations. This work provides fundamental insights on the mitigation of the seismic hazard of Athens and on the dynamics of normal fault systems.

Chapter 8

Discussion

This chapter discusses the implications of the results in previous chapters in terms of (1) palaeoseismology studied through trenching, (2) gaining deformation rates from normal faults using cosmogenic isotopes (3) scaling relationships, (4) fault spacing, (5) seismic hazard, (6) off-fault deformation, (7) the long-term geomorphology and geology of extensional basins, (8) the effect of fault bends on behaviour and development of reverse and strike slip faults.

8.1 Summary of findings from previous chapters and questions that arise.

This PhD thesis provides a series of studies on the relationship between the non-planar geometry and the seismic behaviour of active normal faults. Several examples presented herein have shown that throw and fault dip increase within along-strike fault bends in order to preserve the horizontal strain-rate within the bend and along the fault. This has been demonstrated for a variety of normal faults (a) located in different geodynamic domains and (b) for measurements of throw taken over different time periods (coseismic throw, Holocene throw and geologic throw). Furthermore, throw enhancement within fault bends has been observed on (1) immature faults, where fault bends are still propagating up to the surface and are not yet fully established, (2) well-established single fault segments, where fault bends affect one continuous fault segment, and (3) densely-spaced fault systems arranged across strike, where a change in strike across several fault

segments creates an overall bend in the system. Overall, the studies carried out in Italy and Iceland, together with studies of coseismic events in USA, Mexico and Greece, show that the “Geometry-dependent throw-rate theory” applies over different geological domains, and it is not only confined to Italy, where it was developed (Faure Walker et al., 2009; 2015).

Another aspect is that it appears that the deformation described in previous chapters shows some elements of scale independence: throw enhancements occur in the same way for faults at different scales, from faults a few-kilometres long to broad fault systems ~50 km long. This means that the control that the fault geometry exerts on the distribution of throw and throw-rates must be included in different sets of studies, from studies concerning one single fault (e.g. Manfield and Cartwright, 2001), to analysis of the behaviour of entire fault systems (e.g. Cowie and Roberts, 2001; Roberts and Michetti, 2004).

In the following sections the above results are used to investigate the following questions.

- 1) What is the effect of the non-planar fault geometry on interpretations of palaeoseismic datasets and what future work is required?
- 2) In terms of the cosmogenic dating of fault scarps, if the presence of bends is not recognised and the sampling site is located within a fault bend, how much this would affect the modelled slip history, and what future work is required?
- 3) What is the effect of the non-planar fault geometry on interpretations of fault scaling and stress drops and what future work is required?

- 4) What are the implications for studies of strain accumulations for fault systems with varied fault spacing?
- 5) How much does the variability of slip-rates due to fault bends affect seismic hazard assessments and what future work is required?
- 6) Can fault bends be one of the possible explanations for the complex patterns of off-fault deformation associated with normal-faulting earthquakes, as shown by satellite interferograms, and what future work is required?
- 7) Is non-planar fault geometry relevant in modelling the long-term evolution of the tectonic geomorphology associated with normal faulting and what future work is required?
- 8) Do along-strike fault bends affect also the distribution of throw for reverse and strike slip faults, and what future work is required?

8.2 Implications for palaeoseismology

This section explores the effect of the non-planar fault geometry on the interpretations of palaeoseismological studies, carried through trenching site interpretations and cosmogenic dating of exposed fault planes.

8.2.1 Trench site interpretations

The scale-independence and the persistence through time of the effect of non-planar fault geometry on the distribution of throw may affect palaeoseismological studies that do not take fault bends into account. Trenches located within a still immature fault bend, within a well-established fault bend along a single fault, or across a fault segment located within

a bend that affects an entire fault system may present values of D_{max} biased by the effect of the bends itself. This complication is raised because in Chapter 4 it was noted that coseismic throw was enhanced in bends for the earthquakes in 2016 on the Mt. Vettore fault in central Italy, and for the 1983 Borah Peak, USA, 1981 Gulf of Corinth, Greece, and 1887 Sonora, Mexico earthquakes. Therefore, the magnitudes derived from the D_{max} measured in the trenches located in bends, but not recognised as such, might overestimate the real magnitudes of the palaeoearthquakes. This suggests that extreme care should be applied in choosing the location of a palaeoseismological trench, in order to avoid biased measurement of coseismic D_{max} .

An example of this may be in the study by Pantosti et al. (1996) from central Italy (Figure 8.1). They excavated trenches in the Piano di Pezza, located at the extreme NW tip of the overall Fucino fault defined by Roberts and Michetti (2004), where the fault displays a major fault bend with its strike changing from NW-SE to WNW-ESE (Figure 8.1; other interpretations of the fault segmentation in the area are in Giraudi, 1988; Blumetti et al., 1993; Galadini and Messina, 1994). They found surprisingly large coseismic throws of 2.8-3.4 m per event for palaeoearthquakes within a few hundreds of metres of the overall fault tip defined by Roberts and Michetti (2004). These large coseismic throws were associated with total offsets across the scarp of up to 11.5 m in ~7-10 ka (implying a throw-rate of 1.15-1.64 mm/yr), so again these offsets are surprisingly large given their proximity to the overall fault tip.

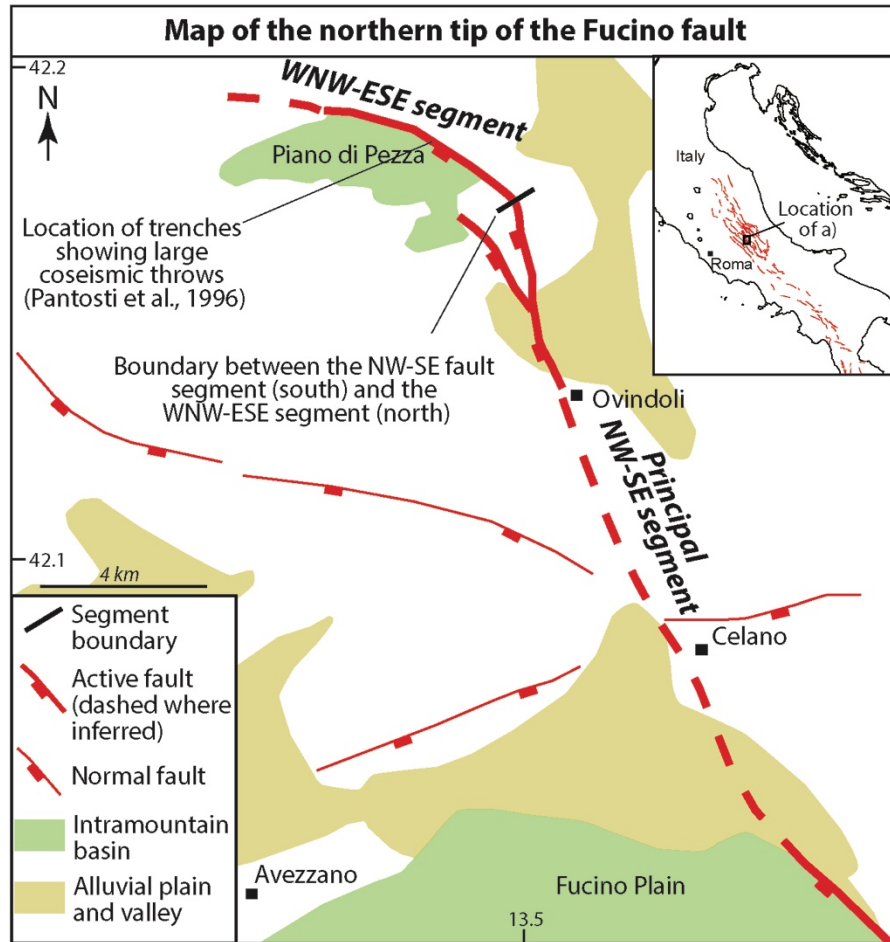


Figure 8.1: Map of the northern tip of the Fucino fault. Principal fault trace (thick red line) is adapted from Pantosti et al., (1996) and Roberts and Michetti (2004). Thin red lines are other normal faults. Intramountain basins and alluvial plain and valley are adapted from Pantosti et al., 1996. This figure shows that the northern tip of the Fucino fault presents a prominent bend, and this can explain the large coseismic throws observed in trenches excavated in the Piano di Pezza by Pantosti et al., (1996).

One explanation for this may be the change in fault strike. Following the findings presented in this thesis, one would expect the throw to be enhanced by 2 or 3 relative to the portion of the fault with a NW-SE strike, as shown in Chapter 4. Thus, although Pantosti et al. (1996) interpret that this fault accommodates a horizontal extension rate of ~ 1.1 mm/yr, a value that is $\sim 1/3$ of the total extension rate across this part of the Apennines, the results of this thesis suggest that the significance of the D_{max} value and extension-rate at this site should be re-appraised. In other words, this thesis suggests that local measurements of D_{max} and extension-rate from palaeoseismology should be

interpreted only once calculations that take into account the local fault geometry have been accomplished. Further work in palaeoseismology should involve a review of all existing palaeoseismic datasets with a view to establishing the extent to which the derived deformation rates result from local 3D fault geometry as opposed to regional deformation.

The uncertainty in palaeoseismological studies given by the effect of fault bends on the distribution of throw adds up to other uncertainties that are carried by palaeoseismological measurements. For instance, as described in Chapter 2, Section 2.3.1, faults might be complex structure formed by several splays, and coseismic ruptures might not rupture always the same location. Hence, palaeoseismological studies based on trench excavation across one fault splay might not be representative of the overall fault behaviour. To solve this issue, some authors have introduced the concept of the “seismic landscape”, defined as the cumulative geomorphological and stratigraphic effect of the signs left on the environment of an area by its past earthquakes over a geologically recent time interval (Serva and Slemmons, 1995; Serva et al., 1997; Michetti and Hancock, 1997; Michetti et al., 2005; Guerrieri et al., 2009; Blumetti et al., 2013). The concept of the “seismic landscape” suggests that the magnitude assigned to a seismic event identified, for instance, by trenching analysis should be consistent with the geomorphology and stratigraphy of the area. A seismogenic structure capable of a M 7 earthquake should form a characteristic “seismic landscape” that differs from the seismic landscape formed by a structure capable only of M 6 earthquakes. Hence, the comparison between the results obtained from palaeoseismological analysis and the “seismic landscape” of the fault should help to check that the assessed magnitude and recurrence interval are consistent with the geological and geomorphic evidences around the causative earthquake source. However, at the time of writing the definition of the seismic landscape of a normal active

fault does not include the effects that fault bends can produce on the seismic landscape of normal faults. The results shown in this thesis suggests that more slip accumulation within fault bends might cause (1) more hangingwall subsidence in front of the bend, influencing the drainage pattern in the hangingwall of the fault, and (2) maxima in the fault relief associated with a normal fault. It therefore seems that bends might play a role in the seismic landscape of a normal fault. Hence, more work is needed to study how the effect of fault bends can affect the seismic landscape of active normal faults.

8.2.2 Cosmogenic dating of exposed fault planes

This section explores whether non-planar fault geometry might influence the choice of sites for *in situ* ^{36}Cl cosmogenic dating of fault scarps. As Chapter 7 has shown, cosmogenic dating of fault planes is performed across fault scarps which are exclusively exposed by tectonic activity, and therefore the fault scarp height represents the amount of slip accumulated by the fault since the scarp started growing (e.g. usually since the demise of processes associated with the LGM, 15 ± 3 ka, in the Mediterranean area). To retrieve the fault slip history, the code available in Beck et al. (2018) models the measured cosmogenic ^{36}Cl concentrations along a fault scarp of a measured height. However, this thesis shows that throw and throw-rate enhancements occur for measurements taken over the last 15 ± 3 ka. Therefore, if the fault bends are not acknowledged and the sampling site is located within a bend segment, the recovered slip history might not be representative of the overall fault, because the slip and slip-rates at that site are biased due to the effect enhanced slip within the bend (Figure 8.2).

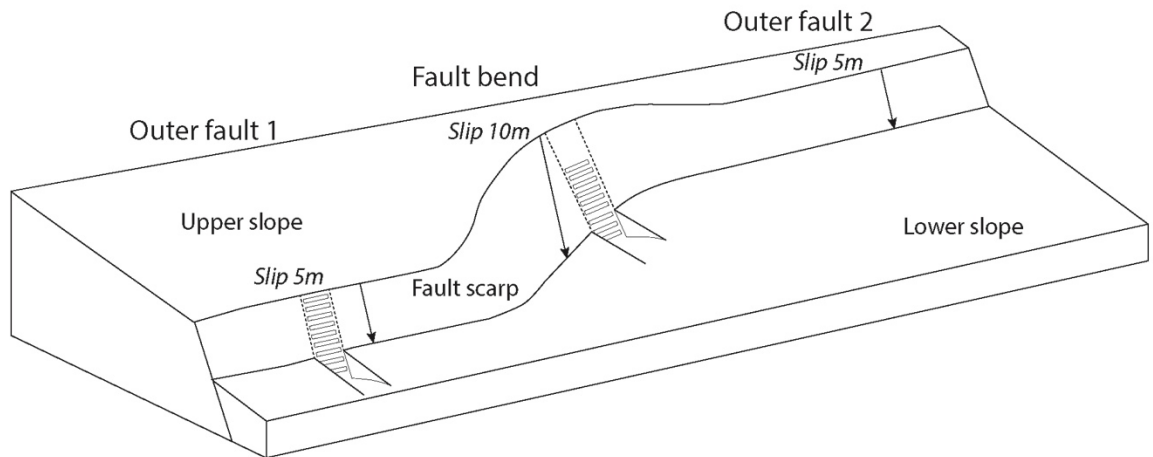


Figure 8.2: Schematic fault with a prominent bend in its central part. The slip accumulated within the bend doubles the slip on the outer faults. Two sampling sites, on one outer fault and on the bend, are hypothesized. Arrows show consistent slip vector along the entire fault.

To examine the strength of the influence of fault bends on cosmogenic dating of fault planes, and hence model sensitivity, modelling of cosmogenic ^{36}Cl concentrations has been performed in two different locations along a hypothetical fault (Figures 8.2 and 8.3). The hypothetical fault is characterized by an along-strike fault bend in its central part and two outer faults with the same strike and same cumulative slip since the demise of the LGM (5 m). In agreement with the findings of this thesis, the slip within the fault bend is set to be double the value for slip on the outer faults (i.e. 10 m). The modelling has been performed following the methodology outlined in Chapter 3. The parameters needed to perform the modelling are maintained exactly the same for sites within and outside the bend, including the same concentrations of cosmogenic ^{36}Cl up the fault plane, taken from the Milesi fault sampling site (see Chapter 7), except that the amount of slip on fault is varied from 5 m to 10 m. This situation simulates a case where the entire fault scarp can be sampled on the outer faults, whilst only the lower part of the fault scarp can be sampled within the bend.

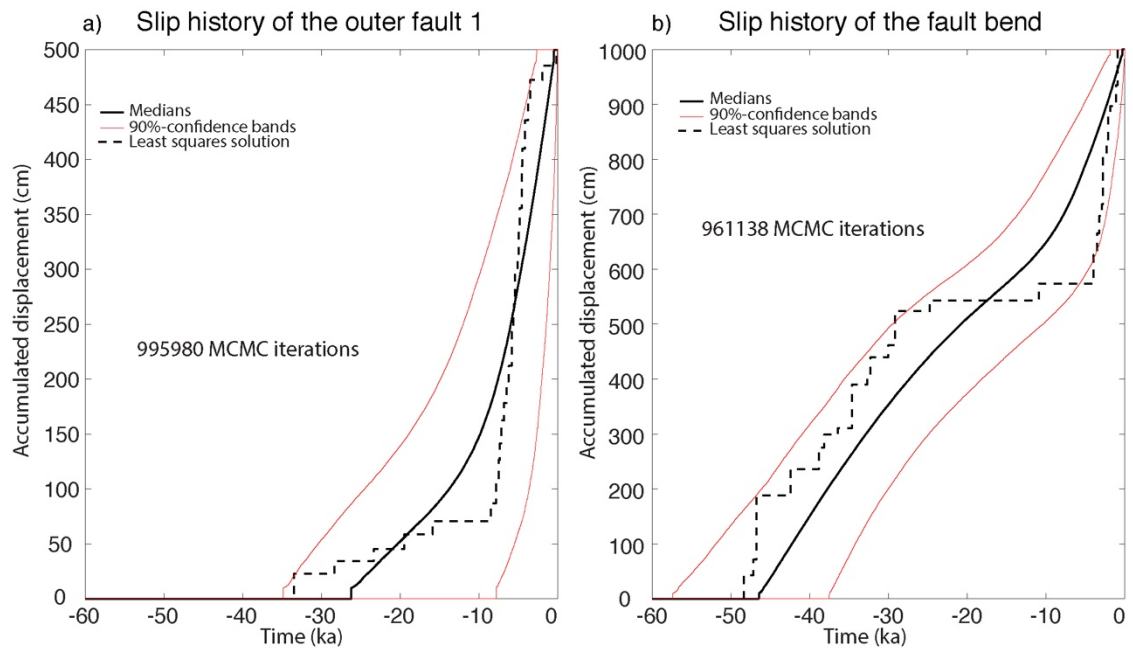


Figure 8.3: Modelling the ^{36}Cl concentrations on the hypothetical fault shown in Figure 8.2. a) is the derived slip history for the outer fault 1, b) is the derived slip history for the fault bend. This figure shows that if a fault bend is not recognised, and cosmogenic sampling is performed on the fault bend, the slip history derived within the bend will be different from the slip history derived from cosmogenic sampling on a straight fault segment, and therefore not representative of the overall behaviour of the fault.

The results in Figure 8.3 show that the slip history retrieved within the fault bend differs from the slip histories retrieved by the outer fault. This could be because within the bend the Beck et al. (2018) code has to model the same concentration of ^{36}Cl on a fault plane that is double the height of the fault plane on the outer fault. Therefore, the required slip histories for the bend and the outer faults must be different, in order to reproduce the same ^{36}Cl concentrations on two fault planes with different on-fault slip. For instance, Figure 8.3 show that the code requires the slip history within the fault bend to start earlier in time, compared with the slip history on the outer fault, in order to model the larger amount of slip within the bend.

These findings highlight also the importance of building the fault scarp profile on the same location of the sample site. In fact, it might be the case that a good fault plane for

sampling does not have clear upper and lower slopes, and therefore the fault scarp profile, needed to constrain the on-fault slip, might be constructed on another location in the surroundings of the sample site. The test herein performed shows that changing the value of on-fault slip has an important impact on the retrieved slip history, and therefore modelling the ^{36}Cl concentrations using an on-fault slip gained on a different location might lead to derive slip histories that are not representative of the real fault behaviour.

Overall, this work suggests that if cosmogenic sampling is performed across an unrecognised fault bend, the retrieved slip history might not be representative of the actual fault slip history. Therefore, future studies (for instances, a sampling campaign along the same fault within and outside a fault bend) should be performed in a way that takes the results of this section into account, in order to better understand what is the effect of fault bends on the cosmogenic dating of fault planes.

8.3 Implications for scaling relationships

This thesis shows that along-strike fault bends can be one plausible explanation of the scatter in D_{max} values shown in empirical scaling relationships of D_{max} /rupture length and M_w/D_{max} (see Chapters 2 and 4; e.g. Wells and Coppersmith, 1994; Manighetti et al., 2007; Wesnousky et al., 2008). This prompts the idea that future and revised empirical scaling relationships should report whether the D_{max} is measured within bends or it is measured along other fault segments. This could help to build empirical scaling relationships that avoid biased measurements of D_{max} due to fault bends, and that can therefore be more representative of the behaviour of normal faults. Chapter 4 also shows that biased D_{max} values lead to biased inferences of stress drop. It appears that claims of

differences in stress drop of 3.5-9.0 MPa implied by D_{max} to fault length scaling (Manighetti et al., 2007) must be re-examined given that 1 order of magnitude variation in stress drop can be explained by local 3D fault geometry (Iezzi et al., 2018; Chapter 4). This is important because stress drop is used to infer the manner in which segmented faults rupture (Manighetti et al., 2007) and the contribution of individual earthquakes to the amount by which the regional tectonic stress imposed by plate tectonics is released. Future work should focus on applying calculations of the kind developed by Faure Walker et al. (2009) and this thesis to strike-slip and thrust settings not covered herein.

8.4 Implications for studies of strain accumulations for fault systems with varied fault spacing.

Chapter 5 and Iezzi et al. (2019) show that in dense normal fault systems, where faults are spaced ≤ 5 km, single faults work together to accommodate the regional deformation. To the contrary, Chapter 7 suggests that where faults are spaced > 5 km (e.g. 6-15 km spacing in Attica), cosmogenic dating of exposed fault planes shows a switching of activity between across-strike faults, with alternation of earthquake clusters and anti-clusters on individual faults, synchronised with the opposite on faults across strike. These findings imply that analysis of fault spacing is important in order to establish the behaviour of faults within regional fault networks. Closely-spaced faults are likely to be working together to accommodate the deformation, with the possible occurrence of multi-fault earthquakes. On the other hand, more distant faults are likely to share the activity in order to accommodate the deformation, with the temporal alternation of activity.

One implication of this is how we should interpret slip-rate databases for faults. The occurrence of earthquake clusters and anti-clusters on single faults complicates interpretation of measurements of fault slip-rates. For instance, if a palaeoseismological trench is excavated on a fault currently experiencing a cluster, the derived slip-rate would be anomalously large, and hence unrepresentative of the long-term fault slip-rate. Therefore, this thesis highlights that extreme care must be used where interpreting measurements of fault slip-rates, because both non-planar fault geometry and earthquake clustering can affect single measurements of slip-rates, and therefore these might not represent the long-term behaviour of the fault. Future work should re-examine studies where slip-rates are used to infer regional deformation rates or rates of earthquake occurrence.

8.5 Effect of non-planar fault geometry on the seismic hazard assessments.

As shown in Chapter 1, modern probabilistic seismic hazard assessments (PSHA) derive fault activity rates from geological measurements of fault slip-rates. A question that arises is how the effect of the non-planar fault geometry on the slip-rate should be included into PSHA. That is because on one hand this thesis shows that during surface-rupturing earthquakes the coseismic throw increases within fault bends (Figure 8.4a). On the other hand, it is also shown that Holocene slip-rates are consistently larger within fault bends (Figure 8.4b). The effect is variable due to details of the exact geometry for each example, but in general, Figure 8.4 shows that slip-rates can be increased by up to $\sim 2x$ in fault bends. The implication of this doubling of slip-rate is explored below.

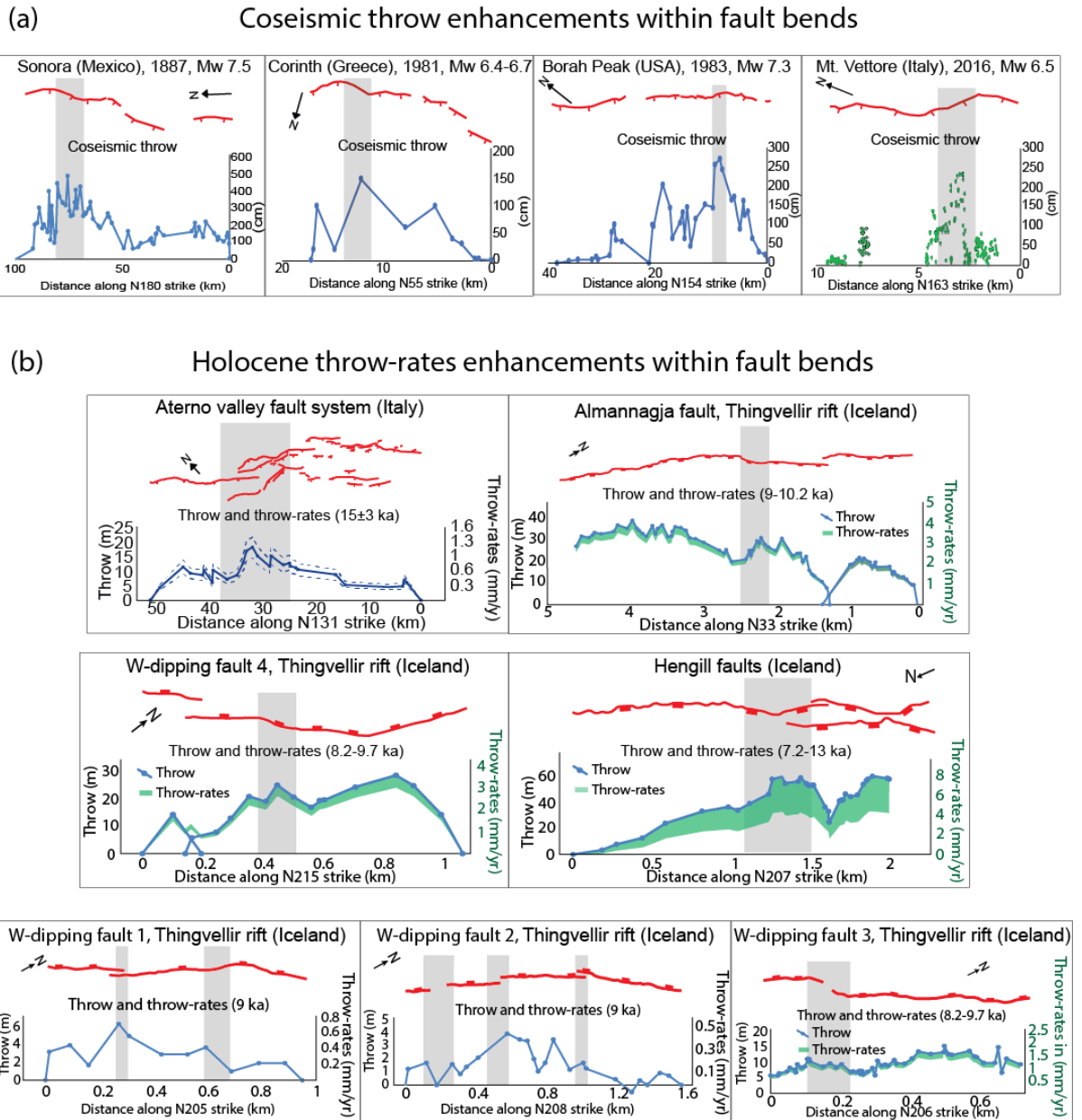


Figure 8.4: Overview of the results of this thesis. a) Coseismic throw enhancements within fault bends. b) Holocene throw-rates enhancements within fault bends. Grey areas highlight the fault bends; green-shaded areas in profiles of faults mapped in Iceland marks the uncertainty in the slip-rate values, due to the uncertainty in ages of the dislocated lava flows. Adapted from Iezzi et al. (2018; 2019) and Chapters 4, 5 and 6.

The above can lead to two different interpretations of the role of fault bends into PSHA. First, Holocene slip-rate enhancements within fault bends can play a role in calculations of magnitude-frequency distributions for a given fault. For instance, if fault bends are not acknowledged and the slip-rate used in PSHA is measured within a fault bend, how much will this affect the probability of occurrence of the next earthquakes?

To test this, calculations of the magnitude-frequency distribution in 50 years associated with two identical hypothetical faults, but with different slip-rates, are performed using the Matlab package FISH (Pace et al., 2016). FISH is a graphical user interface (GUI)-supported tool that is designed to help seismic-hazard modellers analyse fault data. It allows one to evaluate expected earthquake rates, given certain fault data constraints, and to test the consistency between the magnitude-frequency distribution and any available observations (Pace et al., 2016). For this thesis, two of the Matlab tools available in FISH have been used: the MB tool (Moment Budget) and the AR tool (Activity Rates). The FISH MB tool combines standard geological data from faults, like fault length and dip, empirical size-magnitude scaling relationships and rheological properties, to calculate the moment budget of the fault, which is expressed as the expected maximum magnitude (M_{max}) and the associated mean recurrence time (T_{mean}). The output file of MB is then used as input file for the AR tool, to calculate the probability of earthquake occurrences and the expected annual rates.

For both hypothetical faults, the fault length is set at 20 km, the fault dip at 60° and the seismogenic thickness is 15 km. One fault, hereafter termed Fault 1, has minimum and maximum slip-rates set at 0.6 mm/yr and 0.8 mm/yr (Table 8.1; Figure 8.5a). The other fault, termed Fault 2, has doubled values of slip-rate, mimicking the variation shown in Figure 8.4, with minimum and maximum values set at 1.2 mm/yr and 1.6 mm/yr (Table 8.1; Figure 8.5a). No information on previous earthquakes have been included.

Fault name	ScR	Leng th (km)	Dip (°)	Seis thick (km)	SR _{min} (mm/yr)	SR _{max} (mm/yr)	M _{obs}	σ M _{obs}	Last eq time
Fault 1	WC94-N	20	60	15	0.6	0.8	NaN	NaN	NaN
Fault 2	WC94-N	20	60	15	1.2	1.6	NaN	NaN	NaN

Table 8.1: Input values used to perform modelling into the MB tool. ScR = Scaling relationship used; Seis_thick = seismogenic thickness; SR_{min} = minimum slip-rate; SR_{max} = maximum slip-rate; M_{obs} = maximum observed magnitude; σ M_{obs} = maximum magnitude standard deviation; WC94-N = Wells and Coppersmith (1994) – normal faulting regression; NaN = not available.

The MB tool performs calculations based on the input values in Table 8.1, and produces an output file with values of M_{max} and the associated T_{mean} per each fault:

id	M _{max}	sdM _{max}	T _{mean} (yr)	CV	T _{elap}	M _{0_rate}	Fault name
1	6.5	0.2	973	0.71	NaN	7.2759e+15	Fault 1
1	6.5	0.2	487	0.7	NaN	1.4537e+16	Fault 2

Table 8.2: Output values released by the MB tool. id = identification number; M_{max} = maximum magnitude; sdM_{max} = standard deviation of the maximum magnitude; T_{mean} = mean recurrence interval; CV = coefficient of variation of T_{mean}; T_{elap} = time elapsed since the last assigned earthquake; M_{0_rate} = seismic moment rate (N x M x yr⁻¹).

The results in Table 8.2 show that although the two faults have the same expected maximum magnitude M_{max}, the recurrence interval of Fault 1 is almost double the recurrence interval of Fault 2. Table 8.2 has been used as input in the AR tool to model the probability of occurrence of earthquakes using a classic Gutenberg-Richter (GR) distribution (Figure 8.5b). The AR tool calculates the GR distribution as $\log_{10} N_{(M)} = a - bM$, in which $N_{(M)}$ is the number of earthquakes with magnitude less than M_{max} and a is the logarithm of the number of earthquakes with $M \geq 0$. AR computes a to balance the total seismic moment rate with the seismic moment rate that was obtained by the pair M_{max} and T_{mean} . In this model, the lower threshold magnitude of the distribution is set at 5.5 and the b-value is set at 1. The probability window is set at 50 yrs. These parameters have been maintained the same for both faults.

The GR distribution shows the annual cumulative rates for each magnitude calculated in 50 years on the y-axis and the magnitudes on the x-axis (Figure 8.5b):

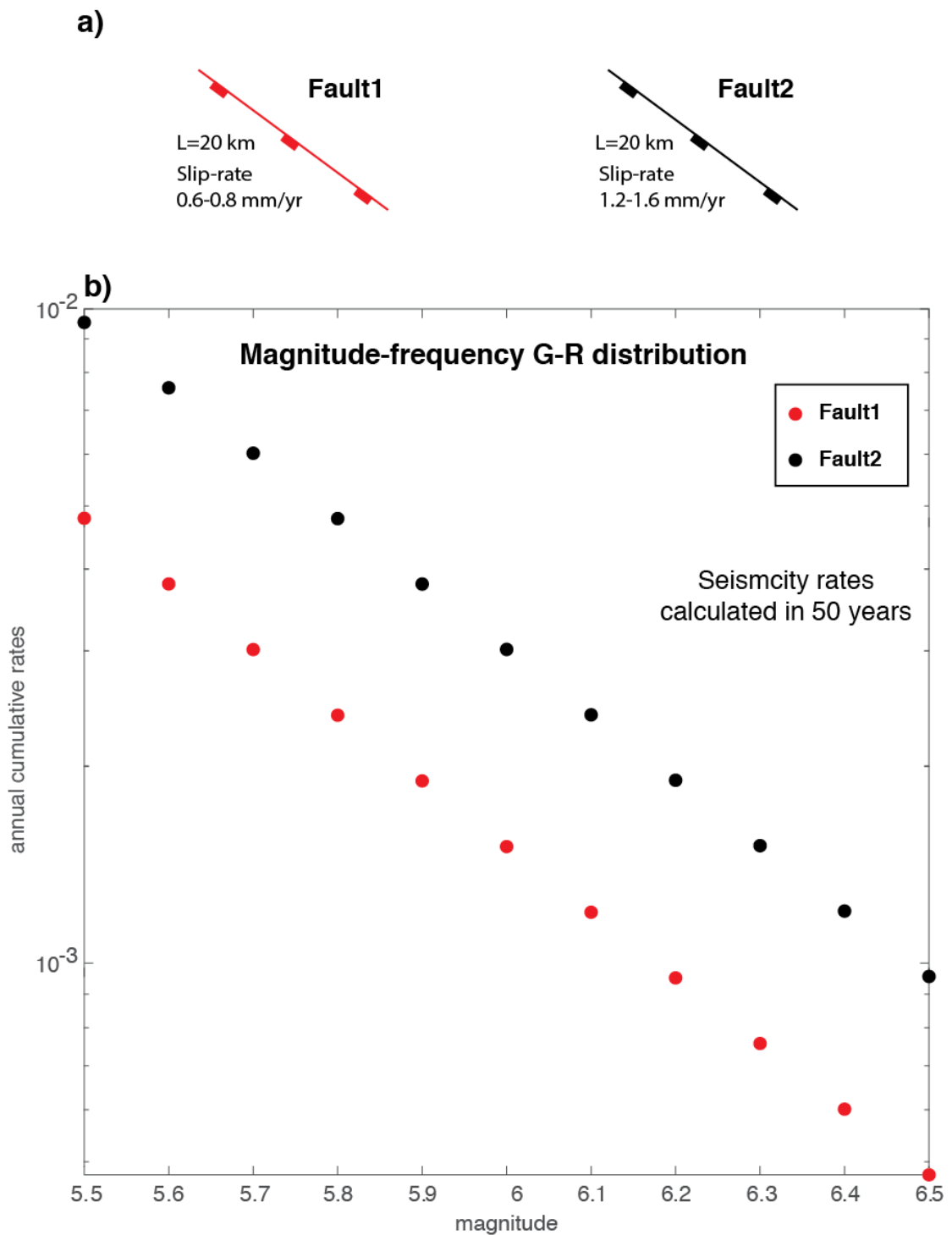


Figure 8.5: The effect of slip-rate enhancements on the seismicity rates of faults. a) Two identical faults but with different slip-rates; Fault 2 has double the slip-rate of Fault 1. b) Magnitude-frequency Gutenberg-Richter distribution calculated in 50 years. The graph shows that the fault with higher slip-rates have annual rates of earthquakes higher than the fault with lower slip-rates.

The graph in Figure 8.5 shows the influence of slip-rate enhancements within bends on the probability of earthquake occurrence. The annual cumulative earthquake rates of Fault 2, which has double the slip-rate of Fault 1, are sensibly higher than the rates of Fault 1. Therefore, if the fault bend and enhancements of throw within it are not explicitly considered, using slip-rates measured within a fault bend would lead to PSHA with larger probability of occurrence of earthquakes in 50 years, compared to PSHA performed using slip-rates measured across straight fault segments.

However, this thesis shows also that the coseismic throw increases within fault bends. This could suggest that the slip-rate enhancements measured across fault bends might not be due to a larger number of earthquakes through time, as shown by Figure 8.5b, but rather they may be due to a larger slip-per-event associated with earthquakes within bends (e.g. Chapter 4). If this is true, then calculations as shown in Figure 8.5b might not reflect the actual magnitude-frequency distribution of the fault. Future work should explore more in detail the effect of the fault bends into PSHA, in order to avoid misleading interpretations of magnitude-frequency distributions. It is stressed that without the immediate, post-earthquake studies of coseismic ruptures like that in Chapter 4 (Iezzi et al., 2018), despite the danger to the scientists involved due to aftershocks and rockfalls in the steep, mountainous terrain involved, the insight in this section could not be gained. Immediate, post-earthquake studies of coseismic ruptures are an essential feature of the study of earthquake geology and provide important insight into earthquake recurrence alongside calculations of expected slip enhancement associated with fault bends.

8.6 Effect of non-planar fault geometry on the coseismic off-fault deformation

All the results presented in this thesis have a focus of on-fault deformation. This contrasts with the prevalence of Interferometric Synthetic Aperture Radar (InSAR) and by Global Positioning Systems (GPS) studies of earthquakes that attempt to measure, quantify and model off-fault deformation using planar fault models embedded in elastic half-spaces. This raises the question of how bends in faults influence off-fault deformation. Observations herein of hangingwall lake beds located close to fault bends (as shown for the Mt. Vettore fault and for the Hengill faults, Chapters 4 and 6, respectively) suggest that the fault bends may influence the deformation pattern in the fault surroundings, causing more subsidence in front of the bend due to greater accumulation of on-fault slip. However, observations such as these have not received the attention they deserve, because most of the fault slip models that attempt to reproduce the deformation field shown by InSAR and GPS are based on straight, planar faults, so fault bends are not taken into account.

For instance, following the 30th October 2016 M_w 6.5 Mt. Vettore earthquake in Central Italy, a variety of coseismic slip models were produced to account for the complex deformation pattern shown by InSAR, GPS, seismological data and coseismic field measurements (Lavecchia et al., 2016; Tinti et al., 2016; Cheloni et al., 2017; Chiaraluce et al., 2017; Chiarabba et al., 2018; Huang et al., 2017; Liu et al., 2017; Papadopoulos et al., 2017; Pizzi et al., 2017; Xu et al., 2017; Cirella et al., 2018; Scognamiglio et al., 2018; Walters et al., 2018; Wang et al., 2018; Cheloni et al., 2019) (Figure 8.6). In general, these authors agreed that the rupture of only one single planar fault was insufficient to

reproduce the deformation pattern, and different rupture scenarios have been suggested. Pizzi et al. (2017) and Chiarabba et al. (2018) suggested that a basal thrust (Mt. Sibillini thrust) played a role in the distribution of the coseismic slip of the earthquake (see the geological background in Chapter 4 for details on the regional geology). Similarly, Scognamiglio et al. (2018) proposed that a secondary low-angle fault, oblique to the Mt. Vettore fault and possibly associated with the Mt. Sibillini thrust, ruptured during the earthquake, and hosted a large amount of coseismic slip. To the contrary, Cheloni et al. (2017; 2019) excluded the involvement of low-angle faults and hypothesized that the rupture on the Mt. Vettore fault was accompanied by the rupture of minor antithetic faults located on the opposite side of the Castelluccio plain. A different model proposed by Walters et al. (2018) have instead modelled the Mt. Vettore fault as a number of synthetic and antithetic planar splays, and included the possibility that an additional cross-fault bounding the south flank of the Castelluccio plain slipped during the earthquake (Figure 8.6).

The common feature in these different models is the representation of faults as straight and planar segments. Fault bends are not included in any of these models, although these are suggested to have influenced (1) the distribution of the coseismic surface slip (Iezzi et al., 2018) and (2) the propagation of the mainshocks of the 2016 Central Italy seismic sequence (Mildon et al., 2017). Therefore, a question that arises is if the local non-planar fault geometry can be one of the plausible explanations of the complex deformation patterns.

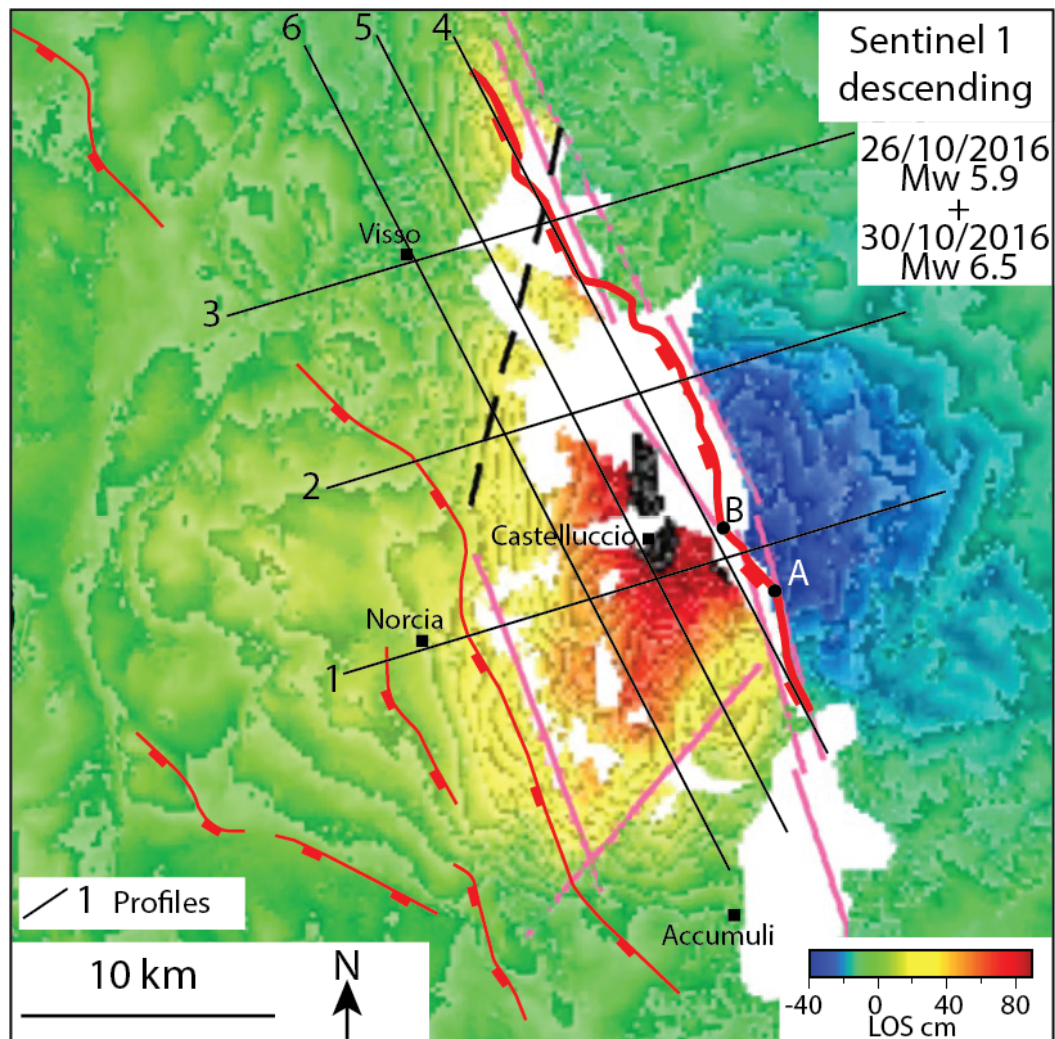


Figure 8.6: Observed InSAR line-of-sight displacement for the 26th October 2016 M_w 5.9 and the 30th October 2016 M_w 6.5 earthquakes, Central Italy (see Chapter 4 for details on the seismic sequence). Warm colours show motion away from the satellite, and fringes show ~ 2.8 cm contours of displacement. Black lines are traces of transects shown in Figure 8.5. Thick red line is the trace of the Mt. Vettore fault; thin red lines are other active faults; pink straight lines are synthetic and antithetic fault splays used in Walters et al. (2018) to model the coseismic slip distribution. Modified from Walters et al., 2018. Note the location of the fault bend A-B, discussed in Chapter 4, close to the maximum subsidence.

To address this question, this thesis attempts to reproduce the observed InSAR line-of-sight displacement for the 26th October 2016 M_w 5.9 and the 30th October 2016 M_w 6.5 earthquakes (Figure 8.6; Walters et al., 2018), using solely the non-planar geometry of the Mt. Vettore fault (Figure 8.7a). The same is performed using the straight geometry of the Mt. Vettore fault for comparison (Figure 8.7b).

The coseismic slip distribution for the non-planar fault geometry is built following the methodology outlined in Mildon et al. (2016b) (Figure 8.7). The non-planar fault trace of the Mt. Vettore fault is defined with fieldwork and published geological maps (see Chapter 4 for details). The fault dip is set at 60° , a common value of dip for normal faults and consistent with the range of dip measurements taken during fieldwork (Iezzi et al., 2018; Chapter 4). The seismogenic depth is set at 15 km, a common value for this region (e.g. Cowie et al., 2013). A bull's eye slip distribution is assumed at depth. The earthquake is assumed to have ruptured the entire fault length.

The Matlab code available in Mildon et al. (2016b) allows one to reproduce earthquakes by setting a variety of parameters: (1) the non-planar fault trace, (2) the amount of slip at depth, (3) the depth of the bull's eye, (4) the skewness of the slip distribution along strike, and (5) the amount of slip that reaches the surface. Parameters (1) and (4) have been held fixed whilst parameters (2), (3) and (5) have been iterated in an attempt to reproduce an earthquake that has values of M_w and D_{max} at the surface consistent with the natural values shown by the 30th October 2016 M_w 6.5 Mt. Vettore earthquake. The modelling shows that a slip distribution with 2.7 m of slip at 5 km depth and with 90% of slip at depth propagating up to the surface releases a M_w 6.6 earthquake with D_{max} at the surface of 2.36 m, values consistent with the natural values of the M_w 6.5 Mt. Vettore earthquake (D_{max} 240 ± 6 cm) (Figure 8.7a.i). Moreover, the along-strike position of the bull's eye has been chosen in order to locate the modelled surface D_{max} consistently with the location of the measured D_{max} at the surface. This slip distribution has been used as an input file within *Coulomb 3.4* (Lin and Stein, 2004; Toda et al., 2005) to calculate the associated off-fault vertical displacement (Figure 8.7a.ii). The same procedure and

parameters have been used for the straight fault geometry of the Mt. Vettore fault (Figures 8.7b.i and ii). Both models share the same value for M_w .

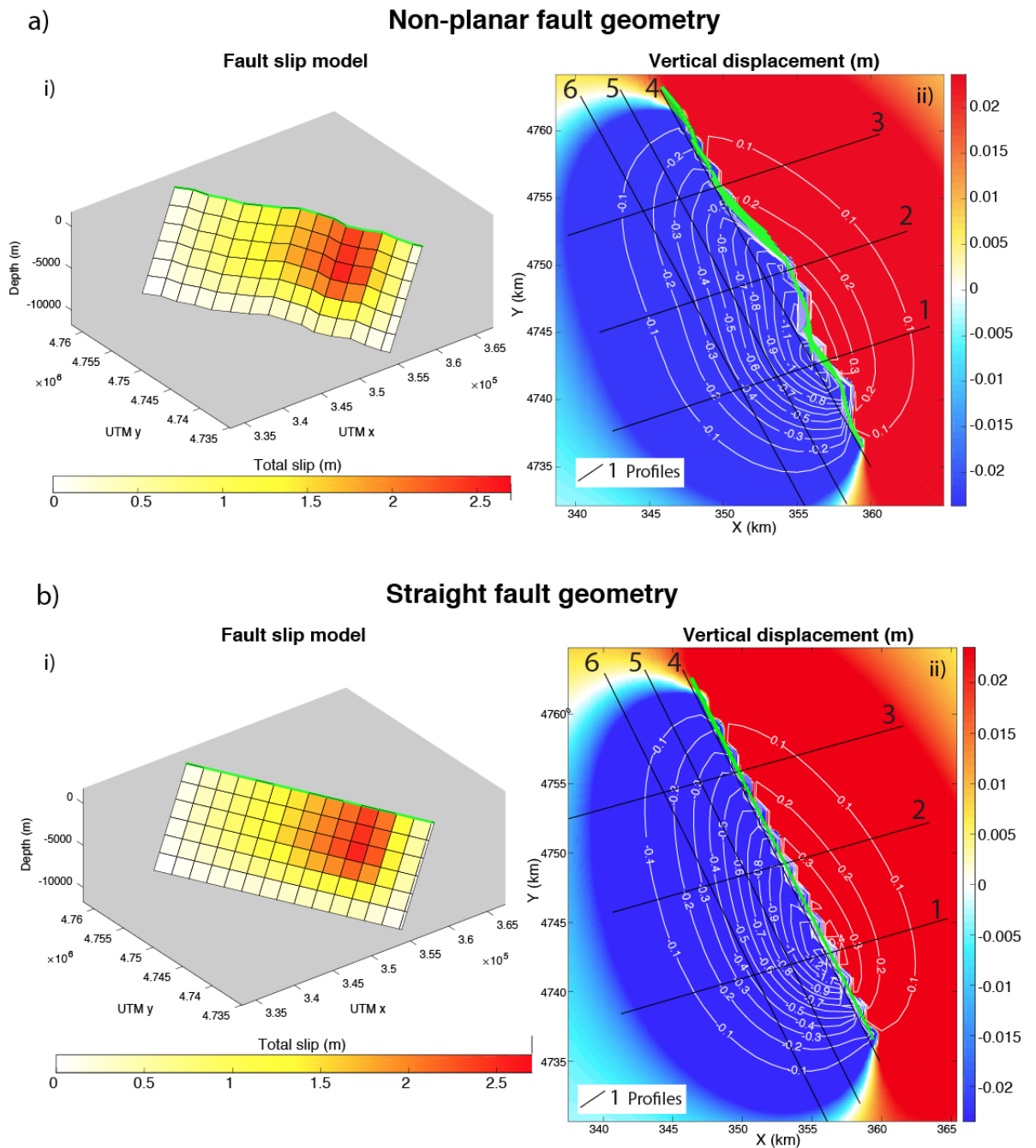


Figure 8.7: Coseismic slip distributions for the Mt. Vettore fault and the related off-fault vertical displacement patterns. a) Slip distribution (i) and associated vertical displacement (ii) for the non-planar fault geometry of the Mt. Vettore fault. b) Slip distribution (i) and associated vertical displacement (ii) for the planar geometry of the Mt. Vettore fault.

To compare these models with the InSAR-derived deformation pattern, six different profiles across the deformed areas have been constructed, three normal to the fault trace and three parallel to the fault trace (Figures 8.6, 8.7 and 8.8).

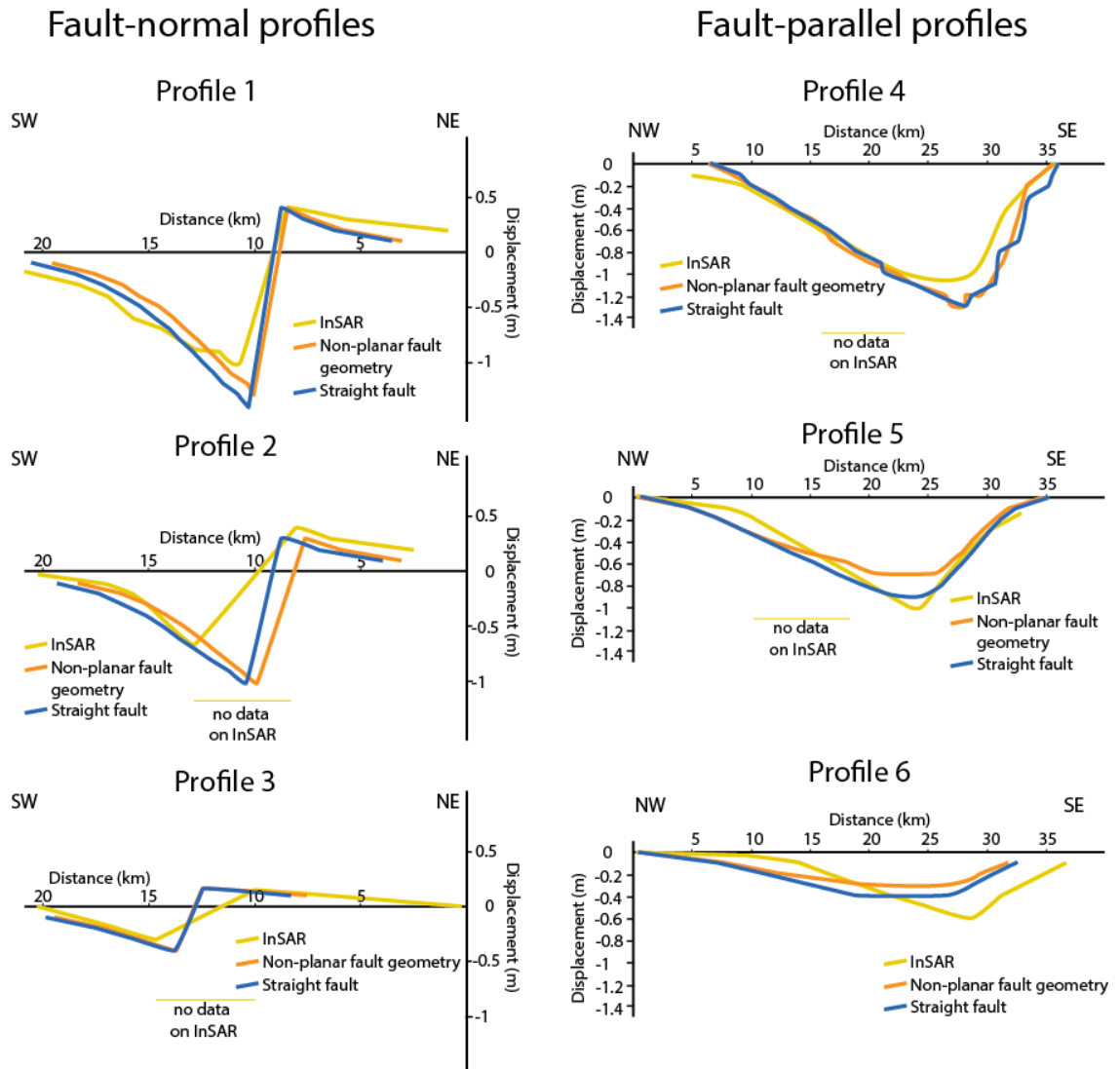


Figure 8.8: Off-fault displacement profiles performed for the InSAR-derived deformation field and for the two models performed in this thesis. Profile traces are shown in Figures 8.5 and 8.6. Yellow lines are InSAR-derived displacement profiles, orange lines are derived from slip models with the real non-planar fault geometry, blue line are derived from slip models with the Mt. Vettore fault expressed as planar fault.

The comparison between the models shows that the use of a different fault geometries can affect the distribution of the off-fault deformation, with different values of

displacement for a given location according to the fault geometry used for most of the profiles (Figures 8.7 and 8.8).

Whilst this is not an exhaustive study, and neither the planar nor the non-planar model adequately explains all the InSAR observations, it is clear that including the non-planar fault geometry does have an effect on the detailed slip distribution and off-fault deformation. In other words, although both models approximate the observed deformation, with off-fault subsidence and uplift located at approximately the correct locations, these results suggest that the use of non-planar fault geometry in coseismic slip distribution models can affect the details of off-fault deformation following normal-faulting earthquakes. It is clear that the locations of maximum uplift and subsidence differ by several kilometres across and along strikes between planar and non-planar models with the same M_w and overall right-skewed slip distribution.

This result is important because it is the difference in the amount and location of maximum uplift and subsidence that are stated as the reasons to justify different source models, with different involvements of the pre-existing thrust, and different arrangements of minor faults and cross-faults (Lavecchia et al., 2016; Tinti et al., 2016; Cheloni et al., 2017; Chiaraluce et al., 2017; Chiarabba et al., 2018; Huang et al. 2017; Liu et al., 2017; Papadopoulos et al., 2017; Pizzi et al., 2017; Xu et al., 2017; Cirella et al., 2018; Scognamiglio et al., 2018; Walters et al., 2018; Wang et al., 2018; Cheloni et al., 2019). The results herein show that suggestions of different involvements of the pre-existing thrust, and different arrangements of minor faults and cross-faults, may be biased by the use of a planar fault geometry.

In summary, future work should focus on developing coseismic slip distribution models using the real non-planar fault geometry, in order to explore whether this can be one of the plausible explanations of the complicated pattern of off-fault deformation shown by InSAR and GPS, and gain a better understanding of the earthquakes in question.

Following these findings, the question that arises is what is the effect of using the non-planar fault geometry in modelling the long-term off-fault deformation? This is discussed in the next section.

8.7 The effect of non-planar fault geometry on modelling the long-term geomorphology associated with normal faulting

The previous section suggests that using the real non-planar fault geometry within coseismic slip distribution models affects the associated coseismic off-fault deformation. Through time, the repetition of normal faulting earthquakes leads to the progressive subsidence of the hangingwall and uplift of the footwall, producing significant topographic fault-related relief (as shown in Chapters 4 and 5). This leads to the formation of footwall mountains, hangingwall basins, and modification of the drainage network in the region around the fault. Guerts et al. (2018) have explored the progressive evolution of drainage networks during active crustal extension in central Italy, studying how the drainage network evolves through time due to the activity of active normal faults. To do so, the authors modelled the total subsidence and uplift associated with the faults since ~3 Ma using a methodology similar to the one applied in Section 8.6 in this thesis, that is, elastic half-space modelling of off-fault deformation, but expanded for the entire fault

history. A key point for this discussion is that the model in Guerts et al. (2018) is based on faults with straight and planar geometry (Figure 8.9).

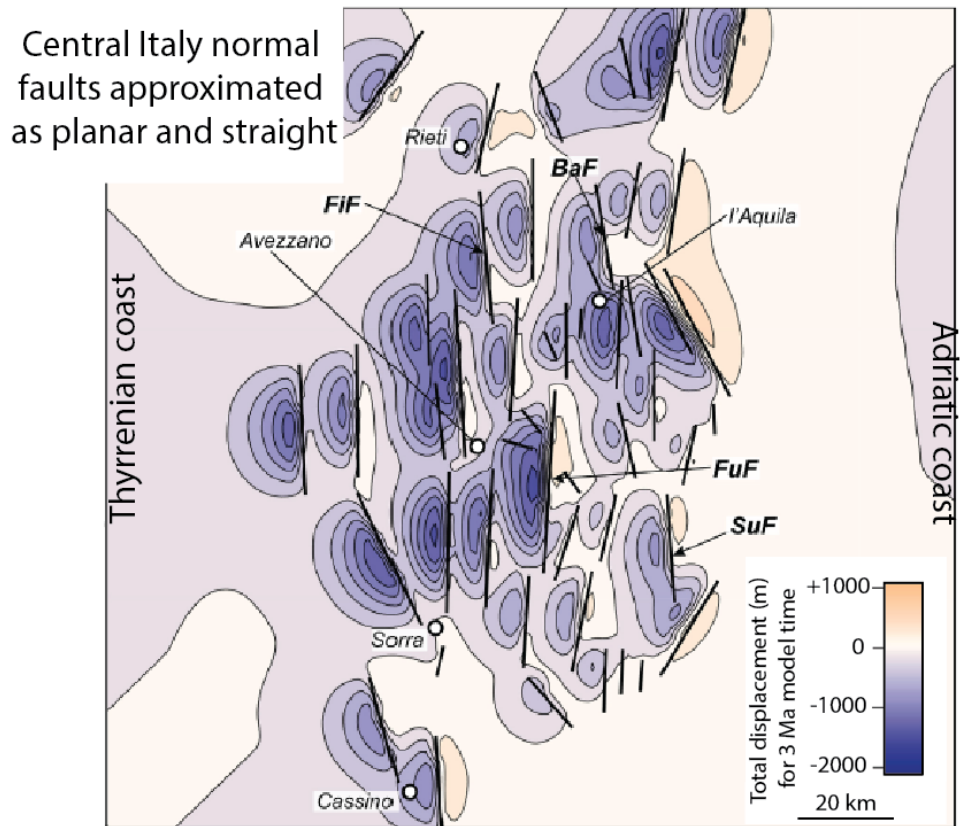


Figure 8.9: Fault model of central Italy from Guerts et al. (2018). All the faults are approximated as having a straight surface trace and planar 3D geometry.

Following the findings shown in Section 8.6, the question arises as to what effect will accrue in models like that in Guerts et al., (2018) if the real non-planar fault geometry is used. In other words, it is important to assess what role the non-planar fault geometry plays in modelling the long-term off-fault deformation pattern, basin and mountain formation and drainage evolution associated with long-term slip and evolution of normal faults. This would be a major undertaking, beyond the scope of this thesis, but an insight can be gained by adapting the off-fault deformation field shown in Figure 8.7 so as to resemble values of the long-term subsidence and uplift of faults in central Italy (Figure 8.10).

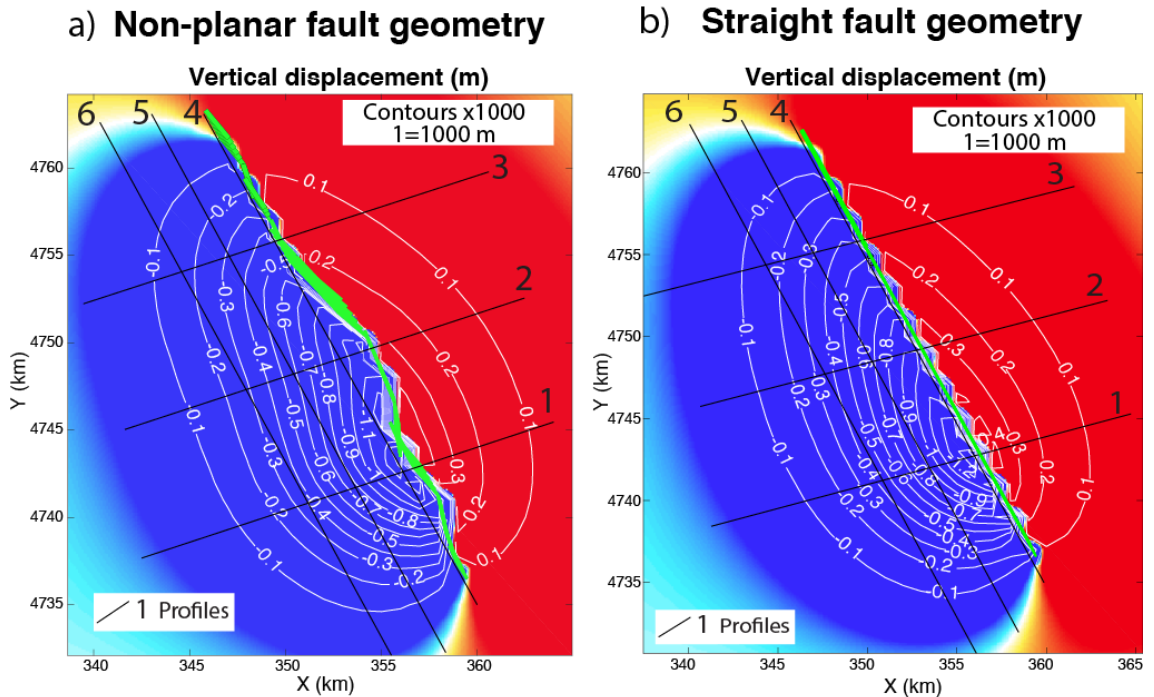


Figure 8.10: Off-fault deformation patterns calculated for a non-planar fault (a) and for a fault with straight geometry (b). Values of contours are multiplied x1000 in order to resemble the values of long-term subsidence and uplift of faults in central Italy.

As in Section 8.6, profiles have been constructed across the two different models to observe the differences in the distribution of uplift and subsidence given the two different fault geometries (Figure 8.11). The comparison between the different profiles shows that the distribution of uplift and subsidence differs according to the chosen fault model. The non-planar model (Figure 8.10a) produces (a) two separate depocenters close to the fault trace that are 2-3 km across, with one located opposite bend A-B and one ~ 5km further to the NW, and (b) a footwall uplift maximum (mountain) that is ~5 km in along strike extent, as opposed the <2-3 km wide localised uplift maximum in the planar model.

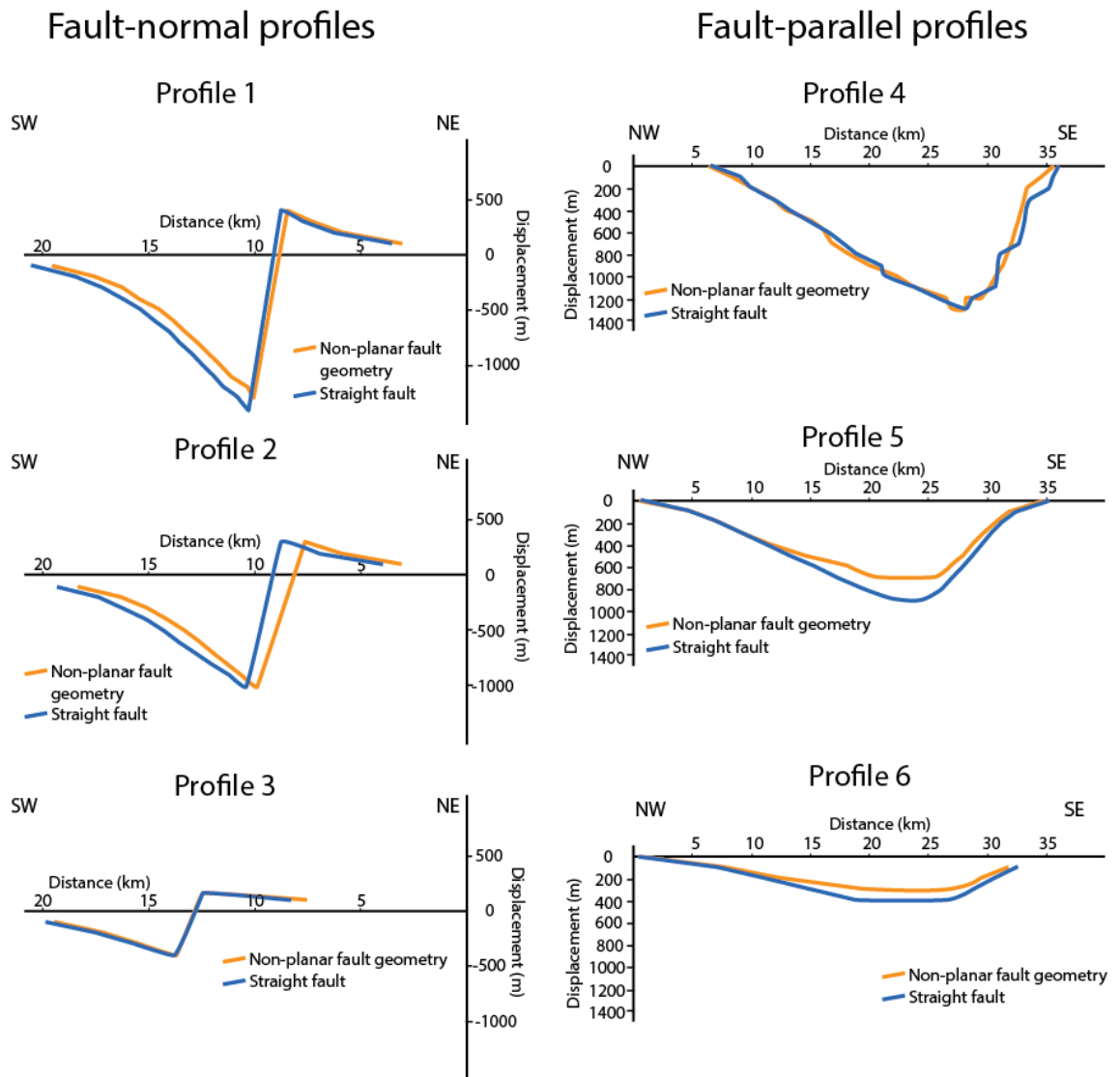


Figure 8.11: Profiles across the subsided and uplifted areas shown in Figure 8.10 for the two different fault models. The traces of the profiles are shown in Figure 8.10. This figure shows that the distribution of uplifted and subsided areas differs if using the real fault geometry compared to the planar fault geometry.

These results are important because Geurts et al. (2018) (1) have a grid resolution of 1000 m in their model, that is appropriate for their model, due to the planar fault geometry they use that produces a relatively uniform surface uplift-subsidence field on a few kilometre length-scale, yet (2) stress the importance for drainage evolution of narrow drainage divides (< 1 km across) and narrow gorges such as the Popoli and Sagittario gorges (which are gorges < 1 km wide in nature). Thus, key features that will control drainage evolution can be < 1 km across, but will not be implicitly modelled in models such as that

in Geurts et al. (2018) because they are not expecting uplift field variations on this length-scale. The results herein are important because they show that uplift field variations on a 1 km length-scale do occur, so the question arises as to whether it is worthwhile upgrading such models to explore the influence of slip distributions that produce topographic features < 1km across. The results herein (Figures 8.10 and 8.11) show that features < 1km across can be produced by non-planar fault models, and so suggest that it may well be worthwhile exploring their influence. In other words, these results suggest that the results of models like those in Guerts et al. (2018), although providing an excellent start in understanding extensional basins, should be upgraded using the real non-planar fault geometries, in order to explore whether these can more accurately reproduce the distribution of uplift and subsidence due to the long-term activity of the faults.

8.8 Implications for reverse and strike-slip faulting

This thesis shows that along-strike fault bends can affect the behaviour and evolution of normal faults. This prompts the idea that it should be investigated whether the same applies for reverse and strike-slip faults.

For instance, the 1999 M_w 7.6 Chi Chi earthquake, Taiwan, ruptured a major reverse fault, the Chelungpu fault, one of the major thrust faults of the fold-and-thrust belt that characterize the island of Taiwan (Lee et al., 1996; Bilham and Yu, 1999; Kao et al., 1999; Mouthereau et al., 2001). The earthquake produced a nearly continuous surface rupture 80-90 km long, trending mainly N-S (Kao et al., 1999; Lee et al., 2002). However, it has been noted that in the northern termination the strike of the surface ruptures changes abruptly of almost 90°, assuming an overall E-W trend (Lee et al., 2002). The along-strike

plot of the throw measured on surface ruptures shows that the fault throw sensibly increases within the fault bend in the northern termination of the fault, with a maximum throw of ~12 m observed within the bend. Following the findings presented within this PhD thesis, the along-strike distribution of the coseismic throw produced by the 1999 M_w 7.6 Chi Chi earthquake suggests that along-strike fault bends might influence the throw distribution also along reverse faults, causing larger throws within the bends. Hence, future works should explore in detail whether fault bends can influence the behaviour and development of reverse and strike slip-faults.

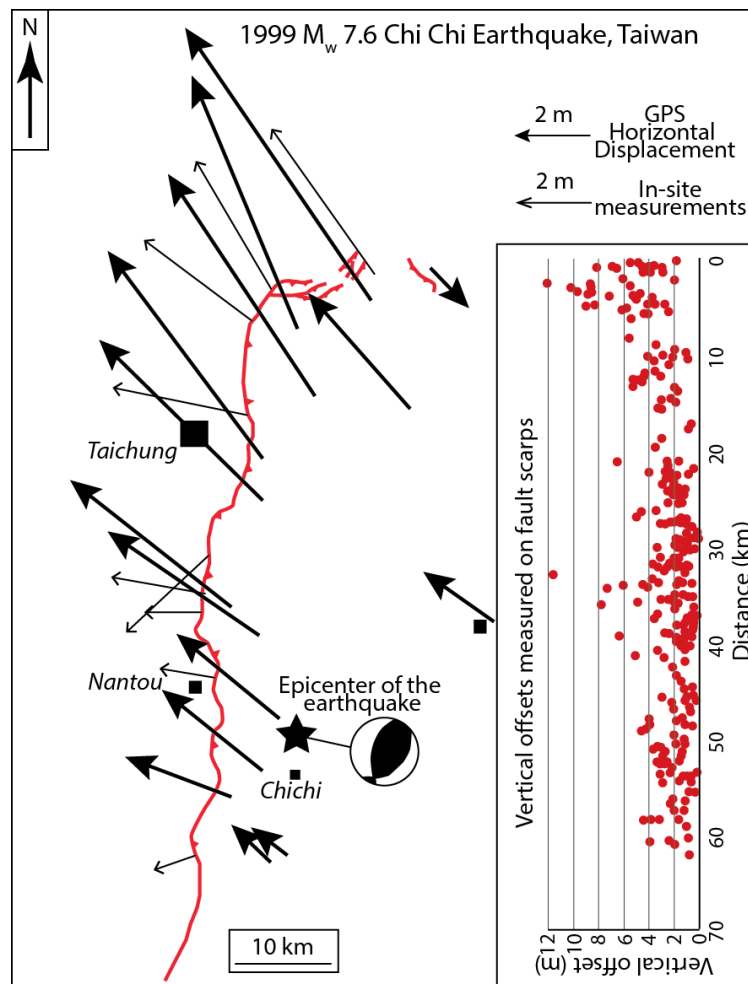


Figure 8.12: Kinematic data of the 1999 Chi Chi earthquake. Red line is the trace of the surface ruptures. Thick arrows are the horizontal displacements of the near-fault GPS coseismic measurements. Thin arrows are the horizontal displacements obtained from the in-site outcrop measurements. The diagram on the right shows the along-strike variation of the vertical offsets measured on fault scarps. Modified from Lee et al., (2002).

8.9 Summary

The studies undertaken in this PhD thesis, on the relationship between the non-planar fault geometry and the spatial and temporal distribution of throw, have profound implications for many aspects of processes associated with fault behaviour and evolution. The control that non-planar fault geometry exerts on fault behaviour is independent from fault maturity and segmentation, to the time span of study and to the geodynamic setting. The results presented in this thesis suggest that this relationship is scale-independent, and can act across systems of faults if they are closely spaced across strike. The results have implications for numerous and diverse aspects of the earthquake geology, such as interpretation of palaeoseismology studies including at trench sites and cosmogenic dating of fault planes, empirical scaling relationships, PSHA, and off-fault deformation. More work is needed in order to explore what is the effect of the non-planar fault geometry in each of these subjects and this could be extended to thrust and strike-slip faults. Overall, much is to be learned from the details of local 3D fault geometry that augment what is already known from simple planar fault models.

Chapter 9

Conclusions

1. The change in strike across fault bends is causative of the change in fault dip of the bend, and studies on 5 normal faulting earthquakes show that fault dip steepens within the fault bend, compared to values of dip outside the bend (Chapters 2 and 4).
2. The along-strike profiles of five different coseismic surface ruptures associated with normal faulting earthquakes (24th August 2016 M_w 6.0 and 30th October 2016 M_w 6.5 Mt. Vettore earthquakes; 1887 M_w 7.5 Sonora, Mexico; 1981 M_w 6.4-6.7 Gulf of Corinth, Greece; 1983 M_w 7.3 Borah Peak, USA) show that the coseismic throw increases where ruptures propagate across bends in well-defined single fault segments characterized by steep fault dip (Chapter 4).
3. The application of quantitative relationships on field data related to the five large normal faulting earthquakes shows that the relatively large coseismic throw observed across the bend are required by the geometry and kinematics of the faulting to maintain the horizontal extensional strain along strike and across the fault bend with its high fault dip (Chapter 4).
4. Studies on the Mt. Vettore fault show that the same bend presenting maxima in coseismic throw for both the 24th August 2016 M_w 6.0 and 30th October 2016 M_w 6.5 earthquakes appears to have produced (i) a local maximum in total finite slip across the fault from offset of pre-rift strata, (ii) a local maximum in fault-related relief, and (iii) internal drainage on the hangingwall, all three of which developed

over several million years, testifying to the long-term influence of the fault bend on the coseismic throw during earthquakes (Chapter 4).

5. The measured D_{max} values for the five studied earthquakes with fault bends are consistently higher than the D_{max} predicted from their lengths using D_{max} versus surface rupture length scaling relationship (e.g. Wells and Coppersmith, 1994) (Chapter 4).
6. Along-strike fault bends are a plausible explanation of the scatter of D_{max} values for normal faulting earthquakes in D_{max} versus surface rupture length scaling relationships (Chapter 4).
7. If the role of bends and high dips in those bends are not considered, this can produce misleading interpretations of (i) M_w from D_{max} values gathered during palaeoseismological studies, (ii) seismic moments and (iii) stress drops influenced by D_{max} (Chapter 4).
8. Faults spaced ≤ 5 km within a segmented fault system (e.g. the Aterno Valley fault system, central Italy, which ruptured during the 2009 M_w 6.3 L'Aquila earthquake) can behave as a single interacting fault segment over time periods containing multiple earthquake cycles (e.g. over 15 ± 3 ka or 2-3 Ma) (Chapter 5).
9. A fault bend in the strike of the Aterno Valley fault system, where strike variations along individual faults are located in a similar along-strike location producing an overall curvature to the trace of the fault system, causes enhancements of throw and throw-rates measured over different time scales (15 ± 3 ka and $\sim 2-3$ Ma) (Chapter 5).
10. Within dense normal faulting systems, single earthquakes can float, causing either partial or total ruptures of the system; the close proximity between mapped fault segments indicates that for the Aterno Valley Fault System seismic ruptures may

be able to jump from one fault to another, producing multi-fault earthquakes (Chapter 5).

11. Along-strike throw and throw-rate profiles measured over faults at different stages of maturity (e.g. the Western Volcanic Zone, Iceland) show that, independently to the stage of maturity of the fault bends, the throw and throw-rates increase within the fault bends, compared to the values on the fault segments immediately outside the bends (Chapter 6).
12. The relationship between the local fault geometry and the conservation of the strain-rate might be driven by processes occurring in the deeper part of the fault (Chapter 6).
13. During fault growth, fault bends in linkage zones are propagating faster than the slip accumulation of the principal fault segments, implying that during the process of fault growth by linkage and coalescence the fault works in order to first establish the fault length and then to accumulate slip (Chapter 6).
14. The “Geometry-dependent throw-rate theory” is valid also in a geodynamic context of a Mid-Atlantic Ridge (Chapter 7).
15. Cosmogenic dating of exposed fault planes in Attica, central Greece, shows that faults spaced > 5 km (e.g. 6-15 km) across the strike are clustered, with a non-systematic alternance of periods of rapid slip accumulation (i.e. earthquake clustering) and periods of quiescence (i.e. earthquake anti-clustering); earthquake clustering on one specific fault is accompanied by low rates of activity on the other faults (Chapter 7).
16. Parallel faults interact in terms of sharing the regional strain-rate, with switching activity that affects the slip-rate on a single fault (Chapter 7).

17. The clustered behaviour of parallel faults implies that the definition of key parameters for seismic hazard assessments (T_{mean} , T_{elap} and CV) is complicated in fault systems with across-strike distributed faults (Chapter 7).
18. In Attica, the preservation of a tectonic fault scarp is strictly related to the elevation above the sea level, with older fault scarps preserved at lower elevations, implying a gradual migration of the demise of the LGM towards higher elevations (Chapter 7).
19. The control that non-planar fault geometry exerts on fault behaviour is independent from fault maturity and segmentation, to the time span of study and to the geodynamic setting (Chapter 8).
20. The relationship between the fault geometry and the distribution of throw shows elements of scale independence: throw enhancements occur in the same way for faults at different scales, from faults a few-kilometres long to broad fault systems ~50 km long (Chapter 8).
21. Palaeoseismological trenches located within (i) a still immature fault bend, (ii) a well-established fault bend along a single fault, or (iii) a fault segment located within a bend that affects an entire fault system may present values of D_{max} biased by the effect of the bends itself; extreme care should be applied in choosing the location of a palaeoseismological trench, in order to avoid biased measurement of coseismic D_{max} (Chapter 8).
22. If cosmogenic sampling is performed across an unrecognised fault bend, the retrieved slip history might not be representative of the actual fault slip history (Chapter 8).
23. Throw and throw-rate enhancements within fault bends may cause ambiguous interpretations of the role of fault bends into PSHA. Higher throw-rates can be

interpreted as more earthquakes occurring in a specific time interval; larger coseismic throws indicates that higher slip-rates in fault bends are due to larger slip-per-event (Chapter 8).

24. In normal fault systems with fault spacing ≤ 5 km, single faults work together to accommodate the regional deformation; in fault systems with fault spacing > 5 km, faults present a switching of activity between across-strike faults, with alternation of earthquake clusters and anti-clusters on individual faults (Chapter 8).

List of references

- Acocella, V., A. Gudmundsson, and R. Funicello (2000), Interaction and linkage of extension fractures and normal faults: examples from the rift zone of Iceland, *Journal of Structural Geology*, 22(9), 1233-1246. [https://doi.org/10.1016/S0191-8141\(00\)00031-6](https://doi.org/10.1016/S0191-8141(00)00031-6)
- Anderson, H, and J. Jackson (1987), Active tectonics of the Adriatic Region. *Geophys J Int*; 91 (3): 937-983. Doi: 10.1111/j.1365-246X.1987.tb01675.
- Armijo, R., B. Meyer, G. C. P. King, A. Rigo, and D. Papanastassiou (1996), Quaternary evolution of the Corinth Rift and its implications for the Late Cenozoic evolution of the Aegean. *Geophysical Journal International*, 126(1), 11– 53.
- Atzori, S., I. Hunstad, M. Chini, S. Salvi, C. Tolomei, C. Bignami, S. Stramondo, E. Trasatti, A. Antonioli, and E. Boschi (2009), Finite fault inversion of DInSAR coseismic displacement of the 2009 L'Aquila earthquake (central Italy), *Geophysical Research Letters*, vol. 36, L15305, doi:10.1029/2009GL039293.
- Beck, J., S. Wolfers, and G. P. Roberts (2018), Bayesian earthquake dating and seismic hazard assessment using chlorine-36 measurements (BED v1), *Geosci. Model Dev.*, 11 (2018), pp. 4383-4397
- Benedetti, L., R. Finkel, D. Papanastassiou, G. King, R. Armijo, F. Ryerson, D. Farber, and F. Flerit (2002), Post-glacial slip history of the Sparta fault (Greece) determined by ³⁶Cl cosmogenic dating: evidence for nonperiodic earthquakes, *Geophys. Res. Lett.*, 29(8), 87_1–87_4.
- Benedetti, L. et al., (2003), Motion of the Kaparelli fault (Greece) prior to the 1981 earthquake sequence determined from ³⁶Cl cosmogenic dating, *Terra Nova*, 15(2), 118–124.

- Bennett, R. A., A. M. Friedrich and K. P. Furlong (2004), Codependent histories of the San Andreas and San Jacinto fault zones from inversion of fault displacement rates. *Geology*, 32(11), 961-964.
- Bergerat, F. and Angelier, J. (2000), The South Iceland Seismic Zone: tectonic and sismotectonic analyses revealing the evolution from rifting to transform motion, *Journal of Geodynamics*, 29(3-5), 211-231. [https://doi.org/10.1016/S0264-3707\(99\)00046-0](https://doi.org/10.1016/S0264-3707(99)00046-0)
- Biasi, G.P and Wesnousky, S.G. (2016), Steps and Gaps in Ground Ruptures: Empirical Bounds on Rupture Propagation, *Bulletin of the Seismological Society of America* 106, 1110-1124.
- Biasi, G.P. and Wesnousky, S. G. (2017), Bends and Ends of Surface Ruptures, *Bulletin of the Seismological Society of America*, 107(6), pp.2543-2560. <https://doi.org/10.1785/0120160292>
- Bilham, R., and Yu, T.T. (1999), The morphology of thrust faulting in the 21 September 1999, Chichi, Taiwan earthquake, *Journal of Asian Earth Sciences* 18, 351-367.
- Billiris, H., D. Paradissis, G. Veis, P. England, W. Featherstone, B. Parsons, ... and V. Ashkenazi (1991), Geodetic determination of tectonic deformation in central Greece from 1900 to 1988. *Nature*, 350(6314), 124.
- Blumetti, A. M., F. Dramis, and A.M. Michetti (1993), Fault-generated mountain fronts in the central apennines (Central Italy): Geomorphological features and seismotectonic implications. *Earth Surf. Process. Landforms*, 18: 203–223. Doi:10.1002/esp.3290180304
- Blumetti, A. M., L. Guerrieri and E. Vittori (2013), The primary role of the Paganica-San Demetrio fault system in the seismic landscape of the Middle Aterno Valley basin (Central Apennines). *Quaternary International*, 288, 183-194.

- Blumetti, A. M., P. Di Manna, V. Comerci, L. Guerrieri, and E. Vittori (2017), Paleoseismicity of the san demetrio ne'Vestini fault (L'Aquila basin, Central Italy): implications for seismic hazard, *Quaternary International*, 451, 129-142.
- Boncio, P., G. Lavecchia, and B. Pace (2004), Defining a model of 3D seismogenic sources for Seismic Hazard Assessment applications: The case of central Apennines (Italy), *J. Seismol.*, 8(3), 407–425, doi:10.1023/B:JOSE.0000038449.78801.05.
- Boncio, P., A. Pizzi, F. Brozzetti, G. Pomposo, G. Lavecchia, D. Di Naccio, and F. Ferrarini (2010), Coseismic ground deformation of the 6 April 2009 L'Aquila earthquake (central Italy, Mw 6.3), *Geophysical Research Letters*, vol. 37, L06308, doi:10.1029/2010GL042807.
- Briole, P., et al. (2000), Active deformation of the Corinth rift, Greece: results from repeated Global Positioning System surveys between 1990 and 1995, *Journal of Geophysical Research: Solid Earth* 105.B11: 25605-25625.
- Brozzetti, F., P. Boncio, D. Cirillo, F. Ferrarini, R. de Nardis, A. Testa, F. Liberi and G. Lavecchia (2019), High- resolution field mapping and analysis of the August–October 2016 coseismic surface faulting (central Italy earthquakes): Slip distribution, parameterization, and comparison with global earthquakes, *Tectonics*, 38, 417–439. <https://doi.org/10.1029/2018TC005305>
- Bull, J. M., T. A. Minshull, N. C. Mitchell, K. Thors, J. K. Dix, and A. I. Best (2003), Fault and magmatic interaction within Iceland's western rift over the last 9 kyr, *Geophysical Journal International* 154, no. 1 (2003): F1-F8 <https://doi.org/10.1046/j.1365-246X.2003.01990.x>
- Caskey, S. J. and Wesnousky, S. G. (1997), Static stress changes and earthquake triggering during the 1954 Fairview Peak and Dixie Valley earthquakes, central Nevada, *Bulletin of the Seismological Society of America* ; 87 (3): 521–527.

- Cavinato, G. P., and PG De Celles (1999), Extensional basins in the tectonically bimodal central Apennines fold-thrust belt, Italy: response to corner flow above a subducting slab in retrograde motion, *Geology* 27, no. 10; 955-958.
- Cavinato, G. P., C. Carusi, M. Dall'Asta, E. Miccadei and T. Piacentini (2002), Sedimentary and tectonic evolution of Plio–Pleistocene alluvial and lacustrine deposits of Fucino Basin (central Italy). *Sedimentary Geology*, 148(1), 29-59, [http://dx.doi.org/10.1016/S0037-0738\(01\)00209-3](http://dx.doi.org/10.1016/S0037-0738(01)00209-3).
- Cello, G., S. Mazzoli, E. Tondi, and E. Turco (1997), Active tectonics in the central Apennines and possible implications for seismic hazard analysis in peninsular Italy, *Tectonophysics*, 272(1), 43-68. [http://dx.doi.org/10.1016/S0040-1951\(96\)00275-2](http://dx.doi.org/10.1016/S0040-1951(96)00275-2)
- Chiarabba, C., P. De Gori, M. Cattaneo, D. Spallarossa, and M. Segou (2018), Faults geometry and the role of fluids in the 2016-2017 Central Italy seismic sequence, *Geophys. Res. Lett.*, doi:10.1029/2018GL077485.
- Chiaraluce, L., L. Valoroso, D. Piccinini, R. Di Stefano, and P. De Gori (2011), The anatomy of the 2009 L'Aquila normal fault system (central Italy) imaged by high resolution foreshock and aftershock locations, *J. Geophys. Res.*, 116, B12311, doi:10.1029/2011JB008352.
- Chiaraluce, L., R. Di Stefano, E. Tinti, L. Scognamiglio, M. Michele, E. Casarotti, M. Cattaneo, P. De Gori, C. Chiarabba, G. Monachesi, A. Lombardi, L. Valoroso, D. Latorre and S. Marzorati (2017), The 2016 central Italy seismic sequence: A first look at the mainshocks, aftershocks, and source models, *Seismological Research Letters*, 88(3), 757-771.
- Cheloni, D., N. D'agostino, E. D'anastasio, A. Avallone, S. Mantenuto, R. Giuliani, M. Mattone, S. Calcaterra, P. Gambino, D. Dominici, and F. Radicioni (2010),

Coseismic and initial post-seismic slip of the 2009 M w 6.3 L'Aquila earthquake, Italy, from GPS measurements. *Geophysical Journal International*, 181(3), pp.1539-1546. <https://doi.org/10.1111/j.1365-246X.2010.04584.x>

Cheloni, D., V. De Novellis, M. Albano, A. Antonioli, M. Anzidei, S. Atzori, A. Avallone, C. Bignami, M. Bonano, S. Calcaterra, R. Castaldo, F. Casu, G. Cecere, C. De Luca, R. Devoti, D. Di Bucci, A. Esposito, A. Galvani, P. Gambino, R. Giuliani, R. Lanari, M. Manunta, M. Manzo, M. Mattone, A. Montuori, A. Pepe, S. Pepe, G. Pezzo, G. Pietroantonio, M. Polcari, F. Riguzzi, S. Salvi, V. Sepe, E. Serpelloni, G. Solaro, S. Stramondo, P. Tizzani, C. Tolomeri, E. Trasatti, E. Valerio, I. Zinno and C. (2017), Geodetic model of the 2016 Central Italy earthquake sequence inferred from InSAR and GPS data, *Geophysical Research Letters*, 44(13), 6778-6787.

Cheloni, D., E. Falcucci and S. Gori (2019), Half- graben rupture geometry of the 30 October 2016 MW 6.6 Mt. Vettore- Mt. Bove earthquake, central Italy. *Journal of Geophysical Research: Solid Earth*.

Chousianitis, K., A. Ganas and M. Gianniou (2013), Kinematic interpretation of present-day crustal deformation in central Greece from continuous GPS measurements. *Journal of Geodynamics*, 71, 1-13.

Cinti, F. R., D. Pantosti, P. M. De Martini, S. Pucci, R. Civico, S. Pierdominici, L. Cucci, C. A. Brunori, S. Pinzi, and A. Patera, (2011), Evidence for surface faulting events along the Paganica fault prior to the 6 April 2009 L'Aquila earthquake (central Italy). *Journal of Geophysical Research: Solid Earth*, 116(B7).

Cinti, F. R., P. M. De Martini, D. Pantosti, S. Baize, A. Smedile, F. Villani,... and L. Pizzimenti (2019), 22kyr-long record of surface faulting along the source of the 30

- October 2016 earthquake (Central Apennines, Italy), from integrated paleoseismic dataset, *Journal of Geophysical Research: Solid Earth*.
- Cirella, A., A. Piatanesi, M. Cocco, E. Tinti, L. Scognamiglio, A. Michelini, A. Lomax, and E. Boschi (2009), Rupture history of the 2009 L'Aquila (Italy) earthquake from non-linear joint inversion of strong motion and GPS data. *Geophysical Research Letters*, 36(19). 10.1029/2009GL039795
- Cirella, A., G. Pezzo, and A. Piatanesi (2018), Rupture Kinematics and Structural – Rheological Control of the 2016 Mw 6.1 Amatrice (Central Italy) Earthquake from Joint Inversion of Seismic and Geodetic Data, *Geophys. Res. Lett.*, doi:10.1029/2018GL080894.
- Clifton, A.E., F. Sigmundsson, K. L. Feigl, G. Gumundsson, and T. Árnadóttir (2002), Surface effects of faulting and deformation resulting from magma accumulation at the Hengill triple junction, SW Iceland, 1994–1998. *J. Volcanol. Geotherm. Res.* 115 (1), 233–255.
- Civico, R., S. Pucci, F. Villani, L. Pizzimenti, P.M. De Martini, R. Nappi and Open EMERGEO Working Group (2018), Surface ruptures following the 30 October 2016 Mw 6.5 Norcia earthquake, central Italy. *Journal of Maps*, 14(2), pp.151-160.
- Cowie, P.A. and G.P. Roberts (2001), Constraining slip rates and spacings for active normal faults. *Journal of Structural Geology*, 23(12), pp.1901-1915
[https://doi.org/10.1016/S0191-8141\(01\)00036-0](https://doi.org/10.1016/S0191-8141(01)00036-0)
- Cowie, P. A., C. H. Scholz, G. P. Roberts, J. F. Walker and P. Steer (2013), Viscous roots of active seismogenic faults revealed by geologic slip rate variations. *Nature Geoscience*, 6(12), 1036.
- Cowie P. A., R. J. Phillips, G. P. Roberts, K. McCaffrey, L. J. J. Zijerveld, L. C. Gregory, J. Faure Walker, L. N. J. Wedmore, T. J. Dunai, S. A. Binnie, S.P. H. T. Freeman,

- K. Wilcken, R. P. Shanks, R. S. Huismans, I. Papanikolaou, A. M. Michetti and M. Wilkinson (2017), Orogen-scale uplift in the central Italian Apennines drives episodic behavior of earthquake faults, *Nature Sci. Rep.* 7., 44858; doi:10.1038/srep44858.
- Crone, A. J., M. N. Machette, M. G. Bonilla, J. J. Lienkaemper, K. L. Pierce, W. E. Scott and R. C. Bucknam (1987), Surface faulting accompanying the Borah Peak earthquake and segmentation of the Lost River fault, central Idaho. *Bulletin of the Seismological Society of America*, 77(3), 739-770.
- D'Agostino, N., S. Mantenuto, E. D'Anastasio, R. Giuliani, M. Mattone, M. Calcaterra, P. Gambino and L. Bonci (2011), Evidence for localized active extension in the central Apennines (Italy) from global positioning system observations. *Geology*, 39, 291–294.
- D'Agostino, N., D. Cheloni, G. Fornaro, R. Giuliani, and D. Reale (2012), Space- time distribution of afterslip following the 2009 L'Aquila earthquake, *Journal of Geophysical Research: Solid Earth* 117, no. B2. 10.1029/2011JB008523
- Davies, R., P. C. England, B. Parsons, H. Billiris, D. Paradissis, and G. Veis (1997), Geodetic strain of Greece in the interval 1892–1992, *Journal of Geophysical Research: Solid Earth*, 102(B11), 24571-24588.
- Deligiannakis, G., I. D. Papanikolaou, I. D. and G. Roberts (2018), Fault specific GIS based seismic hazard maps for the Attica region, Greece. *Geomorphology*, 306, 264-282.
- DePolo, C.M., D. G. Clark, D.B. Slemmons, and A. R. Ramelli (1991), Historical surface faulting in the Basin and Range province, western North America: implications for fault segmentation. *Journal of structural Geology*, 13(2), pp.123-136.

- Doglionni, C. (1993), Some remarks on the origin of foredeeps, *Tectonophysics*, 228(1-2), 1-20.
- Dolan, J. F., K. Sieh, T. K. Rockwell, P. Gupta, and G. Miller (1997), Active tectonics, paleoseismology, and seismic hazards of the Hollywood fault, northern Los Angeles basin, California. *Geological Society of America Bulletin*, 109(12), 1595-1616. [https://doi.org/10.1130/0016-7606\(1997\)109<1595:ATPASH>2.3.CO;2](https://doi.org/10.1130/0016-7606(1997)109<1595:ATPASH>2.3.CO;2)
- Dunai, T. J. (2010). *Cosmogenic Nuclides: Principles, concepts and applications in the Earth surface sciences*. Cambridge University Press.
- DuRoss, C. B., S. F. Personius, A. J. Crone, S. S. Olig, M. D. Hylland, W. R. Lund, and D. P. Schwartz (2016), Fault segmentation: New concepts from the Wasatch fault zone, Utah, USA. *Journal of Geophysical Research: Solid Earth*, 121(2), 1131-1157.
- Einarsson, P. (2008), Plate boundaries, rifts and transforms in Iceland, *Jökull*, 58(12), 35-58.
- Emergeo Working Group. (2010), Evidence for surface rupture associated with the Mw 6.3 L'Aquila earthquake sequence of April 2009 (central Italy), *Terra Nova*, 22(1), 43–51. doi:10.1111/j.1365-3121.2009.00915.x
- Falcucci, E., Gori, S., Peronace, E., Fubelli, G., Moro, M., Saroli, M., . . . Galadini, F. (2009), The Paganica Fault and surface coseismic ruptures caused by the 6 April 2009 earthquake (L'Aquila, central Italy), *Seismological Research Letters*, 80(6), 940–950. <https://doi.org/10.1785/gssrl.80.6.940>
- Falcucci, E., Gori, S., Bignami, C., Pietrantonio, G., Melini, D., Moro, M., Saroli, M., and Galadini, F. (2018), The Campotosto seismic gap in between the 2009 and 2016–2017 seismic sequences of central Italy and the role of inherited lithospheric

faults in regional seismotectonic settings. *Tectonics*, 37.

<https://doi.org/10.1029/2017TC004844>

Faure Walker, J. P., G. P. Roberts, P. A. Cowie, I. D. Papanikolaou, P. R. Sammonds, A. M. Michetti, and R. J. Phillips (2009), Horizontal strain-rates and throw-rates across breached relay zones, central Italy: Implications for the preservation of throw deficits at points of normal fault linkage, *J. Struct. Geol.*, 31(10), 1145–1160, doi:10.1016/j.jsg.2009.06.011.

Faure Walker, J. P., G. P. Roberts, P. R. Sammonds, and P. A. Cowie (2010), Comparison of earthquake strains over 10² and 10⁴ year timescales: Insights into variability in the seismic cycle in the central Apennines, Italy, *J. Geophys. Res.*, 115(B10), B10418, doi:10.1029/2009JB006462.

Faure Walker, J. P., G. P. Roberts, P. A. Cowie, I. Papanikolaou, A. M. Michetti, P. R. Sammonds, M. W. Wilkinson, K. McCaffrey and R. Phillips (2012), Relationship between topography, rates of extension and mantle dynamics in the actively-extending Italian Apennines, *Earth and Planetary Science Letters* 325-326, 76-84

Faure Walker J.P., G. P. Roberts, P. A. Cowie, K. McCaffrey, L. Wedmore, Z. Watson, L. C. Gregory (2015), Long-term strain rates as a tool for understanding the mechanics of continental extension and the importance of local 3D fault geometry for local throw-rates across faults. 6th Int. INQUA Meeting on Paleoseismology, Active Tectonics and Archaeoseismology, 19-24 April 2015, Pescara, Fucino Basin, Italy, 27 150-154.

Faure Walker, J. P., F. Visini, G. Roberts, C. Galasso, K. McCaffrey and Z. Mildon (2018), Variable fault geometry suggests detailed fault-slip-rate profiles and geometries are needed for fault-based probabilistic seismic hazard assessment (PSHA), *Bulletin of the Seismological Society of America*, 109(1), 110-123.

- Feigl, K.L., J. Gasperi, F. Sigmundsson and A. Rigo (2000), Crustal deformation near Hengill volcano, Iceland 1993–1998: coupling between magmatic activity and faulting inferred from elastic modeling of satellite radar interferograms. *J. Geophys. Res. Solid Earth* 105 (B11), 25655–25670. <https://doi.org/10.1029/2000JB900209>.
- Ferrario, M. F. and Livio, F. (2018), Characterizing the distributed faulting during the 30 October 2016, Central Italy earthquake: A reference for fault displacement hazard assessment, *Tectonics*, 37, 1256–1273. <https://doi.org/10.1029/2017TC004935>.
- Ficcarelli, G., and Silvestrini, M. (1991), Biochronologic remarks on the local fauna of Colle Curti (Colfiorito basin, Umbrian-Marchean Apennine, central Italy). *Mucchi*.
- Field E. H., R. J. Arrowsmith, G. P. Biasi, P. Bird, T. E. Dawson, K. R. Felzer, D. D. Jackson, K. M. Johnson, T. H. Jordan, C. Madden, A. J. Michael, K. R. Milner, M. T. Page, T. Parsons, P. M. Powers, B. E. Shaw, W. R. Thatcher, R. J. Weldon and Y. Zeng (2014), Uniform California Earthquake Rupture Forecast, Version 3 (UCERF3)—The Time- Independent Model. *Bulletin of the Seismological Society of America*, 104 (3): 1122–1180. doi: <https://doi.org/10.1785/0120130164>
- Field E.H., G. P. Biasi, P. Bird, T. E. Dawson, K. R. Felzer, D. D. Jackson, K. M. Johnson, T. H. Jordan, C. Madden, A. J. Michael, K. R. Milner, M. T. Page, T. Parsons, P. M. Powers, B. E. Shaw, W. R. Thatcher, R. J. Weldon and Y. Zeng (2015), Long-Term Time- Dependent Probabilities for the Third Uniform California Earthquake Rupture Forecast (UCERF3), *Bulletin of the Seismological Society of America*, 105 (2A): 511–543. doi: <https://doi.org/10.1785/0120140093>
- Field E. H., K. R. Milner, J. L. Hardebeck, M. T. Page, N. van der Elst, T. H. Jordan, A. J. Michael, B. E. Shaw and M. J. Werner (2017), A Spatiotemporal Clustering Model for the Third Uniform California Earthquake Rupture Forecast (UCERF3-

- ETAS): Toward an Operational Earthquake Forecast, *Bulletin of the Seismological Society of America*, 107 (3): 1049–1081. doi: <https://doi.org/10.1785/0120160173>
- Foulger, G.R., 1988a, Hengill triple junction, SW Iceland 1. Tectonic structure and the spatial and temporal distribution of local earthquakes. *J. Geophys. Res. Solid Earth* 93 (B11), 13493–13506. <https://doi.org/10.1029/JB093iB11p13493>.
- Foulger, G.R., 1988b, Hengill triple junction, SW Iceland 2. Anomalous earthquake focal mechanisms and implications for process within the geothermal reservoir and at accretionary plate boundaries. *J. Geophys. Res. Solid Earth* 93 (B11), 13507–13523. <https://doi.org/10.1029/JB093iB11p13507>.
- Friese, N. (2008), Brittle tectonics of the Thingvellir and Hengill volcanic systems, Southwest Iceland: field studies and numerical modeling, *Geodinamica Acta*, 21:4, 169-185, DOI: 10.3166/ga.21.169-185
- Fung Y.C., *A First Course in Continuum Mechanics*, Prentice-Hall, Inc., Englewood Cliffs, New Jersey, 1977.
- Galadini, F., and P. Galli (2000), Active Tectonics in the Central Apennines (Italy)– Input Data for Seismic Hazard Assessment, *Nat. Hazards*, 22, 225–270.
- Galadini, F., and P. Galli (2003), Paleoseismology of silent faults in the Central Apennines (Italy): the Mt . Vettore and Laga Mts . faults, *Ann. Geophysics*, 46(October), 815–836.
- Galadini, F., and P. Messina (1994), Plio-Quaternary tectonics of the Fucino basin and surroundings areas (central Italy), *Giornale di Geologia*, ser. 3^a, vol. 56/2, pp. 73-99.
- Galli, P., F. Galadini, and D. Pantosti (2008), Twenty years of paleoseismology in Italy. *Earth-Science Reviews*, 88(1-2), pp.89-117.

- Galli, P., B. Giaccio and P. Messina (2010), The 2009 central Italy earthquake seen through 0.5 Myr-long tectonic history of the L'Aquila faults system, *Quaternary Science Reviews*, 29(27-28), pp.3768-3789. <https://doi.org/10.1016/j.quascirev.2010.08.018>
- Galli P. A. C., B. Giaccio, P. Messina, E. Peronace and G. M. Zuppi (2011), Palaeoseismology of the L'Aquila faults (central Italy, 2009, Mw 6.3 earthquake): implications for active fault linkage, *Geophysical Journal International*, Volume 187, Issue 3, Pages 1119–1134, <https://doi.org/10.1111/j.1365-246X.2011.05233.x>
- Galli, P., and E. Peronace (2014), New paleoseismic data from the Irpinia Fault. A different seismogenic perspective for southern Apennines (Italy), *Earth-Science Reviews*, 175-201.
- Galli, P., B. Giaccio, P. Messina, E. Peronace, V. Amato, G. Naso, S. Nomade, A. Pereira, S. Piscitelli, J. Bellanova, A. Billi, D. Blamart, A. Galderisi, A. Giocoli, T. Stabile, F. Thil (2017), Middle to Late Pleistocene activity of the northern Matese fault system (southern Apennines, Italy), *Tectonophysics*, 699, 61-81. <http://dx.doi.org/10.1016/j.tecto.2017.01.007>
- Ganas, A., S. B. Pavlides, S. Sboras, S. Valkaniotis, S. Papaioannou, G. A. Alexandris, ... and G. A. Papadopoulos (2004), Active fault geometry and kinematics in Parnitha Mountain, Attica, Greece. *Journal of Structural Geology*, 26(11), 2103-2118.
- Gawthorpe, R. L., C. A. L. Jackson, M. J. Young, I. R. Sharp, A. R. Moustafa and C. W. Leppard (2003), Normal fault growth, displacement localisation and the evolution of normal fault populations: the Hammam Faraun fault block, Suez rift, Egypt. *Journal of Structural Geology*, 25(6), 883-895. [https://doi.org/10.1016/S0191-8141\(02\)00088-3](https://doi.org/10.1016/S0191-8141(02)00088-3)

- Giraudi, C., 1988, Evoluzione geologica della piana del Fucino (Abruzzo) negli ultimi 30.000 anni, *Il Quaternario*, 1 (2), 131-159.
- Gori, S., E. Falcucci, S. Atzori, M. Chini, M. Moro, E. Serpelloni, G. Fubelli, M. Saroli, R. Devoti, S. Stramondo, F. Galadini, S. Salvi (2012), Constraining primary surface rupture length along the Paganica fault (L'Aquila earthquake) with geological and geodetic (DInSAR and GPS) evidence, *Italian Journal of Geoscience*, 131(3), 359–372. doi:10.3301/IJG.2012.21
- Grant, J. V., & Kattenhorn, S. A. (2004), Evolution of vertical faults at an extensional plate boundary, southwest Iceland, *Journal of Structural Geology*, 26(3), 537-557. <https://doi.org/10.1016/j.jsg.2003.07.003>
- Gruppo di Lavoro INGV sul terremoto in centro Italia (2016). Summary report on the October 30, 2016 earthquake in central Italy Mw 6.5, doi: 10.5281/zenodo.166238
- Grützner, C., S. Schneiderwind, I. Papanikolaou, G. Deligiannakis, A. Pallikarakis and K. Reicherter (2015), New constraints on extensional tectonics and seismic hazard in northern Attica, Greece: the case of the Milesi Fault. *Geophysical Journal International*, 204(1), 180-199.
- Gudmundsson, A. (1987), Geometry, formation and development of tectonic fractures on the Reykjanes Peninsula, southwest Iceland. *Tectonophysics*, 139(3-4), 295-308. [https://doi.org/10.1016/0040-1951\(87\)90103-X](https://doi.org/10.1016/0040-1951(87)90103-X)
- Gudmundsson, A. (1992), Formation and growth of normal faults at the divergent plate boundary in Iceland, *Terra Nova*, 4,464-471, 1992. <https://doi.org/10.1111/j.1365-3121.1992.tb00582.x>
- Gudmundsson, A. (2000), Fracture dimensions, displacements and fluid transport. *Journal of Structural Geology*, 22(9), 1221-1231. [https://doi.org/10.1016/S0191-8141\(00\)00052-3](https://doi.org/10.1016/S0191-8141(00)00052-3)

- Guerts, A. H., P. A. Cowie, G. Duclaux, R. L. Gawthorpe, R. S. Huismans, V. Pedersen and L. Wedmore (2018), Drainage integration and sediment dispersal in active continental rifts: A numerical modelling study of the central Italian Apennines. *Basin Research*, 30(5), 965-989.
- Guerrieri, L., A.M. Blumetti, E. Esposito, A.M. Michetti, S. Porfido, L. Serva, E. Tondi and E. Vittori (2009), Capable faulting, environmental effects and seismic landscape in the area affected by the 1997 Umbria–Marche (Central Italy) seismic sequence. *Tectonophysics*, 476(1-2), 269-281.
- Guyodo, Y. and Valet, J.P. (1999), Global changes in intensity of the Earth's magnetic field during the past 800 kyr, *Nature*, 399, 249–252.
- Hampel, A., Li, T. and Maniatis, G., 2013. Contrasting strike-slip motions on thrust and normal faults: Implications for space-geodetic monitoring of surface deformation. *Geology*, 41(3), pp.299-302. DOI: 10.1130/G33927.1
- Huang, M. H., E. J. Fielding, C. Liang, P. Milillo, D. Bekaert, D. Dreger, and J. Salzer (2017), Coseismic deformation and triggered landslides of the 2016 Mw 6.2 Amatrice earthquake in Italy. *Geophysical Research Letters*, 44(3), 1266-1274.
- Iezzi, F., Z. Mildon, J. F. Walker, G. Roberts, H. Goodall, M. Wilkinson, and J. Robertson (2018), Coseismic throw variation across along-strike bends on active normal faults: Implications for displacement versus length scaling of earthquake ruptures. *Journal of Geophysical Research: Solid Earth*, 123. <https://doi.org/10.1029/2018JB016732>
- Iezzi, F., G. Roberts, J. F. Walker and I. Papanikolaou (2019), Occurrence of partial and total coseismic ruptures of segmented normal fault systems: Insights from the Central Apennines, Italy, *Journal of Structural Geology*, 126, 83-99. <https://doi.org/10.1016/j.jsg.2019.05.003>

- Iezzi, F., G. Roberts, and J. F. Walker (2020), Throw-rate variations within linkage zones during the growth of normal faults: Case studies from the Western Volcanic Zone, Iceland, *Journal of Structural Geology*, 103976.
- ISPRA (2009), Cartografia Geologica d'Italia 1:50,000 (Progetto CARG), sheet 359. http://www.isprambiente.gov.it/Media/carg/359_LAQUILA/Foglio.html
- ISPRA (2009), Cartografia Geologica d'Italia 1:50,000 (Progetto CARG), sheet 349. http://www.isprambiente.gov.it/Media/carg/349_GRANSASSO/Foglio.html
- Jackson, C. A. L., R. L. Gawthorpe and I. R. Sharp (2002), Growth and linkage of the East Tanka fault zone, Suez rift: structural style and syn-rift stratigraphic response, *Journal of the Geological Society*, 159(2), 175-187. <https://doi.org/10.1144/0016-764901-100>
- Jackson, J. A., J. Gagnepain, G. Houseman, G. C. P. King, P. Papadimitriou, C. Soufleris, and J. Virieux (1982), Seismicity, normal faulting, and the geomorphological development of the Gulf of Corinth (Greece): the Corinth earthquakes of February and March 1981. *Earth and Planetary Science Letters*, 57(2), 377-397. [http://dx.doi.org/10.1016/0012-821X\(82\)90158-3](http://dx.doi.org/10.1016/0012-821X(82)90158-3)
- Jackson, J. (1994), Active tectonics of the Aegean region. *Annual Review of Earth and Planetary Sciences*, 22(1), 239– 271.
- Kanamori, H., and D. L. Anderson (1975), Theoretical basis of some empirical relations in seismology, *Bulletin of the Seismological Society of America* 65.5,1073-1095.
- Korte, M. and Constable, C.G., (2005), The geomagnetic dipole moment over the last 7000 years—new results form a global model, *Earth planet. Sci. Lett.*, 236, 348–358.
- Kostrov, V. V. (1974), Seismic moment and energy of earthquakes, and seismic flow of rock, *Izv. Earth Phys.*, 1, 23–40. (Engl. Transl. UDC 550.341, 13–21.)

- LaFemina, P. C., T. H. Dixon, R. Malservisi, T. Arnadóttir, E. Sturkell, F. Sigmundsson, and P. Einarsson (2005), Geodetic GPS measurements in south Iceland: Strain accumulation and partitioning in a propagating ridge system, *J. Geophys. Res.*, 110, B11405, doi:10.1029/2005JB003675
- Lavecchia, G., F. Ferrarini, F. Brozzetti, R. De Nardis, P. Boncio, and L. Chiaraluce, 2012. From surface geology to aftershock analysis: Constraints on the geometry of the L'Aquila 2009 seismogenic fault system. *Italian Journal of Geosciences*, 131(3), pp.330-347.
- Lavecchia, G., R. Castaldo, R. De Nardis, V. De Novellis, F. Ferrarini, S. Pepe, ... and P. Boncio (2016), Ground deformation and source geometry of the 24 August 2016 Amatrice earthquake (Central Italy) investigated through analytical and numerical modeling of DInSAR measurements and structural- geological data. *Geophysical Research Letters*, 43(24), 12-389.
- Lee, J.C., C. Y. Lu, H. T. Chu, B. Delcaillau, J. Angelier and B. Deffontaines (1996), Active deformation and paleostress analysis in the Pakua anticline area, western Taiwan. *Terrestrial, Atmospheric and Oceanic Sciences* 7 4, 431-446.
- Lee, J. C., H. T. Chu, J. Angelier, Y. C. Chan, J. C. Hu, C. Y. Lu, and R. J. Rau (2002), Geometry and structure of northern surface ruptures of the 1999 Mw= 7.6 Chi-Chi Taiwan earthquake: influence from inherited fold belt structures, *Journal of Structural Geology*, 24(1), 173-192.
- Leonard, M. (2010), Earthquake fault scaling: Self-consistent relating of rupture length, width, average displacement, and moment release, *Bull. Seismol. Soc. Am.*, 100(5A), 1971-1988.

- Li, K. L., C. Abril, O. Gudmundsson, and G. B. Gudmundsson (2019), Seismicity of the Hengill area, SW Iceland: Details revealed by catalog relocation and collapsing. *Journal of Volcanology and Geothermal Research*, 376, 15-26.
- Licciardi, J.M., Kurz, M.D. and Curtice, J.M., 2007. Glacial and volcanic history of Icelandic table mountains from cosmogenic ^3He exposure ages. *Quaternary Science Reviews*, 26(11-12), pp.1529-1546.
<https://doi.org/10.1016/j.quascirev.2007.02.016>
- Lin J., and Stein R.S. (2004) Stress triggering in thrust and subduction earthquakes and stress interaction between the southern San Andreas and nearby thrust and strike-slip faults, *J. geophys. Res.* 109 B02303, doi:10.1029/2003JB002607.
- Liu, C., Y. Zheng, Z. Xie, and X. Xiong (2017), Ruptures features of the Mw 6.2 Norcia earthquake and its possible relationship with strong seismic hazards, *Geophys. Res. Lett.*, 44,1320-1328, doi:10.1002/2016GL071958.
- Livio, F., A. M. Michetti, E. Vittori, L. Gregory, L. Wedmore, L. Piccardi, E. Tondi, G. Roberts and Central Italy Earthquake Working (2016), Surface faulting during the August 24, 2016, central Italy earthquake (Mw 6.0): preliminary results, *Annals of geophysics*, 59, no. Fast Track 5 (2016): 1-8.
- Ma, X.Q., and Kusznir, N.J., 1995, Coseismic and postseismic subsurface displacements and strains for a dip-slip normal fault in a three-layer elastic gravitational medium: *Journal of Geophysical Research*, v. 100, p. 12,813–12,828, doi:10.1029/95JB00674.
- Manighetti, I., M. Campillo, C. Sammis, P.M. Mai and G. King (2005), Evidence for self- similar, triangular slip distributions on earthquakes: Implications for earthquake and fault mechanics, *Journal of Geophysical Research: Solid Earth*, 110(B5).

- Manighetti, I., M. Campillo, S. Bouley, and F. Cotton (2007), Earthquake scaling, fault segmentation, and structural maturity. *Earth and Planetary Science Letters*, 253(3), 429-438.
- Mansfield, C. and Cartwright, J. (2001), Fault growth by linkage: observations and implications from analogue models. *Journal of Structural Geology*, 23, 745-763.
- Mariucci, M. T., Montone, P., Contemporary stress field in the area of the 2016 Amatrice seismic sequence (central Italy), *Annales of Geophysics*, 59, Fast Track 5, 2016; DOI:10.4401/ag-7235.
- McElhinny, M.W. and McFadden, P.L. (1997), Paleosecular variation over the past 5 Myr based on a new generalized database, *Geophys. J. Int.*, 131, 240–252.
- McLeod, A. E., N. H. Dawers, J. R. Underhill (2000), The propagation and linkage of normal faults: insights from the Strathspey-Brent-Statfjord fault array, northern North Sea. *Basin Research*, 12, 263-284.
- McLeod, A. E., J. R. Underhill, S. J. Davies and N. H. Dawers (2002), The influence of fault array evolution on synrift sedimentation patterns: Controls on deposition in the Strathspey-Brent-Statfjord half graben, northern North Sea, *AAPG bulletin*, 86(6), 1061-1093. <https://doi.org/10.1306/61EEDC24-173E-11D7-8645000102C1865D>
- McCalpin, J. P. (2009), *Paleoseismology* (Vol. 95). Academic press.
- Merrill, R.T. and McElhinny, M.W. (1983), *The Earth's Magnetic Field: Its History, Origin and Planetary Perspective*. Academic Press, London, pp. 401.
- Michetti, A.M., and Hancock, P.L. (1997), Paleoseismology: understanding past earthquakes using quaternary geology, *Journal of Geodynamics* 24 (1–4), 3–10.
- Michetti, A. M., F. A. Audemard and S. Marco (2005), Future trends in paleoseismology: Integrated study of the seismic landscape as a vital tool in seismic hazard analyses.

Tectonophysics, 408(1-4), 3-21.

Mildon, Z. K., G. P. Roberts, J. P. Faure Walker, L. Wedmore, and K. J. W. McCaffrey (2016a), Active normal faulting during the 1997 seismic sequence in Colfiorito, Umbria: Did slip propagate to the surface?, *J. Struct. Geol.*, doi:10.1016/j.jsg.2016.08.011.

Mildon Z.K., S. Toda, J. P. Faure Walker and G. P. Roberts (2016b), Evaluating models of Coulomb stress transfer: is variable fault geometry important?, *Geophys. Res. Lett.* 43(24), 12 407–12 414

Mildon, Z.K., G. P. Roberts, J. P. Faure Walker and F. Iezzi (2017), Coulomb stress transfer and fault interaction over millennia on non-planar active normal faults: the Mw 6.5-5.0 seismic sequence of 2016-2017, central Italy, *Geophysical Journal International* 210 (2) 1206-1218

Mitchell, S.G., A. Matmon, P. R. Bierman, Y. Enzel, M. Caffee and D. Rizzo, D. (2001), Displacement history of a limestone normal fault scarp, northern Israel, from cosmogenic ³⁶Cl, *J. geophys. Res.*, 106(B3), 4247– 4264.

Morewood, N. C., and G. P. Roberts (2001), Comparison of surface slip and focal mechanism slip data along normal faults: an example from the eastern Gulf of Corinth, Greece. *Journal of Structural Geology*, 23(2), 473-487.
[http://dx.doi.org/10.1016/S0191-8141\(00\)00126-7](http://dx.doi.org/10.1016/S0191-8141(00)00126-7)

Mouthereau, F., B. Deffontaines, O. Lacombe, and J. Angelier (2001), Along-strike variations of the Taiwan belt front: basement control on structural style, wedge geometry and kinematics. *Geol. Soc. Am. Spec. Pub.*

Moro, M., S. Gori, E. Falcucci, M. Saroli, F. Galadini and S. Salvi (2013), Historical earthquakes and variable kinematic behaviour of the 2009 L'Aquila seismic event

- (central Italy) causative fault, revealed by paleoseismological investigations, *Tectonophysics*, 583, 131–144. <http://dx.doi.org/10.1016/j.tecto.2012.10.036>
- National Research Council (US) (1988), Panel on Seismic Hazard Analysis, et al. Probabilistic seismic hazard analysis. National Academies, 1988.
- Nicol, A., J. Walsh, K. Berryman, and S. Nodder (2005), Growth of a normal fault by the accumulation of slip over millions of years. *Journal of Structural Geology*, 27(2), 327-342. <https://doi.org/10.1016/j.jsg.2004.09.002>
- Ohno, M. & Hamano, Y. (1993), Global analysis of the geomagnetic field: time variation of the dipole moment and the geomagnetic pole in the Holocene, *J. Geomag. Geoelectr.*, 45, 1455–1466.
- Pace, B., L. Peruzza, G. Lavecchia, and P. Boncio (2006), Layered seismogenic source model and probabilistic seismic-hazard analyses in central Italy. *Bulletin of the Seismological Society of America*, 96(1), pp.107-132.
- Pace, B., Visini, F., & Peruzza, L. (2016), FiSH: MATLAB tools to turn fault data into seismic- hazard models. *Seismological Research Letters*, 87(2A), 374-386.
- Palumbo, L., L. Benedetti, D. Bourles, A. Cinque, and R. Finkel (2004), Slip history of the Magnola fault (Apennines, Central Italy) from 36 Cl surface exposure dating: evidence for strong earthquakes over the Holocene. *Earth and Planetary Science Letters*, 225(1), 163-176. <http://dx.doi.org/10.1016/j.epsl.2004.06.012>
- Pantosti, D., G. D'Addezio and F. R. Cinti (1996), Paleoseismicity of the Ovindoli- Pezza fault, central Apennines, Italy: A history including a large, previously unrecorded earthquake in the Middle Ages (860–1300 AD), *Journal of geophysical research: solid earth*, 101(B3), 5937-5959.
- Papadopoulos, G.A., A. Ganas, A. Agalos, A. apageorgiou, I. Triantafyllou, Ch. Kontes, I. Papoutsis, and G. Diakogianni (2017), Earthquake Triggering Inferred from

- Rupture Histories, DInSAR Ground Deformation and Stress-Transfer Modelling: The Case of Central Italy During August 2016-January 2017, *Pure Appl. Geophys.*, 174, 3689-3711, doi:10.1007/s00024-017-1609-8.
- Papanikolaou, I.D., G. P. Roberts and A. M. Michetti (2005), Fault scarps and deformation rates in Lazio–Abruzzo, Central Italy: Comparison between geological fault slip-rate and GPS data. *Tectonophysics*, 408(1-4), pp.147-176. <https://doi.org/10.1016/j.tecto.2005.05.043>
- Papanikolaou, D., and Papanikolaou, I. (2007), Geological, geomorphological and tectonic structure of NE Attica and seismic hazard implications for the northern edge of the Athens plain. *Bulletin of the Geological Society of Greece*, 40(1), 425-438.
- Papanikolaou, I. D., D. I. Papanikolaou, and E. L. Lekkas (2008), Low slip-rate faults around big cities: a challenging threat. The Afidnai fault as a case study for the city of Athens, In *Proceedings of the 14th World Conference on Earthquake Engineering* (pp. 12-17).
- Papanikolaou, I. D., R. Van Balen, P. G. Silva and K. Reicherter (2015), Geomorphology of active faulting and seismic hazard assessment: New tools and future challenges. *Geomorphology*, 237, 1-13.
- Papazachos, B. C., & Papazachou, C. (2003), *The earthquakes of Greece*, Ziti Publ. Co., Thessaloniki, Greece, 286.
- Patacca, E., R. Sartori, and P. Scandone (1990), Tyrrhenian basin and Apenninic arcs: kinematic relations since late Tortonian times. *Mem. Soc. Geol. It.*, 45(1), 425-451.
- Pantosti, D., G. D’Addezio, and F. R. Cinti., Paleoseismicity of the Ovindoli- Pezza fault, central Apennines, Italy: A history including a large, previously unrecorded

- earthquake in the Middle Ages (860–1300 AD), *Journal of geophysical research: solid earth* 101.B3 (1996): 5937-5959.
- Pavlidis, S. B., G. Papadopoulos and A. Ganas (2002), The fault that caused the Athens September 1999 Ms= 5.9 earthquake: Field observations. *Natural Hazards*, 27(1-2), 61-84.
- Perlt, J., and Heinert, M. (2006), Kinematic model of the South Icelandic tectonic system, *Geophysical Journal International*, 164(1), 168-175. <https://doi.org/10.1111/j.1365-246X.2005.02795.x>
- Pierantoni, P., G. Deiana, and S. Galdenzi (2013), Stratigraphic and structural features of the Sibillini Mountains (Umbria-Marche Apennines, Italy). *Italian Journal of Geosciences*, 132(3), 497-520. DOI: 10.3301/IJG.2013.08
- Pizzi, A., and V. Scisciani (2000), Methods for determining the Pleistocene–Holocene component of displacement on active faults reactivating pre-Quaternary structures: examples from the central Apennines (Italy), *Journal of Geodynamics* 29, 29(3-5), pp.445-457. [https://doi.org/10.1016/S0264-3707\(99\)00053-8](https://doi.org/10.1016/S0264-3707(99)00053-8)
- Pizzi, A., and F. Galadini (2009), Pre-existing cross-structures and active fault segmentation in the northern-central Apennines (Italy), *Tectonophysics*, 476(1-2), 304-319. <https://doi.org/10.1016/j.tecto.2009.03.018>
- Pizzi, A., A. Di Domenica, F. Gallović, L. Luzi, and R. Puglia (2017), Fault Segmentation as Constraint to the Occurrence of the Main Shocks of the 2016 Central Italy Seismic Sequence, *Tectonics*, 36, doi:10.1002/2017TC004652.
- Roberts, G. P. (1996a), Noncharacteristic normal faulting surface ruptures from the Gulf of Corinth, Greece. *Journal of Geophysical Research: Solid Earth*, 101(B11), 25255-25267. 10.1029/96JB02119

- Roberts, G. P. (1996b), Variation in fault-slip directions along active and segmented normal fault systems. *Journal of Structural Geology*, 18(6), 835-845.
- Roberts, G.P. and Koukouvelas, I. (1996), Structural and seismological segmentation of the Gulf of Corinth fault system: implications for models of fault growth, *Analli di Geofisica*, 39, 619– 646.
- Roberts, G.P. and Ganas, A. (2000), Fault- slip directions in central and southern Greece measured from striated and corrugated fault planes: Comparison with focal mechanism and geodetic data. *Journal of Geophysical Research: Solid Earth*, 105(B10), pp.23443-23462.
- Roberts, G. P., A. M. Michetti, P. Cowie, N. C. Morewood, and I. Papanikolaou (2002), Fault slip- rate variations during crustal- scale strain localisation, central Italy. *Geophysical Research Letters*, 29(8).
- Roberts, G. P., and A. M. Michetti (2004), Spatial and temporal variations in growth rates along active normal fault systems: an example from The Lazio–Abruzzo Apennines, central Italy. *Journal of Structural Geology*, 26(2), 339-376. [http://dx.doi.org/10.1016/S0191-8141\(03\)00103-2](http://dx.doi.org/10.1016/S0191-8141(03)00103-2)
- Roberts, G. P. (2007), Fault orientation variations along the strike of active normal fault systems in Italy and Greece: Implications for predicting the orientations of subseismic-resolution faults in hydrocarbon reservoirs. *AAPG Bulletin*, 91(1), 1-20.
- Roberts, G.P., B. Raithatha, G. Sileo, A. Pizzi, S. Pucci, J.F. Walker, M. Wilkinson, K. McCaffrey, R. J. Phillips, A. M. Michetti, and L. Guerrieri (2010), Shallow subsurface structure of the 2009 April 6 M w 6.3 L'Aquila earthquake surface rupture at Paganica, investigated with ground-penetrating radar, *Geophysical Journal International*, 183(2), pp.774-790. <https://doi.org/10.1111/j.1365-246X.2010.04713.x>

- Rotevatn, A., C. A. L. Jackson, A. B. M. Tvedt, R. E. Bell and I. Blækkan (2018), How do normal faults grow?, *Journal of Structural Geology*.
<https://doi.org/10.1016/j.jsg.2018.08.005>
- Rovida A., Locati M., Camassi R., Lolli B., Gasperini P., 2016. CPTI15, the 2015 version of the Parametric Catalogue of Italian Earthquakes. Istituto Nazionale di Geofisica e Vulcanologia. doi:<http://doi.org/10.6092/INGV.IT-CPTI15>
- Saemundsson, K. (1992), Geology of the Thingvallavatn Area, *Oikos*, 64(1/2), 40-68.
doi:10.2307/3545042
- Saemundsson, K. (2006), The 1789 Rifting Event in the Hengill Volcanic System, SW-Iceland, American Geophysical Union, Fall Meeting 2006, abstract id. T41B-1568
- Schimmelpfennig, I., L. Benedetti, R. Finkel, R. Pik, P. H. Blard, D. Bourles, ... and A. Williams (2009), Sources of in-situ ³⁶Cl in basaltic rocks. Implications for calibration of production rates. *Quaternary Geochronology*, 4(6), 441-461.
- Schlagenhauf, A., Y. Gaudemer, L. Benedetti, I. Manighetti, L. Palumbo, I. Schimmelpfennig, R. Finkel, and K. Pou (2010), Using in situ Chlorine-36 cosmnuclide to recover past earthquake histories on limestone normal fault scarps: a reappraisal of methodology and interpretations. *Geophys. J. Int.* 182 (1), 36e72.
<http://dx.doi.org/10.1111/j.1365-246X.2010.04622.x>
- Schlagenhauf, A., I. Manighetti, L. Benedetti, Y. Gaudemer, R. Finkel, J. Malavieille, and K. Pou, (2011), Earthquake supercycles in Central Italy, inferred from ³⁶Cl exposure dating. *Earth and Planetary Science Letters*, 307(3-4), 487-500.
- Schlische, R. W., S. S. Young, R. V. Ackermann and A. Gupta (1996), Geometry and scaling relations of a population of very small rift-related normal faults. *Geology*, 24(8), 683-686.
- Scholz, C. H., & Gupta, A. (2000), Fault interactions and seismic hazard. *Journal of*

- Geodynamics, 29(3-5), 459-467.
- Scholz, C. H. (2018). The mechanics of earthquakes and faulting. Cambridge university press.
- Scognamiglio, L., E. Tinti, E. Casarotti, S. Pucci, F. Villani, M. Cocco, M. Magnoni, A. Michelini, D. Dreger (2018), Complex Fault Geometry and Rupture Dynamics of the MW 6.5, 30 October 2016, Central Italy Earthquake. *Journal of Geophysical Research: Solid Earth*, 123(4), 2943-2964.
- Serva, L., and Slemmons, D.B. (1995), Perspective in paleoseismology, A.E.G. Special Publication, vol. 6. Peanut Butter Publishing, Seattle, Washington (138 pp.).
- Serva, L., E. Vittori, L. Ferrelì and A.M. Michetti (1997), Geology and seismic hazard, In: Grellet, B., Mohammadioun, B., Hays, W. (Eds.), Proceedings of the Second France–United States Workshop on Earthquake Hazard Assessment in Intraplate Regions: Central and Eastern United States and Western Europe, October 16, 1995, Nice, France, 20–24, Ouest Editions, Nantes, France.
- Sinton, J., K. Gronvold, and K. Sæmundsson (2005), Postglacial eruptive history of the Western Volcanic Zone, Iceland, *Geochem. Geophys. Geosyst.*, 6, Q12009, doi:10.1029/2005GC001021
- Sonnette, L., J. Angelier, T. Villemin, and F. Bergerat (2010), Faulting and fissuring in active oceanic rift: Surface expression, distribution and tectonic–volcanic interaction in the Thingvellir Fissure Swarm, Iceland. *Journal of Structural Geology*, 32(4), 407-422. <https://doi.org/10.1016/j.jsg.2010.01.003>
- Stein, R.S. (1999), The role of stress transfer in earthquake occurrence. *Nature*, 402(6762), pp.605-609.
- Stein, S., R. J. Geller and M. Liu (2012), Why earthquake hazard maps often fail and what to do about it. *Tectonophysics*, 562, 1-25.

- Stirling, M., D. Rhoades and K. Berryman (2002), Comparison of earthquake scaling relations derived from data of the instrumental and preinstrumental era, *Bulletin of the Seismological Society of America*, 92(2), pp.812-830. <https://doi.org/10.1785/0120000221>
- Stone, J. O., G. L. Allan, L. K. Fifield, and R. G. Cresswell (1996), "Cosmogenic chlorine-36 from calcium spallation." *Geochimica et Cosmochimica Acta* 60, no. 4: 679-692.
- Suter, M. (2008a). Structural configuration of the Otates fault (southern Basin and Range Province) and its rupture in the 3 May 1887 Mw 7.5 Sonora, Mexico, earthquake. *Bulletin of the Seismological Society of America*, 98(6), 2879-2893.
- Suter, M. (2008b). Structural configuration of the Teras Fault (southern Basin and Range Province) and its rupture in the 3 May 1887 Mw 7.5 Sonora, Mexico earthquake. *Revista Mexicana de Ciencias Geológicas*, 25(1), 179-195.
- Suter, M. (2015). Rupture of the Pitáycachi Fault in the 1887 Mw 7.5 Sonora, Mexico earthquake (southern Basin- and- Range Province): Rupture kinematics and epicenter inferred from rupture branching patterns. *Journal of Geophysical Research: Solid Earth*, 120(1), 617-641. DOI: 10.1002/2014JB011244
- Stewart, I. S., and Hancock, P. L. (1990), What is a fault scarp. *Episodes*, 13(4), 256-263.
- Tarquini S., I. Isola, M. Favalli , F. Mazzarini, M. Bisson, M.T. Pareschi, E. Boschi (2007). TINITALY/01: a new Triangular Irregular Network of Italy, *Annals of Geophysics*, 50, 407-425.
- Tarquini S., S. Vinci, M. Favalli, F. Doumaz, A. Fornaciai, L. Nannipieri, (2012), Release of a 10-m-resolution DEM for the Italian territory: Comparison with global-coverage DEMs and anaglyph-mode exploration via the web, *Computers & Geosciences* , 38, 168-170. doi: doi:10.1016/j.cageo.2011.04.018

- Tinti, E., L. Scognamiglio, A. Michelini and M. Cocco (2016), Slip heterogeneity and directivity of the ML 6.0, 2016, Amatrice earthquake estimated with rapid finite-fault inversion. *Geophysical Research Letters*, 43(20), 10-745.
- Toda S., R.S. Stein, K. Richards-Dinger and S. B. Bozkurt (2005), Forecasting the evolution of seismicity in southern California: animations built on earthquake stress transfer, *J. geophys. Res.* 110(B5), B05S16, doi:10.1029/2004JB003415.
- Trippanera, D., V. Acocella, J. Ruch, and B. Abebe (2015), Fault and graben growth along active magmatic divergent plate boundaries in Iceland and Ethiopia, *Tectonics*, 34, doi:10.1002/2015TC003991.
- Tryggvason, E. (1990), Höggun Almanagjár. Mælingar á Þingvöllum 1990 [Displacement of Almanagja. Measurements at Thingvellir 1990], Nord. Volcanol. Inst., Univ. of Iceland, Reykjavik.
- Tucker, G. E., S. W. McCoy, A. C. Whittaker, G. P. Roberts, S. T. Lancaster, and R. Phillips (2011), Geomorphic significance of postglacial bedrock scarps on normal-fault footwalls, *J. Geophys. Res.*, 116, F01022, doi:10.1029/2010JF001861.
- Valentini, A., F. Visini, and B. Pace (2017), Integrating faults and past earthquakes into a probabilistic seismic hazard model for peninsular Italy. *Natural Hazards Earth System Sciences*.
- Vezzani, L., and F. Ghisetti (1998), Carta Geologica dell'Abruzzo, Scala 1:100,000. Firenze: S.EL.CA.
- Vezzani, L., A. Festa and F. C. Ghisetti (2010), Geology and tectonic evolution of the Central-Southern Apennines, Italy (Vol. 469). Geological Society of America.
- Villamor, P. and K. Berryman (2001), A late Quaternary extension rate in the Taupo Volcanic Zone, New Zealand, derived from fault slip data, *New Zealand Journal of*

Geology and Geophysics, 44(2), pp.243-269.

<https://doi.org/10.1080/00288306.2001.9514937>

Villani, F., and V. Sapia (2017), The shallow structure of a surface-rupturing fault in unconsolidated deposits from multi-scale electrical resistivity data: The 30 October 2016 Mw 6.5 central Italy earthquake case study, *Tectonophysics* 717 (2017): 628-644.

Villani, F., R. Civico, S. Pucci L. Pizzimenti, R. Nappi, P.M. De Martini and the Open EMERGEO Working Group (2018), A database of the coseismic effects following the 30 October 2016 Norcia earthquake in Central Italy, *Scientific Data*, doi: 10.1038/sdata.2018.49

Villemin, T., and Bergerat, F. (2013), From surface fault traces to a fault growth model: the Vogar fissure swarm of the Reykjanes Peninsula, Southwest Iceland, *Journal of Structural Geology*, 51, 38-51. <https://doi.org/10.1016/j.jsg.2013.03.010>

Visini, F., A. Valentini, T. Chartier, O. Scotti and B. Pace (2019), Computational Tools for Relaxing the Fault Segmentation in Probabilistic Seismic Hazard Modelling in Complex Fault Systems, *Pure and Applied Geophysics*, 1-23, <https://doi.org/10.1007/s00024-019-02114-6>.

Walsh, J. J., A. Nicol and C. Childs (2002), An alternative model for the growth of faults. *Journal of Structural Geology*, 24(11), 1669-1675. [https://doi.org/10.1016/S0191-8141\(01\)00165-1](https://doi.org/10.1016/S0191-8141(01)00165-1)

Walsh, J. J., W. R. Bailey, C. Childs, A. Nicol and C. G. Bonson (2003), Formation of segmented normal faults: a 3-D perspective. *Journal of Structural Geology*, 25(8), 1251-1262. [https://doi.org/10.1016/S0191-8141\(02\)00161-X](https://doi.org/10.1016/S0191-8141(02)00161-X)

Walters, R. J., J. R. Elliott, N. D'Agostino, P. C. England, I. Hunstad, J. A. Jackson, B. Parsons, R. J. Phillips, and G. Roberts (2009), The 2009 L'Aquila earthquake

- (central Italy): A source mechanism and implications for seismic hazard, *Geophys. Res. Lett.*, 36, L17312, doi:10.1029/2009GL039337.
- Walters, R. J., L. C. Gregory, L. N. J. Wedmore, T. J. Craig, K. McCaffrey, M. Wilkinson, J. Chen, Z. Li, J. R. Elliot, H. Goodall, F. Iezzi, F. Livio, A. M. Michetti, G. Roberts and E. Vittori (2018), Dual control of fault intersections on stop-start rupture in the 2016 Central Italy seismic sequence. *Earth and Planetary Science Letters*, 500, 1-14.
- Wang, L., H. Gao, G. Feng, and W. Xu (2018), Source parameters and triggering links of the earthquake sequence in central Italy from 2009 to 2016 analyzed with GPS and InSAR data, *Tectonophysics*, 774, 285-295, doi:10.1016/j.tecto.2018.07.013.
- Wells, D. L., and K. J. Coppersmith (1994), New Empirical Relationships among Magnitude, Rupture Length, Rupture Width, Rupture Area, and Surface Displacement, *Bull. Seismol. Soc. Am.*, 84(4), 974–1002.
- Wesnousky, S. G. (2008), Displacement and geometrical characteristics of earthquake surface ruptures: Issues and implications for seismic-hazard analysis and the process of earthquake rupture, *Bull. Seismol. Soc. Am.*, 98(4), 1609-1632.
- Whittaker, A. C., P. A. Cowie, M. Attal, G. E. Tucker, and G. P. Roberts (2007), Bedrock channel adjustment to tectonic forcing: Implications for predicting river incision rates. *Geology*, 35(2), 103-106.
- Wilkinson, M., K. J. W. McCaffrey, G. Roberts, P. A. Cowie, R. J. Phillips, A. M. Michetti, E. Vittori, L. Guerrieri, A. M. Blumetti, A. Bubeck, and A. Yates (2010), Partitioned postseismic deformation associated with the 2009 Mw 6.3 L'Aquila earthquake surface rupture measured using a terrestrial laser scanner, *Geophysical Research Letters*, 37(10) DOI: 10.1029/2010GL043099
- Wilkinson, M., G. P. Roberts, K. McCaffrey, P. A. Cowie, J. P. Faure Walker, I.

- Papanikolaou, R. J. Phillips, A. M. Michetti, E. Vittori, L. Gregory, L. Wedmore, Z. K. Watson (2015), Slip distributions on active normal faults measured from LiDAR and field mapping of geomorphic offsets: an example from L'Aquila, Italy, and implications for modelling seismic moment release, *Geomorphology*, 237, 130–141, doi:10.1016/j.geomorph.2014.04.026.
- Wilkinson, M.W., K.J.W. McCaffrey, R. R. Jones, G. P. Roberts, R. E. Holdsworth, L. C. Gregory, R. J. Walters, L. Wedmore, H. Goodall, F. Iezzi, (2017) Near-field fault slip of the 2016 Vettore M_w 6.6 earthquake (Central Italy) measured using low-cost GNSS. *Nature Scientific Reports*.
- Wolfe, C. J., I. T. Bjarnason, J. C. VanDecar and S. C. Solomon (1997), Seismic structure of the Iceland mantle plume. *Nature*, 385(6613), 245. <https://doi.org/10.1038/385245a0>
- Working Group on Utah Earthquake Probabilities (WGUEP), 2016, Earthquake probabilities for the Wasatch Front region in Utah, Idaho, and Wyoming: Utah Geological Survey Miscellaneous Publication 16-3, 164 p., 5 appendices.
- Xu, G., C. Xu, Y. Wen, and G. Jiang (2017), Source Parameters of the 2016-2017 Central Italy Earthquake Sequence from the Sentinel-1, ALOS-2 and GPS data, *Remote Sens.*, 9, 1182, doi:10.3390/rs9111182.
- Yang, S., Odah, H. and Shaw, J. (2000), Variations in the geomagnetic dipole moment over the last 12 000 years. *Geophys. J. Int.*, 140, 158–162.
- Yu, S. B., L. C. Kuo, Y. J. Hsu, H. H. Su, C. C. Liu, C. S. Hou,... and T. F. Tseng, (2001), Preseismic deformation and coseismic displacements associated with the 1999 Chi-Chi, Taiwan, earthquake. *Bulletin of the Seismological Society of America*, 91(5), 995-1012.
- Zreda, M. and Noller, J.S. (1998), Ages of prehistoric earthquakes revealed by

cosmogenic Chlorine-36 in a Bedrock fault scarp at Hebgen Lake, *Science*, 282, 1097–1099.

Appendix

Supplementary material on a CD-ROM is submitted with this thesis. A guide of the material is outlined below.

Appendix A presents the structural data collected along the Mt. Vettore fault following the 2016 Central Italy earthquakes. A1 shows the database of structural data collected following the 24th August 2016 M_w 6.0 earthquake. A2 shows the database of structural data collected following the 30th October 2016 M_w 6.5 earthquake.

Appendix B presents the modelling of the coseismic throw within the fault bend following the 2016 Central Italy earthquakes. B1 presents the spreadsheet used to model the coseismic throw within fault bends using structural data as input. B2 shows the modelling of the coseismic throw within the bend following the 24th August 2016 M_w 6.0 earthquake. B3 shows the modelling of the coseismic throw within the bend following the 30th October 2016 M_w 6.5 earthquake.

Appendix C presents field measurements and modelling following the other historical large normal faulting earthquakes that ruptured along fault bends. C1 shows field measurements and modelling of the 1887 M_w 7.5 Sonora earthquake, Mexico. C2 shows

field measurements and modelling of the 1981 Corinth M_w 6.7-6.4 earthquake, Greece. C1 shows field measurements and calculations of the 1983 M_w 7.3 Borah Peak earthquake, USA.

Appendix D presents the measurements of the long-term throw of the Mt. Vettore fault obtained from the geological cross sections shown in Figure 4.3, and used to build the long-term throw profile shown in Figure 4.9a.

Appendix E presents the calculations to evaluate the effect of the fault bends on scaling relationships, seismic moment and stress drop, as shown in Figures 4.16 and 4.17. E1 shows calculations based on Wells and Coppersmith (1994) empirical scaling relationships. E2 shows calculations based on Wesnousky (2008) empirical scaling relationships.

Appendix F presents measurements of slip along the Aterno Valley Fault System. F1 shows measurements of long-term throw obtained from the geological cross sections shown in Figure 5.4, and used to build the long-term throw profile shown in Figure 5.8a. F2 shows measurements of the coseismic slip obtained from different geodetic and seismological fault models (Atzori et al., 2009; Walters et al., 2009; Cheloni et al., 2010; Cirella et al., 2010; D'Agostino et al., 2012), and used to build profiles shown in Figure 5.8e.

Appendix G presents the scarp profiles constructed across normal faults in Iceland.

Appendix H presents measurements obtained from the scarp profiles built across normal faults in Iceland. H1 shows measurements across the Almannagja fault. H2 shows measurements across the Hengill faults. H3 shows measurements across the Wdf1. H4 shows measurements across the Wdf2. H5 shows measurements across the Wdf3. H6 shows measurements across the Wdf4.

Appendix I presents structural data collected along the faults sampled in Attica, Greece, in the surroundings of the sampling sites. I1 shows structural data collected along the Milesi fault. I2 shows structural data collected along the Malakasa fault. I3 shows structural data collected along the Fili fault.

Appendix L presents the results of the analysis performed with an electron microprobe of the thin sections obtained from samples collected on the Fili fault, Greece. L1 shows the analysis of the thin section obtained from the sample FIL-16. L2 shows the analysis of the thin section obtained from the sample FIL+256.

Appendix M presents the input files for the application of the Beck et al. (2018) code to model the cosmogenic ^{36}Cl concentrations on fault planes in Attica, Greece. M1 shows the values used to fill the “.m file”. M2 shows the rock files, containing the chemical composition of the rock samples and the content of cosmogenic ^{36}Cl per each fault; values from each fault are used as input in the “rock.txt” files. M3 shows the chemical composition of colluvium used in the modelling; highlighted in yellow are the values used as input for the “colluvium.txt” file. M4 shows the calculations to obtain scaling factors for the spallation and muons capture, following Stone et al. (2000), used as input in the “magfield.txt” file.

Appendix N presents the modelling of the slip distribution of the 30th October 2016 M_w 6.5 Mt. Vettore earthquake using the real non-planar fault geometry. N1 shows modelling performed with depth of the bull's eye at 2.5 m. N2 shows modelling performed with depth of the bull's eye at 2.6 m. N3 shows modelling performed with depth of the bull's eye at 2.7 m (in yellow are highlighted the iterated values better representing the real values of M_w and coseismic slip at the surface of the earthquake, used to model the coseismic vertical displacement). N4 shows modelling performed with depth of the bull's eye at 2.8 m. N5 shows modelling performed with depth of the bull's eye at 2.9 m. N6 shows modelling performed with depth of the bull's eye at 3.0 m. N7 shows modelling performed with depth of the bull's eye at 3.2 m.